# Spectral Measurements of Hydrogen Lyman-alpha in the Atmospheres of Venus and Jupiter Using a Sounding Rocket and the Hubble Space Telescope

by

Benjamin Andrew Corbin

B.S. Aerospace Engineering
University of Central Florida, 2008

Submitted to the Department of Aeronautics and Astronautics
and
Department of Earth, Atmospheric, and Planetary Sciences
in Partial Fulfillment of the Requirements for the Degrees of
Master of Science in Aeronautics and Astronautics
and
Master of Science in Planetary Science
at the
MASSACHUSETTS INSTITUTE OF TECHNOLOGY
February 2011





Signature of Author: .....
Department of Aeronautics and Astronautics
and
Department of Earth, Atmospheric, and Planetary Sciences
January 27, 2011

Certified by: .....
Jeffrey Hoffman
Professor of Aeronautics and Astronautics
Thesis Supervisor

Certified by: .....
John T. Clarke
Professor of Astronomy, Boston University Center for Space Physics
Thesis Supervisor

Read by: .....
Maria T. Zuber
Professor of of Earth, Atmospheric, and Planetary Sciences
Department Thesis Reader

Accepted by: .....
Eytan H. Modiano
Associate Professor of Aeronautics and Astronautics
Chair, Committee on Graduate Students

# Spectral Measurements of Hydrogen Lyman-alpha in the Atmospheres of Venus and Jupiter Using a Sounding Rocket and the Hubble Space Telescope

by

Benjamin Andrew Corbin

Submitted to the Department of Aeronautics and Astronautics
and
Department of Earth, Atmospheric, and Planetary Sciences
on January 27, 2011, in Partial Fulfillment of the
Requirements for the Degrees of
Master of Science in Aeronautics and Astronautics
and
Master of Science in Planetary Science

## Abstract

The Lyman-alpha emission is a key signature of the presence of hydrogen, and from this emission many properties of planetary atmospheres can be analyzed. Two projects are studying this emission on two planets for two different scientific purposes. On Venus, the Lyman-alpha emission is being studied to measure the deuterium to hydrogen (D/H) ratio of the atmosphere's exobase. One of the mysteries of Venus is why it is so dry compared to Earth, and this measurement will constrain how much water Venus has lost since planetary formation. The measurement will be made using a telescope with a spectrograph launched on a sounding rocket scheduled for launch in early 2012 from White Sands Missile Range. On Jupiter, the Lyman-alpha emission was observed to better characterize an anomalously bright region near the equator called the Lyman-alpha Bulge. Images and spectra taken by the Hubble Space Telescope while the Bulge was on the limb were analyzed. The brightness and scale height of the atmosphere along the limb was derived from the image data.. The spectral data confirm evidence of a superthermal component and that is moving more than 15 km/s faster than remaining hydrogen. This analysis shows evidence that the Bulge is influenced by similar processes that create equatorial anomalies similar to the ones on Earth.

Thesis Supervisor: Jeffrey Hoffman
Title: Professor of Aeronautics and Astronautics

Thesis Supervisor: John T. Clarke
Title: Professor of Astronomy, Boston University Center for Space Physics

# Acknowledgments

First and foremost, I want to thank my loving family for all the years of support they have given me. Mom, Dad, Brian, and Claire, you are the best family anyone could ask for and I love you all. You have given me encouragement when I needed it most, taught me discipline to follow through with my commitments, and gave me sense of humor that has gotten me through even the most difficult chapters of my life.

I would also like to thank the many teachers who have inspired me to explore further and widen the breadth of my education. Mr. Webster's 7th grade science class and Mr. Griffith's Current World Problems class were especially important for me as a growing student. I also could not be where I am without Charla Cotton and the entire staff of the Northwest Florida State College (formerly Okaloosa-Walton Community College) Collegiate High School.

Scouting was also a tremendous influence in my decision to pursue space exploration. I want to thank the adult leadership of Boy Scout Troop 529 and Venture Crew 520, especially George Pelfrey and Mike Stanley for their efforts to help me attain the rank of Eagle Scout.

Finally, I would like to thank Dr. Jeffrey Hoffman, Dr. John Clarke, and Carol Carveth for working with me over the past two and a half years. It has been a pleasure working VeSpR and the Hubble data and the experience in both engineering and science has been incredible.

**TL;DR -** I worked on a sounding rocket payload to study Venus and designed a lot of the new components, but the launch got delayed so we don't have data yet. I also studied the Lyman-alpha Bulge on Jupiter using Hubble data from an earlier campaign and found evidence of other activity that had not been seen before..

# Contents

# List of Figures

# List of Tables

# Chapter 1

# Introduction

Although the public may not understand the difference between scientists and engineers because the two groups are so closely related, in reality scientists and engineers are vastly different. One of the major problems in the design of spacecraft for scientific missions is communication between the scientists acting as the Principal Investigators or customers and the engineering teams designing the spacecraft to meet the expectations of the scientists. Without a mutual understand of the needs and expectations from both sides, mission costs can inflate beyond their budgets and mission success can be compromised because a spacecraft was designed for the wrong mission.

For that reason, it is important to have personnel that have worked with and are familiar with both groups to ensure mission success. This work is the synthesis of two scientific projects to study planetary atmospheres. The first is Project VeSpR, or the Venus Spectral Rocket, is currently in a stage of engineering. The second is an analysis of high-resolution spectra from Jupiter's Lyman-alpha Bulge, which is primarily a scientific project.

The immediate goal of Project VeSpR is to measure the deuterium to hydrogen ratio (D/H) in the upper atmosphere of Venus as it varies with altitude. This will be accomplished with a telescope and an ultraviolet spectrograph launched aboard a suborbital sounding rocket.

Scientifically, understanding how the D/H ratio varies in Venus' atmosphere is critical to modeling the atmospheric escape processes of not only Venus but also

Earth and all planets. In addition, it is especially important for understanding how water is lost from planetary surfaces and atmospheres, since an elevated D/H ratio is evidence that a body has lost a significant amount of water in its history. This is a key factor in understanding global climate change here on Earth and in searching for extraterrestrial life beyond Earth. Furthermore, knowing the D/H ratio of Venus and how it varies in the upper atmosphere can help create a better understanding of planetary formation by constraining the conditions under which Venus was formed in the planetary nebula, which also constrains the conditions under which Earth and other Earth-like planets could have formed.

However, Project VeSpR is more than a pure science experiment; it is also an engineering challenge. The VeSpR payload had been launched many times before, but due to previous failures, obsolete electronics, and degrading systems, a lot of engineering work was needed before VeSpR would be a success. Although this is not a deep-space or human space mission, from a systems engineering perspective, VeSpR is very complex. Many subsystems within the VeSpR payload were redesigned and rebuilt. The interfaces of the payload needed to be designed to work with new interfaces on the rest of the vehicle. Verification and validation testing needed to be done on all subsystems, which sometimes required redesigning and rebuilding of laboratory testing equipment. Just like all science-driven space missions, the engineering comes long before the science starts.

Because the launch of VeSpR was delayed passed the deadline for this work, the sections detailing work on VeSpR will be focused mostly on engineering work with some modeling of the expected scientific data. The data from VeSpR will be analyzed after its launch, now expected to take place between December 2011 and February 2012.

The second scientific project in this work is a study of a region in Jupiter's upper atmosphere aligned with the magnetic equator that has an anomalously bright Lyman-alpha emission. This anomaly is known as the Lyman-alpha Bulge. Spectra from the Hubble Space Telescope are being analyzed to better characterize the motion and brightness and hydrogen in this region compared to other regions on the opposite

side of the planet and in northern and southern latitudes near the auroral regions of Jupiter.

Jupiter has the strongest magnetic field in the Solar System. Understanding what is causing this region to emit more Lyman-alpha radiation compared to other areas in the planet is important understanding magnetospheric processes in Jupiter and other giant planets and exoplanets. While there are many hypotheses to what could be causing this extra brightness, none have been conclusively proven. In addition to discovering the source of this added energy in the Bulge, a secondary goal of this study is to fit data to a radiative transfer model and hopefully improve the model's fidelity.

Both of these projects involve the measurement of the Lyman-alpha emission from the upper atmosphere of planets using ultraviolet spectrographs with identical echelle gratings, one inside the Hubble Space Telescope's Space Telescope Imaging Spectrograph and one inside the VeSpR payload's spectrograph. While the fundamental physical processes producing the observed phenomena and the goals of the two projects may be completely different, they are both using the same natural phenomenon as a means to learn more about the Solar System. VeSpR focuses on the Lyman-alpha emission from both hydrogen and deuterium to obtain the D/H ratio of Venus, and the Jupiter Bulge study focuses on solely the hydrogen Lyman-alpha emission to understand energetic activity in Jupiter.

Chapter 2 provides background for much of the planetary science and fundamental physics involved with both projects as well as details on the hardware used for both studies. Chapter 3 covers previous work in sounding rockets and past observations of Venus and Jupiter that led to these two studies. Chapters 4 and 5 cover the work done on the Venus Spectral Rocket up to this point; Chapter 4 outlines the mission, laboratory preparations, and preliminary testing, while Chapter 5 details the systems-level design considerations, component design, fabrication, and testing in preparation for integration testing at Wallops Flight Facility. Chapter 6 details work on the Jupiter Bulge by presenting the data, describing the data reduction and analysis pipeline, and discussing results. Chapter 7 discusses conclusions and details

future work and the timetable in which more deliverables will be expected in both projects.

# Chapter 2

# Background

## 2.1 The Lyman-alpha Emission

The universe is a vast and wondrous place filled with exotic structures, like stars, planets, galaxies, and superclusters. However, there is evidence that astronomers are only able to observe about 4% of all the mass in the universe [50]. That 4% of matter is almost entirely baryonic matter, or matter made of baryons, which are mostly protons and neutrons. The remaining observable matter in the universe, leptons and photons, composes a much smaller fraction of the overall mass. The majority of matter in the universe is categorized for now as Dark Matter and Dark Energy until a ways to study or interact with them are discovered.

Of the baryonic matter in the universe, nearly three-quarters of it is made of the element hydrogen, around 23% is made of the element helium, and less than two percent is made of all the other elements on the periodic table. Hydrogen is so abundant in the universe because it was the first element to form from the ashes of the Big Bang. It is also the simplest element, composed of only one proton and one electron.

### 2.1.1 Energy States of Electrons in Atoms

The Lyman-alpha emission is a key signature of hydrogen. Whether hydrogen is in the Sun, in a distant star, at the top of a planetary atmosphere, or clumped in an interstellar dust cloud thousands of light-years across, it can be identified by its Lyman-alpha emission. Understanding what the Lyman-alpha emission is essential to both projects encompassed by this thesis since both are directly measuring this signature of hydrogen.

According to the Bohr model of atom, an electron in a hydrogen atom has an energy that is determined by its principal quantum number $n$, where the energy of the electron is

$$E_{electron} = -\frac{\mu e^4}{32\pi^2\epsilon_0^2\hbar^2} \cdot \frac{1}{n^2} = -13.6eV\frac{1}{n^2} \tag{2.1}$$

where $\epsilon_0$ is the permittivity of free space, $\hbar = h/2\pi$, $h$ is Planck's Constant, $n$ is the principal quantum number (which must be an integer), and $\mu$ is the reduced mass given by

$$\mu = \frac{m_e m_n}{m_e + m_n} \tag{2.2}$$

where $m_e$ is the mass of an electron and $m_n$ is the mass of the atomic nucleus [7]. For a hydrogen atom, the nucleus is simply a proton with a mass of 1.67 x $10^{-27}$kg.

When an electron moves from a higher quantum state to a lower quantum state, the difference in energy between the two quantum states is emitted as a photon. A transition from any quantum state down to the ground state $n = 1$ is called a Lyman transition. The transition between the $n = 2$ quantum state to the $n = 1$ ground state in a hydrogen atom is called the Lyman-alpha transition, and the emitted photon's energy is equal to

$$E_{photon} = E_{electron_{n=2}} - E_{electron_{n=1}} = -13.6\left(\frac{1}{2^2} - \frac{1}{1^2}\right) = 10.2eV \tag{2.3}$$

The wavelength of the photon is equal to

$$\lambda_{photon} = \frac{hc}{E_{photon}} = 1215.668\text{Å} \tag{2.4}$$

where $c$ is the speed of light. Light with a wavelength of 1215.668 Å is called Lyman-alpha light because of this electron transition and photon emission.

Deuterium is an isotope of hydrogen, meaning is has the same chemical properties and reacts chemically with other atoms in the exact same processes that hydrogen does, but its nucleus is composed of one proton and one neutron, so it weighs almost twice as much as a hydrogen atom's nucleus.

This changes the reduced mass $\mu$ and the energy of an electron $E_{electron}$ in any quantum state $n$. Since the quantum states have different energies, there is a difference between the Lyman-alpha transition energies, corresponding to a different wavelength of the Lyman-alpha transition.

In deuterium, the Lyman-alpha electron transition produces a photon with a wavelength of 1215.330 Å. This small difference between the Lyman-alpha emissions of hydrogen and deuterium is how the two can be separately identified.

### 2.1.2 The Origins of Hydrogen and Deuterium

At a time t $\approx$ 0.1 seconds after the Big Bang, the temperature of the universe was close to T $\approx$ 3 x $10^{10}$ K [50]. Protons and neutrons were in equilibrium with each other since a neutron and an electron neutrino could combine to form a proton and an electron (the reverse is also true) or a neutron and a positron could combine to form a proton and an electron anti-neutrino. However, because of the greater rest energy of the neutron, protons were becoming more abundant as the universe cooled. Had this trend continued, the ratio between neutrons and protons would be a million to one within by the time the universe was t $\approx$ 6 minutes old.

However, neutrons and protons only stay in equilibrium because of the interactions of baryonic matter with the weak force. The cross-section for interaction varies with the square of the temperature, and by the time the universe was t $\approx$ 1 second old, the temperature had dropped to T $\approx$ 3 x $10^9$ K. At this temperature, the Hubble

expansion parameter overcame the rate at which the weak force interacted with baryonic matter, so the ratio of neutrons to protons froze at about 0.2. This explains why the Big Bang left three quarters of the baryonic matter in the universe as unfused protons; there were simply less neutrons left over.

Free neutrons are unstable. The decay time of a free neutron is $\tau = 890$ seconds, or about 15 minutes. This means, given a collection of free neutrons, half of them will be gone after 15 minutes, three-quarters will be gone after 30 minutes, and so on. Neutrons are only stable in the nuclei of atoms, so in order to survive much longer after the Big Bang, they had to fuse with protons.

The weak force is now too weak to interact with most baryonic matter. In order to fuse two protons together or two neutrons together, it requires neutrinos and the weak force. A proton and a neutron, however, can fuse using the strong force and all that is required is a photon. Since the average temperature of the universe was still extremely high, protons and neutrons were fusing to form deuterium atoms.

Once a significant amount of deuterium formed, a number of nuclear reactions could take place. The most common reactions quickly turned most of the matter containing neutrons (deuterium) into helium. Since the required binding energy per nucleon after helium fusion is lower than that of helium fusion, heavier elements did not start forming until stars had collapsed and started their own fusion reactions in their cores.

Even though most of the universe's supply quickly fused into helium, there is still some primordial deuterium left over from the time of nucleosynthesis. Observations have shown that the current ratio of deuterium to hydrogen, or the D/H ratio, within the local interstellar medium is about 2 x $10^{-5}$ [49, 50].

## 2.2 Atmospheric Escape

A planet's atmosphere is not static over long periods of time. The relative abundance of the molecules that comprise an atmosphere change because of activity within the planet, surface processes, and influences from outside of the planet. For instance, the

atmosphere of Earth changed drastically as life evolved and molecular oxygen grew in abundance.

Planets can also lose their atmospheres over long periods of time. Bigger planets usually can hold on to their atmospheres, but the atmospheres of small planets can boil away during the life of the star they orbit. Atmospheric escape mechanisms are responsible for depleting planetary atmospheres.

### 2.2.1 Atmospheric Scale Height

Gas is a state of matter that expands to fill the volume in which it is contained. Planets with gaseous atmospheres do not have a shell to contain the gas on the planet; the force of gravity holds an atmosphere onto a planet. Gas in a planetary atmosphere is balanced by the force of gravity pulling the mass of the gas downward and the pressure of the gas pushing it in all directions. This balance is known as hydrostatic equilibrium. The gas giant planets and even the stars are held between escaping and collapsing because of the balance between the two forces .

The pressure in an atmosphere decreases with increasing altitude. The change in pressure $\Delta P$ given a change in altitude $\Delta z$ is given by how much a column of air in that altitude change weighs

$$\Delta P = -g_p \rho \Delta z \tag{2.5}$$

In general, both the gas density $\rho$ and gravitational acceleration of the planet $g_p$ change with altitude, so the equation of hydrostatic equilibrium in differential form is

$$\frac{dP}{dz} = -g_p(z)\rho(z) \tag{2.6}$$

The relationship between pressure, density, and temperature in the collisional part of planetary atmospheres is well approximated by the Ideal Gas Law

$$P = NkT = \frac{\rho R_{gas} T}{\mu_a} = \frac{\rho k T}{\mu_a m_{amu}} \tag{2.7}$$

where $N$ is the particle number density, $k$ is Boltzmann's constant, $R_{gas}$ is the universal gas constant, $\mu_a$ is the mean molecular weight of the gas in atomic mass units, and $m_{amu}$ is the mass of an atomic weight unit, which is slightly less than the weight of a hydrogen atom [23]. Near the surface of Earth, the mean molecular weight of air is close to 28.8.

The differential hydrostatic equilibrium equation can be combined with the third form of the Ideal Gas Law shown here to solve for the pressure as a function of altitude.

$$P(z) = P(0) e^{-\int_0^z \frac{dr}{H(r)}} \tag{2.8}$$

where the pressure scale height is

$$H(z) = \frac{kT(z)}{g_p(z)\mu_a(z)m_{amu}} \tag{2.9}$$

The pressure scale height is equal to the altitude over which the pressure decreases by a factor of $e$, which is Euler's number. On Earth, the scale height of the atmosphere near the surface is approximately 8 km, so at that altitude, the pressure is $1/e$ times the pressure at sea level, or about 36%, assuming no change in temperature or gravity. At 16 km, the pressure is $1/e^2$ or about 13% of the pressure at sea level, and so on.

Gas in planetary atmospheres is well mixed. A parcel of air at any given temperature (above the freezing point of its constituent components and below the temperature that would ionize the atoms) is mixed by eddy diffusion. Eddy diffusion keeps gas particles well mixed so a parcel of gas can be approximated as one gas rather than the sum of its constituents. However, when the pressure is sufficiently low, eddy diffusion forces are overcome by molecular diffusion forces. Molecular diffusion forces the heavier molecules to settle towards the bottom, allowing the lighter gasses to move higher into the atmosphere. When molecular diffusion exceeds eddy diffusion, gases are no longer well mixed and cannot be treated as one mass. Additionally, the

scale heights of the different constituents must be considered separately. The level where eddy diffusion and molecular diffusion rates are equal is called the homopause; on Earth, it is at an altitude of approximately 100 km [51].

Scale height is inversely proportional to the molecular mass of gas particles above the homopause. Heavier gases like carbon dioxide ($\mu_a = 44$) have smaller scale heights, so the partial pressure (and as a result, the number density) of the heavier gases falls more quickly with increasing altitude. Lighter gases like atomic or molecular hydrogen ($\mu_a = 1$ and 2, respectively) can extend much higher in altitude without dropping in number density. This is why the top layers of planetary atmospheres are mostly hydrogen; the scale height is generally an order of magnitude larger than other common atmospheric molecules like molecular oxygen, methane, and carbon dioxide.

### 2.2.2 Jeans Escape

Gas particles high in the atmosphere sometimes gain enough energy to overcome a planet's gravitational pull and escape into interplanetary space. This is called atmospheric escape, and there are number of ways that gas particles can gain this energy. The primary and most simple escape method is by Jeans Escape, which is when gas boils off a planet through thermal energy.

In order for a particle to escape, it must not only have enough energy to escape the force of gravity, it must also be moving on a trajectory in which it does not collide with other particles first and be moving upward. A gas particle with sufficient energy to overcome gravity has virtually no chance of escaping if it is in a parcel of gas at atmospheric pressure because it will collide with other molecules first. The average distance a particle will travel before it collides with another particle is called the mean free path and is defined as

$$l_{pf} = \frac{1}{\sigma_x N} \tag{2.10}$$

where $\sigma_x$ is the collision cross section and $N$ is the number density [7]. At high altitudes and lower pressures, the mean free path becomes longer. The exobase is

defined as the altitude where the mean free path of a gas particle is equal to the atmospheric scale height. Above this level, a particle has a high probability of escaping the pull of gravity if it has enough energy because the chances of it colliding with another particle and losing that energy are low. The exobase is much higher than the homopause.

The Boltzmann constant relates the temperature of a gas to the average kinetic energy of the individual particles of that gas and has units of Joules per Kelvin. The relationship between the average kinetic energy of an ideal gas molecule and its temperature is given by

$$\frac{1}{2}mv_0^2 = kT \tag{2.11}$$

where $v_0$ is the average velocity of the particle and $m$ is the mass of the particle, which can also be written as $\mu_a m_{amu}$. The average velocity can then be expressed as

$$v_0 = \sqrt{\frac{2kT}{m}} \tag{2.12}$$

However, the actual distribution of velocities of individual particles is given by a Maxwellian distribution. While the average velocity is usually well below the velocity required to escape from a planet, the sheer number of particles means there exists some small fraction that do have the velocity required to escape. Escape occurs when the kinetic energy overcomes the gravitational potential energy. The escape velocity at a given altitude is defined as

$$v_{esc} = \sqrt{\frac{2GM_P}{(R+z)}} \tag{2.13}$$

where $G$ is the universal gravitation constant, $M_P$ is the mass of the planet, $R$ is the radius of the planet, and $z$ is the altitude [55]. The ratio of the potential energy to the kinetic energy is called the escape parameter

$$\lambda_{esc} = \frac{GMm}{kT(R+z)} = \frac{(R+z)}{H(z)} = \left(\frac{v_{esc}}{v_0}\right)^2 \tag{2.14}$$

Integrating the Maxwellian velocity distribution gives the Jeans Formula for the escape rate of gas particles by thermal energy in units of atoms per square centimeter per second

$$\Phi_J = \frac{N_{ex} v_0}{2\sqrt{\pi}} (1 + \lambda_{esc}) e^{-\lambda_{esc}} \tag{2.15}$$

where $N_{ex}$refers to the number density of a gas at the exobase [23]. From this equation, several observations can be made. First, as the escape parameter $\lambda_{esc}$ decreases, the Jeans escape rate increases exponentially. As temperature increases, not only does the escape parameter decrease, so does the average particle velocity.

An important factor for the work detailed in this thesis is the molecular mass; as molecular mass increases, the escape parameter increases, so the Jeans escape rate decreases exponentially. Jeans Escape is therefore much more probable for light gases that it is for heavy gases. Because Jeans Escape happens above the homopause, it does not act on all atmospheric constituents equally, so gas species escape at rates that are independent of the escape rates of other species.

### 2.2.3 Other Atmospheric Escape Mechanisms

Jeans or thermal escape is not the only way an atmosphere can lose mass. There are many other ways particles can gain energy that do not involve thermal heating alone. Some methods are from particle interactions, some are dependent on the escape rates of other gases, and sometimes atmospheres are lost because of massive collisions.

There are many non-thermal particle interactions where energy exchange can leave one particle with enough energy to escape the gravitational pull of a planet. One method is dissociation and dissociative recombination. Ultraviolet radiation can be absorbed or energetic electrons can collide with a molecule and break it into smaller pieces. The energy left over after breaking the molecular bonds is translated into kinetic energy. If one of the pieces gains enough kinetic energy from this interaction, it may escape [23].

A planet's magnetic field can also deliver high-energy into the atmosphere. Ener-

getic ions travelling along magnetic lines may collide with neutral atoms high in the atmosphere to provide the kinetic energy needed to escape.

The Earth's magnetosphere protects the planet from the Solar wind. On planets with no magnetosphere, the Solar wind interacts directly with gas in the upper atmosphere and can carry atmospheric constituents away.

These non-thermal escape mechanisms also preferentially boil off the lighter particles, but it is much more difficult to measure or predict the contribution that these actions have to atmospheric escape. This is why the Jeans Escape flux gives a lower limit to the escape rate.

Other escape mechanisms do not discriminate against lighter particles and can remove large quantities of atmosphere from a planet at altitude below the exobase. Hydrodynamic escape occurs when light gasses escape from beneath heavier gasses with such high rates that they form shockwaves, bringing heavier atmospheric constituents with them as well. This requires a large amount of energy and much higher escape rates than reasonable Jeans escape rates. It is usually not possible with Solar energy alone. Heat of formation or collapse within a gas giant may provide enough energy.

Additionally, large amounts of gas and even debris can escape during a large-scale impact. It is thought that the Moon was formed when a Mars-like object struck the Earth and a large amount of mass into orbit. Such a collision may drastically change the composition and structure of an atmosphere or deplete it entirely. Meteorites such as ALH84001, which was shown to be of Martian origin, may have escaped the gravity of Mars in a large collision. Such a collision would blow off atmospheric gas in addition to heavier, rocky objects.

### 2.2.4 Photodissociation, Water Loss, and the D/H Ratio

Photodissociation is a process where a photon with sufficient energy is absorbed by a molecule and breaks the molecular bonds apart. Usually, this occurs with ultraviolet or more energetic radiation since the bond strengths of simple molecules found in planetary atmospheres require more energy than visible or less energetic photons

have. Stronger bonds require more energetic photons than weaker bonds.

It is well known that water is an essential molecule for life on Earth. There is evidence that water should be more abundant throughout the Solar system than what can be detected now. According to some models, the inner planets should have a much higher water content.

Ordinary water is composed of two hydrogen atoms and one oxygen atom ($H_2O$). However, deuterium is an isotope of hydrogen; therefore, deuterium has the same chemical properties and can form similar bonds as hydrogen. Because of this, water can also be composed of one part hydrogen, one part deuterium, and one part oxygen (HDO), or two parts deuterium and one part oxygen ($D_2O$). Since the universal ratio of D/H is low, HDO is much less abundant than $H_2O$. The abundance of $D_2O$ is practically negligible in comparison to $H_2O$ and HDO. Water on Earth that has a higher abundance of HDO and $D_2O$ relative to $H_2O$ compared to the average abundance is often called "heavy water."

On Earth, water exists in all three (traditional) phases of matter; solid, liquid, and gas. On other planets and moons with thin atmospheres, it can exist in solid and gas form. The Earth's atmosphere is thick enough that high energy photons like far-ultraviolet light do not penetrate to the surface. However, ultraviolet light does interact with gas in the upper atmosphere. Water vapor near the homopause is subjected to a high flux of ultraviolet photons. It is in this area where water vapor ($H_2O$ or HDO) is easily photodissociated and broken into a hydroxyl group (OH or OD) and a hydrogen atom (H or D) or broken into purely atomic constituents.

Usually these atomic constituents recombine, possibly to form water again or any number of compounds. The photochemical reactions in the upper atmosphere are very diverse. However, some photodissociated hydrogen and deuterium atoms may travel higher into the atmosphere and enter the exosphere. Hydrogen and deuterium often recombine into $H_2$ or HD and diffuse higher up into the atmosphere, where they experience even higher ultraviolet flux and as a result higher photodissociation rates. Here, hydrogen and deuterium have the potential to escape since they both have low atomic mass.

Since deuterium weighs twice as much as hydrogen, its escape parameter $\lambda_{esc}$ is twice as large. Given a set of characteristics of a planetary exobase, the relative escape rate of deuterium will be different from hydrogen. Using the Jeans Formula, and assuming a temperature $T = 900$ K at the exobase altitude $z = 500$ km, the relative escape rate (the escape rate $\Phi_J$ divided by the number density $N_{ex}$) of hydrogen from Earth's exobase will be 1,800 times more than the relative escape rate of deuterium.

Over long time periods, like the age of the Solar system, photodissociation of water followed by atmospheric escape can lead to hydrogen being preferentially lost relative to deuterium. This leads to an elevated atmospheric D/H ratio compared the average Solar system ratio. The D/H ratio of the Sun, Jupiter, and Saturn is around $2 \times 10^{-5}$, whereas the D/H ratio on Earth is $1.6 \times 10^{-4}$ [36]. This is evidence that Earth may have indeed lost some of its water content since the formation of the Solar system, and other planets with elevated D/H ratios may have also lost a significant amount of water.

## 2.3 Venus' Atmosphere and Evolution

Long ago, people thought Venus was a lush jungle world, slightly hotter but potentially habitable. Venus is often called Earth's sister planet because the two are so similar in size and mass, but astronomers from long ago were never able to peer through the thick clouds to see the surface of the planet. However, when Venus was explored further in the 20th century, astronomers learned that the surface of Venus is not similar to Earth's at all; it is a hellish wasteland constantly bombarded with acid rain with an average surface temperature hot enough to melt lead.

What is more puzzling is that, according to the current understand of planetary formation, Venus and Earth should be more similar. Earth has a powerful magnetic field; Venus does not. Earth has nearly a 3 km-thick global equivalent layer (GEL) of water; Venus barely has a 3 cm-thick GEL. Earth's atmospheric pressure is close to 100 kPa; Venus' atmospheric pressure is nearly 90 times that. Earth's average surface temperature is close to 288 K, not very different from its calculated effective

temperature of 263 K; Venus' global temperature is 735 K, a huge difference compared to its calculated effective temperature of 238 K, and it is almost constant around the entire planet, day and night (effective temperature will be discussed in Section 2.3.2) [23, 36].

It is important to understand why Earth and Venus are different. It is even more important to understand how to prevent Earth's atmosphere from becoming like Venus'.

### 2.3.1 Composition and Structure

The composition of Venus' atmosphere is very different from Earth's. Venus' atmosphere is primarily composed of carbon dioxide, which makes up nearly 96.5% of its mass. Molecular nitrogen is the second most abundant constituent, making up nearly 3.5% [36]. After these species, others are measured in parts per million (ppm). Sulfur dioxide is the third most abundant component, ranging from 25-150 ppm between 12km and 22km altitude and 150±30 ppm between 22 km and 42 km altitude. Water vapor is the fourth most abundant component, ranging from 30-70 ppm below 5 km altitude and 30±5 ppm below 40 km.

Venus' atmosphere can be divided into three distinct regions, the upper, middle, and lower layers. The lower and middle layers are separated by a thick layer of clouds. The temperature at the top of the cloud layer is near 240 K, which is very close to the effective temperature calculated from solar radiation alone. Beneath this cloud layer, the temperature increases rapidly down to the surface.

The middle layer, between 60 km and 100 km altitude, and upper layer, 100 km and above, are similar to the stratosphere, mesosphere, and thermosphere on Earth. The temperature between 70 km and 80 km is nearly constant. Above 200 km, the temperature rises to approximately 300 K on the day side, but goes down beneath 150 K on the night side; this is due to Venus' slow rotation. In contrast, Earth's temperature above 200 km rises past 1000 K [23].

### 2.3.2 The Runaway Greenhouse Effect

The expected temperature of an object such as a planet can be calculated based on the amount of solar energy the object encounters and how effectively it absorbs it. If the object is rotating rapidly, it will uniformly reradiate the absorbed radiation as a blackbody until temperature equilibrium is achieved.

The amount of power (in Watts) an object absorbs from the Sun can be calculated by

$$L_{abs} = (1 - A_B)\frac{L_\odot}{4\pi r^2}\pi R_P^2 \tag{2.16}$$

where $A_B$ is the albedo of the object, $L_\odot$ is the Solar luminosity, $r$ is the distance from the Sun, and $R_P$ is the radius of the object. The object will reradiate power according to the Stephan-Boltzmann law,

$$L_{out} = 4\pi R_P^2 \varepsilon \sigma_B T^4 \tag{2.17}$$

where $\varepsilon$ is the blackbody emissivity of the object and $\sigma_B$ is the Stephan-Boltzmann constant. For thermal equilibrium, the power absorbed will equal the power emitted and the equilibrium temperature is

$$T_{eq} = \left[\frac{(1 - A_B)L_\odot}{16\pi\sigma_B r^2}\right]^{1/4} \propto \frac{1}{\sqrt{r}} \tag{2.18}$$

Venus has a high albedo, so it absorbs solar energy less effectively. Effective temperature is the equilibrium temperature adjusted for internal power sources, such as radioactive decay, which was a factor in the early solar system, and gravitational collapse, which is a factor in giant planets. However, Venus' high surface temperature is not due to an internal energy source, it is due to a runaway greenhouse effect.

The atmospheres of some planets are quasi-transparent to photons in the ultraviolet, visible, and near-infrared wavelengths, assuming there are no clouds. These photons heat the planetary surface, and the surface reradiates that energy in the form of low-energy photons in the far-infrared spectrum. The greenhouse effect oc-

curs when atmospheric constituents are transparent at high-energy wavelengths, such as ultraviolet, visible, and near-infrared, but are opaque at lower-energy wavelengths, such as far infrared and microwave, causing the energy to be trapped in the atmosphere and reradiated isotropically. Gases that have strong absorption bands in the far-infrared and microwave include carbon dioxide, water, and methane [51].

An approximation for relating the ground temperature $T_g$ in a greenhouse environment to the equilibrium temperature $T_{eq}$ (or effective temperature $T_{eff}$ in the presence of an internal power source) and the optical depth $\tau$ of the greenhouse gases at the wavelength that the ground is emitting energy can be found using radiative transfer equations. Assuming no other heating effects are present, the ground temperature of a greenhouse planet is

$$T_g^4 = T_{eq}^4 \left(1 + \frac{3}{4}\tau_g\right) \tag{2.19}$$

For Venus, with a ground temperature $T_g = 735$ with an effective temperature $T_{eff} = 238$, the optical depth of the atmosphere at the ground is $\tau_g = 120$. For Earth, with $T_g = 288$ and $T_{eff} = 263$, the optical depth is only $\tau = 0.6$ [36].

Venus' greenhouse effect is mostly caused by carbon dioxide, which accounts for 65% of the excess heat. The sulfuric acid clouds account for 21% of the excess heat, and what little water vapor there is in Venus' atmosphere accounts for 11% of it [51].

### 2.3.3 Evidence of Change

If there ever was liquid water on the surface of Venus at any point in time, it has certainly evaporated because of the high temperatures caused by the greenhouse effect. As the water evaporated, it would have risen from the surface and mixed with the rest of the atmosphere, eventually making its way to the upper layers near the homopause. Since ultraviolet light can penetrate to this layer, and because Venus is relatively close to the Sun, the water vapor would have been photodissociated at a high rate – that is, if it ever existed on Venus.

Photodissociated water leaves behind hydrogen and deuterium that can be boiled

off the planet. As described in Section 2.2.2, deuterium escape at a significantly slower rate than hydrogen. Given Venus' mass, radius, and a temperature of 300 K at an exobase altitude of 500 km, the relative hydrogen escape rate is 300 million times the relative deuterium escape rate; however, such a low temperature corresponds to a very low overall flux rate. The real question is how was Venus' exosphere different in the past? How different was the solar ultraviolet flux rate in the early solar system? How has the flux rate changed over time?

Previous measurements of the D/H ratio have estimated that it is as high as 0.1, nearly three orders of magnitude higher that the terrestrial value and four orders of magnitude higher than the Solar value [44]. In-situ measurements have measured the $HDO/H_2O$ ratio between 30 km and 50 km to be $1.6 \times 10^{-2}$ [53], and more recent solar occultation measurements have measured $HDO/H_2O$ in the polar regions between 70 km and 95 km varying between 0.06 and 0.15 [29]. However, other Lyman-alpha measurements have restricted the D/H ratio above 100 km to an upper limit of $2 \times 10^{-3}$ (see Section 3.2).

Understanding how D/H varies with altitude on Venus is fundamental for understanding the water history of Venus because the escape rates depend not just on the densities but also on the diffusion rates to the exobase to replace the atoms that escape. The measured D/H ratios have shown that Venus may have lost at least 0.3% of an Earth ocean since the formation of the Solar system [53]. That estimate is a minimum because an elevated D/H ratio only accounts for atmospheric escape mechanisms that preferentially deplete hydrogen over deuterium, like Jeans Escape, and does account for other escape mechanisms that do not discriminate against atomic or molecular mass, like hydrodynamics escape.

Not only is measuring D/H fundamental to understanding the evolution of Venus' atmosphere, it can also be used to better understand water loss and runaway greenhouse effects on Earth. While the timescale for losing oceans of water may be longer than the remaining life of the Sun, the significance of water vapor as a greenhouse gas cannot be underestimated on Earth. As global temperatures rise, water vapor will increase in abundance, causing more warming that will evaporate more water. This

positive feedback loop could cause the atmosphere to heat uncontrollably, turning Earth into an arid, hellish wasteland as hot as Venus.

## 2.4 Jupiter's Atmosphere and Magnetosphere

Jupiter is the Solar system's largest planet, more than twice as massive as all the other planets combined, and yet it is only a thousandth of the mass of the Sun. It is the closest gas giant to the Sun, and the asteroid belt is heavily influenced by its strong gravitational pull. It is possible that Jupiter is the reason why comets and asteroids have bombarded the inner planets since the birth of the Solar system, leaving the ones with little or no atmosphere heavily scarred with craters.

Although Jupiter has been studied for centuries, its significance takes a new meaning today as astronomers, armed with more powerful telescopes and a firmer understanding of orbital mechanics, discover more and more planets beyond our Sun. Over 80% of the exosolar planets discovered so far are at least as massive as Saturn, and over half are more massive than Jupiter [52]. Understanding our Solar system's largest planet will help astronomers learn more about the most common type of exoplanet discovered so far.

### 2.4.1 Composition and Structure

Jupiter, like the Sun, is primarily composed of hydrogen and helium. In fact, if Jupiter was an order of magnitude bigger, its core might be hot enough to fuse deuterium, which would officially classify it as a brown dwarf. Jupiter's atmosphere is 86.2% hydrogen, 13.6% helium, and the rest is trace amounts of methane, ammonia, and water [36].

The most prominent feature on Jupiter is the Great Red Spot, thought to be a massive storm the size of six Earths. It also has a number of prominent bands called Hadley cells that divide the planet longitudinally. Hadley cells are caused by uneven distribution of energy from the Sun circulating in the atmosphere [51]. They are heavily influenced by the rotation period of the planet, and Jupiter has so many

Hadley cells because its rotation period is so fast; a day on Jupiter is less than 10 hours. This fast rotation speed causes the planet to bulge at the equator, and the rotation speed at the equator is over 12 km/s.

Jupiter has no solid surface. It is thought that at the center of Jupiter, there is a small rocky core surrounded by ice. On top of that is a thick layer of metallic hydrogen and helium that makes up 80% of Jupiter's radius, and the last 20% is made of molecular hydrogen and helium [36]. The "surface" or "0 km altitude" of Jupiter is usually defined as the level in the gas layers where the pressure is equal to the atmospheric pressure of Earth or where cloud layers make the atmosphere opaque.

The top layers of Jupiter's hydrogen atmosphere are much hotter than the atmosphere near the cloud tops. The estimated effective temperature of Jupiter is 123 K, but the top layers of hydrogen are approximately ten times hotter. This heat cannot be generated by the absorption of ultraviolet sunlight alone, so there must be other heating mechanisms at work within the upper atmosphere.

### 2.4.2 Jupiter's Magnetosphere

Jupiter has the largest magnetosphere of any planet in the Solar system. It extends over 70 Jupiter radii out into interplanetary space, protecting its moons from the Solar wind but blasting them with charged plasma from its poles [23]. If it could be seen with the naked eye, it would appear several times larger than the full moon in the night sky. It magnetic field is over ten times as powerful as Earth's, making it the strongest planetary magnetic field in the Solar system.

Because Jupiter is a gas giant, it is difficult to determine what its rotation period is. There are three coordinate systems, Systems I, II, and III. System I refers to the rotation period within $\pm 10$ degrees latitude of the equator. System II refers to all latitudes north and south of this equatorial range. System III refers to the rotation of the internal magnetic field, which most likely is the rate that the solid core is rotating far beneath the cloud layers [23].

Like Earth's magnetic dipole, Jupiter's magnetic dipole is tilted by approximately 10 degrees from the rotational poles. As a result, the magnetic equator and the

rotational equator are not aligned.

The magnetosphere also is responsible for Jupiter's powerful aurorae. Magnetic field lines funnel charged particles from the magnetosphere and the solar wind into the poles. When they strike the atmosphere, gasses are ionized as electrons are stripped away and then recombine to produce the auroral emissions. Magnetospheric plasma interacts with the Galilean satellites, causing spots and tails to appear in the aurorae.

### 2.4.3 The Lyman-alpha Bulge

There are still many mysterious phenomena that have been observed on Jupiter that scientists cannot fully explain. One of them is the Lyman-alpha Bulge, an area in the upper atmosphere that is mysteriously brighter in Lyman-alpha light than the rest of the planet.

When it was first discovered, the extra Lyman-alpha brightness was thought to be an uneven accumulation of hydrogen in that region as if the planet was bulging out in one direction, hence the name "Lyman-alpha Bulge" [32] Follow-up observations showed that the Bulge was a long-term feature that rotates with Jupiter's magnetic equator. The bright region appears to be located near a central meridian longitude (CML) near 110 degrees in the System III magnetic coordinate system and is nearly 36% brighter in Lyman-alpha compared to the rest of the planet when illuminated by the Sun.

Further studies of the Bulge have shown that the hydrogen in the region is very turbulent. Spectral analysis and modeling have shown that while most of the hydrogen in the region is behaving similarly to hydrogen in other areas of the atmosphere, there is a small fraction of the gas that is superthermal [40]. Even though the superthermal component is less than one percent of the total density of hydrogen, it can account for the increased brightness. See Section 3.3 for more on the properties of the Lyman-alpha Bulge.

Several hypotheses have been proposed, but more observations over the last three decades have disproved some of them. One leading hypothesis is that the Bulge is being powered by the aurorae. There is so much energy in the aurorae that some

could be coming from the high latitudes at high altitudes into the equatorial region from both poles in the form of neutral high altitude jets. When these two jets meet, the turbulence could produce the superthermal neutral hydrogen that scatters the solar emission to produce a brighter Lyman-alpha emission.

A second hypothesis is that the Bulge is caused by an equatorial anomaly analogous to a process observed on Earth. On Earth, there are tropical arc emissions seen along the magnetic equator. Such a phenomenon has been predicted on Jupiter but has not yet been observed.

An additional hypothesis for the cause of the Bulge is the movement of charged particles in the magnetosphere. Charged particles can move down magnetic field lines high in the atmosphere. As they move, they may collide with neutral hydrogen with enough energy to produce fast atoms that reflect the Solar Lyman-alpha emission and produce the line profile broadening seen in the Bulge. Like the South Atlantic Anomaly on the Earth, the flux of charged particles would be higher where the magnetic field is weaker.

## 2.5 Application of Spectroscopy to Study Planetary Atmospheres

"We see how we may determine [the stars'] forms, their distances, their bulk, but we can never know anything of their chemical or mineralogical structure." - Auguste Comte, Positive Philosophy, 1835

Thankfully, Auguste Comte was wrong, and astronomers do have the tools necessary to understand the compositions of not only the stars but of anything that can be observed. Spectroscopy is the study of spectral lines. Isaac Newton showed how a prism could be used to diffract sunlight to produce the rainbow spectrum. Later, William Wollaston showed that there were a number of dark lines in this spectrum. These spectral lines are how astronomers can determine the composition of objects far away without touching them.

### 2.5.1 Formation of Spectral Line Profiles

Spectral lines are the result of the way photons and atoms or molecules interact with each other. The hydrogen Lyman-alpha emission, for instance, is the transition of an electron from its first energetic state down to its ground state. This transition creates the Lyman-alpha spectral line. Every atom and molecule has unique electron transition energies and unique resonance properties that act like atomic fingerprints, enabling astronomers to identify the atomic and molecular components.

Kirchhoff's Laws govern how spectroscopy works and how atoms interact with photons differently. His three laws are:

1. A hot, dense gas or hot solid object produces a continuous spectrum with no dark spectral lines.

2. A hot, diffuse gas produces bright spectral lines

3. A cool, diffuse gas in front of a source of a continuous spectrum produces dark spectral lines.

The first law is explained by blackbody physics, which says objects or dense gases emit continuous spectra with a peak wavelength dependent on the temperature of the object or gas [7].

A hot, diffuse gas will emit light only at wavelengths that are characteristic of its structural properties, which is what creates the bright spectral lines, but it does not produce a continuous spectrum. That same gas, when cooled, will absorb or scatter photons from a continuous spectrum at the exact same wavelengths that it would emit when it is hot, which is what creates the dark lines on a continuous spectrum.

Some spectral absorption from a specific gas is at specific wavelengths. These are usually the result of an electron transition. However, entire bands of electromagnetic radiation can be absorbed by some molecules, while other bands are entirely unaffected by the presence of the gas. For instance, greenhouse gases allow visible light frequencies through unobstructed but absorb large amounts of infrared frequencies.

### 2.5.2 Spectral Line Shifting

A property of spectral lines that is a very powerful tool in astronomy and spectroscopy is how the emission lines change with the speed relative to the observer. Even though the spectral wavelengths of an atom or molecule do not change, the way the spectral lines are measured does. Since photons are both waves and particles, they are subject to the same phenomena as other waves.

The Doppler Effect is the apparent change in frequency of a wave due to the relative motion between the observer and the source. The common example is of an approaching fire truck blaring a siren; the apparent pitch is higher as it approaches then goes lower as it speeds away and is dependent on the speed of the fire truck and the speed of sound. Photons are also affected by the Doppler shift. A particle with some spectral emission line with a wavelength $\lambda_{rest}$ when measured at rest will appear to have changed in wavelength by

$$\Delta\lambda = \frac{v_r \lambda_{rest}}{c} \tag{2.20}$$

where $v_r$ is the recessional velocity of the particle and $c$ is the speed of light [7]. For instance, if a hydrogen atom is emitting Lyman-alpha light at 1215.668 Å and is moving away from the observer at 10 km/s, the wavelength measured by the observer will be 0.041 Å longer than the rest wavelength. This is known as red-shift, because the spectral line is now at a longer wavelength and therefore closer to the red side of the visible light spectrum. When the target object is moving towards the observer, the measured wavelength is shorter. This is called blue-shift because the new wavelength is closer to the blue side of the visible spectrum.

Spectral line shifting also has an additional purpose in astronomy. When astronomers look into the night sky, they are usually not looking only at their target. From the ground, astronomers are looking through a column of Earth's atmosphere and a column of the interplanetary medium. For spatial imaging in the visible spectrum, these factors do not matter very much because this sky background is dim compared to the target object.

For ultraviolet spectroscopy, and especially for spectral measurements of Lyman-alpha, this is a major factor. Orbiting telescopes are high above most of the mass of Earth's atmosphere, but there is still a layer of hydrogen surrounding Earth that the telescope orbits within and looks through. This hydrogen has a Lyman-alpha emission as well, and produces what is called the geocoronal emission by scattering solar photons. The geocoronal hydrogen also scatters incoming Lyman-alpha from the target, diminishing the total count rate from the target in addition to adding to the uncertainty from the background subtraction. Its influence on any Lyman-alpha measurements cannot be ignored.

The interplanetary medium is extremely diffuse, but it is composed primarily of hydrogen. Over long distances, its Lyman-alpha emission is measureable. The geocoronal and interplanetary medium Lyman-alpha emissions form a sky background that must be subtracted from a spectrum before the target's emission can be analyzed.

If an astronomer attempted to measure the Lyman-alpha emission spectrum of a planet while the planet was motionless relative to the astronomer, the emissions from the target planet, the Earth's geocorona, and the interplanetary medium would all be stacked on one another. When this happens, it is difficult to subtract the sky background because of the amount of noise generated.

However, if the planet is moving with high velocity along the line of sight relative to the astronomer, the emission from the planet is red- or blue-shifted relative to the geocoronal and interplanetary emissions. The sky spectrum can be easily subtracted from the measured spectrum without adding substantial error to the spectrum from the planet. For this reason, the Lyman-alpha measurements in both projects take place when the targets are moving close to their maximum line of sight velocity relative to Earth.

### 2.5.3 Spectral Line Profile Broadening Mechanisms

Even though a spectral line from a particular atom or molecule is at a discrete wavelength, the width of the spectral line, even with the most sensitive equipment will not see an infinitesimally narrow spectral line in wavelength or frequency. There are

many mechanisms that broaden the spectral profiles of emission lines.

In any parcel of gas where the temperature is not absolute zero, the gas particles are in motion. The hotter the gas is, the faster the particles are moving. The velocity distribution of the particles is characterized by a Maxwellian distribution, but the direction that the individual particles are moving in is random. The direction that some particles are moving in will be towards the observer, so the emission from those particles will be blue-shifted, while some particles will be moving away from the observer, so the emission from those particles will be red-shifted.

The combination of the velocity distribution and the directional distribution gives a Gaussian distribution for the broadening of the spectral line. This profile has a standard deviation relative to wavelength equal to

$$\sigma_\lambda = \sqrt{\frac{kT}{mc^2}}\lambda_{rest} \tag{2.21}$$

The width of this distribution measured at half of its peak value, or full-width half maximum (FWHM) is equal to

$$\Delta\lambda_{FWHM} = \sqrt{\frac{8kT\ln 2}{mc^2}} \tag{2.22}$$

The amount of Doppler broadening a line profile will experience is primarily determined by the temperature of the gas [51]. Hotter gases have broader spectral line profiles compared to cooler gases.

Additionally, collisions between gas particles perturb the energy levels that are emitted and absorbed by the gas particles. As pressure increases, particle collisions become more frequent, and the spectral line profile is represented mathematically by a Lorentzian profile that is dependent on the temperature and the pressure of the gas.

The combination of Doppler and collision broadening can be represented as a Voigt profile, which combines the Gaussian profile from Doppler broadening with the Lorentzian profile from collision broadening. The ratio $l_v/l_c$, which is the intensity of the spectral profile at some point $l_v$ relative to the intensity at line center $l_c$, is

defined as

$$\frac{l_v}{l_c} = \frac{a}{\pi} \int_{-\infty}^{+\infty} \frac{e^{-y^2}}{a^2 + (v-y)^2} dy = H(a, v) \tag{2.23}$$

where $a = \Gamma/4\pi\Delta\nu_0$, $\Gamma$is the damping broadening constant, $\Delta v_0$is the Doppler width, and $v$ is the change in frequency from the line center in units of Doppler widths, or $v = \Delta\nu/\Delta\nu_0$ [17].

Other mechanisms that broaden line profiles are the Stark and Zeeman effects, caused by interactions with electric and magnetic fields, respectively. However, these effects are weaker by several orders of magnitude compared to Voigt broadening and are not considered when studying the Voigt profiles of planetary emissions.

### 2.5.4 Radiative Emission and Scattering

Matter is visible because it interacts with photons; it reflects and scatters some light in all different directions. Matter varies in visible color because it absorbs some wavelengths of visible light but scatters and reflects others; a dark object absorbs more light but a white object reflects light. The way matter interacts with light is dependent on its atomic structure.

Objects in the Solar system are seen because the Sun emits light that is scattered by those objects. In the study of the hydrogen Lyman-alpha emission, the effect of resonant scattering plays an important role. Resonant scattering occurs when a photon of a particular frequency (or wavelength) strikes an atom or molecule that has an electron transition energy that is the same as the photon. An electron will absorb the photon and be raised to a higher quantum state. However, the higher energy state is unstable, so the electron quickly reradiates the photon and moves back to the lower energy state.

Lyman-alpha light produced by the Sun's energetic hydrogen will strike other hydrogen atoms in some parcel of gas, raising the electrons in the gas from a quantum state n = 1 to n = 2. The electron will then move back to n = 1 and emit the photon in a random direction. If there are more hydrogen atoms in that parcel of gas, those

atoms will absorb and re-emit more photons, some of which will be pointed toward an observer that can measure the brightness of the Lyman-alpha emission.

Single-scattering is when light enters a parcel of gas, interacts with and is scattered by exactly one gas particle, and is re-emitted by the gas without interacting with any other gas particle. The amount of light that is scattered by the gas is proportional to the number of gas particles in the gas parcel and the number of photons that are going into the gas. It is therefore possible to solve for the number density of gas particles given the brightness of the parcel and the known photon flux being emitted by the Sun [43].

### 2.5.5 Optical Depth and the Curve of Growth

Matter is not completely transparent because it interacts with passing photons. While some matter may appear transparent, like the atmosphere or a glass window, a fraction of the incoming photons are prevented from being transmitted through to the other side. Optical devices in telescopes, such as mirrors, lenses, gratings, and prisms, define the ratio of the amount of light that is reflective or transmitted by the optic over the total light on the optic as the reflective or transmission efficiency.

In the study of diffuse gases in an atmosphere, the ability of photons to pass through is defined differently. As light passes through a gas, its intensity is continuously weakened as it passes through a thicker column of matter. The relationship between the intensity of light before it passes through a gaseous medium $I_0$ and the intensity of light after it passes through the medium $I$ is

$$I = I_0 e^{-\tau x} \tag{2.24}$$

where $\tau$ is the optical depth of the column of gas [7]. This means if the optical depth of a gas $\tau = 1$, the amount of incoming light will be decreased by a factor of $1/e$, meaning about 36% of photons get through. For optical depth equal $\tau = 2$, the incoming light will be decreased by $1/e^2$, meaning about 13% of photons get through, and so on.

The optical depth of a gas is dependent on the density of the gas and the length through which the observer is looking, but it is also related to the wavelength that is being observed. Some gases may allow the transmission of visible light but completely block ultraviolet light. This is an important property in the greenhouse effect (Section 2.3.2).

Optical depth is also a factor when determining the density of a gas. In the case of parcel of hydrogen gas scattering Solar Lyman-alpha light, an optical depth $\tau << 1$ means a low density, but it also means that the light that is being scattered is most likely only being scattered once in its time inside the parcel. However, as the optical depth rises, the chances of photons being scattered twice or multiple times within the parcel rises.

Optical depth can be thought of as the number of mean free paths from one side of the gas to the other. The mean free path is the average distance a photon will travel before it collides with an atom and is a function of the density of the gas and the resonant scattering cross section of the particle. If photons must travel further than one mean free path through a gas, it will interact with more than one atom between the time it enters the parcel and the time it exits.

As the density of a gas increases and the optical depth nears $\tau = 1$, the relationship between the brightness of the gas parcel and the number density of the gas becomes nonlinear. Scattering processes within the gas as particles trade more photons with each other instead of transmitting them into space cause the relationship between brightness and density to become logarithmic at optical depths greater than $\tau = 1$ [51]. This is known as line saturation and can be seen on the curve of growth, shown in Figure 2-1.

This effect causes the peak of an emission line profile to grow more slowly as density increases compared to the wings of the line profile caused by broadening mechanisms. This causes the emission profile to becoming even broader because the photons at wavelengths that are higher standard deviations away from the line center are not absorbed as easily.

The resonant scattering cross section is dependent on the temperature of the gas

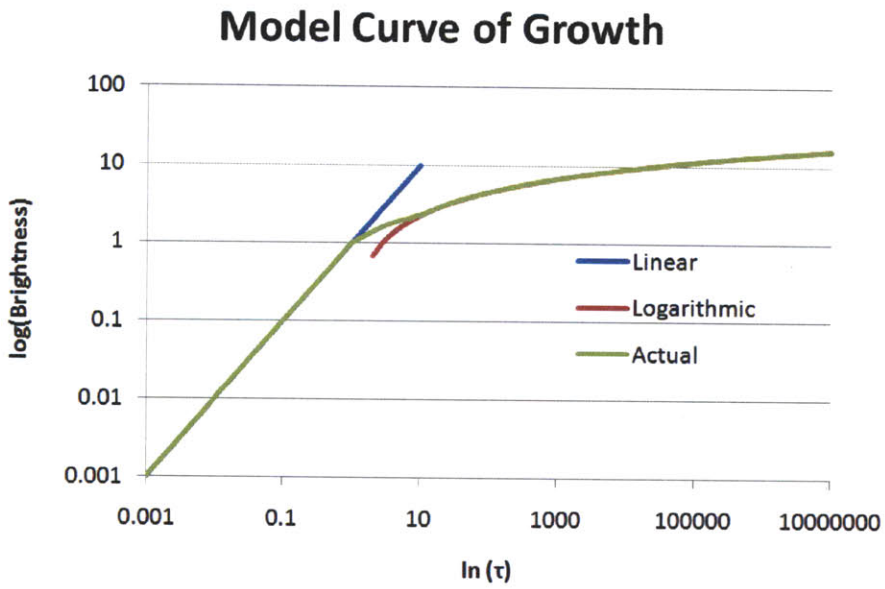


Figure 2-1: Model curve of growth. Brightness increases linearly with optical depth when optical depth is beneath $\tau = 1$. Brightness increases logarithmically with optical depth when optical depth is above $\tau = 1$.

and can be modeled with a Voigt profile. Photons at slightly different wavelengths than Lyman-alpha do not interact with hydrogen. However, if the hydrogen is moving such that the apparent line shift causes the incoming light to appear to have the same frequency as Lyman-alpha, the photon will be absorbed and re-emitted. This is how hot gases that are scattering Lyman-alpha instead of emitting it through another energy source can have broad line profiles.

When the density of the gas is preventing increases in brightness near the line center, the optical depth of the gas at wavelengths further from line center is less than the optical depth of the gas at line center. These photons have not achieved line saturation and are still being scattered by only one molecule, unlike the photons close to line center. This widens the spectral line profile so that if it was modeled with a Voigt profile, the temperature needed to achieve a similar width would be extremely high and inaccurate. In order to model the spectral profile of a high density gas correctly, the effects of radiative transfer must be considered. Radiative transfer analysis is very complex and is beyond the scope of this project.

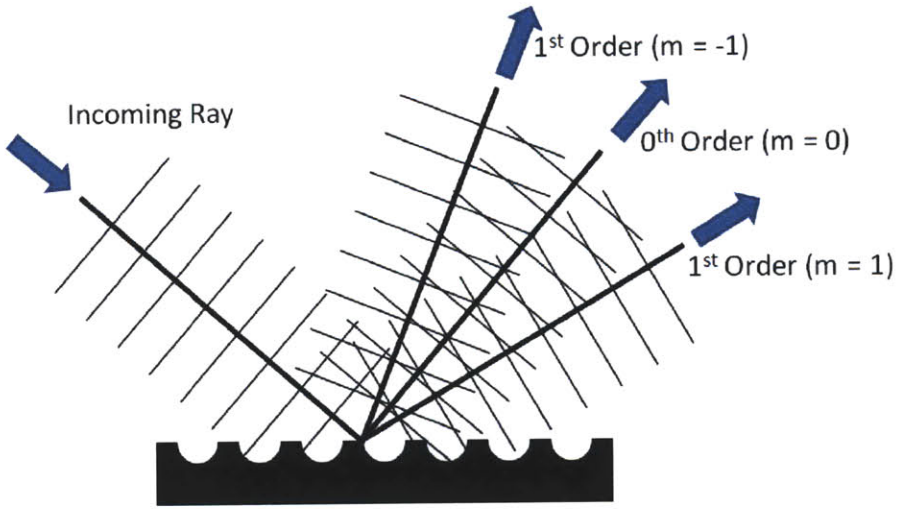


Figure 2-2: A reflection grating showing the orders of light produced by an incoming ray.

## 2.6 Spectrograph Optics

The human eye is limited to seeing a range of colors on the electromagnetic spectrum between approximately 400nm (violet) and 800 nm (red). Other wavelengths on the electromagnetic spectrum provide information on the objects that are being observed that must be detected by some other method. Because of the importance of spectroscopy, it is also useful to divide incoming electromagnetic radiation into a spectrum so its spectral characteristics can be studied in addition to its spatial characteristics.

### 2.6.1 Spectrograph Basics

A spectrograph is an instrument that disperses light so that the brightness in individual wavelengths of light can be measured. Light enters a spectrograph through a narrow slit, gets collimated by a parabolic mirror, and is directed at a diffraction grating. A diffraction grating can be transmissive or reflective, but on its surface are many narrow, evenly-space parallel lines. These grating lines act like a long series of double slits to produce periodic alterations in the phase of light due to wave interference called orders [22]. Figure 2-2 shows how the wave-like nature of light can create these orders.

The wavelengths of light have their maxima occurring at different angles $\theta$ after

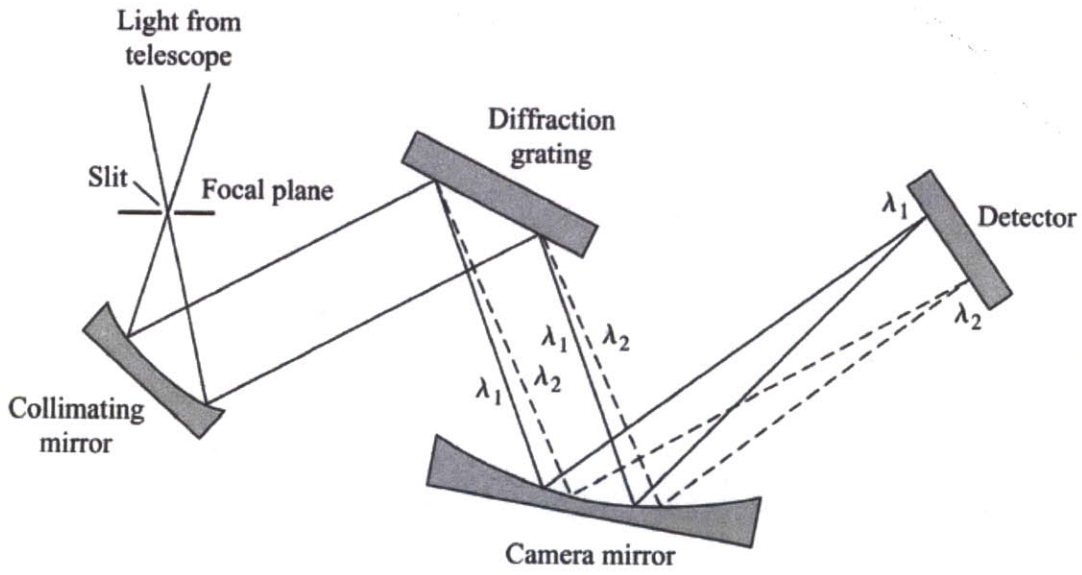


Figure 2-3: A spectrograph (Figure 5.2 in Carroll and Ostlie [7])

leaving the grating that can be solved using the Grating Equation

$$d \sin \theta = m\lambda \tag{2.25}$$

where $d$ is the distance between the lines on the grating, $\lambda$ is the wavelength of light, and $m$ is the order of light . The light then reflects off another mirror before being directed to the focal plane. Now, light is separated spatially by wavelength, as shown in Figure 2-3.

It is useful to know the minimum difference between wavelengths that a spectrograph can separate, or resolve. The wavelength separation $\Delta\lambda$ depends on the order $m$ and the total number of lines on the grating that light is on $N$, which is dependent on the size of the slit that light from the telescope comes through and the distance between grating lines. The smallest difference in wavelength that a spectrograph can resolve is given by

$$\Delta\lambda = \frac{\lambda}{\Delta\lambda} \tag{2.26}$$

which is also known as the minimum spectral resolution of the spectrograph [21]. The resolving power of a spectrograph is defined as the wavelength over the minimum

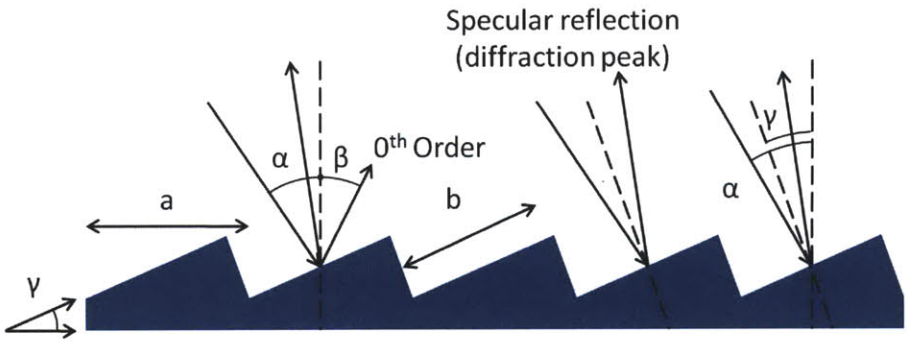


Figure 2-4: Section of a blazed reflection grating.

spectral resolution.

$$R = \frac{\lambda}{\Delta\lambda} \tag{2.27}$$

Most gratings used in modern spectrographs are blazed. Blazed gratings have rectangular cuts made across the surface at an angle as shown in Figure 2-4. Different orders of light reflect off the grating at different angles, so the incoming angle of light must be taken into account. The more general form of the Grating Equation becomes

$$d(\sin\alpha \pm \sin\beta) = m\lambda \tag{2.28}$$

where $\alpha$ and $\beta$ are the angles of incidence and diffraction [22]. Now the resolving power can be defined in terms of other constraints

$$R = \frac{W}{\lambda}(\sin\alpha \pm \sin\beta) \tag{2.29}$$

where $W = dN$ is the ruled width of the grating.

According to Formula 2.29, the highest resolution occurs when the angle of incidence equals the angle of diffraction, so the resolution becomes

$$R = \frac{2W\sin\beta}{\lambda} \tag{2.30}$$

and the dispersion becomes

$$\frac{d\beta}{d\lambda} = \frac{2\tan\beta}{\lambda} \tag{2.31}$$

### 2.6.2 Echelle Spectrographs

According to these equations, the resolution is only limited by how small the grooves on the grating can be manufactured. However, as the density of grooves increases, difficulty arises because orders of light start overlapping with each other, making it difficult to spatially separate different orders of light. The free spectral range is the spectrum interval between successive orders and is given by the formulas

$$F_\sigma = \frac{1}{2t} \tag{2.32}$$

$$F_\lambda = \frac{\lambda^2}{2t} \tag{2.33}$$

where $2t$ is the optical path difference between successive orders, which is related to the order m by the formula

$$m = \frac{2t}{\lambda} \tag{2.34}$$

An echelle spectrograph, instead of using a grating with a high density of grooves, uses a lower density and operates are much higher orders [21]. An echelle grating can be seen in Figure 2-5.

Notice that $A/W$ is equal to $\cos\beta$ and $t/s$ is equal to $\tan\beta$. Now the dispersion equation can be written as

$$\frac{d\beta}{d\lambda} = \frac{2W\sin\beta}{A\lambda} = \frac{2t}{\lambda s} = \frac{m}{s} \tag{2.35}$$

The resolving power equations can be rewritten as

$$R = \frac{2W\sin\beta}{\lambda} = \frac{2A\tan\beta}{\lambda} = \frac{2At}{\lambda s} = mA \tag{2.36}$$

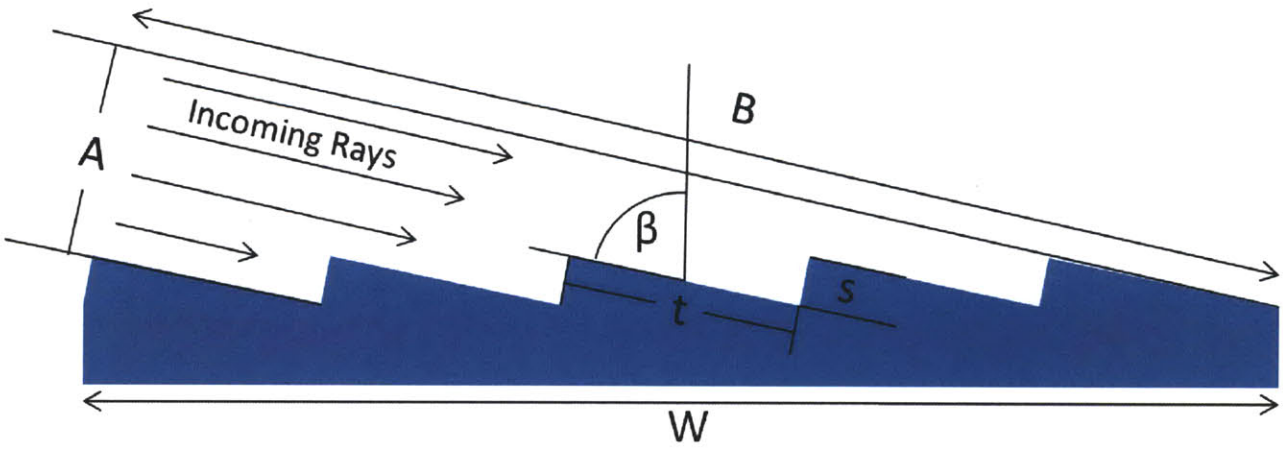


Figure 2-5: An echelle grating. $W$ is the ruled width, $A$ is the aperture, $B$ is the optical path length, $s$ is the step width, and $t$ is the step depth. The angles of incidence and diffraction of the rays of light are in and out of the page and are not shown.

Thus, at higher orders and wider apertures, an echelle spectrograph will have higher resolving power.

## 2.7 Ultraviolet Detectors

Even though the human eye is limited to sensing visible light, scientists have found ways to capture other types of electromagnetic radiation. Radio waves, for instance, can be intercepted by large antennae, and standard cameras can very easily detect infrared light. A common way to capture ultraviolet light is to use microchannel plate (MCP) detectors.

### 2.7.1 Microchannel Plates (MCPs)

A MCP is an array of small electron multiplier tubes encased in a matrix of insulating glass (Figure 2-6(left)). The tubes have small diameters, usually 12-15 $\mu m$, and lengths that vary from 40 to 100 times the diameter [59]. When the tubes are charged with a high negative voltage, electrons are easily stripped away from the inner surface of the tube. If a photon or particle enters the tube (an "event") with a high enough energy, it will strike the inner surface and release electrons (Figure 2-6(right)). These

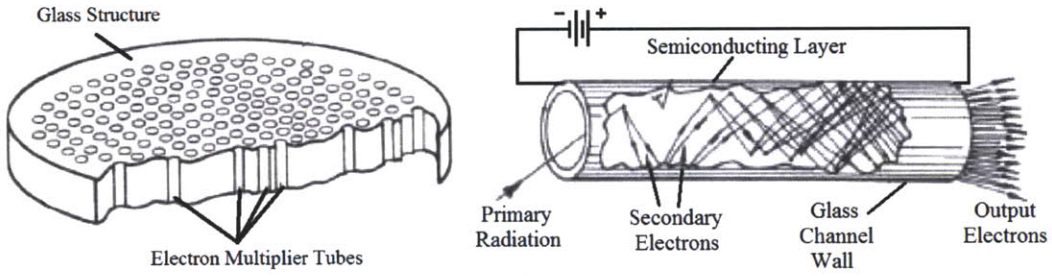


Figure 2-6: (Left) A microchannel plate (MCP) filled with electron multiplier tubes. (Right) An electron multiplier tube generating a cascade of electrons from a single incoming photon or particle (taken from [59]).

electrons will travel down the tube, colliding into the sides multiple times. With each collision, more electrons are released.

Because of a single particle collision at the entrance to the tube, somewhere between $10^4$ and $10^7$ electrons exit the tube, creating a small current that can be measured. The gain of a multiplier tube is the number of electrons released because of a single event. These tubes can be used to measure incoming particle or radiation with extremely high temporal resolution, on the order of 100 picoseconds, and the spatial resolution is only limited by how tightly the electron multiplier tubes can be packed together in the housing.

However, just because a photon or particle enters an electron multiplier tube does not mean that a shower of electrons will occur or will be detected. The quantum efficiency of a detector is the ratio between how many photons or energetic particles actually enter the MCP and how many events are recorded. For energetic electrons and ions, an MCP detector can have a quantum efficiency as high as 85%. For ultraviolet light, it is much less efficient, sometimes as low as 5%.

In order to increase the efficiency of the MCP detectors when counting ultraviolet photons, a photocathode is usually placed above the MCP. A photocathode is a negatively charged electrode that is sensitive to light. When a photon strikes the photocathode, it releases electrons via the photoelectric effect. Albert Einstein earned the Nobel Prize in Physics in 1921 for first describing this phenomenon. An electron is bound to an atom but can be freed if it absorbs enough energy to overcome the binding energy. Individual photons with enough energy can strip electrons away from

atoms [7].

The negative voltage applied to the photocathode lowers this binding energy so ultraviolet photons can release electrons with enough energy so that they fall into the electron multiplier tubes. Since electrons are more successful at creating large enough showers of electrons in the electron multiplier tube, the photocathode and MCP combination has a much higher quantum efficiency when detecting ultraviolet light than an MCP alone would.

Common ultraviolet photocathodes include cesium iodide (CsI) and potassium bromide (KBr). Cesium iodide has emission wavelengths in the ultraviolet spectrum at 310 nm and 460 nm whereas potassium bromide has none. Both are hygroscopic, meaning they absorb water from the atmosphere, so they must be kept in dry containers, usually in vacuum during operation or in a pure dry nitrogen environment while in storage.

### 2.7.2 Types of Detectors

The MCP does not count the events nor does it record the electron multiplier tube where an event happened. Behind the MCP is the anode that measures the cloud of electrons streaming from the electron multiplier tubes that get turned into data. The three types of anodes used in the course of this project are the Wedge-Strip-Zigzag (WSZ), Cross-Delay Line (XDL), and Cross Strip (XS) anode array.

In a WSZ detector, an anode sits behind the MCP is split into three arrays, the wedge, the strip, and the zigzag, as shown in Figure 2-7. The width of the wedges varies linearly with respect to the x-axis and the width of the strips varies linearly with respect to the y-axis. The zigzag array fills the remaining space on the detector. The x- and y-position of the cloud of electrons cascading onto the detector are given by

$$x = FQ_w/S \tag{2.37}$$

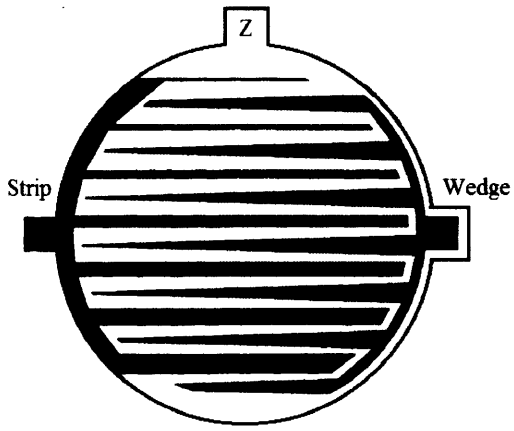


Figure 2-7: A wedge-strip-zigzag (WSZ) anode array (taken from [46].

$$y = FQ_s/S \tag{2.38}$$

where $F$ is a normalization factor, $Q_w$ is the charge received by the wedge anode, $Q_s$ is the charge received by the strip anode, and $S$ is the sum of the charge received by all three anodes [46].

The resolution of this detector is limited by the spacing of the elements in the wedge and strip arrays. The cloud of electrons cascading from an electron multiplier tube is allowed to drift for approximately 15 mm before landing on the WSZ anodes. This is so the cloud's size grows larger than the distance between two wedge and strip elements. As the spacing between elements decreases, the electron cloud can be smaller until the resolution is limited by the MCP. Typical resolution of WSZ detectors is 80 $\mu m$ but can be as low as 50 $\mu m$.

The XDL detector anode works by measuring the time difference between two pulses produced by an electron cloud at two ends of a delay line [35]. The different in the times the signals are received can determine the position where the electron cloud lands on the anode. There are two anodes in the XDL, one measuring x-position and one measuring y-position, shown in Figure 2-8(left). The resolution is limited by the spacing of the anode lines. Four bandwidth amplifiers are needed to reach high spatial resolutions, but large gains ($10^7$ electrons per event) are necessary. A typical XDL detector has a resolution of about 25 $\mu m$.

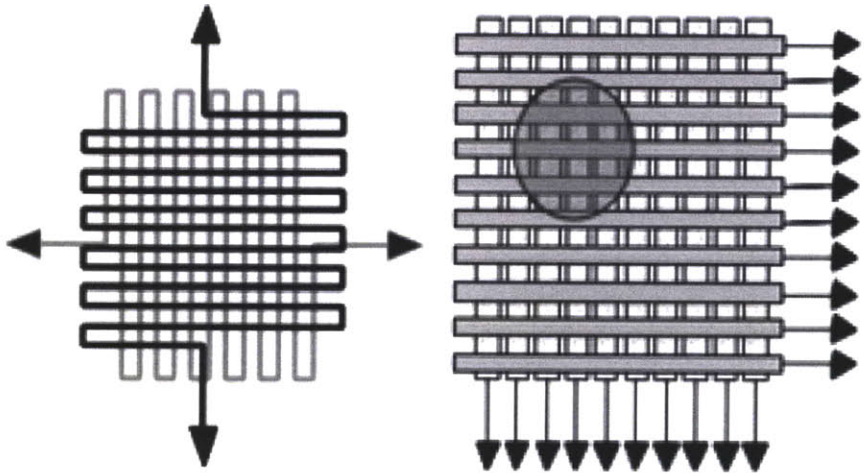

Figure 2-8: Cross Delayline (XDL) (left) and Cross Strip (XS) (right) anode arrays (taken from [35].

The XS detector is made of a series of strips each with their own charge amplifier (Figure 2-8(right)). The strips detect the centroid of the cloud to determine the x- and y-position of the event. The strips can be packed very tightly to achieve resolutions as high as 5 $\mu m$, high enough to resolve the electron multiplier tubes, with gains as low as 5 x $10^5$.

### 2.7.3 Detector Dead Time

The count rate of all detectors is limited by their dead time. Dead time is the time after the processing of an event begins when the system is unable to record another event. Dead time can be limited by the processing electronics because computation speed is too low to handle high volumes of data. In space-based systems, dead time may be limited by the transmission rate of data. When any of these digital limitations exist, the count rate has a set maximum that abruptly limits the data rate. There is no way to estimate how much higher the count rate actually is if the maximum rate is achieved.

Dead time is also limited by the MCP and the anode arrays because of analog dead time. When the count rate of a system is low, the rate of events recorded will be linearly proportional to the rate of actual events (the ratio of the two is the quantum

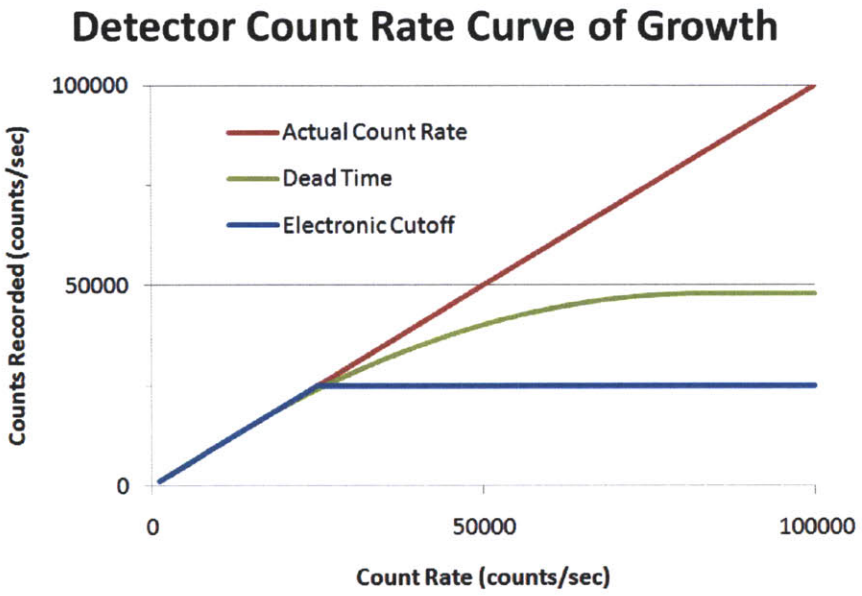


Figure 2-9: Example curve of growth of data on a detector (recorded vs actual count rates)

efficiency, and it is constant at low count rates). As the actual event rate increases, the detectors cannot keep up with the events, so the rate of events recorded grows more slowly than the rate of actual events. This relationship, shown in Figure 2-9, is a dead time function. Eventually, the recorded event rate will reach a maximum even as the actual event rate continues to grow. As opposed to how digital dead time limitations abruptly limit the count rate, the analog dead time error grows gradually. The dead time function can be used to estimate the actual count rate given the recorded count rate, but this error increases with increased count rate.

The dead time in an electron multiplier tube can be estimated by modeling the tube as a parallel-plate capacitor and using the known gain and resistance to calculate the time constant of the RC circuit. A single electron multiplier tube may have a dead time on the order of milliseconds as the channel regains electrons that were lost, but for a uniform field across the entire MCP, dead time is on the order of nanoseconds and is not a major factor in the measured dead time of the detector [59].

Dead time in WSZ and XS is caused by a similar phenomenon. Pulses from the electron clouds are measured and must be cleared from the anode before another electron cloud strikes. In a WSZ detector, the energy in each pulse is measured as

the sum of total charge put on the anode. If there are two events detected as one, the sum of the charge from the two pulses will be much higher than the sum from just one pulse. High-charge events can be discarded as bad counts, and the average charge per pulse can be monitored. The error in the recorded event rate grows as more events corresponding to double-counts grows. WSZ detectors count rates are usually limited to approximately 5 kHz because of the signal processing electronics [46].

XS detectors must also recharge the strips, but since each strip uses its own amplifier and the required gain is low, dead time is very low and is usually limited by the supporting electronics. Count rates above 100 MHz can be achieved with state-of-the-art systems before dead time error becomes a serious issue [35].

XDL detectors are limited by the length of the delay lines. If an event occurs on a delay line before the previous event has cleared, the XDL will read an incorrect position of both events. The global count rate of the detector is limited by how quickly electricity passes through the lines. In practice, XDL detectors are limited to a count rate of 1 MHz, but in practice 200 kHz can be measured with 10% dead time error, i.e. the recorded event rate would be 180,000 counts per second when the detector should measure 200,000 counts per second if dead time error was not a factor. If the quantum efficiency was 50%, the actual count rate would be 400 kHz, or 400,000 counts per second.

## 2.8 Comparison of the Hubble Space Telescope and VeSpR

The Hubble Space Telescope (HST) was launched in 1990 as the first telescope of NASA's series of Great Observatories, along with the Compton Gamma Ray Observatory, the Chandra X-Ray Observatory, and the Spitzer Space Telescope. After a servicing mission in 1993 to fix a spherical aberration caused by errors in manufacturing the primary mirror, HST delivered the highest-quality images of the universe

that had ever been observed. HST's primary mirror is 2.4 m in diameter, giving it a total collecting area of 4.5 $m^2$, and after the optics were corrected in 1993, the angular resolution was 0.05 arcsec at 500 nm.

One of HST's instruments is the Space Telescope Imaging Spectrograph (STIS). STIS was installed on HST during the second servicing mission in 1997 and replaced the High Resolution Spectrograph and the Faint Object Spectrograph. The optics and detectors can observe wavelengths between 115nm and 1000 nm. STIS uses 16 diffraction gratings, 12 of which operate in the first order and four of which are echelle gratings, which operate on higher orders (see Section 2.6). The high-resolution echelle mode, E140H, has a spectral resolving power that ranges from 105,000 to 220,000 and 0.057 Å resolution at Lyman-alpha with a 0.5 arcsec aperture width [2].

STIS has three primary detectors, one Charged-couple device (CCD) camera to cover the near-ultraviolet to near-infrared spectral ranges and two MCP Multi-anode Microchannel Array (MAMA) detectors to cover the far-ultraviolet to near-ultraviolet spectral ranges (MAMA anode arrays are similar to XS anode arrays). Both MAMA detectors are coated with photocathodes; the near-ultraviolet (NUV) MAMA is coated with cesium telluride ($Cs_2Te$) while the far-ultraviolet (FUV) MAMA is coated with cesium iodide (CsI). Both MAMA detectors are protected by a magnesium fluoride ($MgF_2$) window. Figure 2-10 shows the STIS optical concept taken from Woodgate et al. [2].

HST and STIS certainly have the resolving power to measure the D/H ratio of Venus. Observations made with the less-powerful GHRS in 1997 (before the second servicing mission to install STIS) were able to observe the deuterium Lyman-alpha line with an intensity of 23±6 Rayleighs [56]. A follow-up campaign with STIS in May 2001 measured D/H on Mars with even higher resolution (Figure 2-11) [34].

Given that HST and STIS are so powerful, and the D/H ratio on Venus is higher than it is on Mars, it should be easy to resolve D/H on Venus using this instrument. Unfortunately, HST is limited in its pointing range. If sunlight enters the telescope, light reflecting off the inner walls could damage HST's instruments and cause thermal damage to the optics. Unlike Mars, Venus orbits inside of Earth's orbit, so it never

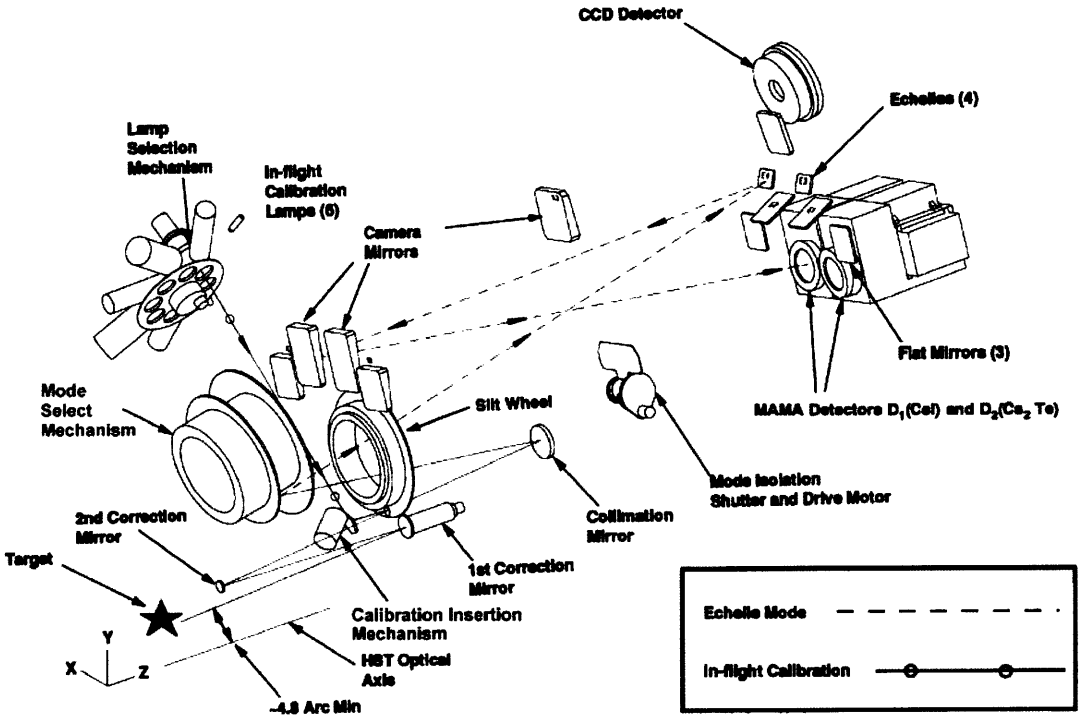


Figure 2-10: STIS Optical Concept Design take from [2]. Hubble's primary and secondary mirrors are not shown here.

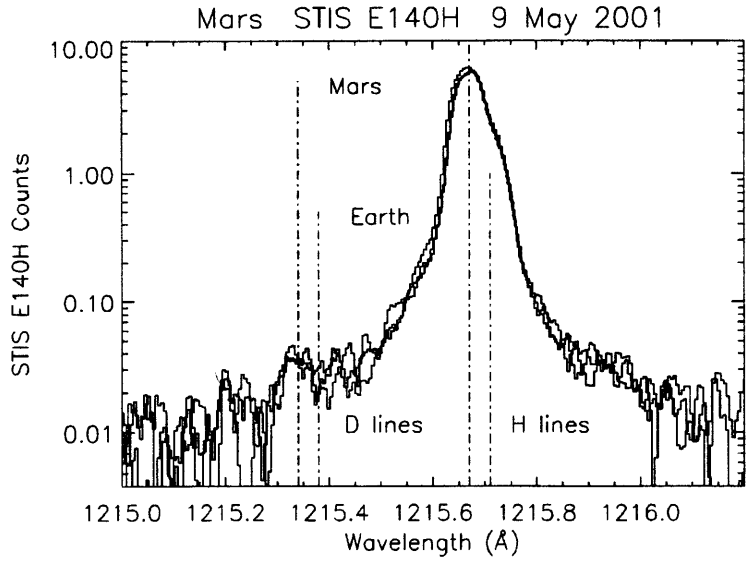


Figure 2-11: STIS spectrum showing detection of both hydrogen and deuterium emissions from Earth and Mars taken from [34].

is seen too far away from the Sun. Hubble is not allowed to point within 50 degrees of the Sun; Venus is never more than 48 degrees away from the Sun at maximum elongation.

Hubble has been able to observe Venus in the past, however, for short times after Venus has risen above the horizon and before the sun rises. Two short observations were attempted but were unable to resolve the D/H ratio. Proposals were accepted but never scheduled to observe Venus using GHRS. It now appears that HST will never observe Venus for more than short images. In order to measure D/H on Venus, a different instrument is needed. The Venus Spectral Rocket is the only existing instrument that can make that measurement.

The Venus Spectral Rocket, or VeSpR, also carries a high-resolution echelle spectrograph. The grating VeSpR uses is a replica of the one flown on STIS. The primary mirror is much smaller than Hubble's, only 35 cm in diameter with a total collecting area of 0.064 $m^2$. However, VeSpR makes up for this with a system that is optimized for Lyman-alpha light.

STIS uses a 0.2 x 0.2 $arcsec^2$ aperture for its high-resolution echelle spectroscopy. In comparison, VeSpR uses a 3 x 5 $arcsec^2$ aperture. This means VeSpR's spectrograph views a solid angle on the sky that is 375 times bigger than STIS can, so there is a higher flux of light entering the spectrograph.

In addition, STIS has more optical components than VeSpR does. Since the reflective efficiency of any optical component is low, removing unnecessary reflections will increase the total throughput of the system. Two of STIS's light reflections only correct for the aberration of the primary mirror and nothing else; VeSpR does not need such optics [2]. STIS uses a cross-dispersion grating to prevent the overlap of different orders on the detector; VeSpR uses an objective prism to separate Lyman-alpha from other wavelength bands coming through the telescope before they enter the spectrograph, and the throughput efficiency of the prism is greater than the reflective efficiency of the cross-dispersion gratings.

Even though the light collecting area of HST's primary mirror is approximately 50 times larger than VeSpR's, the larger aperture size and higher efficiency on VeSpR

means it can achieve the same objective as Hubble in less time. A Hubble observation that requires on the order of one hour to achieve an acceptable signal to noise ratio would take VeSpR approximately five minutes. Even if Hubble was able to point at Venus, the amount of observation time required to measure the D/H ratio could prevent such a proposal from being accepted considering how oversubscribed Hubble observation time already is.

# Chapter 3

# Previous Work

## 3.1 Previous Flights of the VeSpR Payload

The work being done in most of this project is preparing the Venus Spectral Rocket for its first mission to study Venus using high-resolution spectroscopy. The science payload as it exists now has never been flown before, but components of the payload have been used since the late 1960s.

The first flight of components that would eventually become the Venus Spectral Rocket was on December 5th, 1967 [42]. The payload was launched from White Sands Missile Range (WSMR) on an Aerobee 150 rocket. The payload carried a Dall-Kirkhan telescope with a 25 cm diameter primary mirror, a lithium fluoride (LiF) prism spectrometer, and a star tracker to adjust the pointing accuracy (Figure 3-1). During this flight, the payload observed Venus, Jupiter, and Ursa Majoris and reached an apogee altitude of 157 km.

The second flight occurred on June 2nd, 1970 [18]. This time, the payload was outfitted with a Czerny-Turner LiF prism spectrometer [20] and observed the Lyman-alpha emission of Arcturus. Due to a malfunction in the star tracker, Arcturus was only centered within the field of view of the telescope for 6 seconds, but Earth's Lyman-alpha airglow and the emission from the interplanetary medium was monitored during the rest of the flight.

The third flight occurred on January 25, 1971 [19] The payload was identical

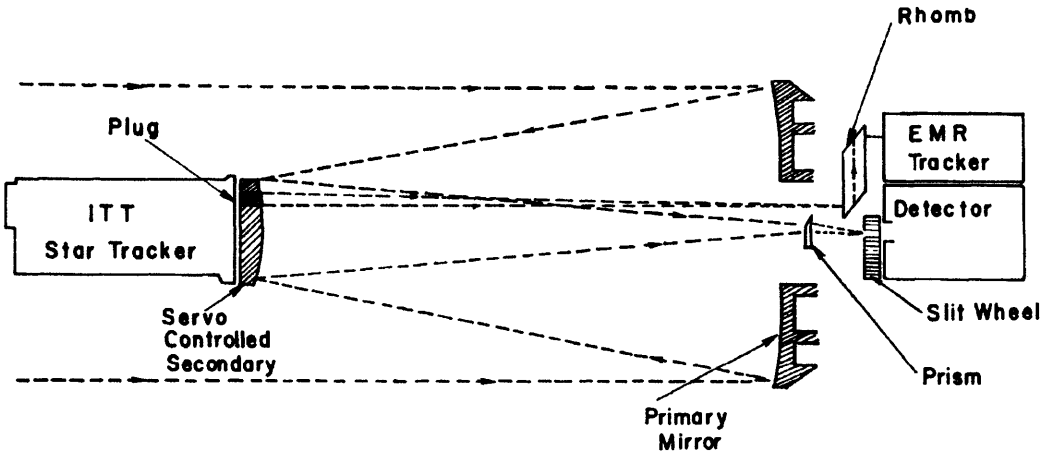


Figure 3-1: Telescope and detector configuration on the first flight of the science payload that would eventually become VeSpR.

to the previous flight and observed Venus while it was at maximum elongation to observe neutral oxygen and hydrogen emissions to prevent resonance absorption by terr[8]estrial oxygen and hydrogen. This flight successfully recorded 26 spectra of Venus between 1190 and 1340 Å.

The fourth flight of the payload was on September 1st, 1972. It was flown on an Aerobee 170 sounding rocket and reached a peak altitude of 159 km . For this flight, a new 10-channel Czerny-Tuner lithium fluoride prism spectrometer was installed [25]. Arcturus was observed again, this time in a wider ultraviolet spectrum from 1180-1950 Å.

Later, the payload was rebuilt and its fifth flight occurred on December 1st, 1978 [32]. This flight used a micro-channel plate (MCP) detector and a lithium fluoride objective prism to disperse light at wavelengths higher than 1500 Å and cut off light at wavelengths beneath 1200 Å [8]. This allows the MCP detector to record ultraviolet images, specifically Lyman-alpha images. Figure 3-2 shows this new instrument configuration.

The payload was flown on an Astrobee-F rocket and observed above an altitude of 130 km for 265 s. During this flight, the payload observed Jupiter to record a Lyman-alpha image of the planet. The goal of the flight was to study the Lyman-alpha emission of the auroral regions, but no significant auroral emission was found.

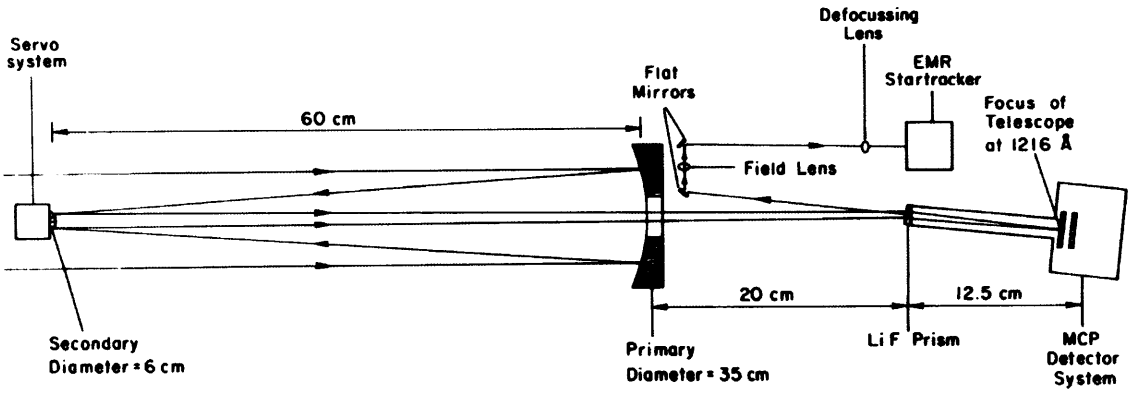


Figure 3-2: Telescope and detector configuration on the 1979 flight of the science payload that would eventually become VeSpR.

Instead, a bright spot near the equator was observed. This flight marked the discovery of the Jupiter Lyman-alpha Bulge (see Section 3.3).

In the early 1990s, the payload was once again reconfigured. This time, it was fitted with the high-resolution imaging spectrograph that is still in the payload. This payload was used in a campaign throughout the 1990s to study the Lyman-alpha emission from Jupiter's auroral regions, but the payload was capable of studying other planetary targets as well. The payload was officially names the Jovian Auroral Spectrograph Rocket, or JASpR.

A detailed description of the instrumentation was given by Harris et al. [58]. The same Dall-Kirkham telescope with a 35 cm diameter primary mirror was fit with a spectrograph designed with a modified Ebert-Fastie configuration (Figure 3-3) [16]. The spectrograph sacrifices broad spectral coverage to allow the study of individual line profiles at very high resolution. The echelle grating is a replica of the one on the Hubble Space Telescope (HST) Space Telescope Imaging Spectrograph (STIS) and has been optimized for the 221st order for 1216 Å at a blaze of 68.8 degrees. Two wedge-strip-zigzag (WSZ) micro-channel plate (MCP) detectors with a 10,000 Å potassium bromide (KBr) photocathode deposited on the upper plate record scientific data and have quantum efficiencies as high as 35%.

Previous missions were launched on Aerobee rockets, but all JASpR missions were launched on Black Brant IX rockets. JASpR 1, designated 36.062, launched on May

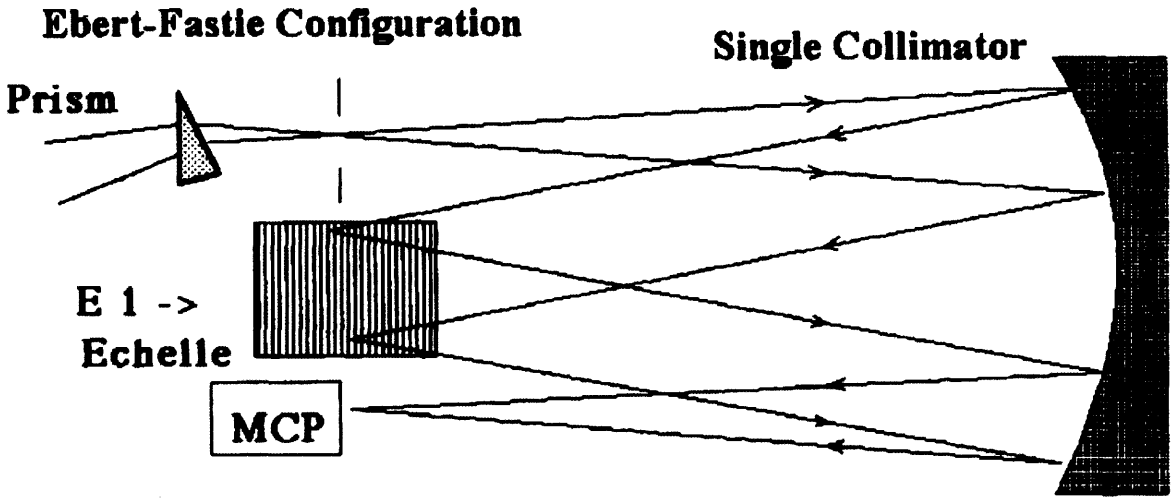


Figure 3-3: Ebert-Fastie configuration of the spectrograph installed on the Jovian Auroral Spectrograph Rocket (JASpR)

4th, 1991 and achieved an apogee of 300 km. During this flight, a yaw crosstalk error associated with the NASA star tracker prevented the acquisition of Jupiter by the telescope. However, a detailed spectrum of Earth's geocoronal and the interplanetary medium Lyman-alpha emissions were recorded and analyzed following the flight.

The star tracker error was unique to that particular star tracker and was characterized by a change in the yaw position readout that is dependent on the input line voltage. This problem was resolved by using a different NASA star tracker. In later JASpR flights, both Jupiter and the acquisition star were acquired to within one arc min, and the image of Jupiter was positioned on the aperture and held to 1-2 arc sec accuracy.

JASpR 2, designated 36.101, launched on June 16th, 1993 and achieved an apogee of 253 km. During this flight, there was a failure in the telemetry data from the MCP detectors, and the data received on the ground was distorted and unreadable. The evidence from extensive post-flight testing suggested that the detector performed nominally, but that an intermittent connection had corrupted the NASA telemetry stream.

To ensure this would not affect future flights, several changes were made to the payload. All wiring was replaced between the detector and the NASA telemetry

encoder to ensure solid electrical connections. A backup flight data recorder was added to store MCP data directly from the detector so it could be recovered after flight if there was a failure in the telemetry data received on the ground. Finally, the MCP detectors were replaced with newer, higher-resolution detectors and associated signal processing electronics.

JASpR 3, designated 36.104, launched on April 1st, 1995 and achieved an apogee of 253 km. During this flight, the telemetry recorded a high voltage discharge on the MCP detector. This was later traced to a Reynolds 600 series connector that provides high voltage to the detector housing that had not been properly cleaned and tightened before flight. Protocol was introduced where the Principal Investigator inspects and attaches all high voltage connectors before flight.

JASpR 4, designated 36.149, launched on October 29th, 1996 and achieved an apogee of 300 km. During this flight, none of the previously encountered problems were present, but the overall count rate recorded by the MCP detectors was significantly lower than necessary to meet the science goals of the mission. This was likely due to contamination of the optics during the extensive high vacuum testing the payload underwent before flight to demonstrate that there would be no high voltage arcing on either detector at any pressure. The vacuum chamber used diffusion pumps to achieve vacuum, and there is evidence that diffusion pump oil entered the chamber and contaminated the optics.

This contamination would have been discovered had the payload gone through an additional absolute calibration before the flight. Unfortunately, the testing chamber at the University of Colorado that was used to show the optics were in alignment did not have the ability to perform an absolute calibration of the whole system. In response, the Vacuum Calibration and Testing Facility (VACTEF) was designed and built to perform clean, high vacuum payload calibration and testing for future flights. The optics were recoated to achieve higher efficiency on later flights.

JASpR 5, designated 36.174, was never launched due to budget cuts in the sounding rocket program. In addition, there was a failure of the data stream during testing. Data from the spectrograph detector stopped coming through the ground support sys-

tem, and because the program had been canceled, the exact cause of this problem was never discovered. Furthermore, one of the servos on the secondary mirror that controlled the tip/tilt had burned out, so the mirror was only able to adjust itself in one direction during flight. The payload was put in to storage in 2003 with constant power to the VIPs to hold the detectors at vacuum until they were used again.

## 3.2 Previous Measurements of the Deuterium/Hydrogen Ratio on Venus

VeSpR will not be the first mission to study the water history on Venus. Several other missions have attempted to understand the elevated D/H ratio that has been measured on the planet, but none have been able to unambiguously constrain the D/H ratio above the homopause. Other missions have measured $HDO/H_2O$ with significant accuracy at lower altitudes; however, in order to understand atmospheric escape of hydrogen and the photodissociation of water in planetary atmospheres, the D/H ratio above the altitude where photodissociation occurs must be better understood. This section reviews some of the previous work that has attempted to measure the D/H ratio or the $HDO/H_2O$ atmosphere in various areas of the Venus atmosphere.

### 3.2.1 Mariner 5 (1967)

Mariner 5 was launched on June 14th, 1967 and flew by Venus on October 19th of that year. Among its scientific instruments was an ultraviolet photometer that measured ultraviolet light through three filters. The effective passbands for the three channels were 1050 to 2200 Å, 1250 to 2200 Å, and 1350 to 2200 Å [10]. The difference between the signals observed by the first two channels was the Lyman-alpha emission from atomic hydrogen. The results initially implied that the temperature several hundred kilometers above the surface was much lower than the temperature at comparable altitudes on Earth; this would imply that the escape rate of atomic hydrogen by Jean's escape was also much lower than on Earth.

Further analysis of this data showed that these Lyman-alpha measurements could only be fit with barometric-exospheric equations if a two-component model of the atmosphere was used [5]. Three possible hypotheses for these two components were proposed. The first was that there was an abundance of molecular ($H_2$) molecules in addition to atomic hydrogen in the upper atmosphere. This atomic-molecular hydrogen model was initially considered the most realistic explanation for the Mariner V Lyman-alpha data. The second was a two-temperature model, but this model would require two separate sources of hydrogen. The third model was a deuterium-hydrogen model. This model was not preferred over the atomic and molecular hydrogen model because it required a D/H ratio of 10 or higher.

The deuterium-hydrogen model was later re-examined. It was shown that the D/H ratio of 10 predicted by Barth [5] could be reconciled with transport and diffusion mechanisms. McElroy and Hunten [44] showed that the D/H ratio could be 0.1, which is still an enhancement of several orders of magnitude compared to the terrestrial value of 1.6 x $10^{-4}$. Their work was the first to conclude that an elevated D/H ratio was a serious possibility.

### 3.2.2 Pioneer Venus (1978)

The Pioneer Venus mission was a two-vehicle combination of an orbiter and a multi-probe launched by NASA. The multiprobe consisted of a bus that carried one large and three small probes that all entered Venus' atmosphere on December 9th, 1978 [37]. The large probe's neutral mass spectrometer (LNMS) entered near the equator and measured the abundances of atmospheric constituents as it descended into the Venus atmosphere, slowed by a parachute [24].

At an altitude of 64 km, two microleak channels on the instrument allowed gas from the atmosphere into the spectrometer [53]. The instrument scanned the mass spectrum from 1 to 208 atomic mass units once every 64 seconds.

There is debate about the validity of the data from the LNMS. The instrument was backfilled with helium and nitrogen during its voyage to Venus. There is evidence that it was also contaminated with terrestrial moisture, and that moisture had a

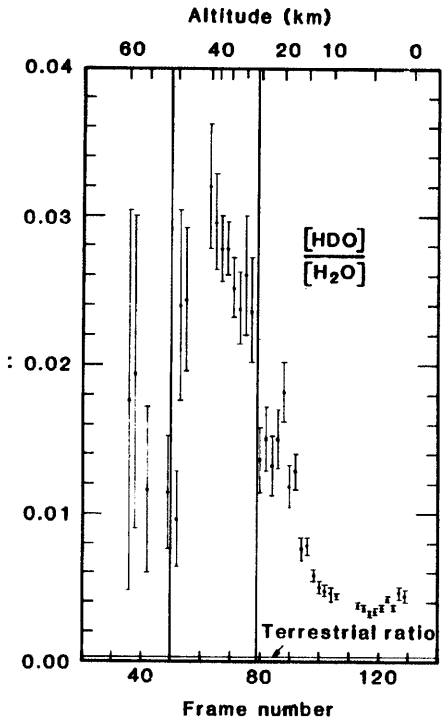


Figure 3-4: Ratio of counting rates of $HDO/H_2O$ as a function of data frame taken from Donahue et al. [53]. The horizontal axis indicates the frame number of the data (bottom scale) and altitude in km (top scale). The vertical axis indicates the D/H ratio. The data between the two vertical lines indicate the time when the spectrometer inlet was clogged with droplets of sulfuric acid.

terrestrial value for the $HDO/H_2O$ ratio. The inlet tubes were heated to prevent condensation, which would have produced terrestrial water vapor that the spectrometer then measured.

When the large probe descended beneath 50 km, the spectrometer microleak channels clogged with sulfuric acid, most likely from cloud droplets. One of the microleak channels was shut off at 47 km and the other cleared between 29 and 26 km. Donahue et al. argue that the best measurements of the $HDO/H_2O$ ratio come when the inlet is clogged with Cytherean droplets. When this happened, the count rate dramatically increased and with it the signal-to-noise ratio of the data. Figure 3-4 shows the ratio of $HDO/H_2O$ calculated from the raw data as a function of frame number and altitude.

The analysis from the LNMS data shows that the D/H ratio within this altitude

range in the atmosphere is 1.6 x $10^{-2}$. This agrees with the ratio of $10^{-2}$ found by McElroy et al. [45] using the same spectrometer data, who argue that the ion with a mass of 2 atomic mass units found by LNMS was ionized deuterium and not hydrogen molecules (which also have a mass of 2 atomic mass units). Donahue et al. further argue that this hundred-fold increase in the D/H ratio compared to Earth's D/H ratio sets a lower limit of 0.3% of a terrestrial ocean of water has escaped from Venus (see Section 2.2).

It was later shown that the densities of hydrogen and deuterium in the nightside thermosphere varied with the Solar cycle [47]. In-situ measurements made using the Pioneer Venus Orbiter Ion Mass Spectrometer (OIMS) during its pre-entry phase when the Solar cycle was close to Solar minimum show enhancements in hydrogen of 6.5 times and deuterium of 4 times compared to later years when the Solar cycle was at Solar maximum. This showed that the buildup during Solar minimum is caused by a reduction in the escape fluxes of hydrogen and deuterium.

However, these in-situ measurements were only taken above 170 km, which is several scale heights above the lower boundary where carbon dioxide absorption of Lyman-alpha decreases the photodissociation rates of $H_2O$ and HDO. In addition, the spectrometer did not measure deuterium directly, only the ions with a mass of two. This measurement could correspond to molecular hydrogen in those regions as well as deuterium even though it has been shown that the molecular hydrogen density is low.

### 3.2.3 Telescopic Observations of Venus

In 1980, the International Ultraviolet Explorer (IUE) observed Venus while the planet was at maximum elongation and recorded a series of spectra with a total observation time of 260 minutes. The goal was to measure deuterium in the upper atmosphere above where Pioneer Venus' LNMS measured $HDO/H_2O$. Figure 3-5 shows the data from the combination of the spectra taken from [27]. These results show Venus' hydrogen Lyman-alpha emission to be $21 \pm 5$ kR, which is consistent with measurements from Pioneer Venus.

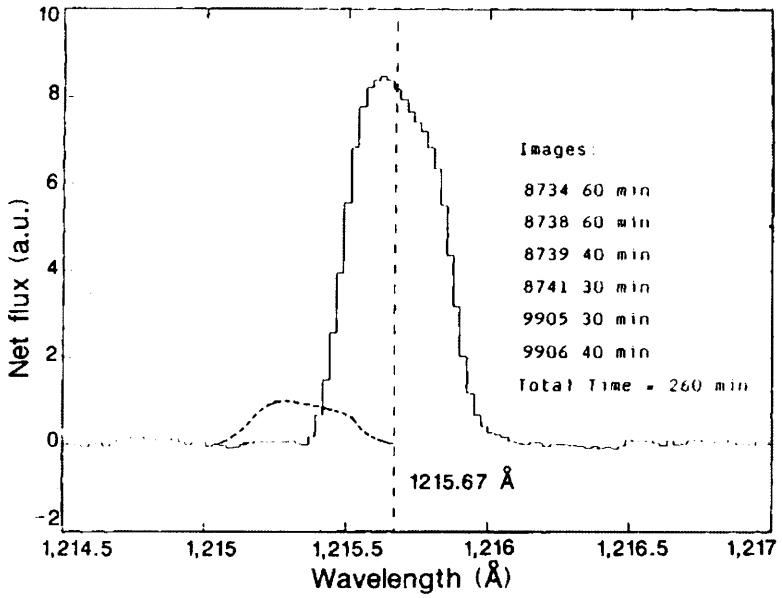


Figure 3-5: Hydrogen Lyman-alpha emission of Venus measured by the International Ultraviolet Explorer (IUE) taken from Bertaux and Clarke [27]. The solid line corresponds to the observed data, a 21 kR emission. The dashed line corresponds to the profile calculated for a 2.5 kR deuterium emission, expected for the D/H ratio measured by Pioneer Venus of 1.6 x $10^{-2}$. The Net Flux units (a.u.) denote $10^5$ IUE flux units.

However, the results do not show evidence of a deuterium emission, which was expected to be on the order of 2.5 kR based on the deuterium abundance found by Pioneer Venus. Instead, the IUE observations only placed an upper limit of 300 R on the deuterium emission, which Bertaux and Clarke argued corresponds to a D/H ratio of 2 x $10^{-3}$, a factor of 8 less than the Pioneer Venus measurement.

In view of this discrepancy, Bergh et al. used the Fourier Transform Spectrometer with the 3.6 m Canada-France-Hawaii telescope on Mauna Kea to detect HDO and $H_2O$ in Venus' atmosphere in an altitude range between 32 and 42 km [9]. Their spectral observations in the 3-4 $\mu m$ range found total abundances of $H_2O$ and HDO to be 34±10 and 1.3±0.2 parts per million, corresponding to a D/H ratio of 1.9±0.6 x $10^{-2}$, which is consistent with what was measured by Pioneer Venus. However, these results still do not directly measure D/H in the upper atmosphere.

### 3.2.4 Venus Express (2007)

The European Space Agency (ESA) launched Venus Express on November 9th, 2005. It was the agency's first mission to Venus. The spacecraft is very similar to the successful Mars Express launched two and a half years earlier, but its design was modified to withstand the more severe thermal environment [14]. It carries seven suites of science instruments to study Venus; five were inherited from the Mars Express and Rosetta missions with slight design modifications, and two instruments were specially designed for Venus Express.

The Spectroscopy for the Investigation of the Characteristics of the Atmosphere of Venus (SPICAV) is one of the suites that was borrowed from Mars Express. SPICAV is a suite of three spectrometers, one in the ultraviolet wavelength range and two in the infrared wavelength range. The goal of the experiment is to study the composition and structure of Venus' upper atmosphere [14, 28].

The ultraviolet spectrometer is identical to the one flown on Mars Express [14]. It operates within the 110-320 nm wavelength range with a resolution of 1.5 nm. This instrument does not have the resolution to directly detect the separate Lyman-alpha emissions from deuterium and hydrogen atoms. It was speculated that the combined intensity profile could be separated with data from this instrument by examining the variation with altitude [28]. The optically thick hydrogen emission should vary smoothly with altitude down to where carbon dioxide absorption dims the emissions (near 120 km), while the optically thin deuterium emission would cause a spike above this altitude. However, this technique was not successful in determining the D/H ratio in the upper atmosphere.

One of the other SPICAV instruments is the Solar Occultation Infrared (SOIR) spectrometer. The SOIR spectrometer operates within the 2.2-4.4 $\mu m$ range and was designed and developed specially for Venus Express [14]. It has a resolving power of 15,000-20,000, which is enough to resolve the $H_2O$ and HDO absorption profiles in a stellar occultation.

Between December 21st, 2006 and January 8th, 2007, SOIR measured the abun-

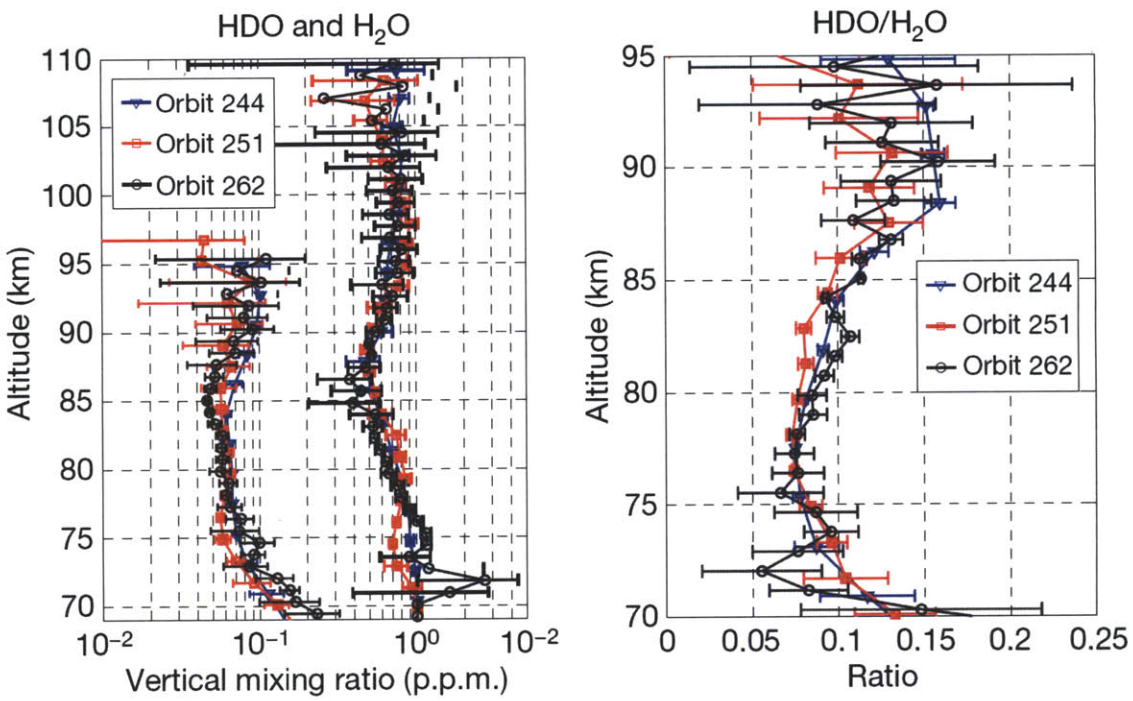


Figure 3-6: Data from Venus Express' SOIR measuring (left) abundance of HDO and $H_2O$ and (right) the $HDO/H_2O$ ratio [29]. The measurements on Orbits 244, 251, and 262 were taken at latitudes of +85, 83, and 73 degrees. Error bars indicate 1 standard deviation.

dance of HDO and $H_2O$ in the Venus atmosphere between 70 and 110 km altitude at high polar latitudes. Figure 3-6 (left) shows the vertical mixing ratios of each molecule and Figure 3-6 (right) shows the ratio of the two abundances [29]. These measurements show little temporal variation. At the lower altitude boundary, the $HDO/H_2O$ mixing ratio is close to 0.1 with an error bar (1 standard deviation) over 50%. This is within the bounds of what has been measured in the bulk atmosphere at lower altitudes [53, 45].

The mixing ratio was expected to decrease with altitude because of the preferential condensation of HDO [26], but it instead increases up to 0.12, which is about 2.5 times the $HDO/H_2O$ ratio in the bulk atmosphere. This suggests that there is no cold trap preventing photodissociation in the upper atmosphere, and that the increase in the ratio is due to the lower photodissociation rate of HDO compared to $H_2O$. Laboratory tests have shown that HDO has a lower ultraviolet cross-section than $H_2O$ at Lyman-alpha, so it is dissociated by photons at a lower rate [6].

The higher $HDO/H_2O$ ratio at higher altitudes could also mean hydrogen atoms are escaping into space much faster than deuterium atoms, which are left behind and recombine with OH radicals [29]. This would be the first measurement of hydrogen escaping more quickly than deuterium, and the presence of deuterium atoms in the photodissociation region indicates deuterium is present in the thermosphere. Quantifying the deuterium and its ratio to hydrogen above this region is essential for understanding the escape mechanisms.

Since the UV spectrometer was unable to measure the D/H ratio in the upper atmosphere directly, this measurement is still missing. The Venus Spectral Rocket Project was proposed specifically to complement the SOIR data to better understand the photodissociation and escape mechanisms and rates. VeSpR will measure the Lyman-alpha flux of deuterium and hydrogen above 110 km.

## 3.3 Previous Observations of the Jupiter Lyman-alpha Bulge

Over the past three decades, there have been a number of space missions to send probes and orbiters to Jupiter. Those missions, along with additional telescopic observations from both ground-based and space telescopes, have greatly broadened our understanding of Jupiter, its atmosphere, its aurorae, and its magnetosphere. However, the upper atmospheric asymmetry known as the Lyman-alpha Bulge still cannot be explained entirely. The leading hypotheses for the source of this energy are summarized in Section 2.4 while the Bulge observations are summarized here.

The Lyman-alpha Bulge was first discovered by a sounding rocket experiment (see Section 3.1) flown on December 1, 1978. The experiment measured the spatial distribution of Lyman-alpha flux on the planetary disk and found an average disk brightness of 13 kR. There was an area on the disk with brightness a few kR higher than the average at 80 degrees System III longitude near the equator [32]. Figure 3-7 shows the data from the experiment.

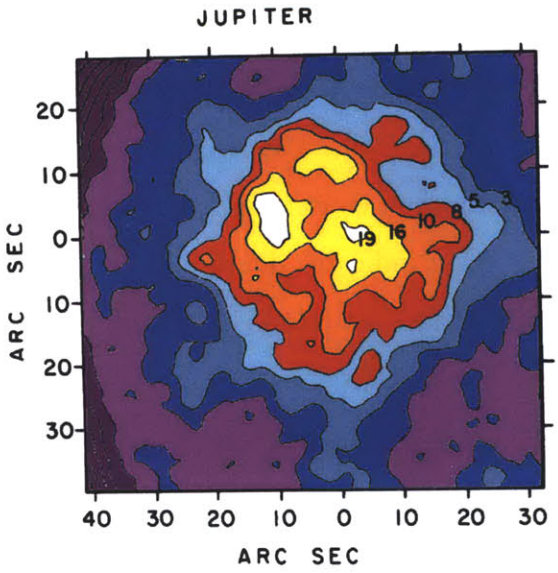


Figure 3-7: Contour plot of the brightness of Jupiter during the rocket observation [32] (color added for clarity). Brightness is in units of kR. The small bright spot where 19 kR is marked is the sub-Solar point, and the larger bright spot is the Bulge.

Additional observations from the ultraviolet spectrometers aboard Voyager 1 and Voyager 2 soon followed in early 1979 [1, 3]. These observations also showed a strongly asymmetry in Lyman-alpha brightness along the equator. A minimum brightness of 14.4 kR was observed around the entire planet with a broad peak at 19.6 kR near a longitude of 110 degrees in the System III magnetic coordinate system, corresponding to a 36% increase in brightness [4].

More observations of the bright region were made using the International Ultraviolet Explorer (IUE) in May-June 1979 and May-July 1980 as follow ups to the sounding rocket experiment. [33]. Spatial imaging was achieved with IUE's short-wavelength spectrograph. The study showed a peak between 50 and 100 degrees in the System III coordinate system and a 20% decrease in brightness from one year to the next even as the brightness along the rest of the disk stayed constant.

A number of explanations for this asymmetry were proposed. The Voyager data authors suggested that the emission represented an increased column density due to dissociation of $H_2$ molecules by hot plasma in the inner magnetosphere [4]. The emission bulge at Lyman-alpha is then due to increased resonant scattering because of this higher column density. Using the radiative transfer model in [32], this would

require a column of hydrogen atoms over 50% more dense compared to the rest of the planet, which is why it was named the Jupiter Lyman-alpha Bulge.

From 1982 to 1988, the IUE observed a series of spectra of the auroral regions of Jupiter. These observations showed that roughly œ of the Lyman-alpha emission from the auroral regions were blue-shifted by 30-60 km/s [30]. This is a significant fraction of the escape speed of Jupiter and is evidence of a large outflow of hydrogen ions and atoms flowing outward into the Jovian magnetosphere from the auroral regions. Although IUE did not observe the Bulge directly, high-velocity hydrogen from the auroral regions may have a significant effect on the Bulge.

An additional long-term observation campaign of Jupiter was conducted from 1978 to 1989 with IUE, this time focusing on variations in the Jovian $H_2$ dayglow emission over time. The study spans the decline in Solar activity from the end of Solar cycle 21 to the rise in Solar activity from the beginning of Solar cycle 22 [41]. This study found no other long-term asymmetrical molecular hydrogen emission feature on Jupiter analogous to the Lyman-alpha Bulge, confirming another finding from Voyager [4].

During this long-term study, spectra were obtained of the equatorial region showing the change in brightness as a function of time and longitude. Figure 3-8 shows the average Lyman-alpha emission brightness from 1985 to 1989 plotted against the System III longitude. This data shows brightening in the longitudinal areas predicted by previous Bulge observations, although the bin size for the averages plotted is not fine enough to constrain the longitude of the Bulge to within $\pm 5$ degree. While the error bars shown in the figure are a significant fraction of the data, it does show evidence that the brightness of the Bulge varies over time with the Solar cycle.

Further observations of the Bulge were conducted with IUE's short wavelength prime (SWP) echelle spectrograph from February 1990 to April 1991 [31]. This data showed that the Lyman-alpha emission line profile is significantly broader than the 0.14 Å spectral resolution of the instrument at all longitudes, the equatorial emission lines are broader than the mid-latitude emission lines, and Bulge emission lines are broader than the emission lines from other areas of the equatorial region. Line-

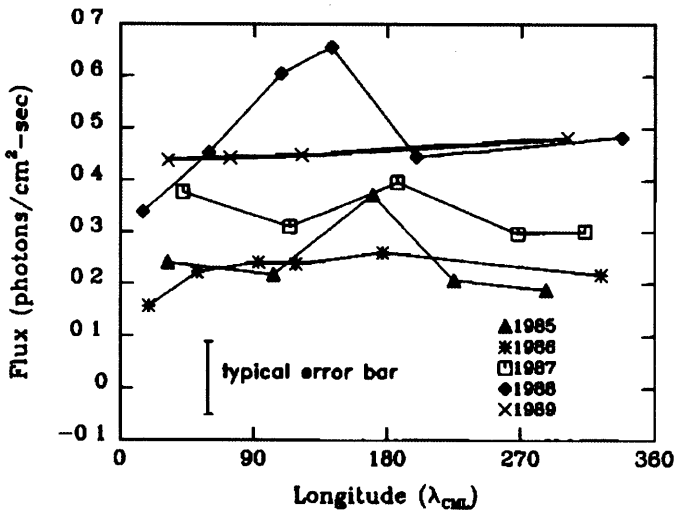


Figure 3-8: Lyman-alpha emission of Jupiter with respect to longitude in System III showing the overall rise in brightness from 1985 to 1989 [41]

broadening effects, such as broadening by collisions and the Stark effect, are ineffective by several orders of magnitude for explaining this result. The line broadening was explained by the presence of superthermal hydrogen atoms in the upper atmosphere, which resonantly scatter the broad solar emission line.

Ben Jaffel et al [40] proposed that this superthermal population could be accounted for with a two-component turbulent model where a fraction of the atomic hydrogen moved in a non-thermal velocity field. The best fit of this model to the IUE data from [31] was when the total hydrogen column density is 3.7 x $10^{17}$ $cm^{-2}$ with a non-thermal component density of less than one percent of the total density and a turbulent velocity of 9 km/s (Figure 3-9). An explanation involving turbulence is not necessary to model the spectra at mid-latitudes because an existing radiative transfer model fit the data well [38].

This model fits the data well and is consistent with other characteristics of the Bulge, such as its existence on the night side of the planet, and it could explain the excess heating in the atmosphere. However, a source of energy is required to drive a turbulent process that would generate the effects shown in the data. A number of explanations have been proposed (Section 2.4) but none have been shown with observations to account for the energy transfer to the Bulge region without requiring

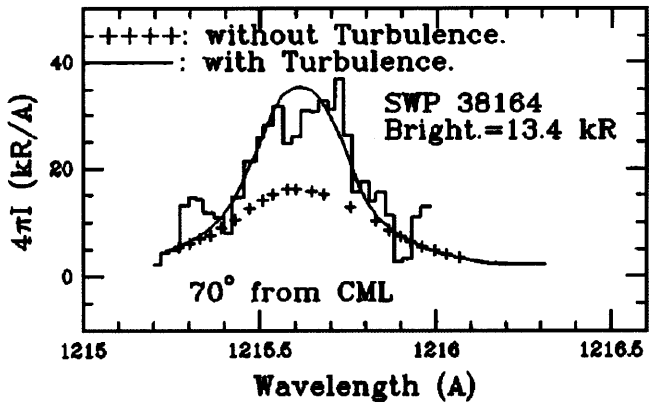


Figure 3-9: IUE spectrum of the Bulge on the limb from [31] shown with model profiles with and without turbulence[40]. The best fit of the turbulent model is obtained with a hydrogen column density of 3.7 x $10^{17}$ $cm^{-2}$ and a turbulent velocity of 9 km/s.

other phenomena that have been shown to not be present.

Observations with the Hubble Space Telescope (HST) Goddard High-Resolution Spectrograph (GHRS) in May 1994 revealed more broadening and brightness of the line core of Bulge spectra compared to the Anti-bulge and mid-latitude spectra [11]. These results confirmed that the Lyman-alpha Bulge is associated with hydrogen line broadening rather than an enhancement of the brightness near the line center, which ruled out the excitation of the Bulge by electron impact on ambient hydrogen atoms that was suggested as part of the electroglow processes.

The GHRS data also showed evidence of supersonic turbulence. When turbulent hydrogen cells are modeled as a two-component Gaussian distribution (shown in Figure 3-10), the best fit to the data is when hydrogen cells moved a 5 km/s with a standard deviation of 40 km/s. This corresponds to a hydrogen escape rate of $\sim 10^{29}$ atoms per second over the Bulge region. Additionally, Ben Jaffel et al. [40] argued that the origin of this velocity field may be related to the Jovian aurora given the supersonic Doppler-shift in the auroral Lyman-alpha emission and the high energy injected into the planets at high latitudes from magnetic particles because the Bulge and the aurorae are both fixed with respect to the magnetic field.

Further spectral observations of Jupiter with GHRS occurred in June 1994. This campaign observed Lyman-alpha spectra of the auroral regions. This study's primary

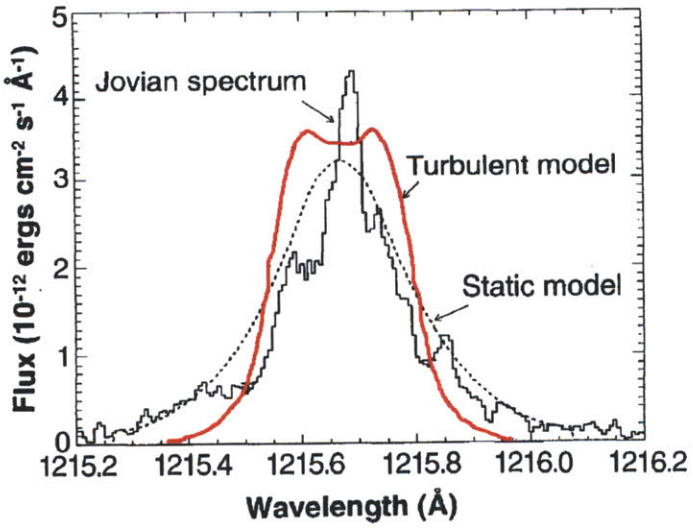


Figure 3-10: Turbulent model and data from Emerich et al. [11]. The turbulent model is colored in red here for clarity. The two peaks in the model come from dual-Gaussian model with line centers shifted corresponding to $\pm 5$ km/s.

result was evidence of a core reversal in the Lyman-alpha line profile, which was predicted by models as a consequence of radiative effects on photons produced deep within the auroral region. This core reversal had never been observed before [48].

However, the secondary result was that the line profiles of the auroral spectra were asymmetric. This could be due to Doppler motions of large masses moving at a few kilometers per second or by a smaller, more Doppler-shifted component flowing at 20 km/s. If the latter case is true, then this small hydrogen component could be making its way down toward the equator. If it is moving asymmetrically with the pole of rotation, this hydrogen could be preferentially streaming into the Bulge region compared with the rest of the equatorial region.

Observations made in August 1997 from the NASA Infrared Telescope Facility (IRTF) on Mauna Kea, Hawaii confirm near-supersonic speeds of hydrogen in the auroral region [15]. These winds were measured to be on the order of 3 km/s. This confirms the auroral electrojet that could be causing turbulence in the Bulge and shows its velocity. Figure 3-11 shows the electrojet from a System 3 longitude of 263 degrees, which approximately 150 degrees away from the Bulge. The electrojet wraps around the planet following a model of the magnetic footprint but there has been

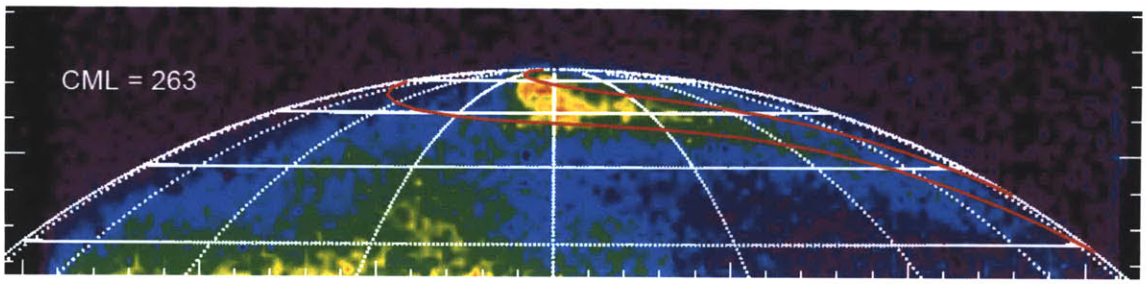


Figure 3-11: Infrared filtered image (3.953 $\mu m$) of the Jovian north pole showing the auroral electrojet [15]. The red lines show the magnetic footprint from a recent Jovian magnetic field model. The latitude lines are separated by 10 degrees, the longitude lines are separated by 18 degrees, and the scale on the sides of the figure are in arc secs.

no evidence presented yet that these jets make their way all the way down to the equatorial region.

In late 1997, the Galileo Ultraviolet Spectrometer (UVS) made additional measurements of the Lyman-alpha Bulge and further constrained properties of the hydrogen corona. These observations are best fit to models when a small amount of hot hydrogen is included, providing even more evidence for the two-component model proposed in [40]. The authors concluded that further long-slit echelle observations of the Bulge to examine the spatial structure would help identify the source of the energy causing the brightness in the Bulge.

An HST Space Telescope Imaging Spectrograph (STIS) campaign in 1999 and 2001 did just that. High-resolution, long-slit echelle spectra were observed at the Bulge, Anti-bulge, and latitudes to the north and south of the Bulge while the targets were on the limb of the planet. These spectra exhibited asymmetries relative to line center, showing that the red-shifted wings of the broad line profile were more prominent than the blue-shifted wings [12, 13]. The observed asymmetries were interpreted as the signature of hot hydrogen atoms propagating in the upper Jovian atmosphere, with a velocity distribution in excess of the planetary rotation speed.

These high-resolution STIS spectra were used in the development of a parametric radiative transfer model [39]. This model takes into account frequency redistribution, phase angle effect, the effect of hydrogen column density, eddy diffusion, and suprathermal hydrogen components to produce spectral line profiles of Jupiter's at-

mosphere. While this model is not yet complete, preliminary results have shown the strength of the model as it gets closer to being ready for widespread use. Further analysis of the STIS spectra can help constrain parameters of the model to more accurately predict spectral line profiles for future observations.

# Chapter 4

# The Venus Spectral Rocket

## 4.1 VeSpR Flight Profile

In December 2008, the science team and the WFF engineers conducted a Design Review, the first of many reviews before launch. This section outlines the payload hardware, mission timeline, mission success criteria, and the simulated analysis of the flight as generated by the WFF engineers for the VeSpR payload's flight.

### 4.1.1 Flight Configuration

The Venus Spectral Rocket consists of three major components, the Terrier booster, the Black Brant IX booster, and the payload section. The entire rocket is 17.03 m long. The complete flight configuration is shown in Figure4-1.

The Terrier Mk70 booster is a surplus missile originally designed for military payloads, but has since been modified as a first stage for suborbital rockets carrying heavy science payloads like VeSpR. The Black Brant is manufactured by Bristol Aerospace specifically for high-performance suborbital flights.

The payload section is customized for the VeSpR flight, although some equipment is used for other suborbital flights, and standard spacecraft buses are used where appropriate. The payload team at Boston University is responsible for the science experiment, which consists of the six sections from left to right labeled Spectrom-

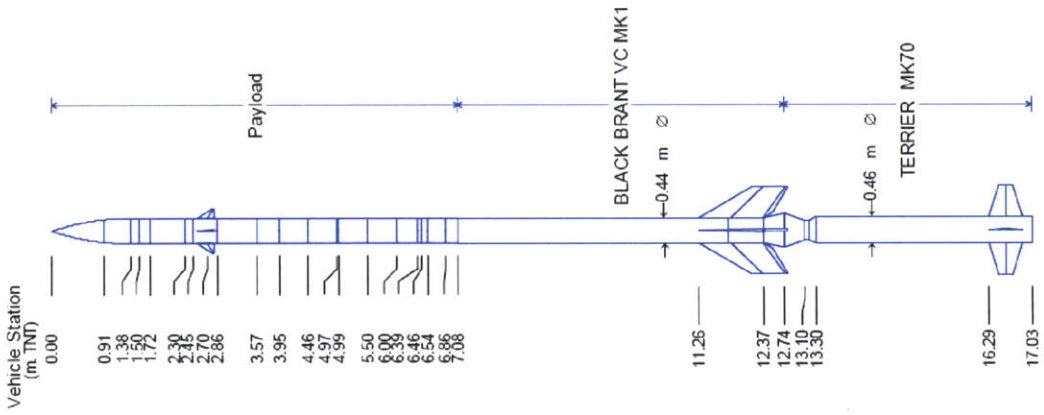


Figure 4-1: Configuration of the full rocket, consisting of two boosters and the payload.

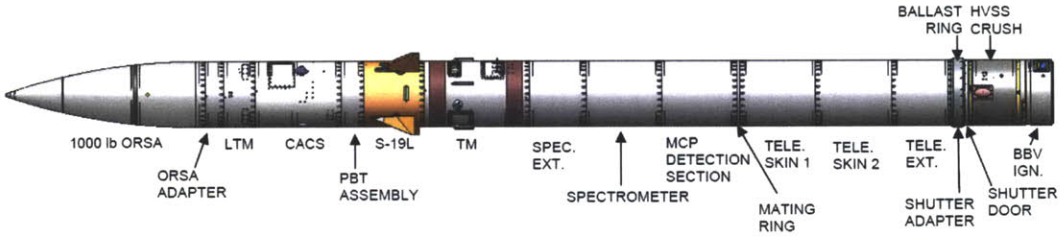


Figure 4-2: Solid model of the payload section configuration.

eter Extension through Telescope Extension in Figure 4-2. A detailed overview of the experiment can be found in Section 4.2. The remaining payload sections are the responsibility of engineers at WFF and will be briefly discussed here, but more information regarding these sections is available the Design Review Documents (4.0 – Mechanical Engineering Package) in the attached Appendix DVD.

At the top of the rocket is the nosecone, formally called the Ogive Recovery System Assembly (ORSA), which houses the parachutes used to recover the payload. It also contains a set of pitch nozzles used in conjunction with a second set located in the next section, the Linear Thrust Module (LTM). The LTM provides for fine pointing capability of the payload and contains a set of pitch nozzles, an LN-251 gyro, and associated electronics and plumbing. Figure 4-3 shows the 1000 lb ORSA, and Figure 4-4 shows the LTM.

The next section is the Celestial Attitude Control System (CACS) and it provides the pointing capability of the payload. It houses the electronics control of the ST-5000

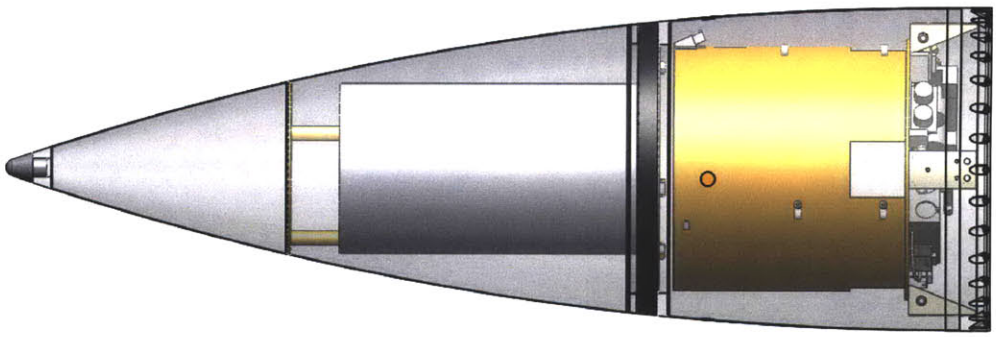

Figure 4-3: 1000 lb ORSA Assembly

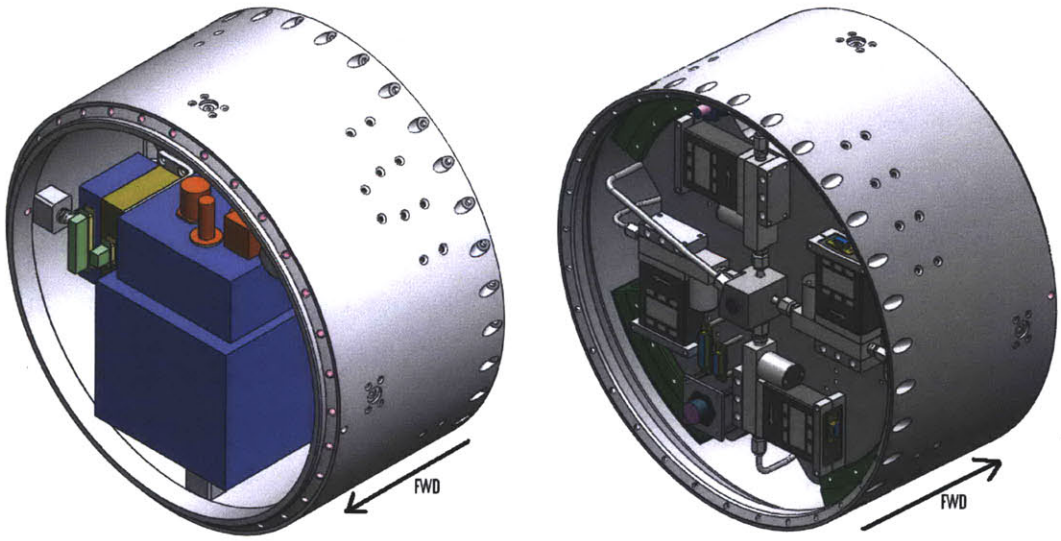


Figure 4-4: Linear Thrust Module (LTM)

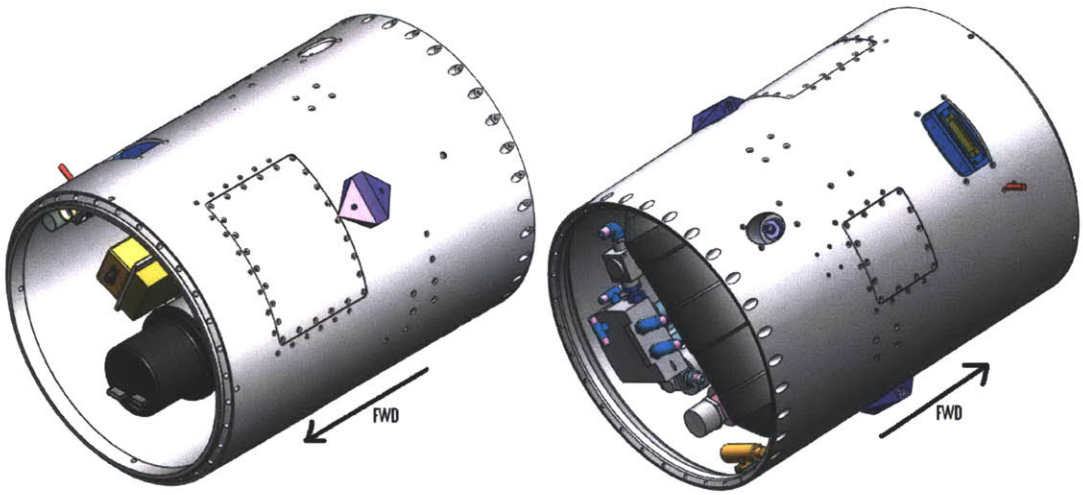


Figure 4-5: Celestial Attitude Control System (CACS)

star tracker, a Gimbaled LN-200 with a Miniature Airborne Computer (GLNMAC) internal measurement unit (IMU), a gas tank, and various associated regulators, plumbing, and electronics. The Piggy Back Tank (PBT) assembly houses two 200 in3 gas tanks for additional attitude control and pointing along with associated plumbing. The additional gas may be necessary because of the number of targets that VeSpR needs to acquire for mission success and if the ST-5000 star tracker has trouble locking on to Venus (see Sections 4.1.2, 4.1.3, and 5.1.3). Figure 4-5 shows the CACS, and Figure 4-6 shows the PBT assembly.

The next section down from the nosecone is the S-19L, a guidance system developed by RUAG Space that functions for the first 18 seconds of flight, actively guiding the vehicle by moving four gimbaled canards. The canards are controlled by a pneumatic system and are decoupled after 18 seconds using a pyrotechnic device. The S-19L is a standard system for suborbital rockets, and it is shown in Figure 4-7.

The final section of the payload before reaching the experiment section is the Telemetry (TM) section. This section is completely customized for VeSpR and contains all of the antennas used to communicate with the ground. This section of the payload houses the WFF-93 Pulse Code Modulator (PCM), an electronic device that houses multiple decks to receive inputs from a variety of different signals sources and types and transmits data to the antennae. Certain details about the TM system are

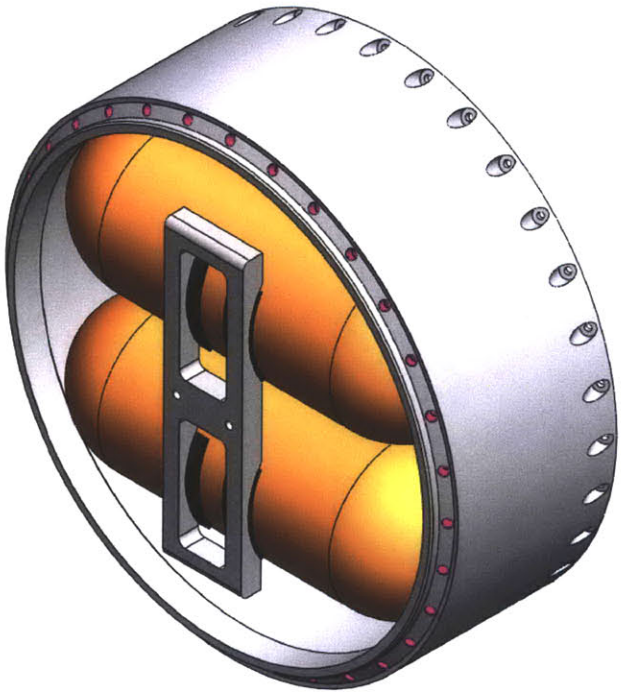

Figure 4-6: Piggy Back Tank (PBT) assembly

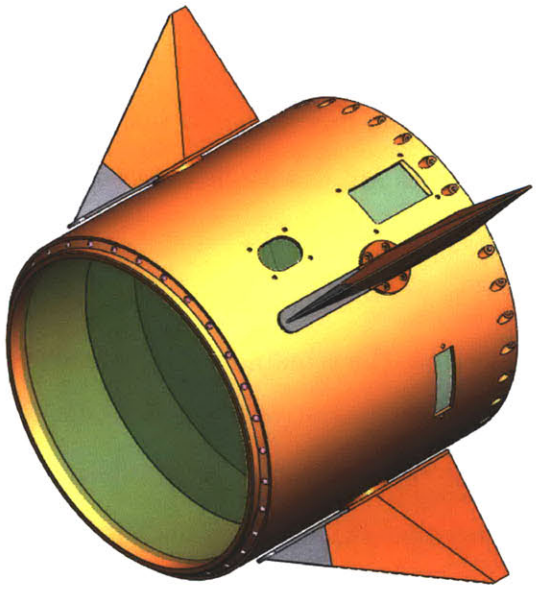

Figure 4-7: S-19L guidance system

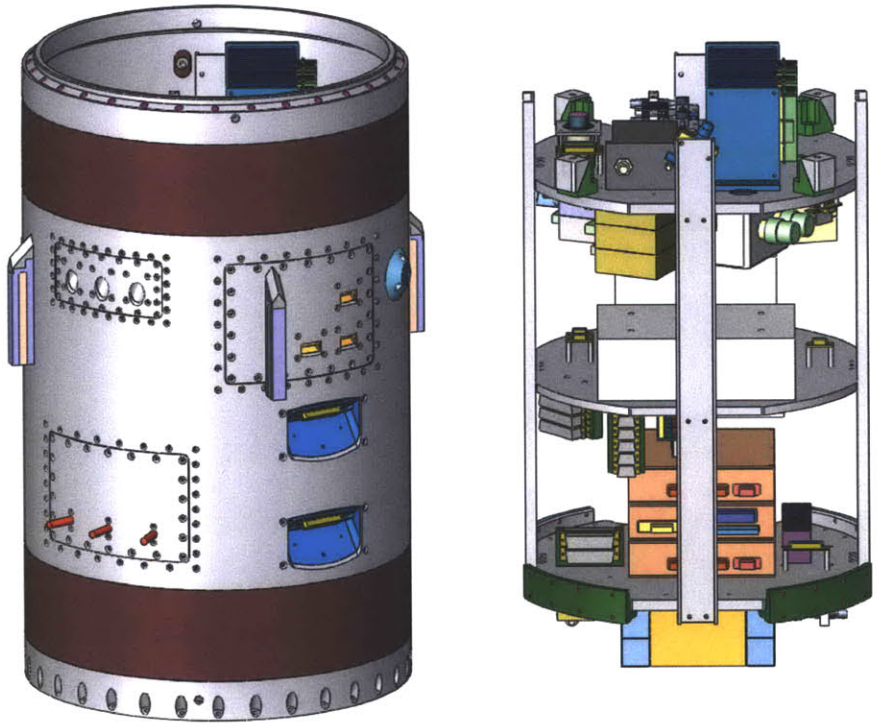

Figure 4-8: Telemetry (TM) section.

not published due to International Traffic in Arms Regulations (ITAR) restrictions. Figure 4-8 shows the TM section.

Next in the payload configuration is the experiment section. The experiment houses a telescope, optics, MCP detectors, a Xybion camera, a SPACOM star tracker, and various other electronics including power transformation and monitoring. The two primary science instruments are the MCP detectors, one attached to a spectrograph and one attached to an ultraviolet reimaging box. A more thorough overview of the payload is presented in Section 4.2.

After the experiment section, the remainder of the non-science payload is attached to the end of the telescope with the Shutter Adapter and the Ballast Ring. Figure 4-9 shows these two parts. After these adapters is the Shutter Door. The Shutter Door only serves as a dust door because the science payload does not need to be in vacuum, so it does not have a vacuum seal. The Shutter Door opens when the payload is above 110 km and closes before the payload descends beneath that altitude. Figure 4-10 shows the Shutter Door.

Figure 4-9: Shutter Adapter (left) and Ballast Ring (right)

Figure 4-10: Shutter Door

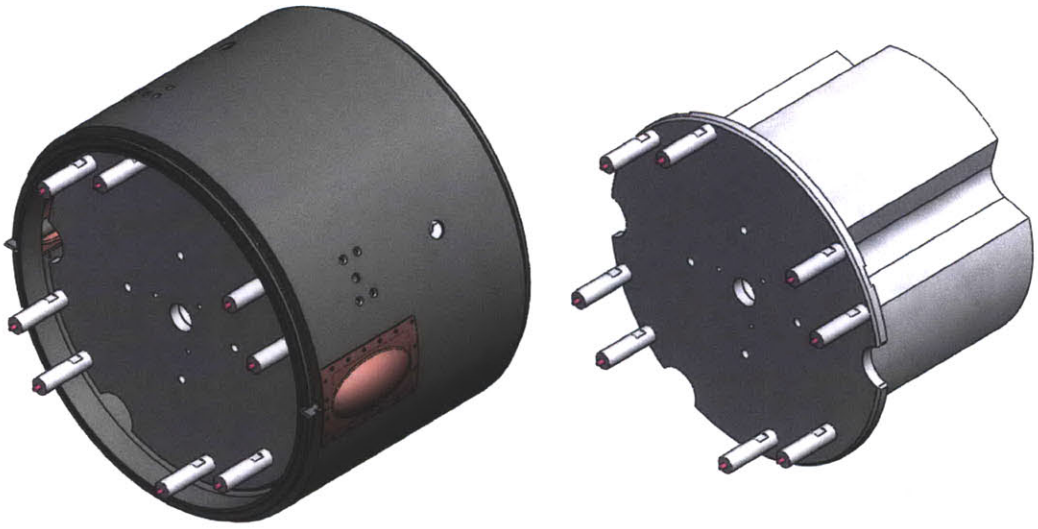

Figure 4-11: HVSS Crush Section

After the Shutter Door is the High Velocity Separation System (HVSS) Crush Section. The HVSS Crush Section contains the separation system that severs the connection between the payload and the vehicle and separates the payload from the vehicle. When the payload lands on the ground, it absorbs some of the impact energy to prevent damage to the rest of the payload. Figure 4-11 shows the HVSS Crush Bumper Section.

The final component of the payload when moving from the nosecone down to the boosters is the Black Brant Ignition Section, shown in Figure 4-12. This section is wholly the responsibility of the booster provider, and is separated from the rest of the payload along with the Black Brant booster after burnout.

### 4.1.2 Flight Profile and Timeline

Figure 4-13 shows a picture of the expected flight profile described here, and Table 4.1 provides a more detailed list of in-flight events. A complete list of events along with more information at each stage of the flight is available in the Design Review Documents (1.0 – Mission Manager Package) in the attached Appendix DVD.

At T+0 seconds, the Terrier booster is ignited and rocket leaves the launch platform. Within 4 seconds, the rocket will already be traveling at Mach 1 and be

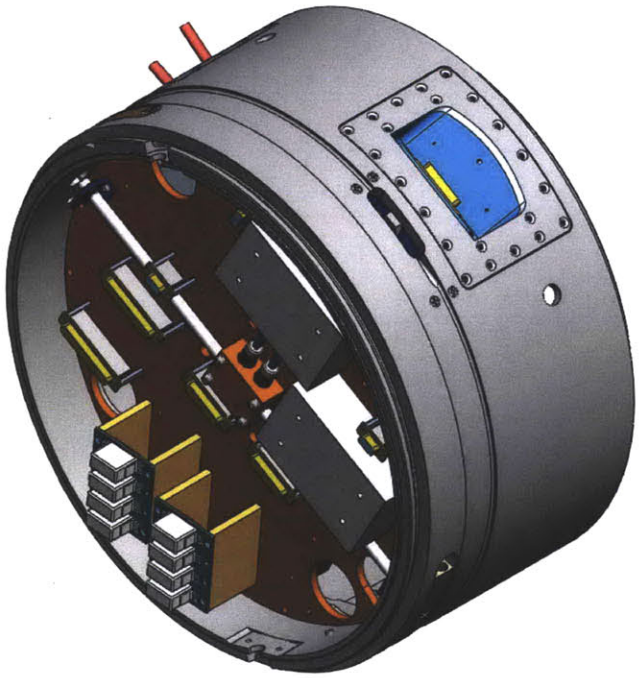

Figure 4-12: Black Brant Ignition Section

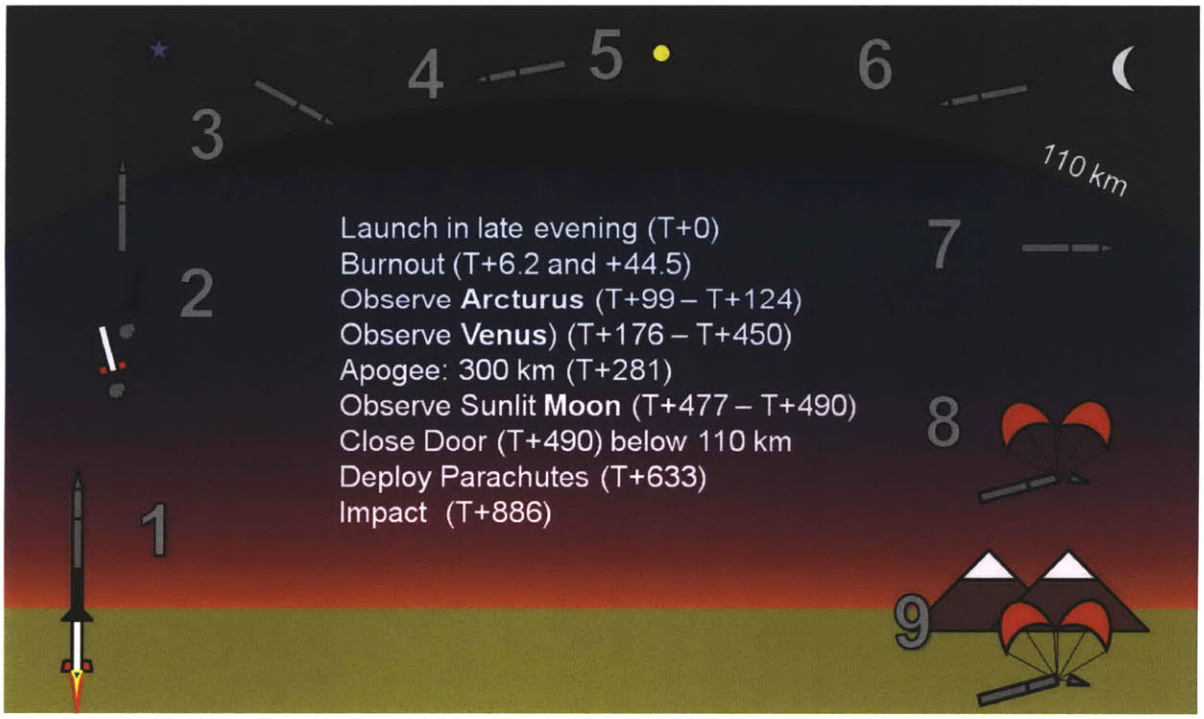


Figure 4-13: Pictorial timeline of major events

| Event | Time (s) |
|---|---|
| Terrier Burnout | 6.2 |
| Black Brant Ignition | 12.0 |
| S-19L Canard Decouple | 18.0 |
| Black Brant Burnout | 44.5 |
| Despin | 60.0 |
| Payload Separation/ACS Start | 64.0 |
| Nosecone Eject | 68.0 |
| Experiment Video On | 72.0 |
| Shutter Door Open | 75.0 |
| 110 km Upleg | 75.9 |
| Experiment HV On | 80.0 |
| Settle on Arcturus | 99.0 |
| Begin Maneuver to 6 Virginis | 124.0 |
| Settle on 6 Virginis | 148.0 |
| Begin Maneuver to Venus | 160.0 |
| Settle on Venus | 176.0 |
| Apogee | 281.4 |
| Uplink to Moon | 450.0 |
| Settle on Moon | 477.0 |
| 100 km Downleg | 486.9 |
| Shutter Door Close | 490.0 |
| 300k ft Downleg | 496.6 |
| Experiment Video Off | 500.0 |
| Experiment Off | 500.0 |
| ACS Spin-up | 500.0 |
| ACS Vent | 520.0 |
| ACS Valves Off | 565.0 |
| Ballistics Impact | 574.8 |
| Chute Deploy | 633.2 |
| ACS Off | 700.0 |
| Payload Impact | 885.7 |

Table 4.1: List of events on the timeline

experiencing more than 10 gs of acceleration (see Section 4.1.4). At T+6.2 seconds, the Terrier booster will burn out and separate. The rocket will coast for less than 6 seconds before the Black Brant booster is ignited at T+12 seconds. The Blant Black will burn out at T+44.5 seconds, after which the rocket will be on a ballistic trajectory.

The Black Brant booster will separate from the payload at T+64 seconds. Since the telescope is facing down during launch, the payload must flip 180 degrees to point toward the zenith. The payload begins rotating toward the sky after separation. At T+75 seconds, the experiment shutter door will open, exposing the star trackers to the sky as the payload passes the 110 km altitude mark. The payload will begin maneuvering to its first target, the star Arcturus, and will be locked onto Arcturus by T+99 seconds. The Lyman-alpha output of Arcturus is very bright compared to other stars and has been studied extensively, making it an ideal candidate for an in-flight calibration of the instrumentation in the payload. This calibration will be crucial for determining the sensitivity of the science instruments and for analyzing the data from Venus. VeSpR will observe Arcturus for 25 seconds.

At T+124 seconds, the telescope will begin its move to point at a guidance star that will be determined before launch. The telescope will settle on the star by T+148 seconds. Once a lock has been acquired, VeSpR will begin its maneuver to point at Venus, and it will lock onto Venus at T+176 seconds. The guidance star is needed as an intermediate point between Arcturus and Venus because the ST-5000 star tracker is unable to track planets. The guidance star will be sufficiently high in the sky such that the sky background will not be too bright for the star tracker to lock onto the star but not so far away that guidance uncertainty in the maneuver from the star to Venus will make it difficult to lock on to Venus (see Section 5.1.3).

While VeSpR is pointed at Venus, apogee will be reached at T+281 seconds. At T+450 seconds, after 274 seconds of observing the target, VeSpR will begin its maneuver to point at the sunlit Moon and lock on by T+477 seconds. By T+490 seconds, VeSpR will have fallen down below the 110 km altitude mark, and Lyman-alpha absorption by Earth's atmosphere will be too high for quality data to be obtained. The

shutter door will close and the experiment will be turned off to prepare for landing. The parachutes will deploy at T+663 seconds, and the payload is expected to impact the ground at T+885 seconds, almost 15 minutes after launch.

### 4.1.3 Mission Success Criteria

The timeline in the preceding subsection was generated based on the nominal mission performance expectations based on mass estimates of the payload and known performance characteristics of the boosters. The mission may not go exactly according to this timeline during flight. It is important that the Principal Investigator and the Mission Manager both have the same understand for what "mission success" is.

Writing down and agreeing on these criteria is a crucial top level that many other mission requirements on which are based. Just like any other NASA mission, VeSpR had a Requirements Definition Meeting (RDM) to detail the mission expectations and finalize the Mission Success Criteria (MSC) so all team members working with all the stakeholders understand what is expected so that lower-level requirements can be written to drive the design process in the systems engineering of the mission.

Not only is it important to establish MSC so that lower level requirements can be written, the MSC can also help determine who is ultimately responsible in the event of a failure. In most cases, the science payload team can take some course of action if the flight provider fails to perform up to these criteria and may be able to launch the experiment on another flight. Likewise, the flight providers can also be absolved of all blame in the event that the Principal Investigator and the science team have failed to specify the MSC with enough detail to complete the intended scientific objective. It is in this area, where hard science objectives and experiment expectations meet engineering requirements that many problems in missions occur. Having a well-defined set of MSC ensures that both the science team and the flight provider have the same interpretation of what constitutes a mission success.

The MSC for VeSpR are split into two categories, Comprehensive Success (CS) criteria and Minimum Success (MS) criteria. In the event that MS is not achieved during the flight, the experiment team has the option to have a reflight free of charge

Table 4.2: VeSpR Mission Success Criteria

| 36.261 Mission Success Criteria | | |
|---|---|---|
| **Category** | **Ref #** | **Requirement** |
| Comprehensive Success Criteria | CSC1 | Acquire calibration star and Venus with CACS and Xybion camera and successfully uplink position adjustments as needed |
| | CSC2 | Total observation time of 250 sec above 110 km on calibration star and Venus |
| | CSC3 | Successful operation of the two MCP detectors |
| | CSC4 | Proper positioning of the spectrograph slit on the sunlit Venus disk and jitter within +/- 1.5 arcsec |
| | CSC5 | Successful recording of scientific data |
| Minimum Success Criteria | MSC1 | Successful positioning of Venus in the instrument field of view |
| | MSC2 | Minimum of one minute integration time on Venus above 100 km |
| | MSC3 | Successful operation of either MCP detector with Venus in the field of view |
| | MSC4 | Successful recording of scientific data |

(assuming the experiment is still intact). However, if MS is achieved but CS is not, then the experiment team will have to obtain funding for a new mission entirely if another flight is desired to complete the scientific objective. Table 4.2 lists the Mission Success Criteria agreed upon for VeSpR following the RDM.

In order for VeSpR to achieve CS, both the calibration star and Venus must be observed with both MCP detectors for a minimum of 250 seconds. Notice that observing the Moon is not a requirement for CS. If launch occurs on a date where the moon is either not in the sky or it is too far away from Venus to be pointed in a reasonable amount of time, this maneuver can be cancelled and Venus can be observed for longer. The reason for pointing at the Moon is to obtain a Solar Lyman-alpha profile that can be used to characterize the Solar Lyman-alpha light that is shining on Venus. Since there are other ways to obtain a Solar Lyman-alpha profile at the time of flight, this is not critical to mission success even though it is desired. However, the calibration star must be observed because an in-flight calibration is crucial to determine the sensitivity of the two detectors in flight.

The telescope may be observing one target, but the two MCP detectors are recording entirely different phenomena. The detector attached to the spectrograph box will be recording the Lyman-alpha spectrum that will measure the D/H ratio in Venus'

atmosphere, which is the primary scientific objective. The detector attached to the ultraviolet reimaging box will be recording the first-ever image of Venus' corona, so even though CS requires both detectors to be operational, MS can be achieved even if only one of them is operated because valuable scientific data is still obtained.

A long observation time on Venus is desired because more time on the target means a higher signal to noise ratio in the data. With higher signal to noise, the telescope can determine with less uncertainty the D/H ratio of Venus. Higher signal to noise is especially important if Venus' deuterium emission is dimmer than expected (see Section 5.5). For CS, 250 seconds of observation is required on both targets, but for MS, only 60 seconds of Venus observation is required.

CSC2 is an example of a poorly written success requirement. As it is written, both the calibration star and Venus must be observed for a total of 250 seconds. A more properly written requirement would have specified minimum observation times for both Venus and the calibration star rather than the observation time of the two combined. Even though both the Principal Investigator and the Mission Manager agreed on the wording of this criterion during the Requirements Definition Meeting and signed the Success Criteria document, it would be beneficial for the mission if this was revised. Granted, changes in top-level requirements late in the program usually lead to many problems and cost and schedule overruns, but considering how little this top-level requirement will change the mission, it would be wise to update its wording to reflect a more accurate expectation of the mission and the declaration of success.

### 4.1.4 Expected Flight Performance

Wallops Flight Facility has experience launching sounding rockets using a flight configuration very similar to what VeSpR will have. VeSpR's length and mass characteristics fall within WFF's flight experience envelope, shown in Figure 4-14. VeSpR is not unusually heavy or long compared to many other sounding rocket payloads, so its performance can be predicted with a great deal of accuracy.

Since time above 110 km (which should be maximized according to the Mission Success Criteria in Table II in Section 4.1.3) is directly related to the apogee altitude

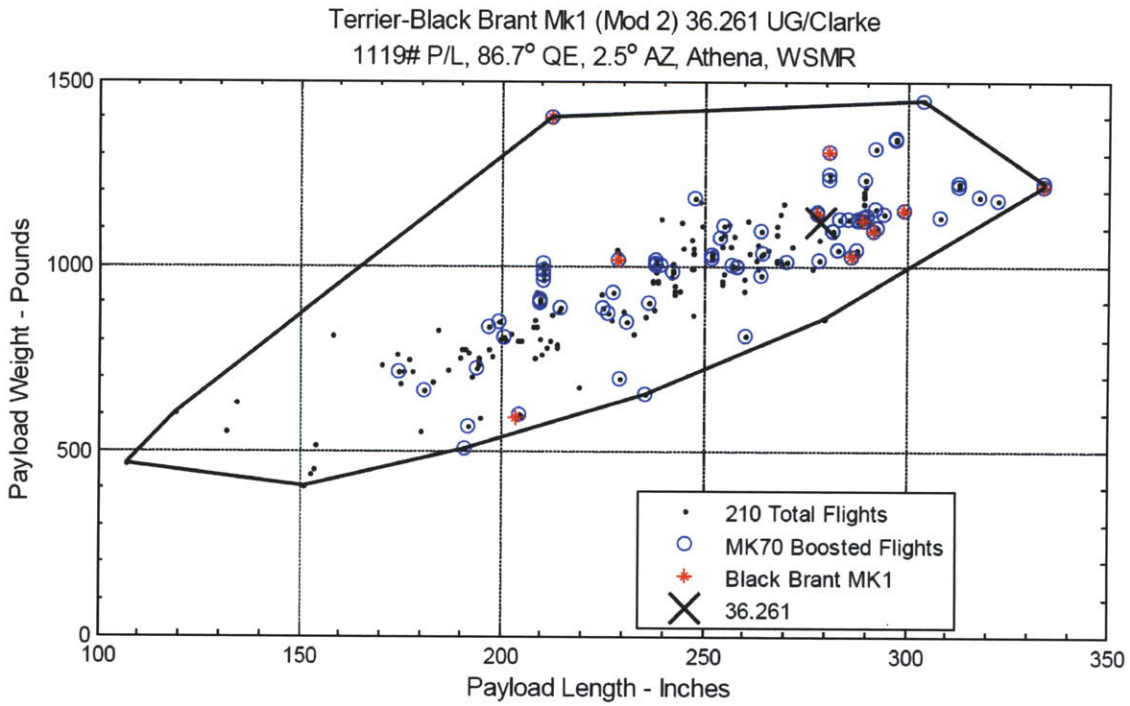


Figure 4-14: Flight experience envelope of the Terrier-Black Brant Mk1 (Mod 2) relative to payload weight in pounds and payload length in inches.

of the payload, it is especially important to have accurate predictions on the flight profile including maximum altitude. The engineers at WFF have run simulations to predict the flight performance of VeSpR during flight. The nominal apogee of the payload is 300 km and the nominal distance from the launch location ("range") is less than 80 km, but due to changes in weather conditions, payload mass, booster performance degradation, and other factors, this may not be the case.

Gaussian statistics used in the model predict a 2-sigma minimum of the apogee altitude to be 275 km, meaning there is a 2.5% chance that VeSpR's apogee will be below this value. In addition, the same 2-sigma maximum range shows there is a 2.5% chance that VeSpR will land more than 93 km away from the launch site. Figure 4-15 shows the predicted flight altitude with respect to time, and Figure 4-16 shows the flight altitude with respect to range.

Apogee altitude is a major factor in determining mission success because mission success is constrained by the time above 110 km, but the flight simulations also provide a wealth of additional information associated with the flight. More of this

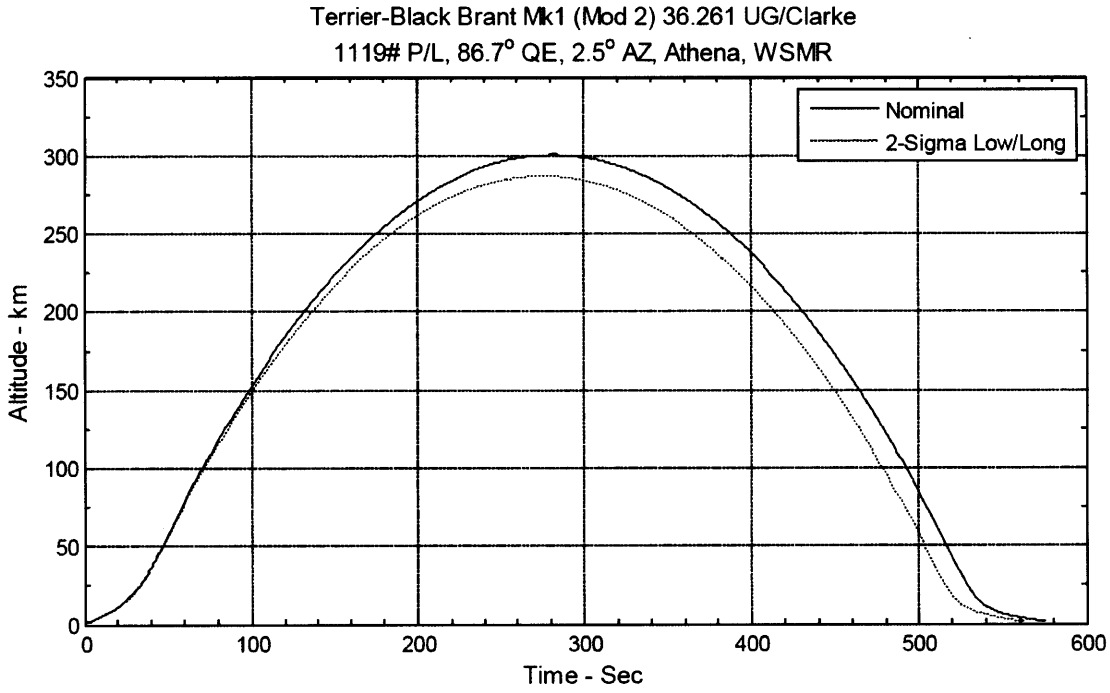


Figure 4-15: Expected flight altitude and 2-sigma low with respect to time.

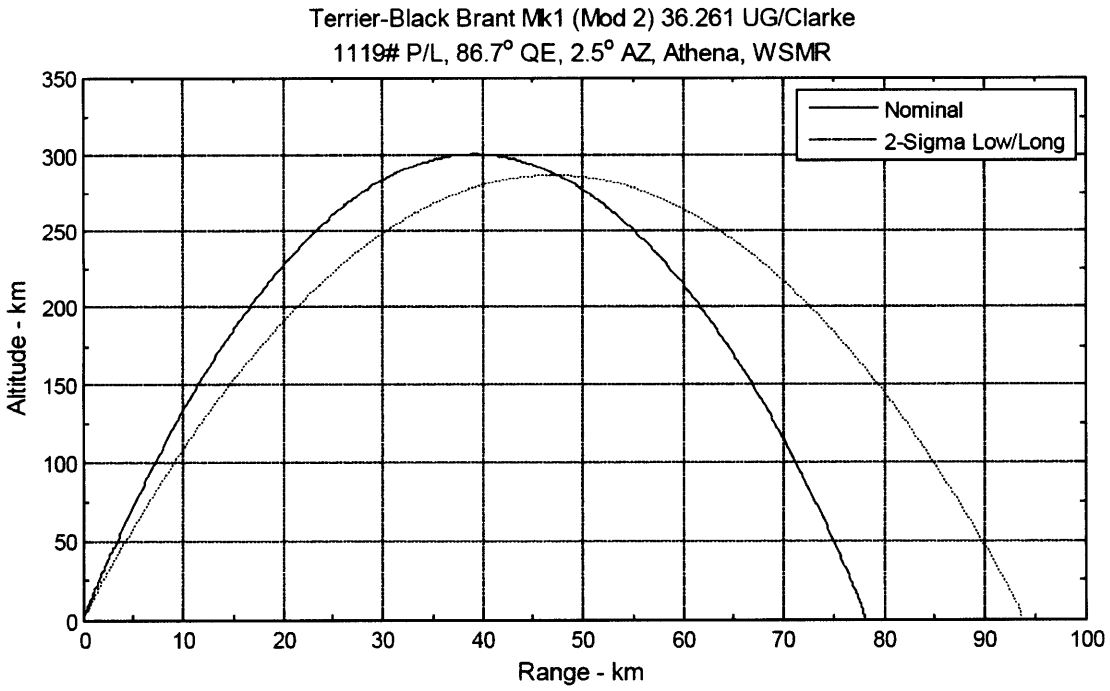


Figure 4-16: Expected flight altitude and 2-sigma long with respect to range.

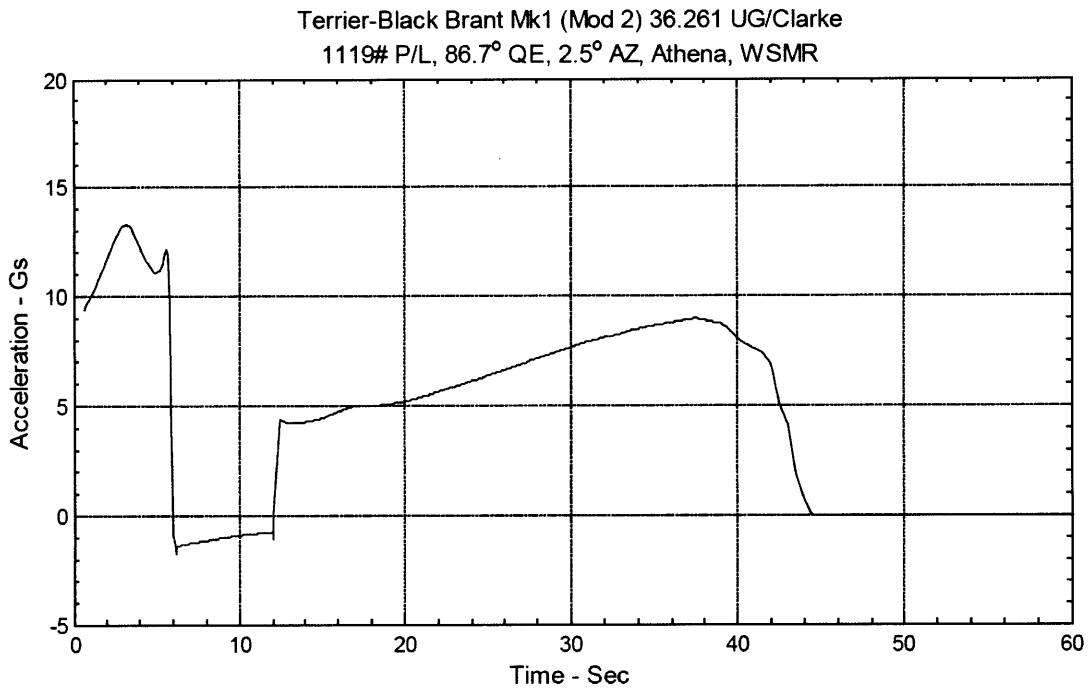


Figure 4-17: Expected acceleration during flight with respect to time.

information is available in the Design Review Documents (3.0 – Flight Performance Package) in the attached Appendix DVD, but some of it will be discussed here.

The acceleration profile of the flight is especially important when designing payload systems or making changes to an existing system. Figure 4-17 shows the acceleration the payload will experience with respect to time for the first minute of flight. Sudden changes in acceleration pose a greater risk to the structural integrity of the payload than constant high accelerations.

The maximum expected acceleration is just above 13 g's, during the first 4 seconds of flight when the Terrier booster is active. Air resistance and gravity begin to slow the rocket in the 6 seconds between the Terrier burnout and the Black Brant ignition, which gives a net negative acceleration during this time. After the Blank Brant is ignited, the acceleration climbs from approximately 4 g's up to over 8 g's.

This slow increase of acceleration is expected; the booster burns propellant and loses mass as it accelerates, so if thrust stays constant, acceleration must increase because of the mass decrease. Thrust also tends to increase because solid propellants are generally cut with circular grains that expand with time and increase the surface

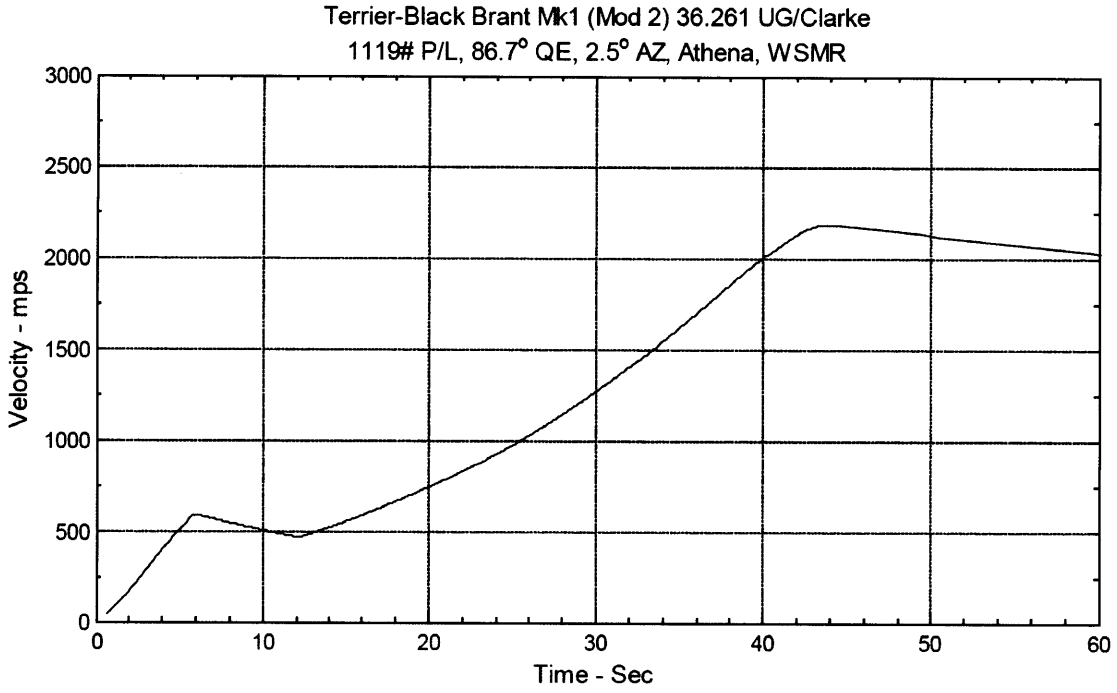


Figure 4-18: Expected velocity during flight with respect to time.

area that is burned at any given time. The rate of change of thrust can be controlled by carving different patterns in the propellant grain.

One reason to have a 6-second delay between the Terrier burnout and the Black Brant ignition is to decrease the dynamic pressure on the rocket during ascent. Since dynamic pressure ($q = 1/2\rho v^2$) is a function of air density as well as velocity squared, and air density drops quickly with altitude, a lot of spacecraft scale back power after achieving some sufficient speed to prevent damage from high dynamic pressure. The Space Shuttle throttles back when it achieves its maximum dynamic pressure, known as "Max Q," and gradually increases thrust beyond this point.

Since solid rocket boosters cannot be throttled, there is simply a delay between the burnout of the first stage and the ignition of the second stage. During this period, the velocity only decreases by approximately 25%, but the dynamic pressure decreases by more than a factor of 2. Compare Figure 4-18, which shows the velocity profile during flight with respect to time, with Figure 4-19, which shows the dynamic pressure during flight with respect to time.

Notice that there are two local maxima in the velocity profile, both after the

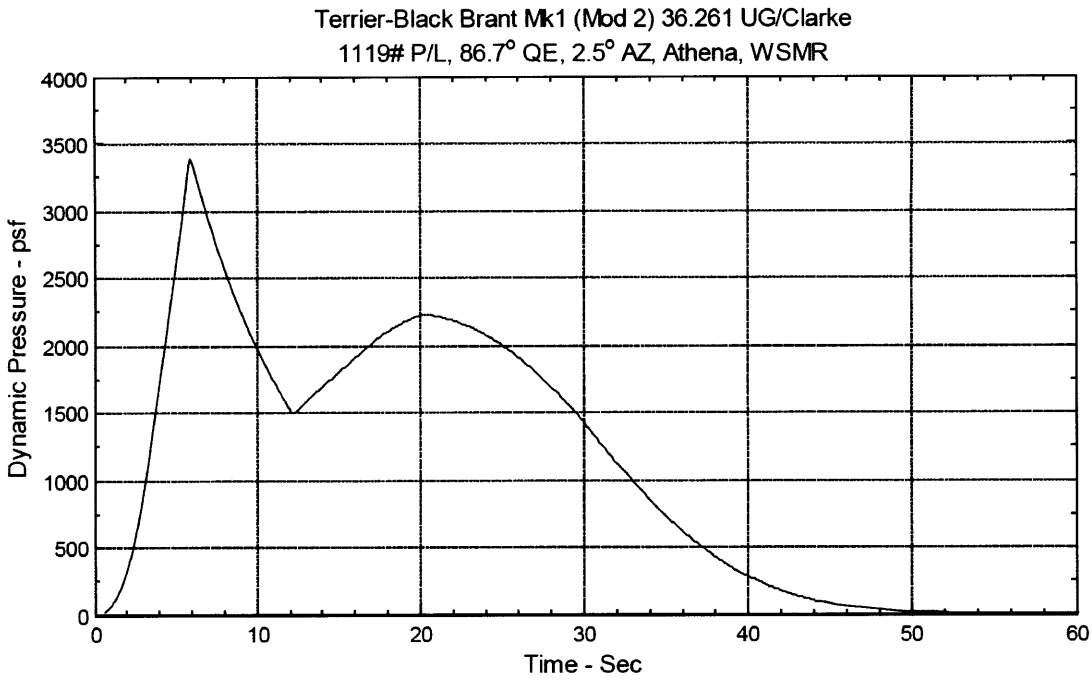


Figure 4-19: Expected dynamic pressure during flight with respect to time.

burnout of each booster. In contrast, the second local maxima occurs early on during the Black Brant burning stage (around T+20 seconds) and is less than 70% of the global maximum dynamic pressure occurring at T+6.2 seconds with the Terrier burnout. This is because of the changing atmospheric conditions as VeSpR passes from Earth's troposphere to the exosphere.

Another important flight characteristic that is strongly coupled with velocity and atmospheric pressure and has ramifications for the rocket's structure is the Mach number. Figure 4-20 shows the Mach number of the payload with respect to time during flight. Notice how the Mach number rises faster than the velocity does during the time the Black Brant is burning (between T+12 and T+44.5 seconds) and continues to rise even as the velocity falls. This is expected because the speed of sound is inversely proportional to the square root of the air density, which decreases exponentially with altitude.

More information on the vehicle performance, stability and dynamics, and reentry analysis is available in the Design Review Documents (3.0 – Flight Performance Package and other sections) in the attached Appendix DVD, but will not be discussed

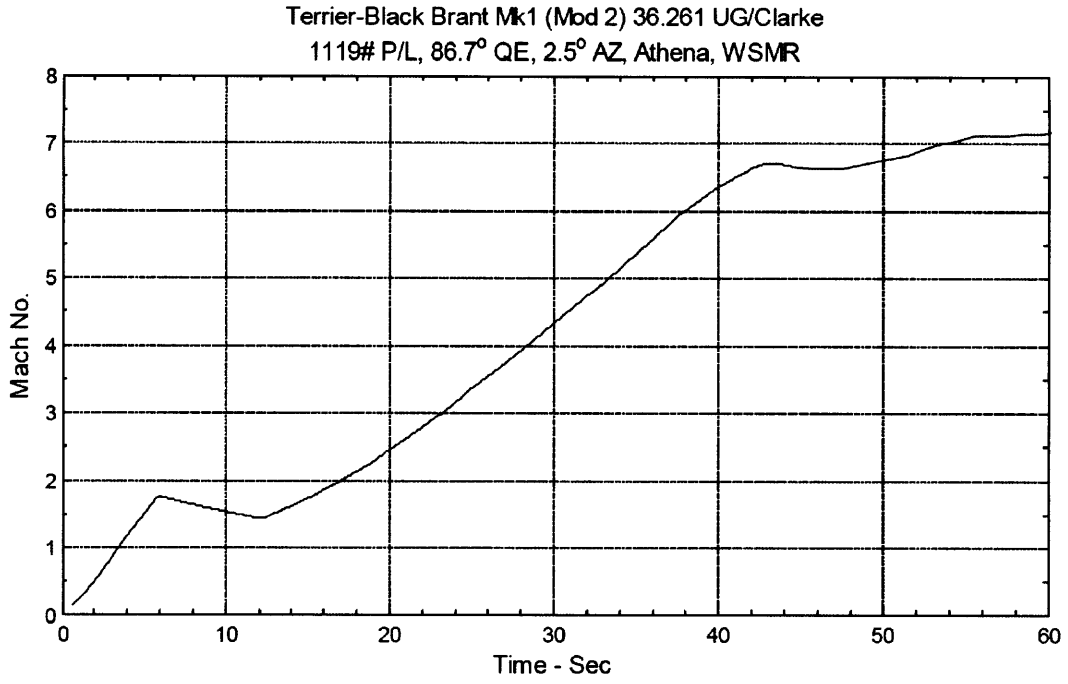


Figure 4-20: Expected Mach number during flight with respect to time.

because the author did not perform this analysis himself nor are the details relevant to the discussion of preparing the scientific payload for flight.

## 4.2 VeSpR Science Payload Overview

While Wallops Flight Facility and White Sands Missile Range are taking care of the majority of the rocket and payload support, the science team at Boston University is preparing the science payload for flight. Here is a detailed description of the major subsystems in the VeSpR experiment. This section describes the payload **as it was before any additional design changes occurred**. Design changes are discussed in Chapter 5.

### 4.2.1 Optics Subsystem

The optics in the VeSpR science payload are split into several distinct sections. There is a telescope, a spectrograph box, an imager box, and a visible optics board. Light passes through the telescope and an objective prism and hits the spectrograph aper-

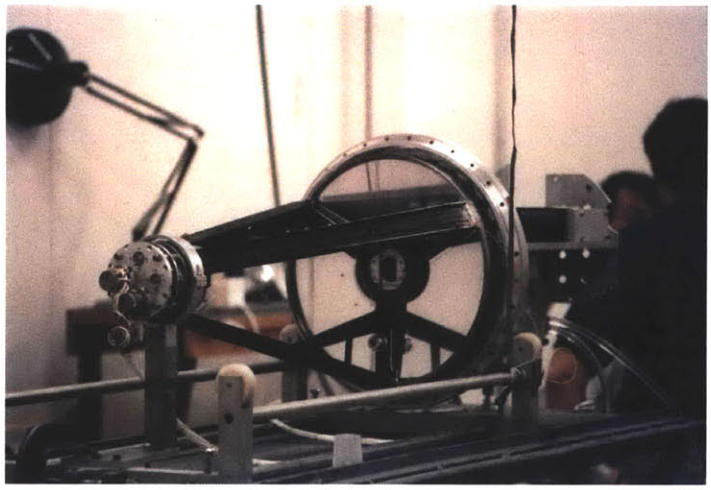

Figure 4-21: The VeSpR telescope.

ture plate. This aperture plate has a slit that feeds ultraviolet light into the spectrograph box, while the remaining light is reflected by the plate. The light then reaches the imager aperture plate; ultraviolet light refracted by the prism passes through a hole in this aperture plate and enters the imager box, and the remaining light, mostly visible, enters the visible optics board.

#### 4.2.1.1 The Telescope

The telescope is a Cassegrain design with a Dall-Kirkham figure. It has a 35 cm diameter ellipsoidal primary mirror and a spherical secondary mirror that provide 1-2 arc sec image quality within a few arc min of the optic axis. The telescope delivers a f/21 beam to the focal plane with a plate scale of 26 arc sec/mm. A 2-degree magnesium fluoride ($MgF_2$) objective prism mounted 48 cm forward of an aperture plate disperses the converging beam from the telescope, bending the incoming light enough so that visible and ultraviolet can be separated and directed into their respective optics. Figure 4-21 shows the VeSpR telescope.

The telescope's secondary mirror is actively controlled by two servomotors that move pushrods against the back of the mirror. The secondary mirror can be adjusted to correct for pointing errors of the payload up to 10 arc sec in both pitch and yaw. Tracking is controlled by a SPACOM star tracker mounted on the visible optics board

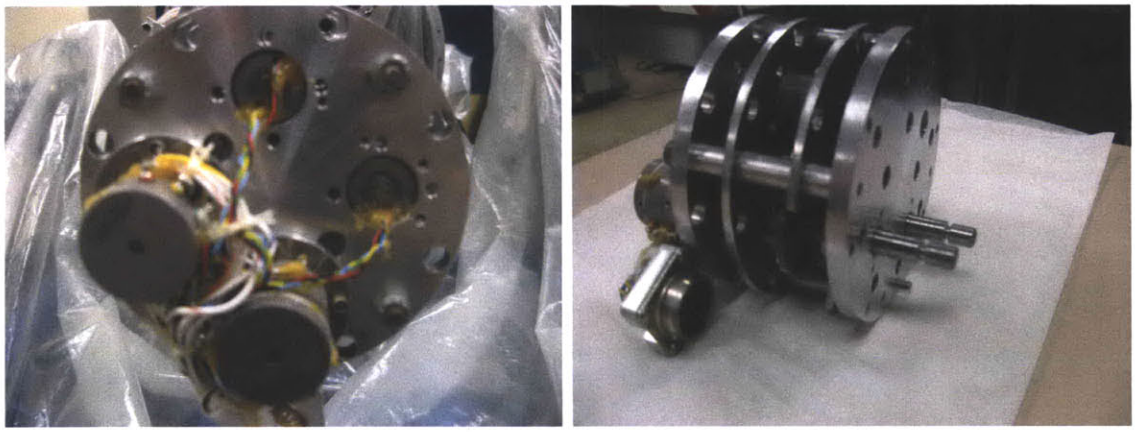

Figure 4-22: Secondary mirror control servos and pushrods.

that is co-aligned with the telescope. The star tracker has a 4-quadrant photodiode that produces error signals that are used to drive the servomotors to control the pointing of the secondary mirror until light from the target object is equal in all four quadrants. In the last two flights of the telescope, 1-2 arc sec pointing accuracy and stability was achieved using this compensation scheme, which when convolved with a telescope image of 1-2 arc sec gives a total point spread function of 2-3 arc sec. Figure 4-22 shows the secondary mirror control system, disconnected from the back of the secondary mirror.

One of the servomotors controlling the secondary mirror has burned out, so corrections can only be made in one dimension. This configuration can still work for the VeSpR mission because the spectrograph aperture slit is so long that the image of Venus can be aligned to within the pointing accuracy of the entire payload along the dimension of the inoperable servomotor and still have light from Venus enter the spectrograph while the other servomotor actively controls the other dimension. However, this situation is risky and undesirable. The pointing accuracy of the CACS for the VeSpR payload is $\pm 1.5$ arc sec, which is better than the CACSs used in JASpR missions. Because of this fact and the projected cost to repair or replace the servomotor assembly, it was decided that this system will be removed for the VeSpR flight. Now, the error signals from the SPACOM star tracker will be sent directly to the Telemetry Section to control the fine pointing of the payload (see Section 5.2.3),

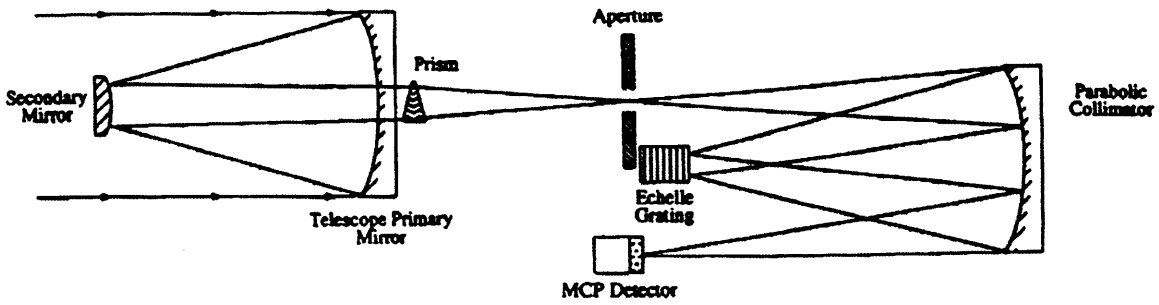


Figure 4-23: Configuration of the telescope and spectrograph optics.

and a passive system will be used to lock the secondary mirror in place (see Section 5.3.6).

#### 4.2.1.2 The Spectrograph Box

The spectrograph was designed and constructed for UV echelle line profile measurements with long-slit imaging. The Ebert-Fastie configuration employed in the design of the spectrograph has many characteristics well suited to the science needs of this mission. The design employs symmetric off-axis reflections from a single collimating mirror to remove aberrations; as a result, the spatial resolution of the system is limited by the telescope, and the spectral resolution is limited by the grating and aperture characteristics. Figure 4-23 shows the configuration of the telescope and the spectrograph box.

The parabolic collimator mirror produces 2 arc sec image quality with minimal astigmatism along the central 2-3 arc min of the image. The Ebert-Fastie configuration has the additional advantage of being relatively insensitive to the incident angle of the incoming beam; near parallel to the optic axis, the spectrograph focuses an image of the aperture at the same location on the detector. This feature greatly facilitates the alignment process and renders the spectrograph insensitive to small movements of the collimating mirror that may occur during launch. With the 1216 Angstrom image focused onto the primary aperture, other wavelengths are excluded from the spectrograph, producing a very low level of scattered light on the detector.

The spectrograph uses a replica of a prototype grating for the STIS, manufactured

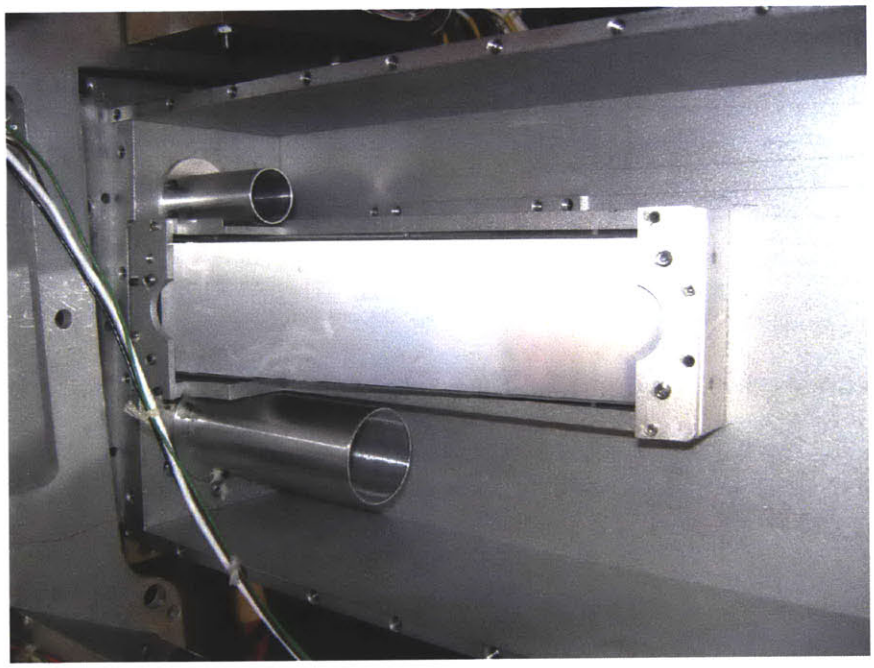

Figure 4-24: Echelle grating mounted in the spectrograph box and the baffles at the entrance and exit of the box.

by the Richardson Grating Lab, which has a 70-degree blaze angle and is optimized to the 221st order of 1216 Angstrom with a groove spacing of 14.5 $\mu m$. For a 5 arc sec aperture width, the measured resolution in the previous JASpR flight was 0.055 Å FWHM, which is comparable to the expected resolution based on ray tracing with the BEAM4 program.

The interior surfaces of the housing have been glass beaded to reduce reflectivity to stray UV light. Both the entrance and exit ports are fitted with baffles, and an additional baffle traps zero order light from the grating. The spectrograph aperture plate is milled stainless steel with an optical quality front surface, housing a slit aperture 5 arc sec (190 microns) wide and 390 arc sec (15 mm) long. The 5 arc sec aperture width is needed for high sensitivity. Figure 4-24 shows the configuration of the echelle grating and the baffles in the spectrograph box.

#### 4.2.1.3 The Imager Box

The imager box was designed and built to re-image the focal plane onto a separate detector, providing an ultraviolet image of the telescope field of view minus the light

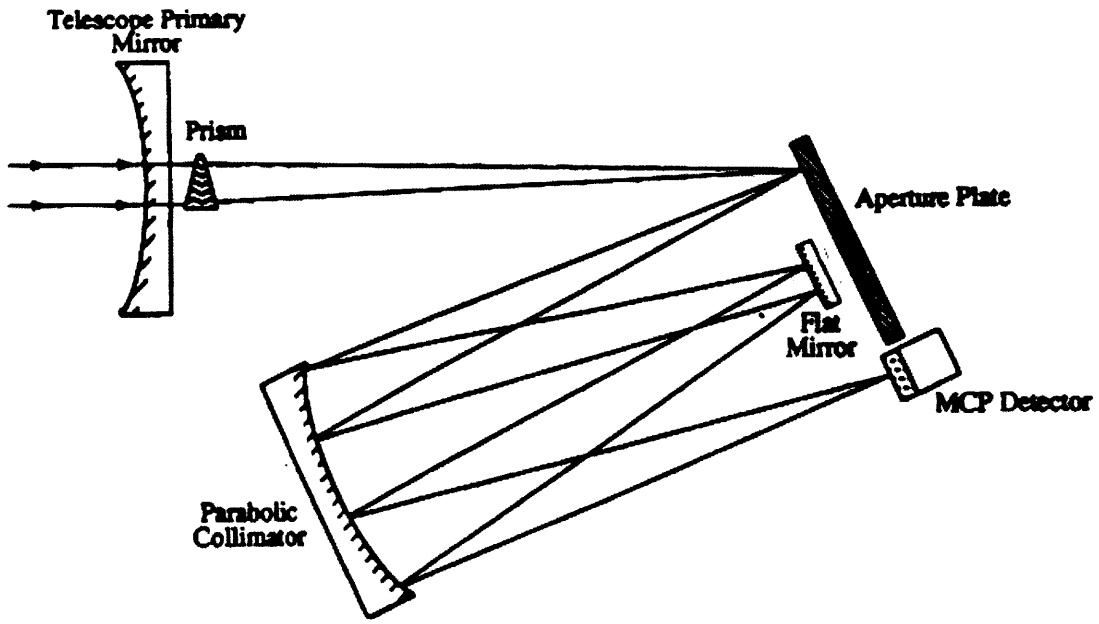


Figure 4-25: Configuration of the telescope and ultraviolet reimaging box optics.

which passes through the spectrograph aperture. The Venus image on the aperture plate is sufficiently dispersed by the objective prism that the Lyman-alpha image will be clearly separated from the longer wavelength continuum and emissions. The imager box aperture plate is stainless steel with an optical quality finish and an aluminum/magnesium fluoride coating to reflect the UV light, and the re-imaging optics are in the same Ebert-Fastie arrangement as the spectrograph box but with a flat mirror in place of the grating. Figure 4-25 shows the configuration of the telescope and imager box.

The image scale at the second detector is the same as at the focal plane, and laboratory tests with a resolution pattern have shown that this system re-images the focal plane with better than 1 arc sec image quality. In this case, the overall system resolution is determined by the image quality and target jitter at the focal plane. Figure 4-26 shows the imager box, and both the spectrograph and the imager box aperture plates can be seen.

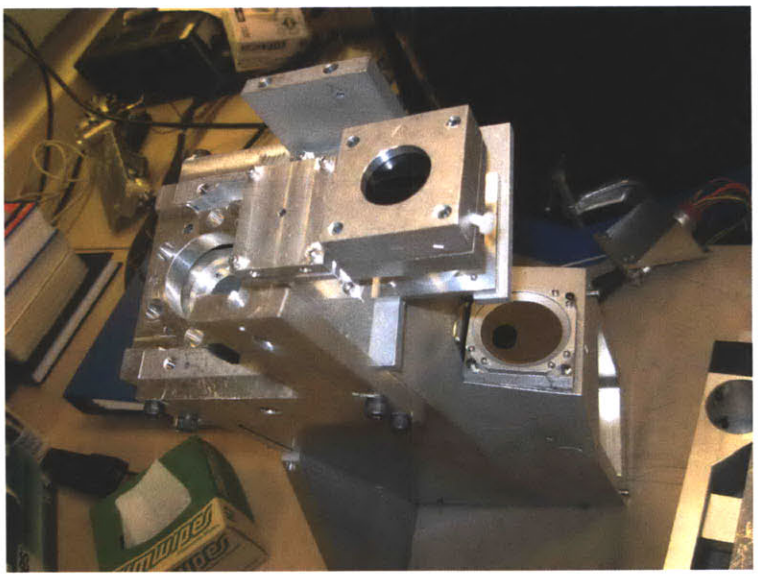

Figure 4-26: The imager box and apertures. The black circle with the long horizontal hole is the back of the spectrograph aperture plate, and the mirror with a nearly-circular hole down and to the right is the imager box aperture plate.

#### 4.2.1.4 The Visible Optics Board

The two primary science instruments, the spectrograph and imager boxes and their detectors, are both imaging ultraviolet light, but visible light entering the telescope is also observed by additional detectors mounted on the visible optics board. The visible optics board houses a Xybion camera and a SPACOM star tracker. Figure 4-27 shows the visible optics board.

Visible light enters through the telescope, passes through the objective prism, reflects off both the spectrograph and imager box aperture plates, and passes up through the large, oval-shaped hole on the visible optics board seen near the top right in Figure 4-27. The light hits another mirror mounted in the very top right of the figure that sends the light down through a baffled tube. A beam splitter sends half of the light to the left where it passes through a field lens, reflects off another mirror, and enters the Xybion camera. The remaining light reflects off two additional mirrors before reaching the SPACOM star tracker.

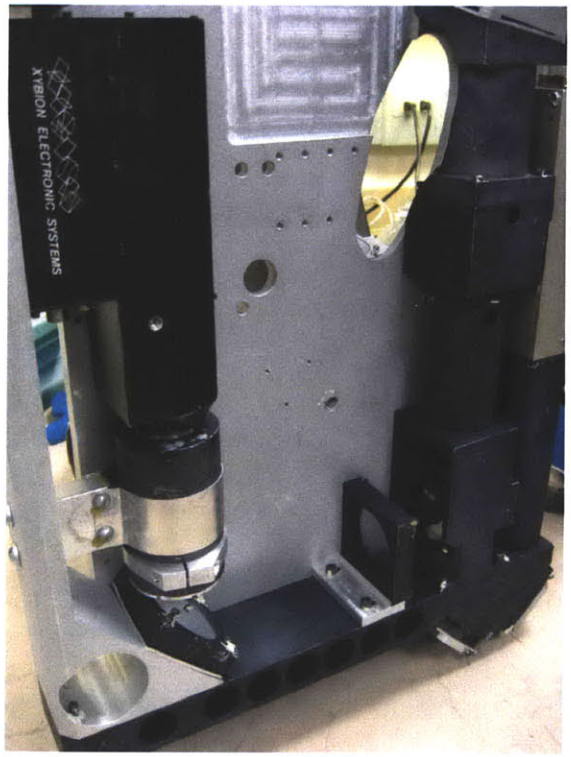


Figure 4-27: Visible optics board. On the left side is the Xybion camera, on the right is the SPACOM star tracker (gold-colored box).

### 4.2.2 Detector Subsystem

Two high resolution microchannel plate (MCP) detectors with wedge and strip positioning anodes and associated electronics were designed and constructed for this payload. The detectors use four MCPs mounted in a back to back configuration, each with a gain of $1.2\text{x}10^7$ electrons per photon, with a 10,000 Å thick potassium-bromide (KBr) photocathode deposited on the upper plate. Measurements with a pin hole mask at the surface of the plates show a resolved pixel of 50 $\mu m$, or 1.3 arc sec at the plate scale of the VeSpR telescope. This provides 2 pixels per 2.6 arc sec resolved point at the telescope focus. The spectrum is well sampled by the MCP detector, with 0.011 $\mu m$/pixel. The detector readout uses a three electrode wedge and strip anode 2 cm in diameter. The wedge and strip electrodes employ a linearly variable surface area to provide 2-dimensional positioning to a high degree of accuracy with minimum geometric distortion.

The sensitivity of these detectors at Lyman-alpha is 0.15 counts/sec-kR for a 3

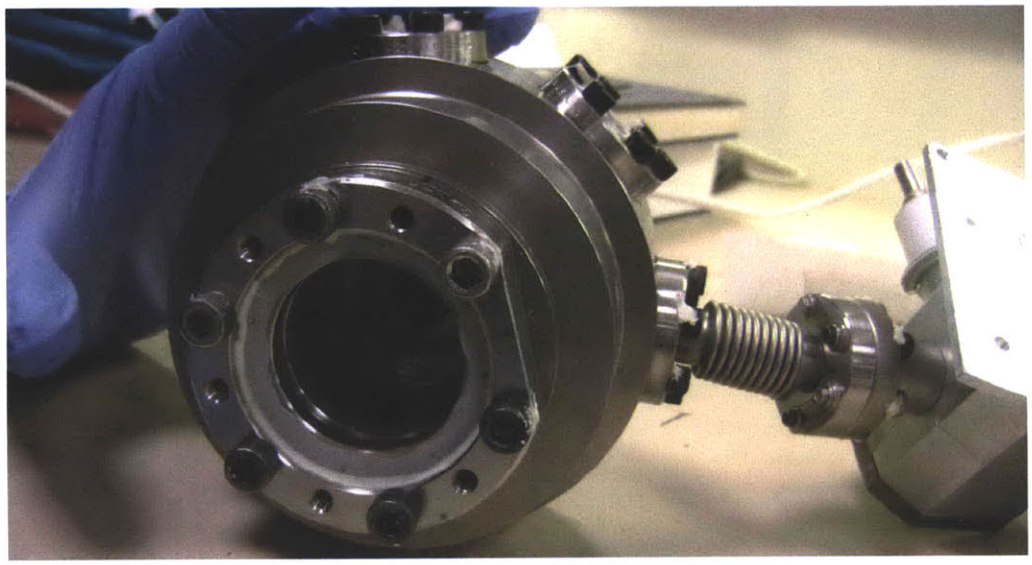

Figure 4-28: VeSpR MCP detector housing, front view.

arc sec source region. For the Venus flight, Venus' light must be blue-shifted by 0.055 Å or 13 km/sec for the detectors to resolve the hydrogen and deuterium emissions from the geocoronal emissions in the spectrograph box.

The detectors and their electronics can process up to 10,000 counts/sec, which is more than adequate for the expected count rate from deuterium in Venus' atmosphere, before dead time effects create significant measurement error. The local count rates on the MCP plates will not induce gain depletion since the counts are spread across the image of the aperture.

The detector is housed in an evacuated stainless steel housing, and light enters the housing through a 3.8 cm diameter magnesium fluoride window mounted in a ConFlat flange attached to the front face of the housing. Vacuum is maintained by 2 liter/sec vacuum ion pump (VIP). VIP power is supplied externally by an umbilical cable and automatically deactivated at launch. On the back of the housing is a plate with the high voltage input and wedge-strip-zigzag outputs. Figure 4-28 shows the front side of a detector housing.

There are mini-ConFlat flange ports on the sides, and one of these is where a flexible vacuum baffle is placed. On the other side of the baffle is a VIP, followed by a vacuum valve. If the VIP goes without power for a long period of time (~15

Figure 4-29: VeSpR MCP detector subsystem.

minutes if the seals in the subsystem are leaky to over a day if the seals are good), it cannot be restarted on its own and it must be connected to a vacuum chamber and pumped before it can maintain a vacuum. The vacuum valve allows the subsystem to easily be connected to and disconnected from any vacuum system with an available mini-ConFlat flange port. Figure 4-29 shows the part of the detector subsystem that is under vacuum.

In addition to the part of the detector subsystem that is under vacuum, there are also associated electronics components that data from the detector passes through before being sent to the Telemetry Section of the payload. The WSZ MCP detectors pass small microampere signals to three charge amplifiers, one for Wedge, one for Strip, and one for Zigzag signals. The charge amplifiers increase the magnitudes of the currents and pass the signals to the analog to digital converter (ADC) where the three signals are converted into the digital signals that are recorded as data. Figure 4-30 shows the series of electronics that data from the detectors pass through before reaching the Telemetry Section.

The digital signals are then passed from the ADC to the Telemetry (TM) Interface. Even though the detectors, charge amplifiers, and ADCs are capable of measuring up to 10,000 counts/sec before dead time effects cause errors (see Section 2.7), the TM Interface is only sampled by the main telemetry system and the ground support system at a rate of 2,500 Hz. While this is still adequate for the count rates expected during flight, it does create a choke that can limit the count rates during calibration

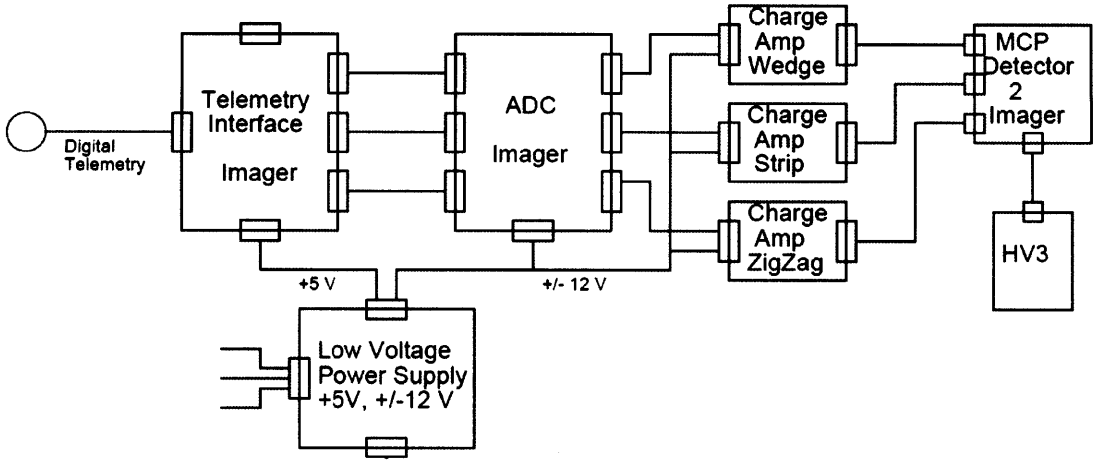


Figure 4-30: Detector data processing electronics leading to the Telemetry Section of the payload.

testing since the maximum measureable count rate using the ground support computers is 2,500 counts/sec. For all calibration tests, the calibrating lights were dimmed so that the count rate was below this threshold.

### 4.2.3 Power Subsystem

The power distribution subsystem of VeSpR is complex because there are so many different power requirements in so many different systems. In addition, because the payload has been modified so much over the last four decades, some power systems and wiring harnesses are still in the payload. Removing some of these harnesses would require more work than the decrease in payload mass would be worth, and some obsolete components in the power subsystem are associated with components that are still required in the operation of the payload.

There is not one single figure that fully encapsulates every aspect of the power system, but there are a series of figures that can adequately describe the system as a whole. There are two main hubs where most of the payload's required power is received and distributed throughout the payload, the Old Low Voltage Power Supply (OLVPS) and the New Low Voltage Power Supply (NLVPS). There are three plugs that supply power to the payload; two of them are umbilical cables that connect through the Spectrometer and Spectrometer Extension skin sections of the payload,

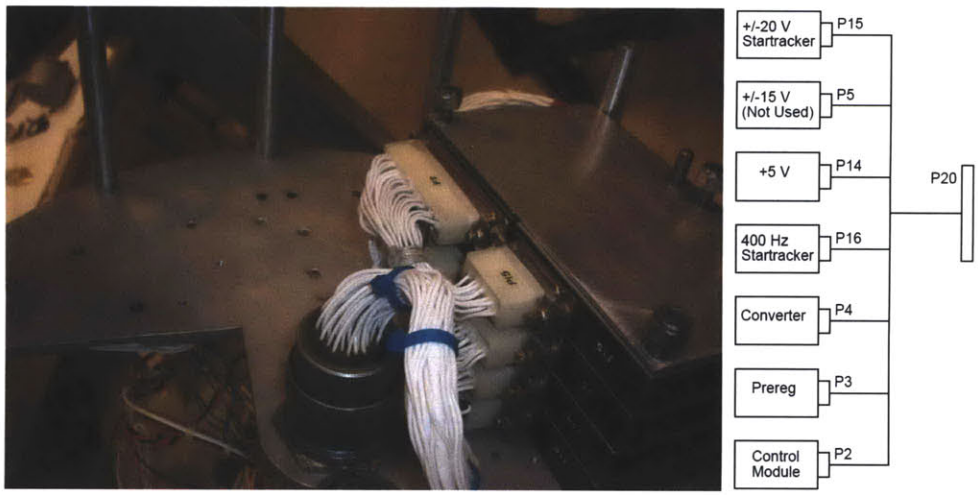


Figure 4-31: Old Low Voltage Power Supply (OLVPS) and a block diagram of its components.

and the other supplies battery power through the Interface Plate.

The first umbilical cable connects through the Spectrometer Extension skin section and directly supplies 28V power to the OLVPS from an outside power supply. This umbilical can be used on the launch pad or during integration testing to power the payload without using power supplied by the payload batteries. The OLVPS consists of a control module, a preregulator, a converter, and several output modules, all connecting through a single Bendix connector. Figure 4-31 shows the OLVPS and the Bendix connector routing all the inputs and outputs on the OLVPS and a block diagram of the modules it contains.

An example of an obsolete system still operating in the payload is the $\pm 15$ V power supply. There are no longer any components that operate at $\pm 15$ V, but removing the $\pm 15$ V power supply would require the three most complex connectors in the entire payload to be remade.

Figure 4-32 shows a block diagram of the distribution of 28 V power in the payload as it is being supplied from the first umbilical cable (top left). This diagram is taken directly from the updated wiring notebook and is meant to show how power is direct within the payload; it does not show accurate locations of the various modules and connectors. For instance, the connection P20/J20 is shown twice, and the three sides of the control module are actually coming from a single connector. Green lines in

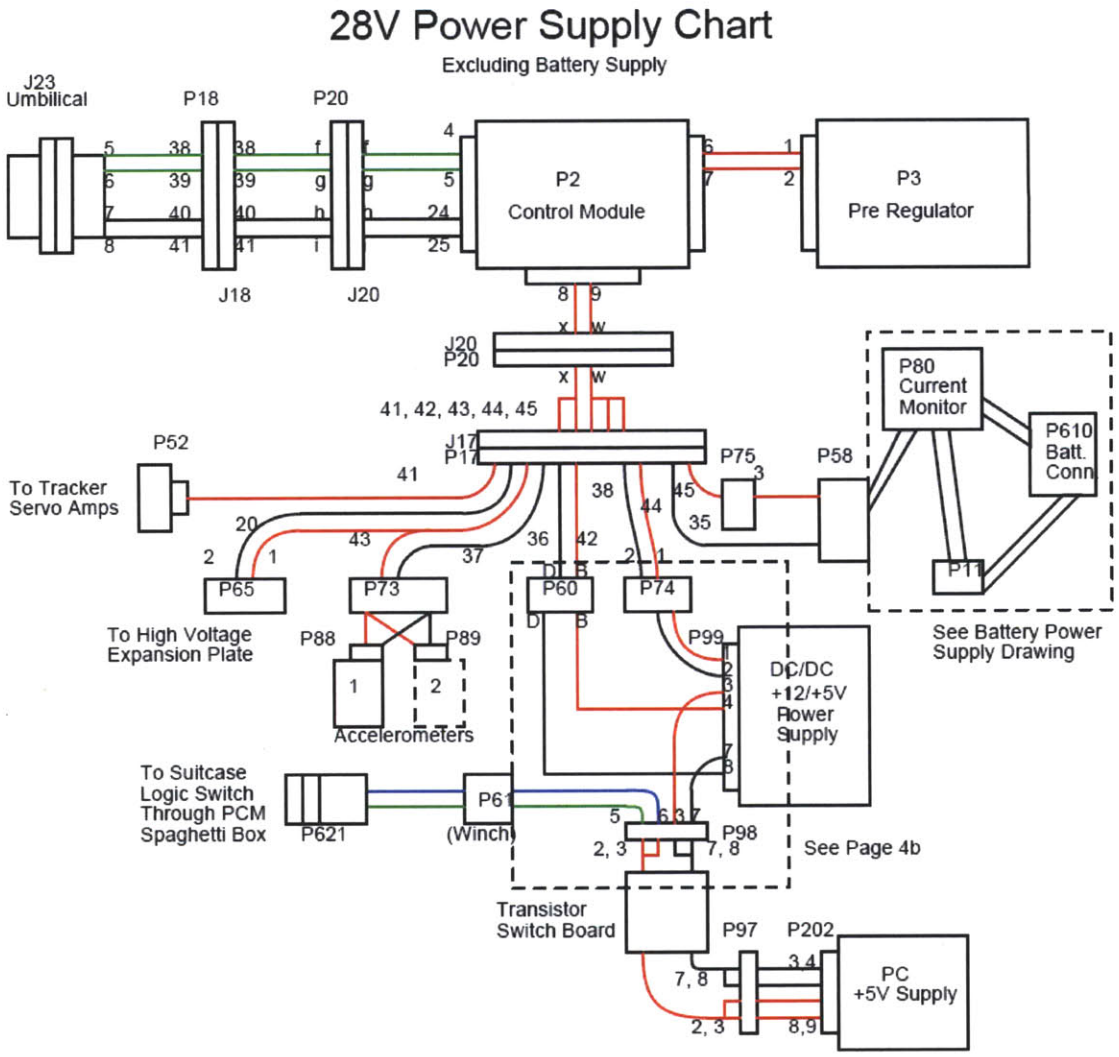


Figure 4-32: 28V power supply chain through the OLVPS. The green lines represent unregulated input power wires, the red lines represent regulated internal power wires, and the black lines are ground wires.

the diagram represent wires carrying unregulated 28 V external power. Red lines represent regulated 28 V internal power. Black lines represent ground wires.

Notice the current monitor and battery connector on the right side of the diagram. If power was being supplied from the battery, it would similarly go through the control module and into the preregulator before being distributed back into other payload systems.

The high voltage expansion plate controls the power input to the MCP detector high voltage power supplies. Switching power on to these supplies can be done with

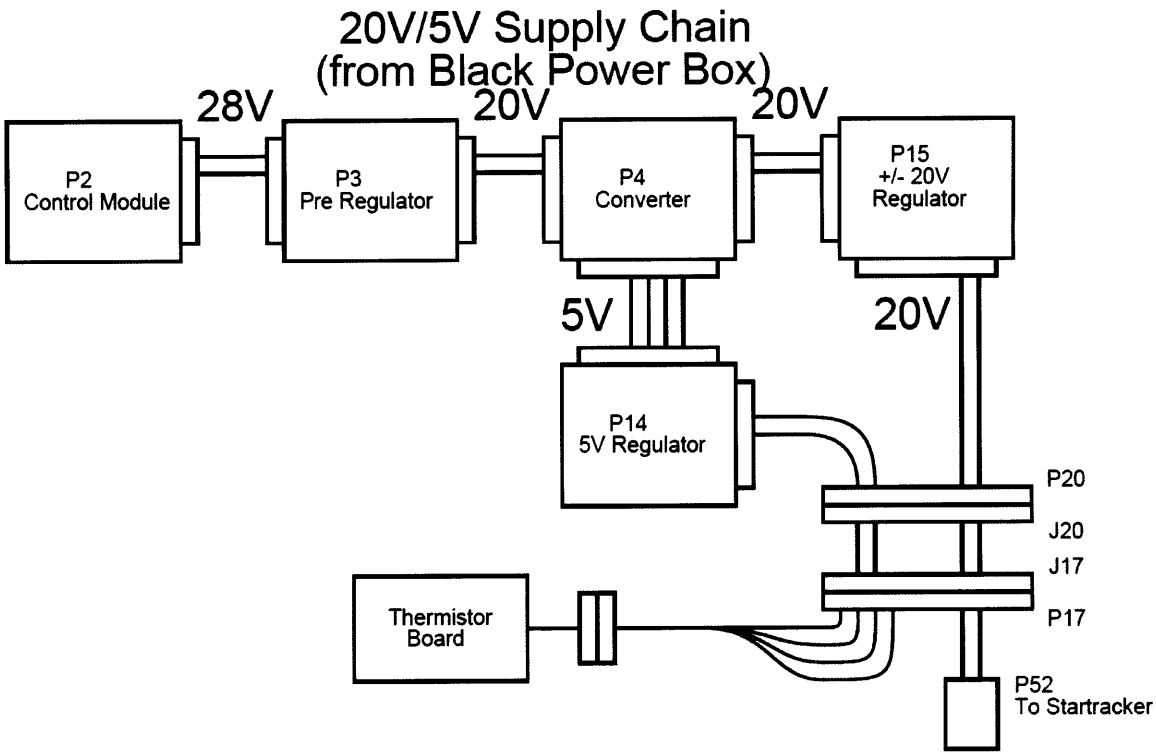


Figure 4-33: 20 V and 5 V power chains through the OLVPS.

the ground support system (see Section 4.2.6) or by the Telemetry Section of the non-science part of the payload. The transistor switch board is controlled similarly to activate the flight computer, labeled "PC" in Figure 4-32. The flight computer contains its own DC/DC 28V/5V power converter and electromagnetic interference (EMI) filter. Also notice the NLVPS in Figure 4-32, labeled "DC/DC +12/+5V Power Supply. This will be described later in this section, but note its location relative to the OLVPS in the power supply chain.

Figure 4-33 shows two more power chains provided by the OLVPS, the 5 V and ±20 V chains. Other power chains are not shown but behave in a similar manner, with external power passing through the control module, preregulator, and the converter before being passed to various other power regulators supplying different voltages.

The NLVPS receives 28 V regulated power from the OLVPS. The NLVPS has two ±12 V power supplies, one 5 V power supply, and one EMI filter that filters the input to the ±12 V supplies (more on this later). Figure 4-34 shows the NLVPS as it is mounted in the payload, and Figure 4-35 shows a solid model of the NLVPS as it was

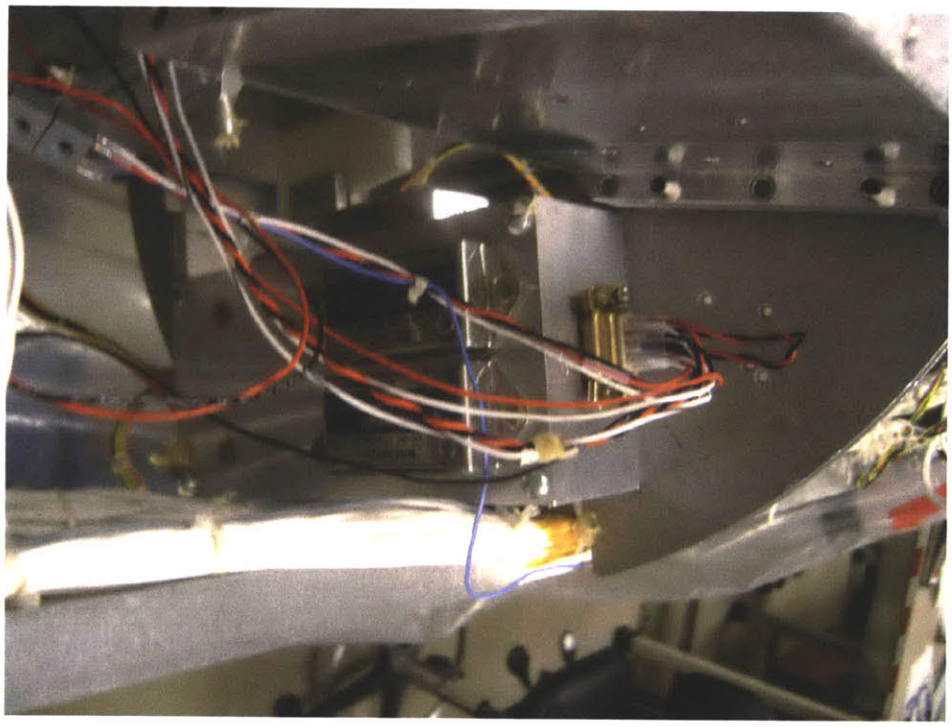

Figure 4-34: NLVPS mounted in the payload.

before modifications were made (see Section 5.2.4).

The NLVPS supplies power to MCP detector's electronics and allow for data to be transmitted from the detectors to the Telemetry Section of the payload. The $\pm 12$ V power needs to be filtered because it supplies power to the charge amplifiers, and even small variations in the current supplied to the amplifiers can have a tremendous impact on the quality of the data as it moves from the charge amplifiers to the ADCs. The 5 V power only supplies digital electronics, which are robust enough to not require EMI filtering.

Data from the spectrograph is also fed through the flight computer, through an RS-422 converter, and out of the second umbilical cable so that it can be read separately from the rest of the ground support system or any WFF electronics; however, since the flight computer is broken, this data chain is obsolete. Figure 4-36 shows a block diagram of the NLVPS system and the components it distributes power to.

The detector high voltage supplies, shown as "HV1" and "HV3" receive power from the high voltage expansion plate, which is not shown in Figure 4-36, but every

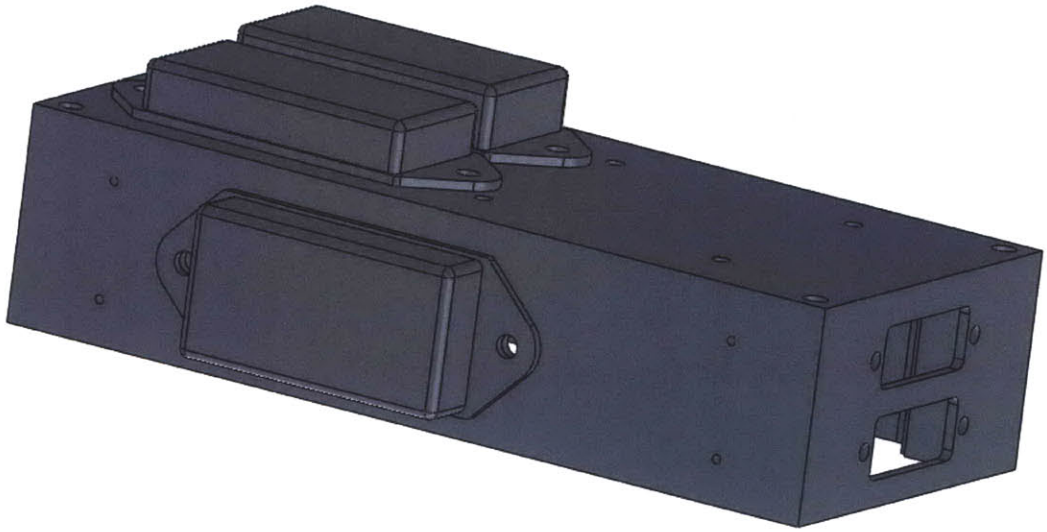

Figure 4-35: Solid model of the NLVPS.

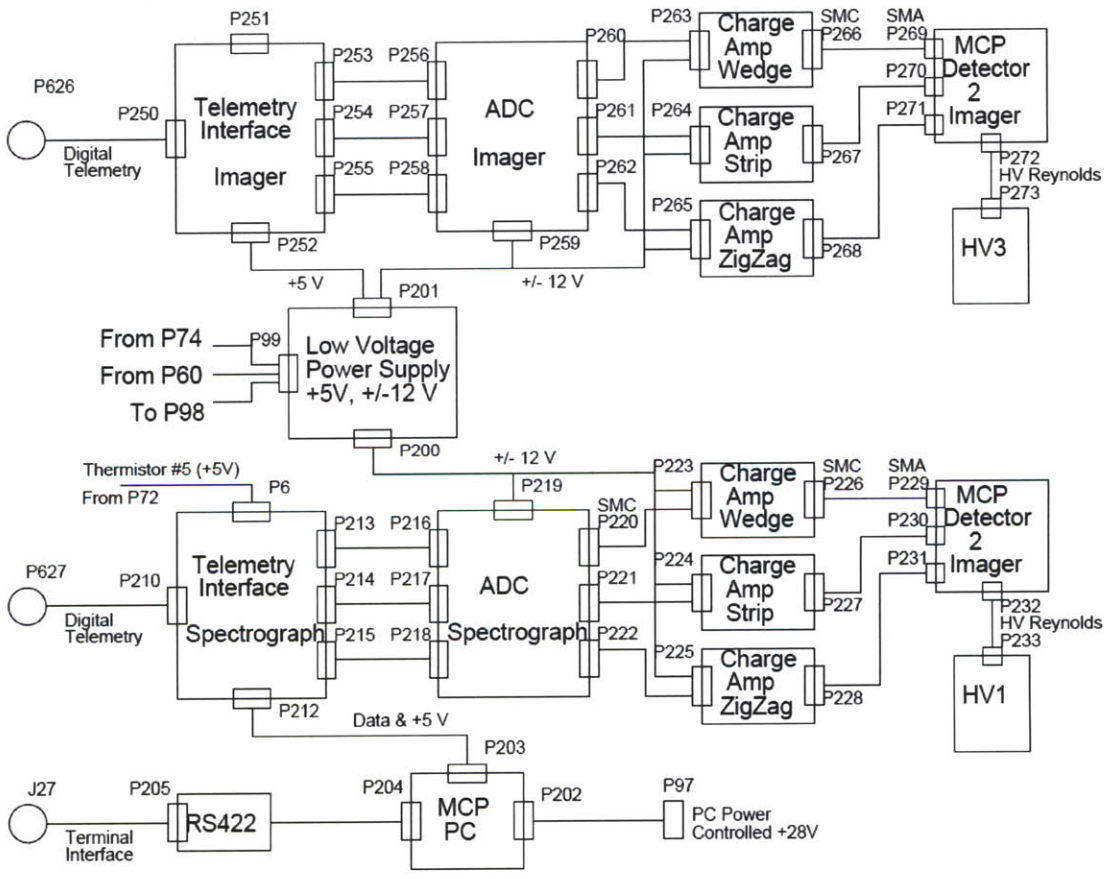


Figure 4-36: NLVPS block diagram and components that are supplied by the NLVPS

other component shown receives power from the NLVPS.

The remaining power input to the payload comes through the second umbilical cable located in the Spectrometer section. The second umbilical cable supplies 28 V power to the VIP high voltage power supplies. This power connection is never interrupted while the payload is assembled because if power is cut for long periods of time, air will slowly leak into the detector subsystem and the VIPs will not be able to maintain a vacuum when they are powered on again. While the rocket is on the launch pad, this umbilical supplies power to the VIPs to keep the detector housings at vacuum until launch.

This presents unique challenges when shipping the payload; historically, the payload has been transported in a moving truck and a power supply is brought along and connected to the cigarette lighter. A cable is connected through the cabin to the back of the truck into the payload storage container where the VIP control box is located. The VIP control box has wires that run through the second umbilical cable and supply power to the VIP high voltage power supplies.

Power to the VIPs can be disconnected for short periods of time without endangering the detectors or making it impossible to restart the VIPs; in fact, the reason power is supplied by an umbilical is because the VIPs are powered up until launch. For the duration of the mission, the VIPs are turned off. The VIPs must be turned off during the mission and during testing because ions from the VIP go into the detector and add a significant amount of noise to the data.

### 4.2.4 Analog Monitor Subsystem

There are a number of analog monitors throughout the payload that provide information on how the payload is operating through the telemetry stream that can be monitored in real time during flight or during testing. There are voltage, current, temperature, and pressure monitors throughout the payload.

The most common analog monitor is the voltage monitor. There are voltage monitors on every high voltage power supply and every low voltage power supply. All of the supplies have a built-in monitor that outputs a voltage that is indicative of the

load on the supply. In the high voltage power supplies, the monitors take the output voltage and divide it by 2000; for instance, a high voltage power supply operating at 4500 V would have an output monitor voltage of 2.25 V. The low voltage power supplies have either no voltage division for the 5 V power supplies or are divided by 3 on the 12 V power supplies, so the proper monitor voltage for a 12 V supply is 4 V.

There is a current monitor box that monitors the total current running through the 28 V supply system that operates whether power is supplied externally through the first umbilical or internally through the battery supply. This monitor is the best indicator of the overall health of the payload when all systems are powered. If the current deviates slightly from the measured test value, there is most likely at least one voltage monitor that is also deviating from the measured test value.

Thermisters are used in various sections of the payload to monitor internal temperature during the flight. These monitors were added for an earlier flight because there was concern that the temperature variations during flight would affect the optical properties through thermal expansion, but flight data showed that the temperature changes inside the payload were minimal and did not contribute to any problems. The thermisters are still on board the payload as an extra experimental measurement. However, there are no thermisters inside any of the electronic components, so careful monitoring of the thermisters would not have prevented any electronics from failing during testing for the previous flight (see Section 4.4).

Finally, there is a barometer switch inside the payload. Most suborbital payloads are vacuum sealed, but VeSpR only requires that the MCP detector subsystems operate in vacuum for the entire flight. Vents in the payload skin sections allow air to escape, so a pressure sensor inside the payload can feed data through the telemetry to decide when to open the shutter door and power on the MCP detectors. This pressure sensor/altitude switch is mounted to the Interface Plate.

### 4.2.5 Structure Subsystem

The payload is split into six total sections and two distinct halves; one half contains the telescope and the other half contains the instruments and electronics. These two

halves are connected by a large center plate. All six sections of the payload have their own external skin sections that provide protection from external elements and structural support during launch. These skin sections are standard for most WFF suborbital flights and can be replaced easily in the event that one of them takes too much damage to be safe for flight. The skin sections connect to each other and to the large center plate at the center of the science payload.

Figure 4-37 shows the three instrument (non-telescope) sections of the payload as they are without their skin section covers. The three sections from top to bottom are the Spectrometer Extension section, the Spectrometer section, and the MCP Detection section (see Figure 4-2 for where these sections are located within the full payload). The three sections that comprise the telescope half of the science payload would be beneath the sections in the figure, and the telescope would be pointing downward.

The three instrument sections are supported and connected by three longirons that span the length of this half of the science payload and connect to the center plate. Various other plates and electronics housings are also attached to the longirons. Teflon shims are mounted on the outward-facing sides of the longirons. When the skin sections cover the payload, the Teflon shims hold the skin sections in place and prevent vibration damage.

At the top of Figure 4-37 is the Interface Plate. If the full payload were assembled, the Telemetry Section would be above the Interface Plate. Figure 4-38 shows all of the connections on the Interface Place and their labels as they were at the beginning of the project.

Beneath the interface plate, two plates hang down and are connected by standoffs. The first is the Semicircular Plate, and the second is the Boomerang Plate. The OLVPS, the current monitor, and connector J20, the largest connector in the rocket and the one that has the most power connections, are mounted on the top of the Semicircular Plate. Several other connectors are mounted to the bottom of the plate. The Boomerang Plate was built to be an expansion to the Semicircular Plate and has other connectors mounted to the bottom of it as well. Both sets of standoffs that


Figure 4-37: Side view of the Spectrometer Extension (top), Spectrometer, and MCP Detection Sections of the payload without their skin sections (see Figure 4-2 for context).

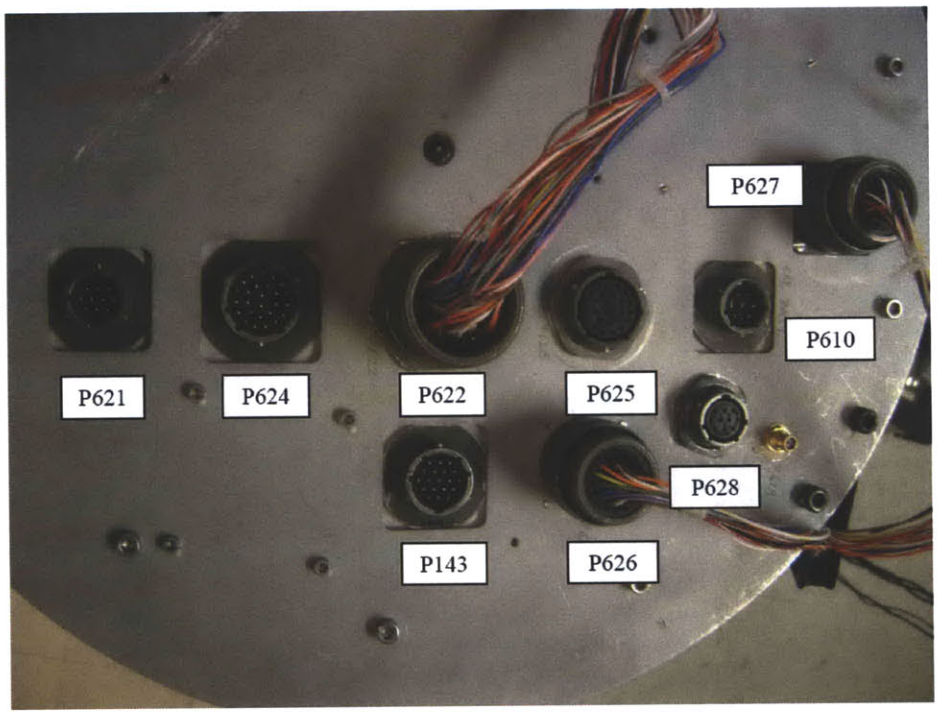


Figure 4-38: Original configuration of the connectors on the Interface Plate.

hold the plates are used to secure wire harnesses. Figure 4-39 shows the Semicircular Plate and the Boomerang Plate.

Beneath the two hanging plates is a structural plate that separates the Spectrometer Extension section from the Spectrometer section. On this plate, the flight computer and NLPVS are mounted. In addition, a hole is cut out in this plate where the spectrograph box extends through. Teflon supports are mounted to the edges that hold the long spectrograph box in place and prevent it from being bent out of align-

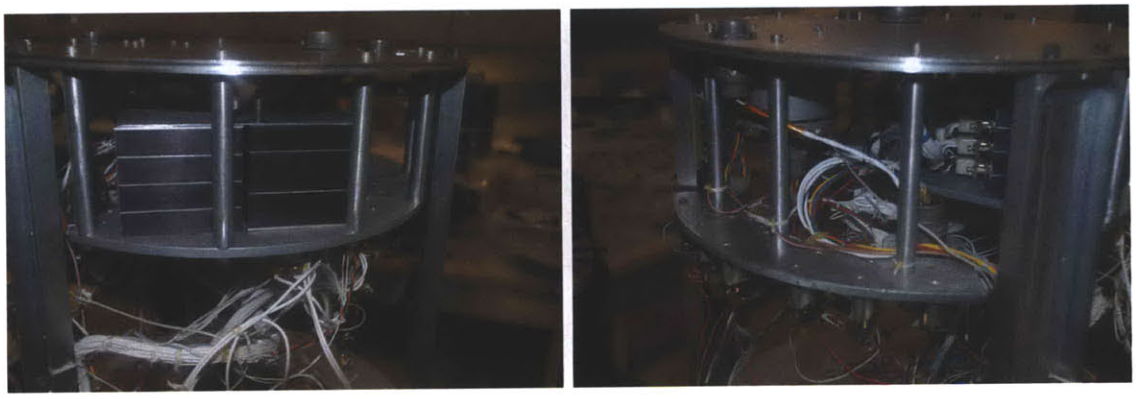

Figure 4-39: Semicircular Plate (left) and Boomerang Plate (right)

ment during launch. This plate is bolted to the three longirons, and it is at these locations where the Teflon shims are mounted that prevent the skin sections from vibrating against the rest of the structure. The RS-422 converter and VIP control module are mounted to the bottom of this plate.

At the bottom of the Spectrometer section, there are two plates. The top plate holds the VIP high voltage power supplies and one set of charge amplifiers. The bottom plate marks the bottom of the Spectrometer section, where the other set of charge amplifiers, the bottom of the spectrograph box, and the high voltage expansion plate are mounted. The spectrograph box also serves as structural support for mounting electronics. Both sets of ADCs and TM Interfaces are mounted to the broad sides of the spectrograph box.

Beneath the Spectrometer section is the MCP Detection section, which contains the Imager box, both detector subsystems, the Xybion camera, the SPACOM star tracker, the accelerometers, and the secondary mirror control box. Some of these modules are mounted to the longirons, but the Imager box is mounted to the center plate that divides the experiment section from the telescope section and the plate that the Spectrograph box is mounted to because it is so heavy.

On the other side of the center plate is the telescope. Aside from the tripod that supports the secondary mirror of the telescope, the three telescope sections are nearly empty and mostly serve as a baffle to prevent light from entering the system. The only other equipment in these sections are the telescope's heat shield, the mount for the ST-5000 star tracker in the Telescope Extension section, and cables that run through the center plate to power the secondary mirror servos and the ST-5000.

The science payload uses only passive thermal control elements to keep the temperature in the payload manageable. The heat shield surrounding the telescope prevents thermal expansion from changing the optical properties of the telescope, but otherwise no elements are in the payload solely to manage heat.

In a vacuum, there is no air to convectively transport heat energy, so conduction and radiation are the only heat transfer mechanisms. Radiative heat transfer is inefficient, especially below the maximum operating temperature of most electronic

components, so conductive heat transfer is the best way to prevent overheating within any electronics in vacuum. Potting and thermal grounding are used to lessen the risk of heat buildup in VeSpR's electronics.

Electronics potting is a practice where an electronics assembly is filled with a solid compound, such as epoxy, silicone, or polyurethane. This greatly increases the assembly's resistance to shock and vibration damage, but if a compound with high thermal conductivity is used it has to added advantage of dissipating heat from the electronics. While conformal coating is often used to protect electronics in standard environments, it does not provide enough protection for electronics in spaceflight applications.

Every electronics board on VeSpR is potted. In addition, the structures the electronics are mounted in are designed with more mass than what would be optimal to survive the loads experienced in flight. Because they are more massive, they have a higher total heat capacity and can act as heat sinks for the electronics. While the heat transfer properties of the payload have never been formally modeled, no electronic equipment has failed in a previous flight due to heat damage. In practice, the electronics are never left powered on for much longer than the length of the flight when they are being tested in vacuum. Components have been damaged in testing in the past (see Section 4.4).

### 4.2.6 Ground Support Equipment

The existing VeSpR ground support equipment (GSE) is overly complex for what is needed for testing, but it was built to be a realistic simulation of the payload as it is configured in flight. Figure 4-40 shows the two GSE computers used to interpret data from the payload and the GSE control suitcase used to control and power the payload.

Data from the imager, spectrograph, and analog monitors all flow through connectors on the Interface Plate at the top of the payload and into the "spaghetti box," a module that contains a WFF-93 Pulse Code Modulator (PCM) stack exactly like the one used in flight. The PCM stack then transmits the data through a bit sync

Figure 4-40: GSE computers (left) and control suitcase (right).

encoder that simulates the transmission of data through an antenna and feed it into the first GSE computer.

The first ground support computer runs a copy of TD+, the telemetry program that WFF used in previous JASpR flights. It displays all analog monitors and counters from the detectors. Although it does not directly display data from the detectors, the detector operation can be monitored by examining the counts coming through the TD+ interface.

Data from the detectors is sent from the first GSE computer through a buffer box into the second GSE computer, which is where data is displayed in real time during calibration testing. Figure 4-41 shows an example of data from a calibration test being shown on the second GSE computer.

Real time information that is displayed includes the total photon counts, the current count rate in counts per second, the total number of rejected counts, and the total number of bad counts. In this particular test, there was excessive background noise because the VIP was not turned off before the detector high voltage power supply was turned on. The thick line running diagonally on the screen in Figure 4-41 is a line profile generated from a Mercury lamp and is similar to a hydrogen Lyman-alpha line profile that is seen in testing and in flight.

Most of the functions on the GSE suitcase are obsolete, but the two most important functions of the suitcase are still operational. Two protected switches control

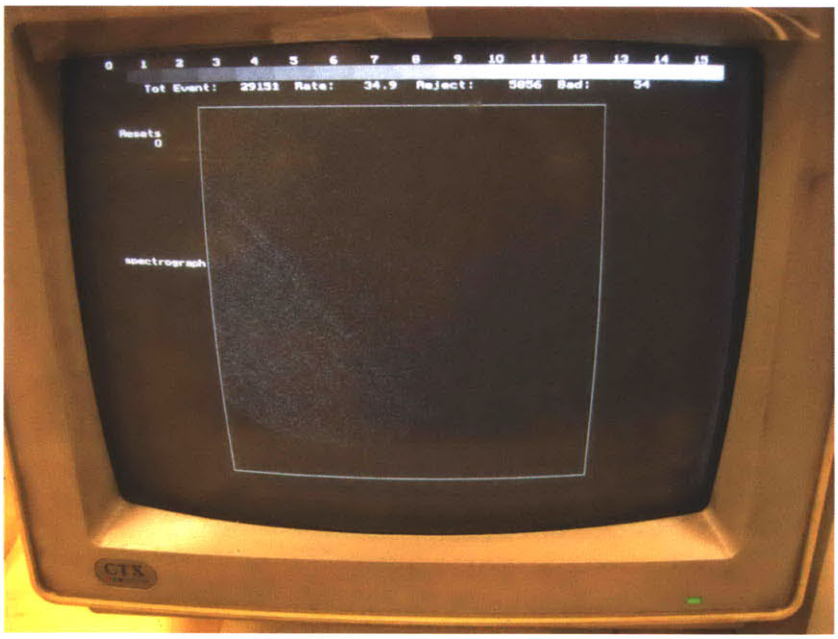


Figure 4-41: Display of the second ground support computer showing data in real time from a calibration test.

power to the MCP detector high voltage power supplies while the payload is on the ground for testing. There are various ports that voltmeter probes can be plugged into to measure analog voltages without needing the GSE computers and the TD+ output. The suitcase also controls the input power through the first umbilical cable, but that can be supplied without the GSE suitcase if needed.

## 4.3 Laboratory Facilities and Challenges

There are a number of facilities at Boston University that were needed to prepare VeSpR for flight. The three primary laboratory facilities that are being used throughout Project VeSpR are the Vacuum Calibration and Testing Facility (VACTEF), the Vacuum Ultraviolet Calibration Laboratory (VUCL), and the Ultraviolet Electronics Laboratory (UVEL).

### 4.3.1 Challenges with Vacuum Chambers and Ultraviolet Testing

Ultraviolet light is absorbed by Earth's atmosphere, which is why the D/H ratio of Venus cannot be constrained with a Lyman-alpha measurement from a ground telescope. The absorption of ultraviolet light by the atmosphere also makes it difficult to test the performance of VeSpR on the ground. Ultraviolet testing must be performed in vacuum chambers where the pressure is low enough for ultraviolet light to travel without interference from air molecules.

Vacuum chambers are complex systems with performances that vary greatly from one system to the next. Some do-it-yourself systems can be very cheap but only achieve low pressures comparable to what airliners experience in the stratosphere. Large systems that can achieve pressures comparable to deep space cost a significant amount of money. In general, the larger the system and the lower the pressure required, the more expensive the systems are.

#### 4.3.1.1 Types of Vacuum Pumps

There are a number of different types of vacuum pumps. The cheapest and least effective are standard scroll pumps. Scroll pumps act like fans with valves that blow air out of the system and are effective at reaching pressures in the 1-10 Torr range (atmospheric pressure is 760 Torr). However, scroll pumps are used as primary vacuum pumps in most vacuum systems because most of the more sophisticated pumps that can achieve lower pressures actually require low pressures before they can even be turned on. Scroll pumps are used as the primary pumps in all three vacuum chamber systems at Boston University. Figure 4-42 shows a scroll pump.

Turbomolecular pumps (or turbopumps), like scroll pumps, use fan-like blades to move air out of the system. Unlike scroll pumps, turbopumps operate at supersonic speeds and use shockwaves to impart momentum to gas particles to move them out of the system. Turbopumps can be expensive and require a sophisticated power controller. Small turbopumps have a tendency to fail easily because they must spin

Figure 4-42: Scroll pump used in the VACTEF as the primary vacuum pump.

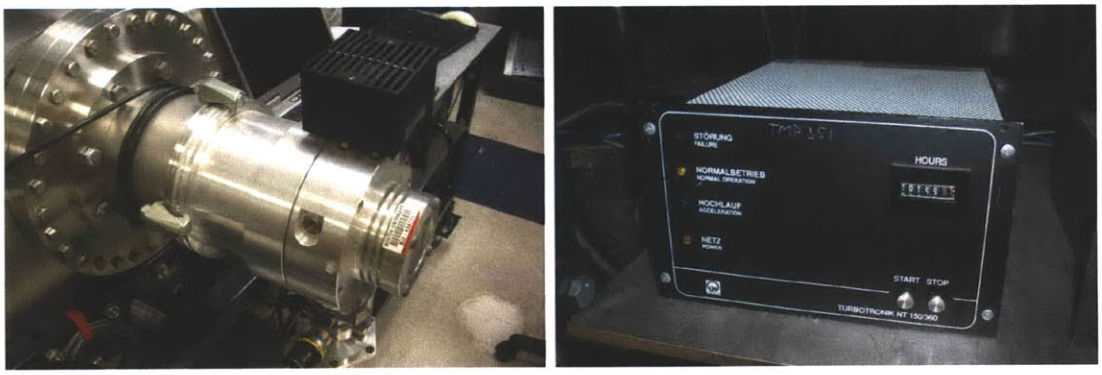


Figure 4-43: Turbomolecular pump used in the UVEL vacuum chamber (left) and its power controller under normal operation (right).

at a higher rate to achieve shockwaves at the tips because of the smaller radius compared to turbopumps with a larger diameter. Depending on the size, turbopumps can achieve pressures as low as $10^{-11}$ Torr. Turbopumps are used in the VUCL in the light source of the monochromator, and in the UVEL as the secondary vacuum pump. Figure 4-43 shows a turbomolecular pump and its power controller.

Another type of vacuum pump that achieves low pressures is a cryogenic pump. Rather than moving gas molecules out of a system entirely, like the turbo and scroll pumps, cryogenic pumps instead act as gas traps that capture moving molecules and freeze them in place. Cryogenic pumps are helium-cooled and reach temperatures very low temperatures. How effective cryogenic pumps are depends on the freezing temperature of the gasses in the chamber, but when vacuuming air with cold traps at

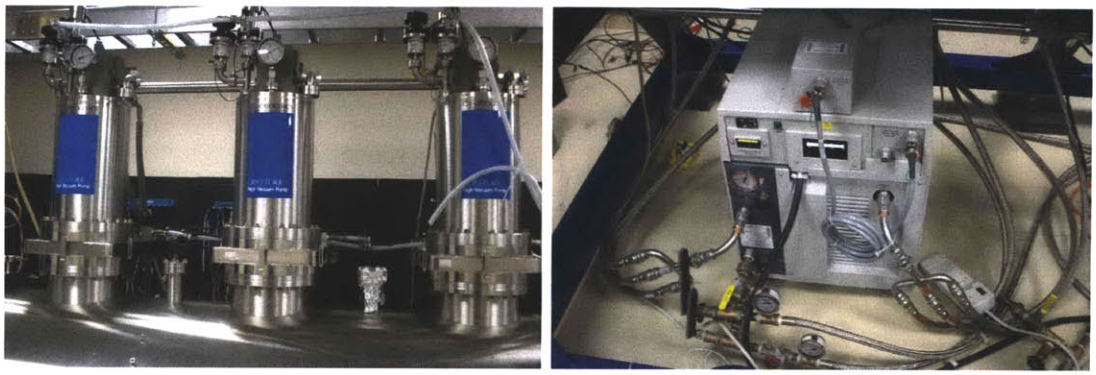

Figure 4-44: Cryogenic vacuum pumps used as the secondary vacuum pumps in the VACTEF (left) and the power control and helium cooling unit that control the cryogenic pumps (right).

10 Kelvin, these can be very effective pumps, reaching pressures as low as $10^{-10}$ Torr. While they are expensive and do not achieve quite as low a pressure as turbopumps, they are low-maintenance, have fewer moving parts, and are overall more robust, since failures do not cause catastrophic internal damage to the pumps. Cryogenic pumps are used in both the VACTEF and VUCL as the secondary vacuum pumps. Figure 4-44 shows three cryogenic pumps and their helium cooling unit and power supply.

A fourth common type of vacuum pump is the diffusion pump. Diffusion pumps use a high-speed jet of gas to move gas molecules at the top of the pump down to the bottom and out the exit. Usually, these pumps use some kind of oil as the working fluid. Diffusion pumps are extremely reliable and have no moving parts, and they can achieve pressures as low as $10^{-10}$ Torr. Figure 4-45 shows a schematic diagram of a diffusion pump. However, despite these advantages, diffusion pumps are forbidden from being used in any vacuum chamber that any component of the VeSpR will be tested in because oil contamination degrades the ultraviolet reflective and throughput efficiencies of optical components.

#### 4.3.1.2 Ultraviolet Testing in Vacuum

The biggest challenge with most vacuum systems is making sure they are airtight. Any vacuum system is only as good as its weakest seal, and some systems may have hundreds of seals. If a feedthrough plate is misaligned or the O-ring is not seated

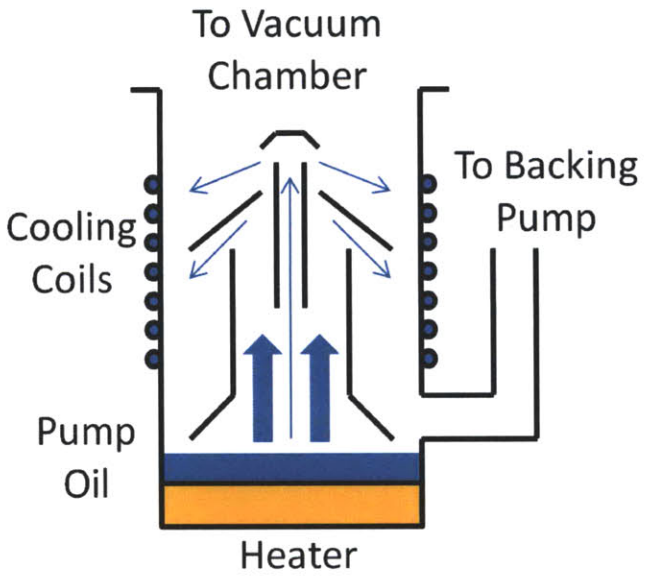


Figure 4-45: Schematic diagram of how a diffusion pump operates.

properly there will be a leak. It is particularly hard to seat O-rings properly when they are vertical.

Finding a leak in a vacuum system can take days, and it usually involves one person systematically squirting isopropanol all around every vacuum seal while another person watches the vacuum gauge to see if there is a change in pressure. If isopropanol is sprayed on a leaking seal, the liquid isopropanol will slowly enter the system instead of the gaseous air, which quickly brings down the system pressure as isopropanol continues to fill the leak. After some time, the isopropanol will evaporate and the pressure will rise again.

The best leak-checking procedure is to use a mass spectrometer and a helium spray. Mass spectrometers measure the mass-to-charge ratio of particles and can identify the molecular weight of molecules. Helium is an inert gas and has a small radius compared to most gas molecules, which means it can easily enter a vacuum system through a leak. If a mass spectrometer is in use in a vacuum system, leaks can be found by spraying the seals with helium and watching for a spike in particles with four atomic mass units – the mass of a helium atom. There should be very little helium in the system before helium gets sprayed on a leak, so if there is a sudden spike, a leak has been found. Mass spectrometers are also useful in identifying the

constituents of the gas and determining the level of contamination in the system.

In most applications, the cleanliness of a vacuum system is usually not an issue. Most vacuum seals that use Viton or rubber O-rings are coated with vacuum grease to prevent leaks. Diffusion pumps tend to put some small amount of the working fluid, usually oil, into the system. A fingerprint inside a vacuum chamber will not drastically affect how quickly the chamber reaches its operating pressure if the minimum pressure of the system is two or three orders of magnitude lower so its impact on system performance is negligible.

Ultraviolet vacuum testing is very different. The reason why ultraviolet astronomy cannot be done on the ground is because Earth's atmosphere absorbs ultraviolet light. However, ultraviolet light is absorbed even more effectively by hydrocarbons. Not only do hydrocarbons absorb ultraviolet light effectively, the energy of the ultraviolet light can cause photochemical reactions that produce bigger hydrocarbons, a process called polymerization. These bigger hydrocarbons block ultraviolet light even more effectively.

Because of this, hydrocarbon contamination is a huge concern when dealing with ultraviolet optics. Even a monolayer of hydrocarbons on an optical surface can decrease its efficiency (whether it is reflective or transmissive efficiency) by a huge factor, enough to make that optic essentially useless. Cleaning ultraviolet optics is very difficult and often results in the optic being replaced in the end.

Despite the fact that its instruments were working properly, the flight profile was accurate, and all targets were observed for longer than the minimum required time, the JASpR V flight was deemed only a partial success rather than a full success because the overall optical efficiency of JASpR was much lower during flight than it was during calibration testing. The reason for this sudden and unexpected degradation of the optics was due to some final testing that was done in a vacuum chamber that used diffusion pumps as the secondary vacuum pumps.

Under normal operating conditions, diffusion pumps can be used to pump down a vacuum chamber without contaminating the system or any ultraviolet optics inside. However, if the vacuum valves and pumps are not operated correctly, oil can back-

stream into the chamber. During JASpR testing, maintenance on one of the diffusion pumps was performed while the system was at vacuum. Before the pump was turned back on, the vacuum valve that connects the pump to the chamber was opened. At this point, the pressure in the vacuum chamber was lower than the pressure at the diffusion pump inlet. This error caused a small amount of oil to be displaced into the vacuum chamber, which, in a gaseous state, expanded into the chamber and diffused into the payload and optics, coating the surfaces with hydrocarbons. Since then, great care has been taken to ensure that contamination of this sort does not happen again.

This is why all of the vacuum chambers that VeSpR uses for testing have been specifically designed to not use oil. Most of the vacuum chamber seals use copper O-rings instead of Viton or rubber. Viton and rubber O-rings work well when they are coated with vacuum grease, but even low-outgassing vacuum grease is a contaminant that is undesirable in the system. Copper O-ring performance exceeds that of Viton and rubber O-rings if vacuum grease is not used. The only vacuum pumps that are used are the types that do not use any hydrocarbon oil whatsoever (scroll, turbo, and cryogenic pumps).

The inside of the vacuum chamber used in ultraviolet testing is kept very clean. Great care is taken to ensure that no fingerprints are made inside the chamber because fingerprints are composed of hydrocarbons. If any fingerprints are put on the inside walls of the vacuum chamber, they are cleaned with isopropanol before the vacuum chamber is brought to low pressures. Gloves are worn at all times when loading equipment into the vacuum chamber and handling system components like O-rings and vacuum flanges.

Any part that is manufactured in a machine shop tends to be coated with machine oil. Before any new component fresh from machining is put in a vacuum chamber or even attached to other components that will go in a vacuum chamber, it is cleaned. First, it is scrubbed with soap and water to get most of the contaminants off the surface. Next, it is bathed and scrubbed in isopropanol, then acetone. Finally, the component is put in an ultrasonic bath before it is cleared to enter a vacuum chamber.

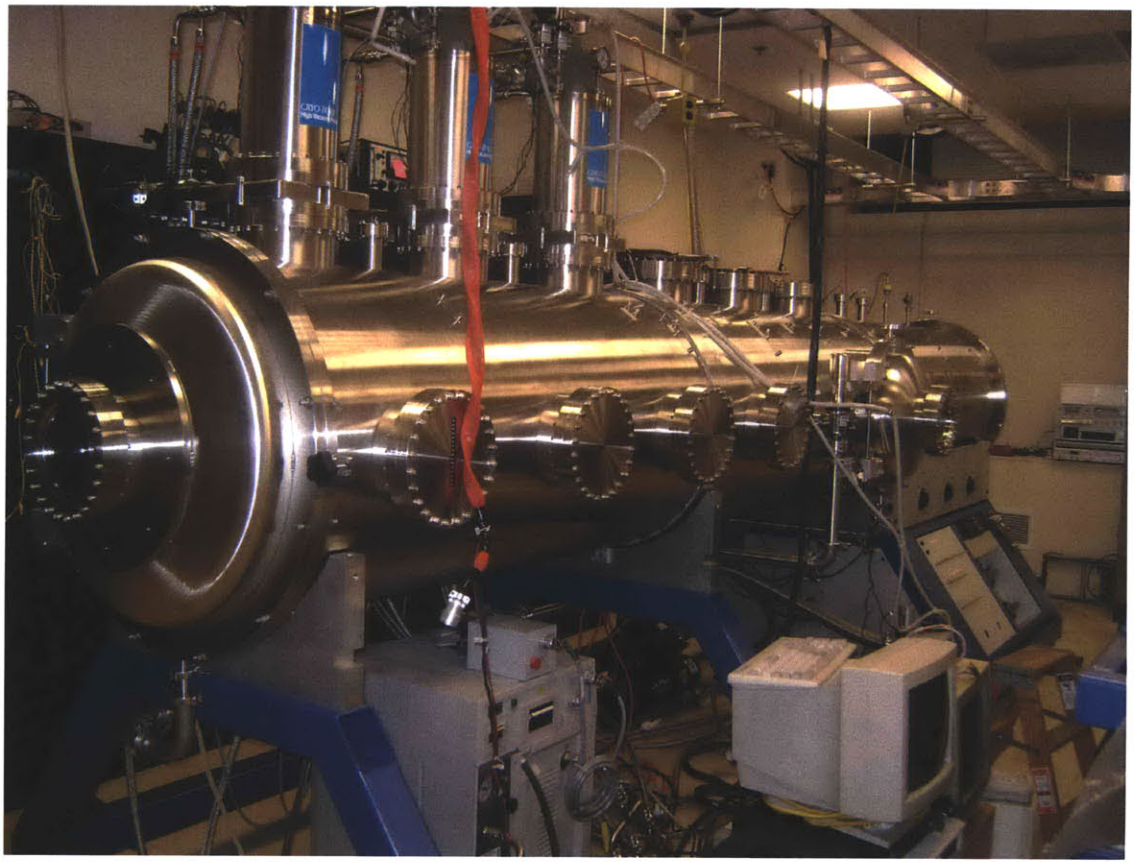

Figure 4-46: The vacuum chamber in the Vacuum Testing Facility (VACTEF)

### 4.3.2 The Vacuum Calibration and Testing Facility (VACTEF)

The VACTEF was specifically built to test the VeSpR payload, and most of the VeSpR documentation, testing equipment, tooling, and other essentials are stored here. The primary purpose of the vacuum chamber in the VACTEF is to test the VeSpR payload in a space-like environment. The vacuum chamber is 18 feet long and 3 feet in diameter, large enough to fit the entire payload in. It has one scroll pump for low vacuum and three cryogenic pumps for high vacuum. A light source chamber installed at one end of the main chamber can house a variety of optics and light sources for testing ultraviolet optics and detectors. Figure 4-46 shows the vacuum chamber in the VACTEF and Figure 4-47 shows a block diagram view from the side.

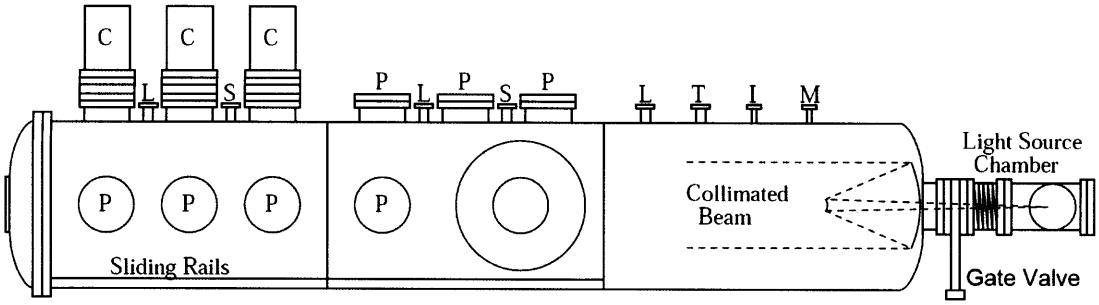


Figure 4-47: Block diagram of the vacuum chamber. C: Cryogenic Pumps; P: Ports; L: Ultraviolet Lamps; T: Thermocouple vacuum gauge; I: Ion vacuum gage; S: Spare small port; M: Manual leak valve. Sliding Rails allow the payload to be set on a mount with Teflon-lined supports so that it can be easily slid further into the vacuum chamber.

#### 4.3.2.1 Systems Overview

The vacuum chamber has pneumatic, electric, and manually actuated valves. The pneumatic valves are all either normally-open or normally-closed, depending on what direction the valve needs to go in the event of a power outage such that the valves would open or close on their own to prevent damage to the parts they connect to the chamber. An air compressor and hose system connects all the valves. The pneumatic and the electric valves are all controlled from a panel near the center door. The manually actuated valves are used only for venting the system and bringing it up to atmospheric pressure.

The cryogenic pumps require cold water to regulate the temperature of the pump's power supply. The water-cooling system routes from the power supply to a flow switch, up through the ceiling, and to an outside water chiller. This chiller occasionally breaks down and the cryogenic pump overheats, but it will automatically shut itself off if the internal temperature goes above 110 degree Fahrenheit.

The volume of the system that experiences vacuum is split into two sections, the main chamber and the forelines. The forelines connect the scroll pump to the cryogenic pumps and the main chamber. At the start of operations, the exhaust valve is opened, the scroll pump is turned on, and the foreline valve opens. When the pressure in the forelines goes below 1 Torr, the cryogenic forevalves are opened

and the cryogenic pumps are brought down to vacuum. When the pressure goes does below 1 Torr again, the cryogenic forevalves are closed, the cryogenic pumps are powered up, and the main chamber is opened to the scroll pump.

The cryogenic pumps require approximately an hour and a half to cool down to 5 Kelvin, and the scroll pump takes approximately half an hour to pump the chamber down to 1 Torr. Once both of these states have been achieved, the foreline valve is closed and the primary cryogenic valves are opened. With the cryogenic pumps exposed to the main chamber, the pressure quickly drops down to operating levels. If the chamber is empty and freshly cleaned, and if none of the copper O-rings are being reused (they are supposed to be replaced every time a seal is opened), the vacuum system can achieve pressures as low as 5 x $10^{-9}$ Torr. The average operating pressure in the vacuum chamber during testing when the payload and other equipment are inside is 5x$10^{-7}$ Torr, which is lower than the pressure of the atmosphere at 110 km altitude (about 1x$10^{-4}$ Torr)

There are three vacuum gauges that measure the pressure in the system. Two are thermocouple (TC) gauges. One is mounted in the forelines on the back of the chamber, and the other is mounted on the top of the chamber ("T" in Figure 4-47). These gauges accurately measure the pressure in the system down to approximately $10^{-3}$ Torr. Beneath this pressure, the TC gauges are no longer accurate. The third pressure gauge is the ion gauge ("I" in Figure 4-47), which accurately measures pressure from $10^{-4}$ to $10^{-11}$ Torr. This gauge cannot be turned on if the pressure is above $10^{-4}$ because the filament will burn out and need to be replaced.

Even though there is an order of magnitude pressure difference between the ranges of these two types of gauges, it does not matter, because when the cryogenic pumps are opened up the chamber pressure drops from ~1 to ~$10^{-5}$ Torr in a matter of seconds and continues dropping after that.

#### 4.3.2.2 Final Systems Design and Building

At the beginning of work on Project VeSpR, the vacuum chamber was inoperable. While all of the hardware components were installed (pumps, hoses, forelines, etc.),

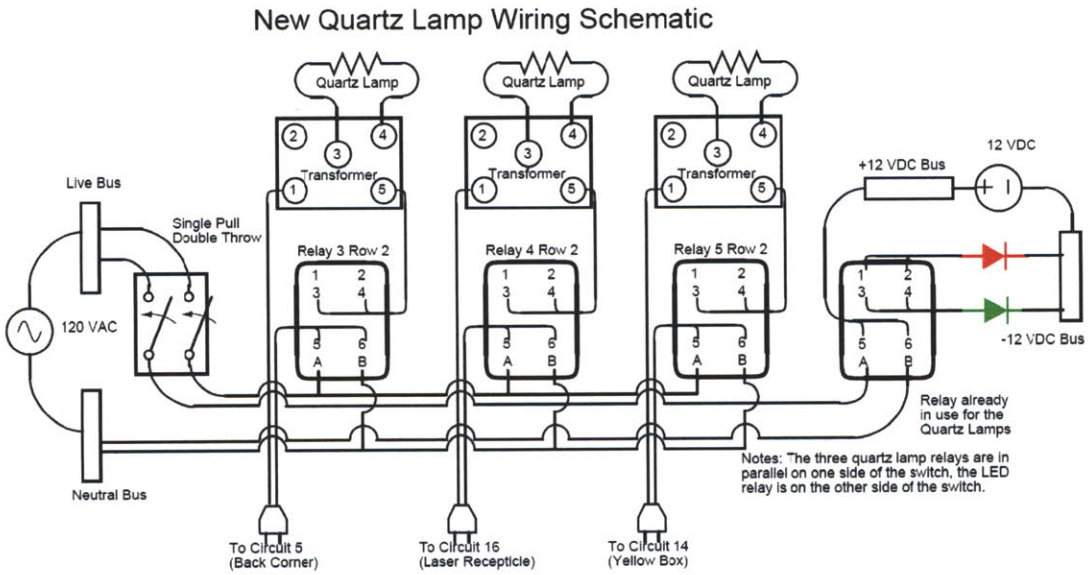


Figure 4-48: Wiring Schematic of the quartz lamps.

major electrical work needed to be done to bring the system online. Most of the electrical parts had been purchased, but the exact wiring had not been designed. The entire control board needed its wiring to be designed and built as well.

The vacuum chamber uses 240V A/C to power the cryogenic pumps, 120V to power the scroll pump, air compressor, gate and switch valves, ultraviolet lamps, and other heavy duty equipment, and 12V to power the relays, LEDs, flow switches, and other minor components. Figures 4-48, 4-49, 4-50, 4-51, and 4-52 show some of the schematic designs of the wiring of various systems for the vacuum chamber. All designs were made in XCircuit.

Once the schematic designs were finished and inspected, the wiring harnesses were constructed. Figure 4-53 shows the stark contrast between what is seen at the front of the control panel and relay switchboard and the complex wiring that is immediately behind both. Figure 4-54 shows the 12 V buses that send power from the 12V power supply to every LED on the panel and every other component that operates at 12V.

Before this wiring work was completed, the valves were actuated manually using a C-clamp, and there was no monitoring system to see whether the valves were operating properly. Once work was completed, the entire system could be operated from the control panel, and any failure point in any valve could be seen because of the LED

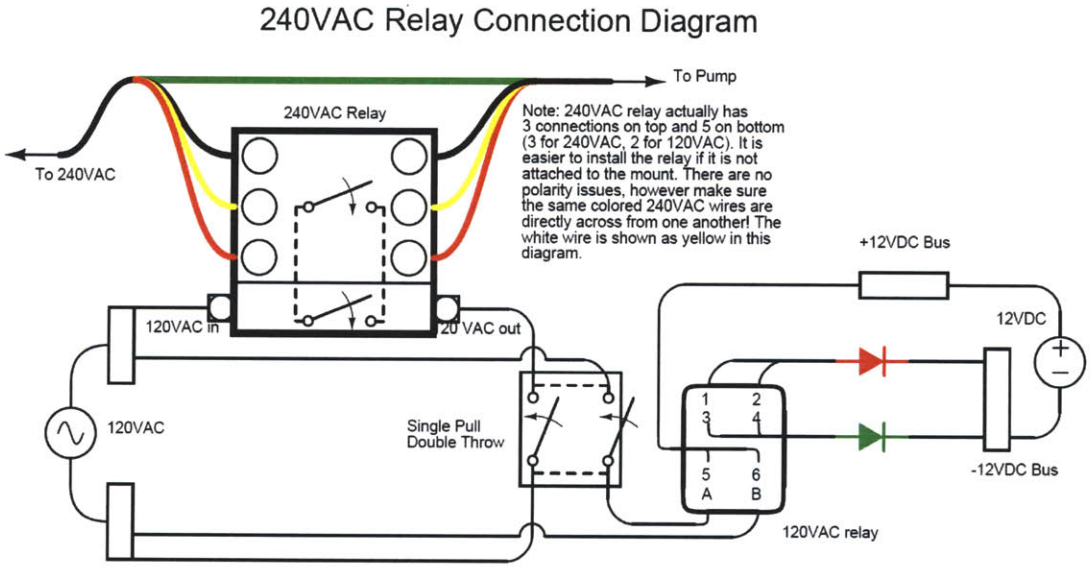


Figure 4-49: Wiring schematic of the 240V relays that supply power to the cryogenic pumps.

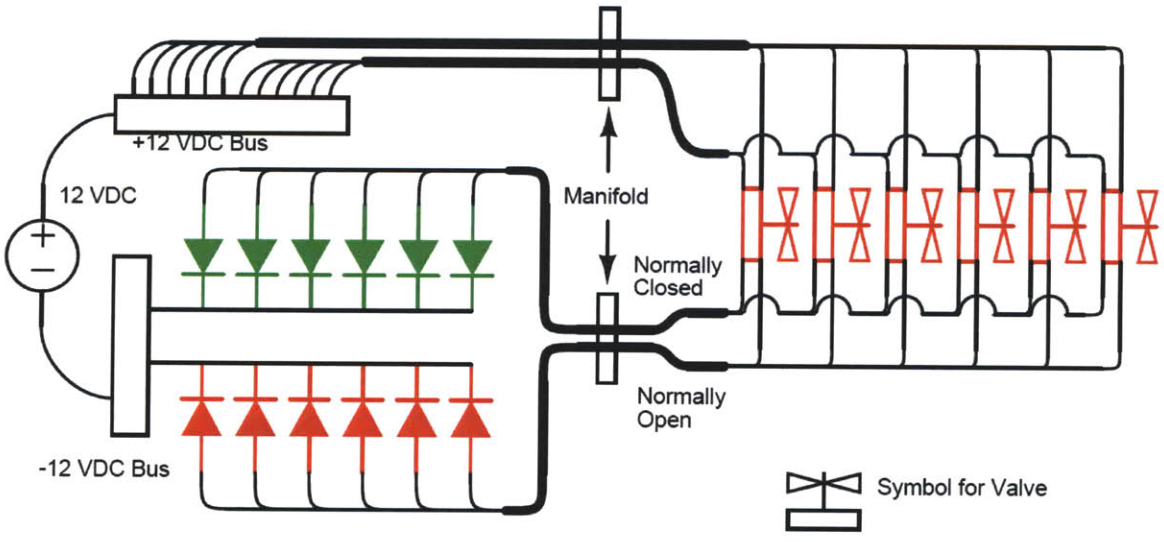


Figure 4-50: Wiring schematic for the LEDs on the control panel.

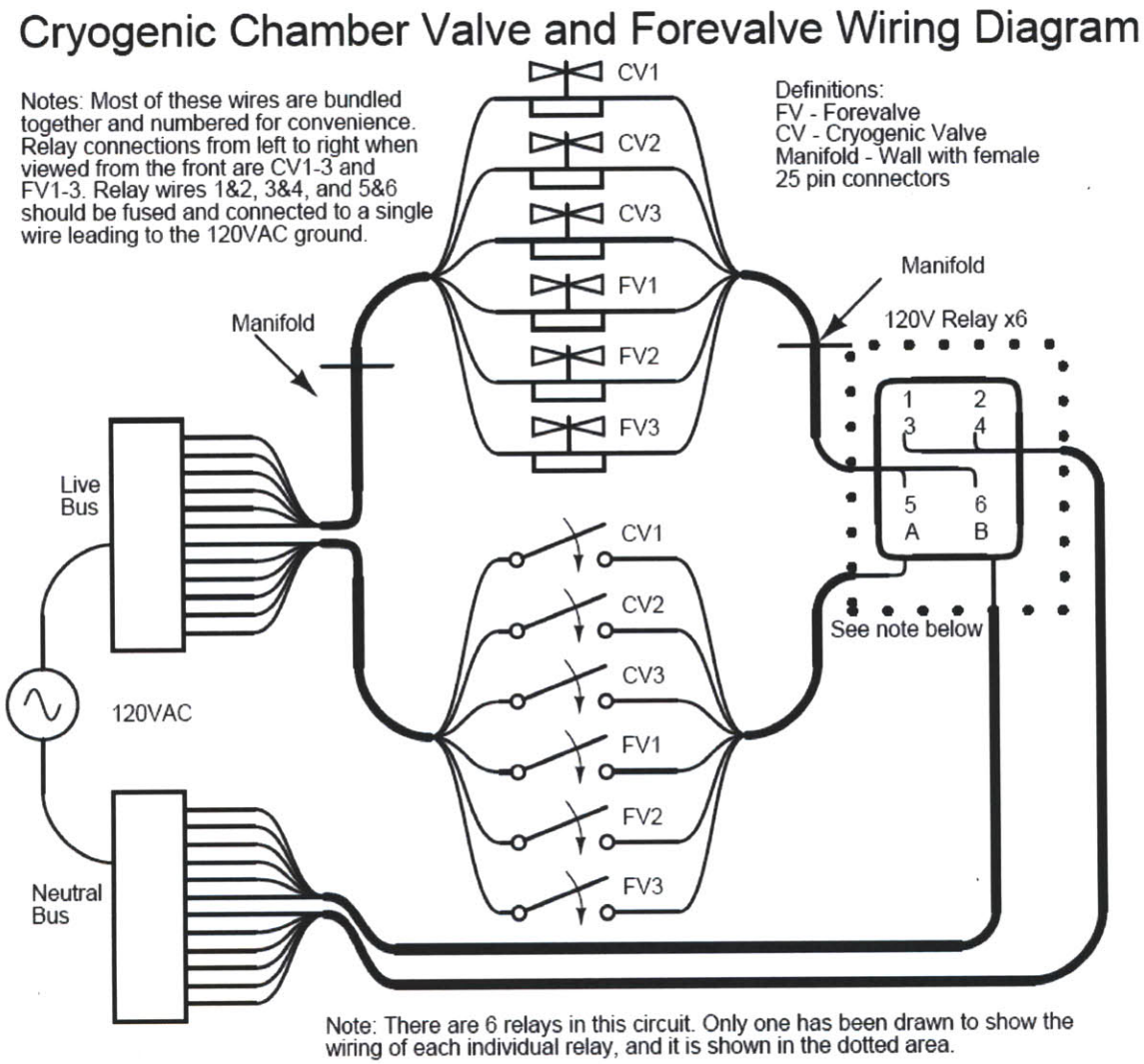


Figure 4-51: Wiring schematic of the valves that control the cryogenic pumps. Foreline valves open the pumps to the scroll pump and forelines while the chamber valves open the cryogenic pumps to the main chamber.

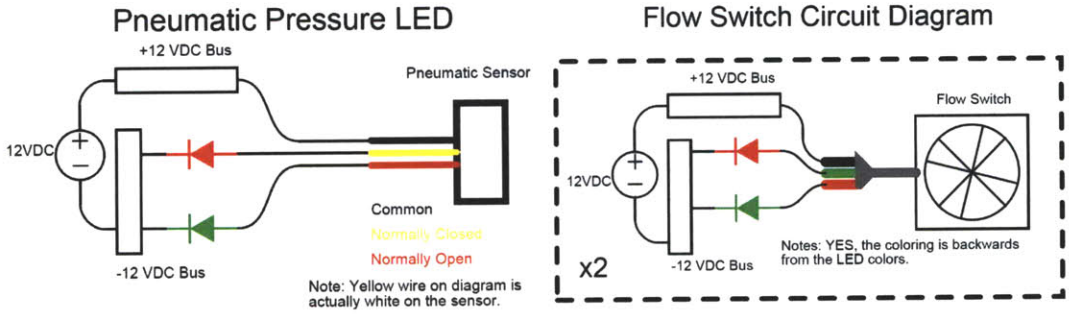


Figure 4-52: Wiring schematics of the pneumatic pressure and flow switch sensor LEDs.

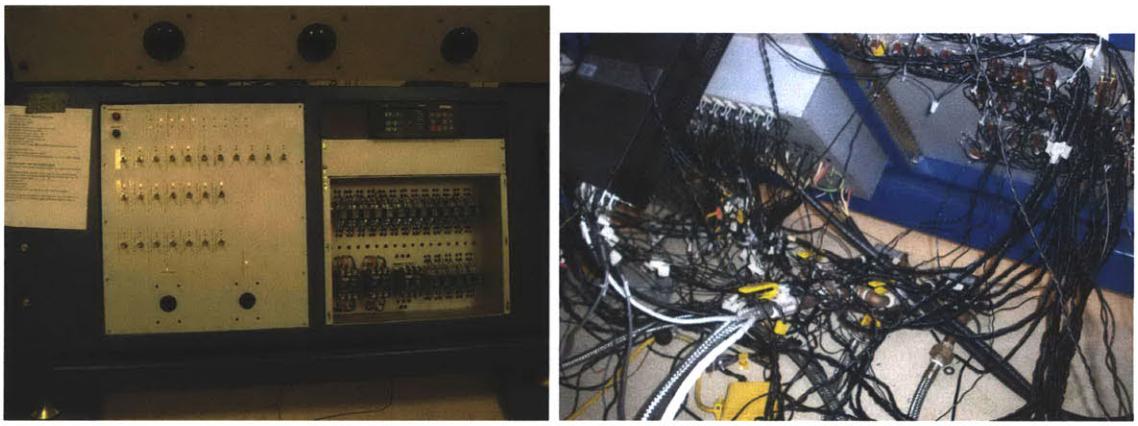

Figure 4-53: Front view of the control panel and relay switchboard (left) and the view from behind the panels (right).

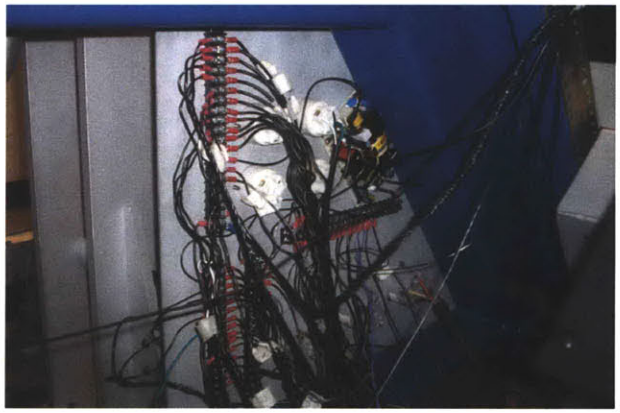

Figure 4-54: 12V buses and 12V power supply. This is a view that is slightly to the left of the view shown in Figure 4-53(right). The black box in the bottom right corner of Figure 4-54 and the top left corner of Figure 4-53(right) is the vacuum gauge control box.

status lights. The simplified operating instructions were written out and attached beside the control panel. The full text is available in the attached Appendix DVD.

#### 4.3.2.3 System Maintenance

Thoroughly cleaning the inside of the chamber is more difficult that one might imagine. A person must don a full clean suit, usually disposable, complete with booties, gloves, hairnet, and face mask, and crawl into the chamber. Smaller people are better for cleaning, but it is still difficult to maneuver inside the chamber. Both doors are opened to allow for maximum air circulation inside the chamber while the cleaner is inside. The cleaner must spray isopropanol onto all surfaces and wipe them down.

The dangerous part about this is working in an enclosed environment while spraying toxic chemicals. The cleaner must have someone on the outside supervising because isopropanol fumes will intoxicate and possibly suffocate the cleaner if the cleaner uses too much isopropanol or stays in the chamber for too long. Even with proper care, the person cleaning the chamber will most likely feel hung over once the job is done without experiencing a state of drunkenness first like one would expect before a hangover.

After the inside is cleaned, the chamber is pumped down to high vacuum and the quartz lamps are turned on. The quartz lamps emit high-energy ultraviolet light that breaks down any contaminant molecules left on the inside of the chamber. This is much faster than simply pumping on the contaminants and waiting for them to evaporate on their own. Removing contaminants also makes the pressure go down faster since nothing is left to evaporate and artificially keep the pressure higher. While the major concern for contaminants is hydrocarbons, water contamination can make pumpdown times increase dramatically while the water gradually evaporates into a gas from a much denser liquid state.

The cryogenic pumps use liquid helium to cool the system, but helium is notorious for its high leak rate as a result of its small atomic radius. The helium tank on the cryogenic pump power supply needs to be refilled occasionally. Refilling is a non-trivial process that requires care not to contaminate the entire helium supply with

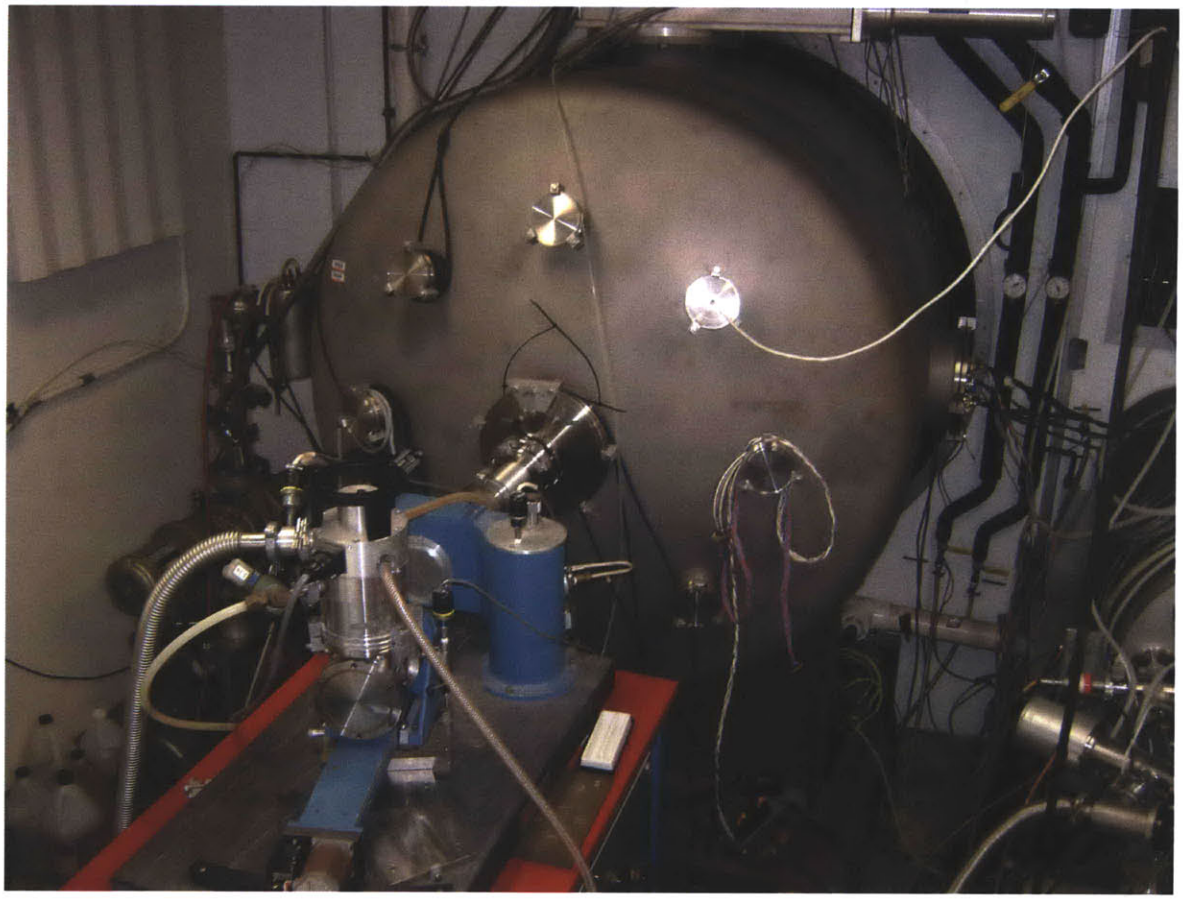

Figure 4-55: The vacuum chamber and the monochromator viewed from outside of the clean room.

other air particles that would freeze at much higher temperatures in the cryogenic system than the helium would. On two occasions a refill was needed, and in both cases no harm was done to the system.

### 4.3.3 Vacuum Ultraviolet Calibration Laboratory (VUCL)

The VUCL houses a vacuum chamber that is 5.5 feet in diameter and 8 feet long. Inside the chamber, there is a fine-motion optical table with three axes of motion controlled from an external computer. On one side of the main chamber is a light source chamber with a monochromator. The other side has a large door that is the main entrance to the chamber that is housed in a clean room. Figure 4-55 shows the vacuum chamber and monochromator from outside the clean room, and Figure 4-56 shows the vacuum chamber from inside the clean room.

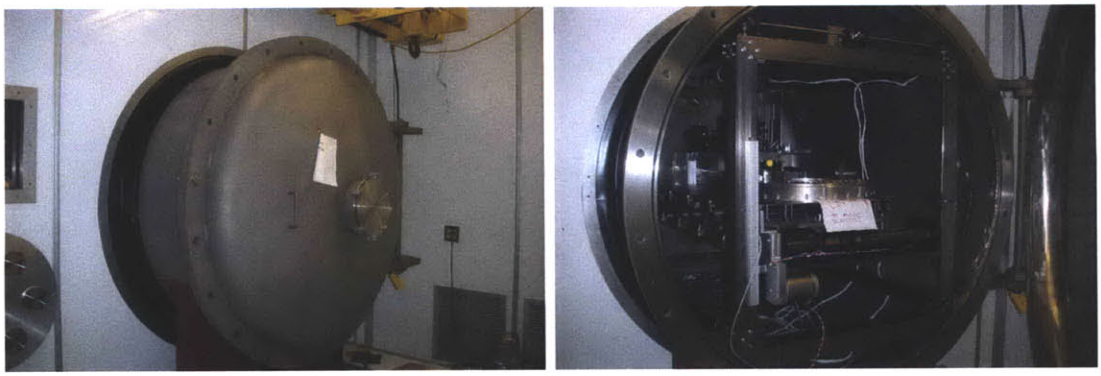

Figure 4-56: Views of the vacuum chamber from inside the clean room (left) and the optics table inside the vacuum chamber (right).

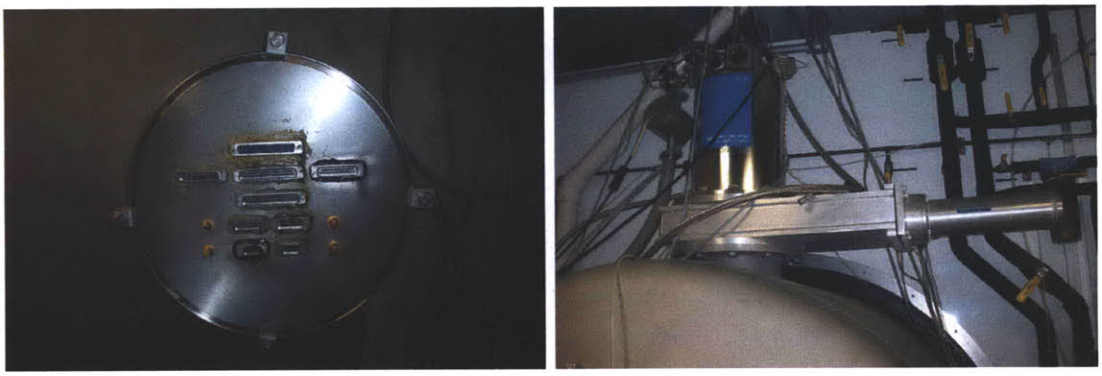

Figure 4-57: Areas of the vacuum chamber that leak. (left) A feedthrough plate with poorly-installed D-subminiature connectors. (right) A gate valve beneath the cryogenic pump.

The vacuum chamber uses a scroll pump as its primary pump and one large cryogenic pump as its secondary pump. While this vacuum chamber was certainly the most well-equipped vacuum chamber for calibrating each optic individually, operations were very difficult due to a variety of problems.

This vacuum chamber is not very well sealed. There are at least two major leaks, the first of which is from a feedthrough plate that uses D-subminiature connectors that were badly installed but are vital to the work the VeSpR team was doing, so it could not be replaced with a more robust plate. The second is the gate valve that separated the cryogenic pump from the main chamber. Due to these leaks, the chamber never able to achieve a pressure below $10^{-6}$ Torr. Figure 4-57 shows these two leak locations.

In the VACTEF, the cryogenic pumps can be opened and closed and the vacuum chamber can be brought up to air multiple times before the cold traps became too full to effectively maintain high vacuum, after which they need to be recharged and vented. The recharge cycle time on the VACTEF cryogenic pumps is on the order of three hours.

In the VUCL, the vacuum leaks take their toll on system performance. Because the lowest achievable pressure is still over an order of magnitude higher than the normal operating pressure of the VACTEF vacuum chamber, the cold traps in the cryogenic pump fill up very quickly. Because the leak in the gate valve is worse, the cryogenic pumps can only be used for one pumpdown before needing to be recharged. In addition, the cryogenic pump on this vacuum chamber has a recharge cycle time of 24 hours, so not only is the pressure barely adequate to do ultraviolet calibration testing to begin with, it also takes over a full day between measurements.

For each measurement, a person would have to suit up, enter the clean room, adjust the optics, reseal the chamber, and come out. Afterward, the chamber would be pumped down and the measurement would be taken, then the cryogenic pump would be full and the pressure would start to rise. The chamber would be brought back up to air and the cryogenic pump would be recycled, and after 24 hours the cryogenic pump would be ready to go again, all so that a person could crawl back in the chamber and make a small, sometimes sub-millimeter adjustment to an optic on the table.

Another major problem with using this vacuum chamber was the fine-motion optics table. Outside a vacuum chamber, a person can use his or her hands and special tools to perfectly align sensitive optics in a laboratory, but inside a vacuum chamber, this cannot be done. In theory, the moving optics table inside the vacuum chamber can make precision motions down to 1/10,000th of an inch in any direction and similarly small angular changes. In practice, problems with the table slowed the VeSpR team down almost as much as the cryogenic pump.

The main problem with the table was that it jams easily. The table has electric motors and a drive system that uses both circular gears and worm gears to move the

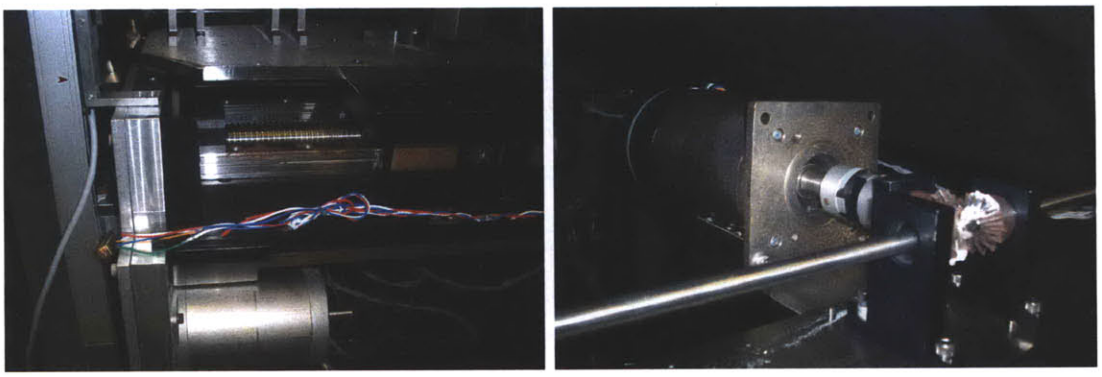

Figure 4-58: Mechanisms to move the optics table. (left) Horizontal motion mechanisms. (right) Vertical motion mechanisms.

table. A horizontal and a vertical drive system are on each side of the table, and for any translational motion the two move in sync with each other. Figure 4-58 shows parts of the horizontal and vertical motion systems on the side of the tank closest to the main door of the vacuum chamber.

One immediate problem with the horizontal motion mechanisms is that the worm gears are slightly rusted on one side but not the other. This can be seen in Figure 4-58 (left). As the worm gears spin, the first half of each rotation was smooth and the second half was not. The circular gears connected to the motor experienced the most resistance on the rusty side, and the horizontal motion mechanisms seemed to always jam then. Cleaning the worm gears would require disassembly of the entire system. The problem cannot be solved by simply lubricating the mechanism because most lubricants and vacuum contaminants. Even low out-gassing vacuum grease that is commonly used to grease O-rings cannot be used because it will still contaminate ultraviolet optics.

Additionally, the gearbox that translates power from the motor to the worm gear was not constructed with great enough precision. There are two gears behind the plate shown in Figure 4-59. This plate has two holes that act as the axial support for these two gears. Not only was this plate poorly made, but because it hangs vertically, the plate can slide downward by a distance equal to the difference between the width of the screws holding them in place and the width of the clearance holes the screws go into. In most applications, this small distance is not an issue, but with a gearbox,

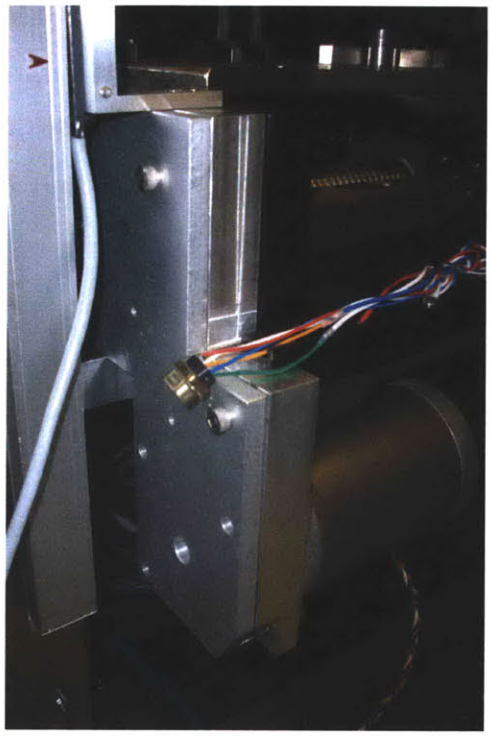

Figure 4-59: Plate on a vertical motion mechanism that houses the two circular gears that jammed.

greater precision is needed.

Sometimes the slight increase in resistance from the rusted worm gear would create a strong enough torque to move the gears out of alignment enough that the force of the electric motor would cause them to move even more off axis and jam. The gears were sometimes so badly stuck in the holes that a wrench was needed to take them out.

The only consistent way to fix this problem was to insert shims near the edges to align the plate with the axes of the gears better. When the plate was back on, a person would spin the worm gear by hand and feel the resistance, changing the positions of the shims if resistance got unusually high. This was difficult because the working space in the back of the chamber was very small and it is hard to grip the worm gear while wearing gloves. Wearing the clean room suit and only having one person in there at a time while another person waited outside to test the table's motion was also difficult. In the end, this trial-and-error approach proved to be successful enough that testing could continue.

The horizontal mechanisms (Figure 4-58 (right)) were also subject to jamming but the exact cause was never isolated. Several fixes were attempted, including adding Teflon tape to the right-angle gears, tightening the motor onto its mount, and tightening the driveshaft directly connected to the motor that spun the first gear.

The leaks and the table jamming caused calibration testing to take much longer than it should have. This partially led to the decision to pursue building a monochromator for the VACTEF vacuum chamber in the near future.

### 4.3.4 Ultraviolet Electronics Laboratory (UVEL)

The UVEL holds the last and smallest vacuum chamber that Project VeSpR utilizes for regular work at Boston University, and it is the only one that a person cannot climb into. It is a T-shaped chamber with a 14" tube diameter. It uses a scroll pump as the primary pump and a turbopump as the secondary, and it can achieve pressures as low as $10^{-7}$ Torr. Figure 4-60 shows the small vacuum chamber.

The black box shown in the top left of Figure 4-60 is a mass spectrometer. Mass spectrometers can measure the masses of molecules, and in the context of vacuum chambers is a great tool for not only measuring the contamination of a system but also to find the smallest leaks that are preventing a vacuum system from reaching lower pressures.

Early on the project, it was suspected that the imager detector housing had a leak because the VIP would not hold a vacuum. A great effort was made to find the leak in the detector; even though it is a small subsystem, there are eight vacuum seals that could have broken (between the detector housing and window, between two unused side ports and the detector housing, the detector housing and its backplate, the detector housing and the flexible pipe, the flexible pipe and the VIP, the VIP and the release valve, and the release valve's exhaust vent). The detector subsystem was connected to the large vacuum chamber in the VACTEF, and each seal was sprayed with isopropanol. No leak was found, but this was not enough evidence that there was no leak.

The detector subsystem was then brought to the small vacuum chamber for ad-

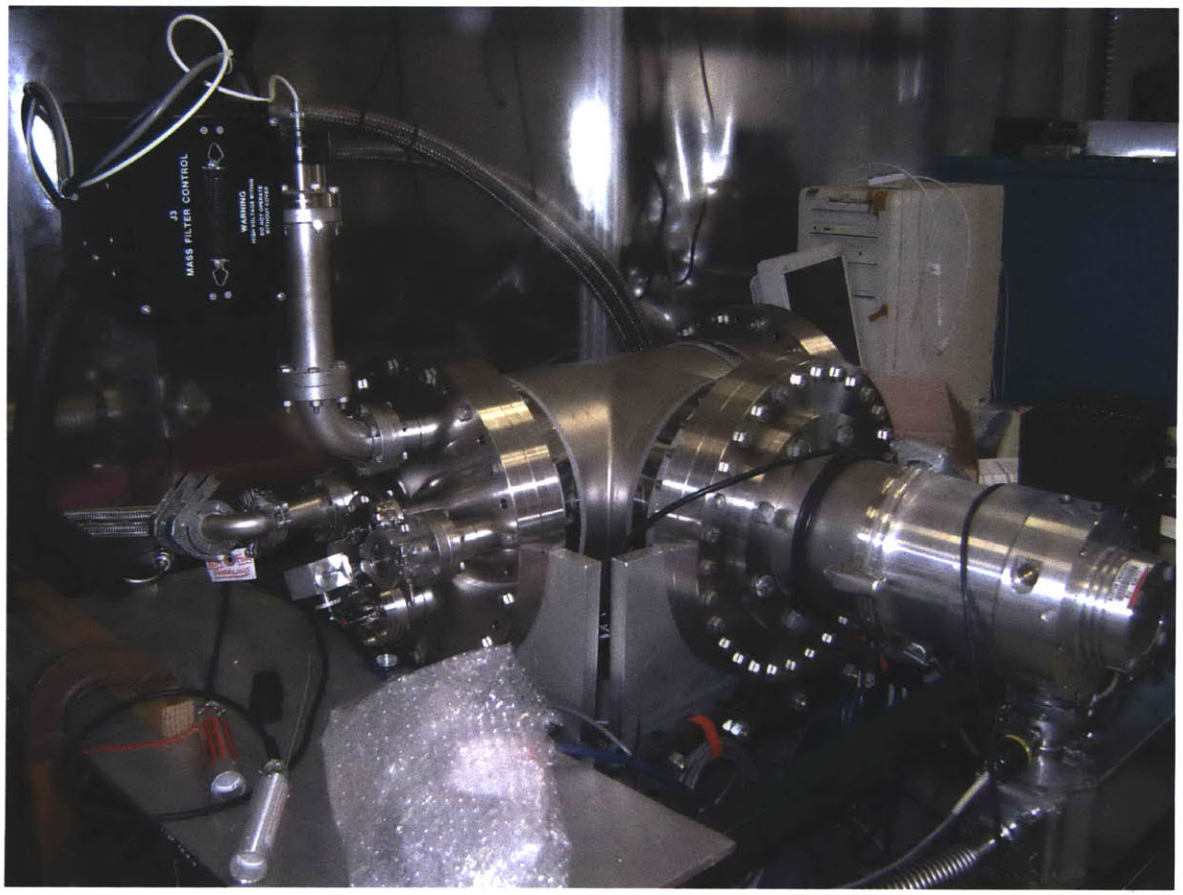


Figure 4-60: Small vacuum chamber in the UVEL.

ditional leak testing, mostly because the smaller size meant that a leak that was sprayed with isopropanol would have a larger effect on the pressure drop. However, with permission from the director of the UVEL, a mass spectrometer was attached and a helium check was done. Once again, no leak was found. Later, it was determined that the VIP itself had failed since it was so old, so it was replaced and the rest of the vacuum components were kept.

The mass spectrometer was also brought down to the VACTEF and used to assess the contamination in the large vacuum chamber. While the main concern for contamination was from hydrocarbons, it was discovered that water was the primary contaminant, which was causing the pumpdown time to be excessively long. The quartz lamps were used to energize the microscopic water contamination in the sides of the chamber and force them to evaporate faster. Water contamination is always a problem with vacuums in a humid environment.

The small vacuum chamber did not require any redesign or repairs from the VeSpR team. It was the only vacuum chamber that operated flawlessly and reliably every time it was needed.

## 4.4 Initial Payload Autopsy

In 2003, during the previous preparation of the JASpR payload for integration testing, data coming from the spectrograph detector suddenly stopped. At this time, it was too late to find the source of the problem, so the project was cancelled. In 2008, after the payload came out of storage, the first task after getting the vacuum chamber working was to find the problem.

A few problems with the payload were already known; for instance, the secondary mirror was only able to adjust itself in one direction but not the other, some of the analog monitors were not outputting a voltage, and the flight computer was unresponsive. None of these problems were related to the cancellation of the previous flight nor would they have caused mission failure had the payload flown, but the exact reason for why the data stream suddenly stopped during testing was unknown.

When most of the VeSpR subsystems were plugged into the ground support system and powered on for the first time since 2003, the system was mostly unresponsive. No data was coming from the detectors, and none of the analog monitors on the GSE suitcase were showing any voltages even though analog signals were present through the TD+ computer. Every power supply feeding power into the rocket was checked to ensure that they were operating properly and plugged into the correct connectors on the Interface Plate, but there were no signs of failure.

The next step to find the sources of failure in the rocket was to check every wire on every connector individually and test it to see if the proper signal was coming through, known as the "rocket autopsy." This signal trace was time-consuming, but there was no better way for the inexperienced payload team to learn about every subsystem and how it interacts with every other subsystem; in retrospect this would have been time well spent even if there were no problems with the payload at all. Figure 4-61 shows the Spectrometer Extension section and most of the Spectrometer section, the two sections with the most wiring, to illustrate the extent of this task.

The first signal traces were checked on the two umbilical cables that externally supplied power to the payload. These two cables were supplying proper power and signals that were expected to go into the rocket, as expected.

Next, D-sub bridges were connected between two D-subminiature connectors to easily test the voltage across each pin. Most of the internal connections are the D-subminiature type, so these bridges were used extensively. Bridges allow the signals on individual wires to be measured without disconnecting the wires, so signals can be checked while power is on without interrupting the power at any point in the chain. Figure 4-62 shows the 9-, 15-, 25-, and 37-pin D-subminiature bridges that were used to trace signals and voltages in D-subminiature connectors throughout the payload.

After hooking the bridges between two connectors, a voltmeter with two probes can be connected to any pair of wires, one of which is usually a ground, to measure the voltage. The same probes can be connected to an oscilloscope to measure voltage variations with respect to time, such as with pulses or digital signals.

Power was successfully traced through the first low voltage power supply, the

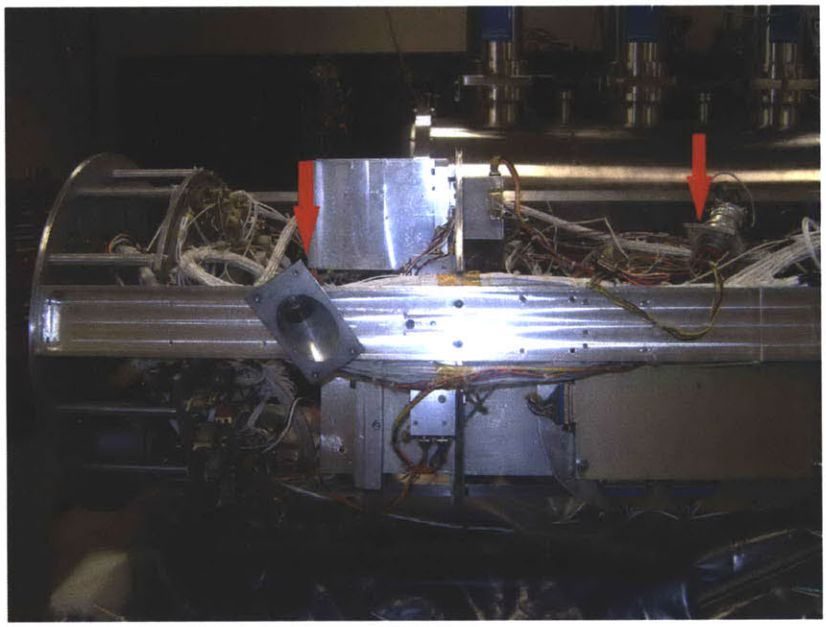

Figure 4-61: Spectrometer Extension section (left side) and most of the Spectrometer section (right side). Red arrows point to the external umbilical connectors. The umbilical on the left provides power input for the majority of the payload and can be used to monitor some of the analog signals. The umbilical on the right provides power to the detector VIPs via high voltage power supplies.

Figure 4-62: D-subminiature connector bridges used to trace signals throughout the payload while the payload is powered.

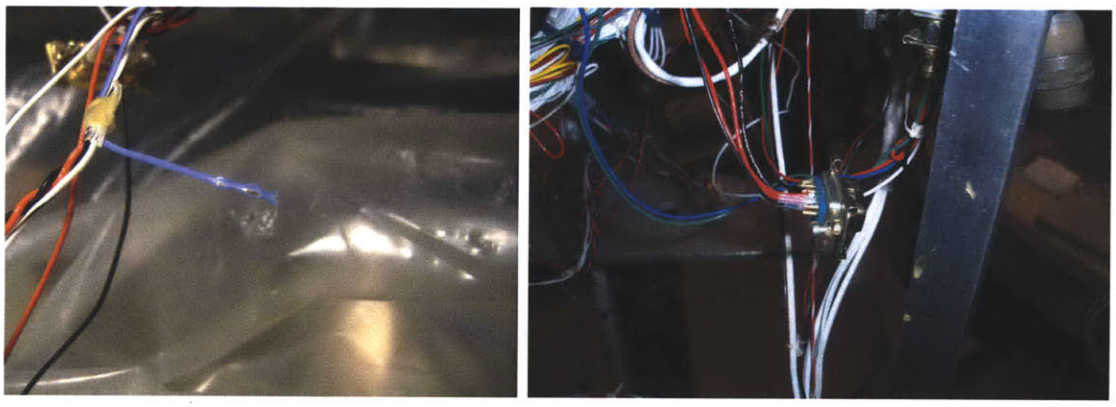

Figure 4-63: (left) A wire that was cut in half by being smashed between two skin sections. (right) A connector that was poorly constructed and has had to be repaired on multiple occasions.

analog monitors, the second low voltage power supply, and to all of the electronics in the data stream. A few connections were found to be broken in the process, but all of them had been broken by the new payload team and were not broken before the payload was taken out of storage. One wire had been cut because it got caught between two skin sections during one of the times the payload team was putting the skin sections back on the payload. Another D-subminiature connector was so poorly assembled that when it was carelessly pulled by its wires instead of its connector shell, two of the wires were disconnected, both of which carried power. These were easily soldered back in place, but it was noted that this connector needed to be replaced. Figure 4-63 shows these two problems.

Once power had been successfully traced to the detector high-voltage power supplies, they were turned on to make sure the switches on the GSE suitcase were still toggling the high voltage, which they were. Testing high voltage power supplies is dangerous and was not needed to see if the detectors were working, so instead of testing the high voltage power supply output, the outputs from the detector charge amps were tested with an oscilloscope.

The oscilloscope showed that the charge amps were outputting pulses corresponding to photons counts on the spectrograph detector but NOT on the imager detector. Another signal trace from the second external umbilical cable through the payload to the high voltage power supplies for the VIPs showed that something was wrong

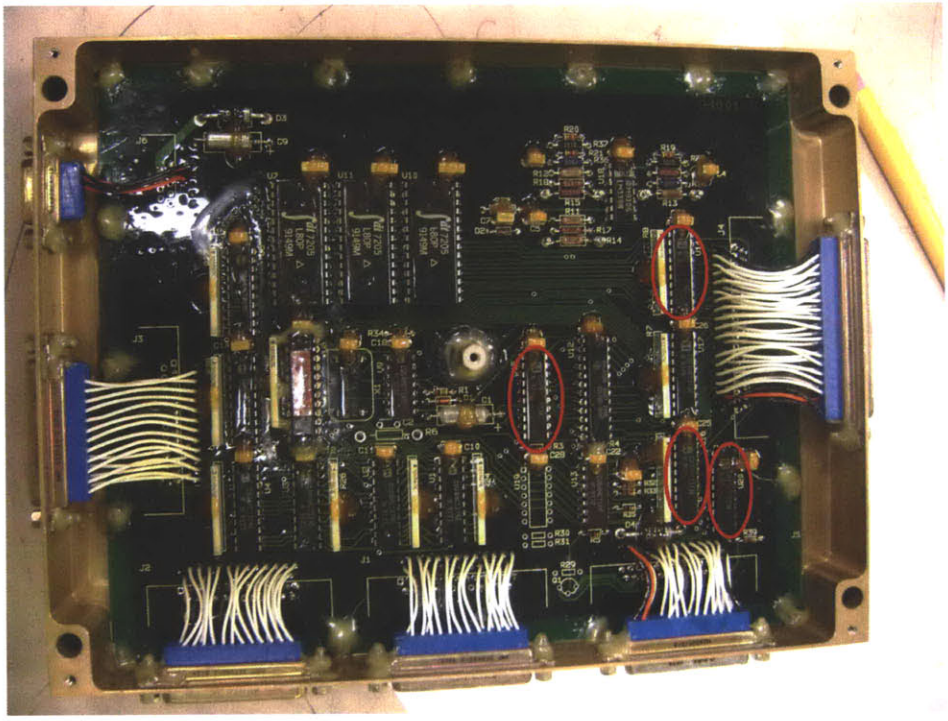

Figure 4-64: Spectrograph TM Interface after it was discovered that four chips (circled) had overheated and burned out.

in the imager detector subsystem, the first major problem discovered by this signal trace. For now, it was removed to be tested later.

The signals from the spectrograph detector charge amps were traced to the ADC and then from the ADC to the TM Interface, and all signals appeared as expected. However, no signals were being output by the TM Interface, which is connected directly to the GSE. The second major problem had been discovered, and this was the one that caused the spectrograph data stream to fail in 2003.

The TM Interface was taken out and opened up, possibly for the first time since 1994, when it was installed. When the lid was removed, the scent of scorched electronics emanated from the box. After close it inspection, it was noted that four of the chips on the board had burn marks. Figure 4-64 shows the board with the burned chips circled.

Although these burn marks are not conclusive proof, they do provide an explanation for why the payload suddenly failed during testing. In a vacuum environment, there is no air to carry out heat by convective processes, so electronics will not be able

to release heat as easily as electronics in air. As a result, the equilibrium temperature for powered electronics in vacuum is much higher than powered electronics in air. The longer electronics are powered in vacuum, the higher the temperature becomes. For short time periods, such as time periods on the same order of magnitude as the rocket flight, this usually is not a major issue. If electronics are left powered on for long periods of time in vacuum, they can overheat very easily. This is the most likely cause of the failure during testing in 2003.

Another phenomenon in vacuum testing that can cause problems in electronics is the higher chance of arcing at low pressures. The highest probability of arcing occurs around 1 Torr, which is near the pressure that the scroll pumps bring the chambers down to before the secondary pumps are activated in all of the BU vacuum chambers. As a result of this phenomenon, no electronics inside a vacuum chamber are allowed to be powered on while the chamber is pumping down. This practice is followed very strictly at BU, so even though it is possible that this is what caused the TM Interface to fail, chances are that it simply overheated in vacuum after being powered on for too long.

After some part searching, it was discovered that the four burned chips cost a grand total of $2.58. The entire project was cancelled because these inexpensive chips failed. However, because the TM Interface board is locked in place with Torr-seal and other protective chemicals, the board cannot be removed from the case and repaired without causing irreversible damage. Luckily, since WFF had long ago upgraded from the TD+ to the GP+ telemetry encoding system, it did not matter since the whole board needed to be redesigned and replaced to operate with the new system.

Since the spectrograph TM Interface was broken and the imager detector was not operable, the imager TM Interface replaced the spectrograph TM Interface. After this, data was coming through to the GSE computers and was being displayed properly. Now there were enough components of the payload working to do initial calibration testing.

The signal trace was nearly complete, and no problem had been found with the analog signals. After tracing all of the analog signals back to the umbilical that

to release heat as easily as electronics in air. As a result, the equilibrium temperature for powered electronics in vacuum is much higher than powered electronics in air. The longer electronics are powered in vacuum, the higher the temperature becomes. For short time periods, such as time periods on the same order of magnitude as the rocket flight, this usually is not a major issue. If electronics are left powered on for long periods of time in vacuum, they can overheat very easily. This is the most likely cause of the failure during testing in 2003.

Another phenomenon in vacuum testing that can cause problems in electronics is the higher chance of arcing at low pressures. The highest probability of arcing occurs around 1 Torr, which is near the pressure that the scroll pumps bring the chambers down to before the secondary pumps are activated in all of the BU vacuum chambers. As a result of this phenomenon, no electronics inside a vacuum chamber are allowed to be powered on while the chamber is pumping down. This practice is followed very strictly at BU, so even though it is possible that this is what caused the TM Interface to fail, chances are that it simply overheated in vacuum after being powered on for too long.

After some part searching, it was discovered that the four burned chips cost a grand total of $2.58. The entire project was cancelled because these inexpensive chips failed. However, because the TM Interface board is locked in place with Torr-seal and other protective chemicals, the board cannot be removed from the case and repaired without causing irreversible damage. Luckily, since WFF had long ago upgraded from the TD+ to the GP+ telemetry encoding system, it did not matter since the whole board needed to be redesigned and replaced to operate with the new system.

Since the spectrograph TM Interface was broken and the imager detector was not operable, the imager TM Interface replaced the spectrograph TM Interface. After this, data was coming through to the GSE computers and was being displayed properly. Now there were enough components of the payload working to do initial calibration testing.

The signal trace was nearly complete, and no problem had been found with the analog signals. After tracing all of the analog signals back to the umbilical that


Figure 4-65: Output from the spectrograph detector showing the 2536.5 Angstrom emission of Mercury, which falls very close to the Lyman-alpha emission in the field of view of the detector.

much further through air at atmospheric pressure than hydrogen Lyman-alpha light (1215.67 Å). In addition, the 106th order of this emission is very close to the 221st order of hydrogen Lyman-alpha on the field of view of the detector. The grating equation (Equation 2.28) shows that the value of the order times the wavelength $m\lambda$ is the same to within 4 decimal places, so the angular displacement between the emission lines on the detector is similarly small. Since the spectrograph box does not contain a second grating to block cross dispersion, both lines will appear on the display.

Figure 4-65 shows the output displayed on the GSE computer screen from the mercury lamp test at atmospheric pressure. The strong mercury emission line is visible, indicating that the telescope and spectrograph were still aligned since the last alignment.

Full payload testing to check the status of other systems and gain experience with the payload in the vacuum chamber was next. The payload was set onto a custom-built stand with Teflon-lined bottoms and pushed into the vacuum chamber. The stand was centered close to the balance point so that it would not require much force

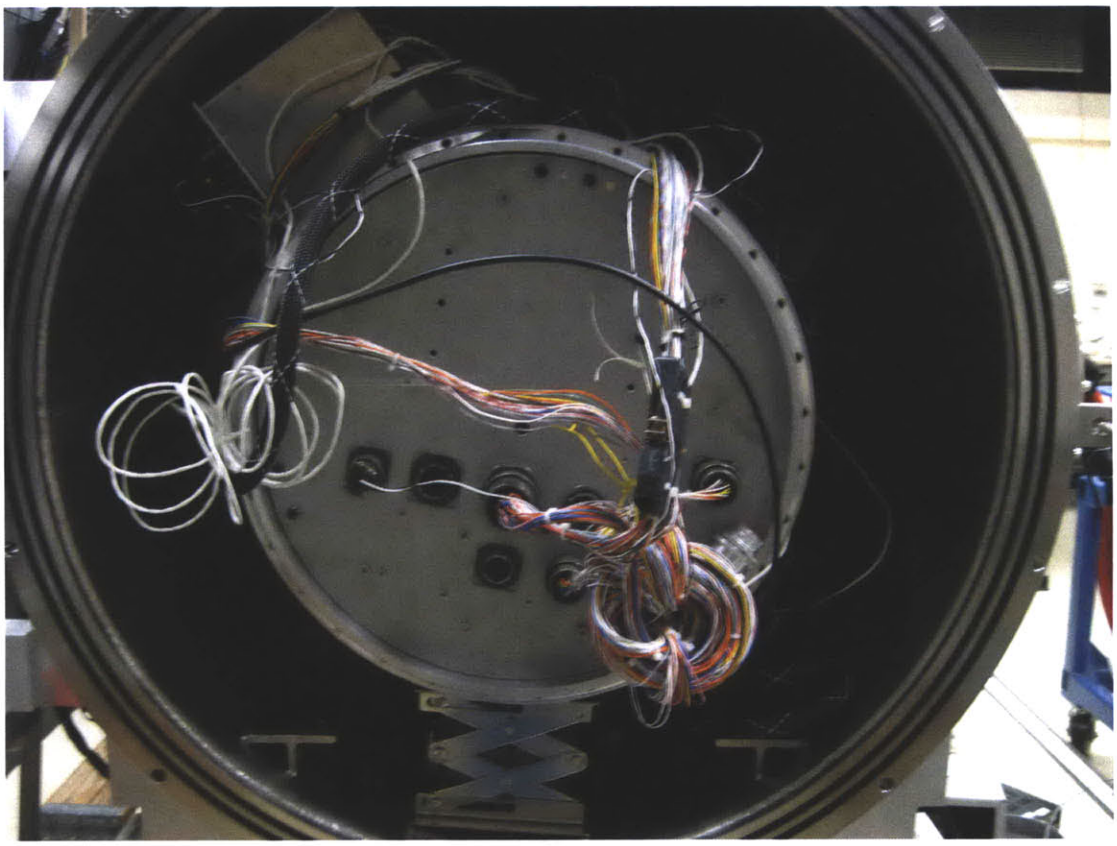

Figure 4-66: Full payload inside the VACTEF vacuum chamber ready for testing.

on the back of the payload to tip the telescope downward. An accordion table was placed beneath the end of the payload to carefully adjust the tilt of the telescope. The "spaghetti box" containing the WFF-93 PCM (see Section 4.2.6) was also placed in the vacuum chamber with the payload, and all the wiring to the outside was connected through a feedthrough plate near the door of the vacuum chamber. Figure 4-66 shows the testing setup as viewed from the primary vacuum chamber door.

The light source chamber was not configured with the collimating mirror setup to produce collimated light to properly test the optics, so a temporary setup was built to supply mechanically-collimated light into the chamber. At the end of the chamber where the light source is located, a flat plate with a small hole was designed, built, and installed so that only a small amount of light could exit the light source chamber. A stand was designed and built to mount existing pinholes that allowed even less light from the light source chamber through to the telescope. This stand was placed in

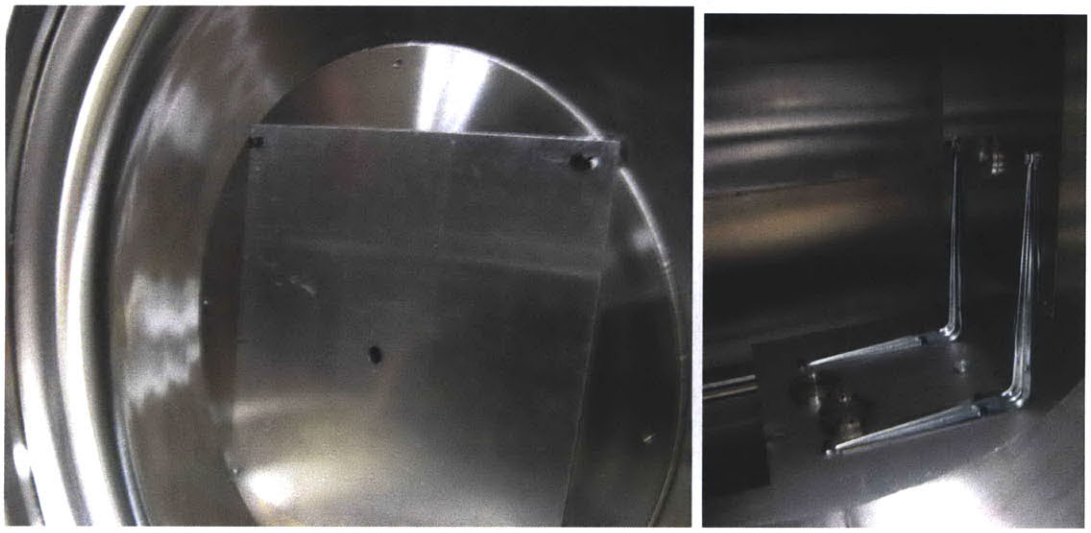

Figure 4-67: Plate with small hole at the back end of the VACTEF vacuum chamber (left), and a stand for mounting pinholes and blocking stray light from entering the telescope (right).

front of the telescope and effectively prevented stray light from entering the telescope while being nearly collimated at short distances. Figure 4-67 shows the plate at the back wall of the chamber and the stand to mount the existing pinholes in.

To ensure that this mechanical collimator setup was working and that no stray light was entering the system, it was tested with visible light at atmospheric pressure using the Xybion camera for feedback. The telescope was rotated from left to right inside the chamber. Each time the payload reached the limit of horizontal motion, the accordion table was raised higher so the telescope pointed lower. This back-and-forth, up-and-down maneuver covered the entire pointing range of the payload inside the vacuum chamber. The only time light was seen in the Xybion camera's field of view was when it was pointed directly at the pinhole on the stand set up near the center of the chamber, which meant that there was not a significant amount of stray light reflecting off the walls of the chamber and entering the telescope.

Figure 4-68 shows the video feed from the Xybion camera during this test. The view is partially obstructed because wires had to be rerouted through the large hole in the visible optics board so the spectrograph detector could be connected to the imager charge amps. This problem had not been considered before alignment but

Figure 4-68: Xybion camera output during testing at atmospheric pressure with visible light.

did not need to be fixed to show that the camera and mechanical collimator were working.

Finally, the full payload was tested at vacuum. The visible light source mounted in the light source chamber was replaced with a deuterium lamp. All systems were powered down while the pressure in the vacuum chamber descended below $10^{-6}$ Torr. When the deuterium lamp was turned on and the detectors were powered up, a Lyman-alpha emission was visible on the GSE computer screen. This also confirmed that the Xybion camera and the spectrograph box were in alignment relative to each other.

This vacuum test did not assess the performance on the SPACOM star tracker or the imager detector, nor did it allow the team to calculate a total efficiency of the optics and spectrograph detector. Once the payload was removed from the vacuum chamber, it was disassembled so each section could be calibrated. The telescope was relatively calibrated with a photomultiplier tube (PMT) in the VACTEF vacuum chamber before the rest of the optics and the PMT were absolutely calibrated with a photodiode in the VUCL.

### 4.5.2 Calibrating the Telescope

The reflectivity of the telescope was calibrated using the PMT. This instrument had not been absolutely calibrated yet, but all that was required to determine reflectivity of the telescope mirrors was a relative calibration. The telescope section and center plate were removed from the rest of the payload and placed in the vacuum chamber with no electronic equipment other than the PMT.

First, the deuterium lamp's output was monitored over time. The photomultiplier tube was set on the accordion stand behind the pinhole holder plate. Visible light was used to align the face of the PMT with the beam of light going through the pinhole. The visible light bulb was replaced with the deuterium lamp and the chamber was brought to vacuum. The deuterium lamp only can be turned on and off; its output is not adjustable but this test showed that the output varies by a few percent over the course of an hour. The results from this test are available in the attached Appendix DVD.

Next, the PMT was moved behind the telescope. Light now passed through the pinhole stand, through the telescope, and hit the PMT. Alignment was checked using visible light before mounting the deuterium lamp and bringing the entire system down to vacuum. After a test, the telescope was rotated 120 degrees so that one relative calibration was done in each of the three sections of the telescope.

The results show that the telescope is not uniformly reflective. One section had an overall reflectivity near 20%, which is much less than what the reflectivity would be with two aluminum mirrors with fresh magnesium fluoride coating. Another section had a total reflectivity near 12%, which is a 60% difference in total reflectivity. An efficiency degradation of this magnitude would cause the VeSpR mission to fail, and most likely does account for the unexpected loss of overall efficiency that JASpR experienced. In addition, the non-uniform degradation is consistent with the possibility that the mirrors were contaminated by oil from a diffusion pump used in the vacuum chamber at WFF that entered the vacuum system due to improper operation of the system. The full results from mirror testing are available in the attached Appendix

DVD.

### 4.5.3 Calibrating the Detectors and Windows

After initial full payload testing, the experiment team moved the structure of the payload from the basement VACTEF to the 5th floor VUCL. This was easier than separating out the control electronics in the GSE and taking only the detectors and optics that would be tested individually. Before testing in the vacuum chamber could begin, new test wiring harnesses had to be fabricated to connect all of the electronics as if they were assembled inside the payload, even though pieces of the system were inside the vacuum chamber.

Testing inside the vacuum chamber required that a detector subsystem (see Figure 4-29), its charge amps, its high voltage power supply, and the VIP high voltage power supply be inside the vacuum chamber. The charge amps must be inside the vacuum chamber with the detector because cables running from the detector to the charge amps must be shorter than 12 inches. If extended cables were used to route signals outside of the vacuum chamber, line losses would make the signal unreadable. The high voltage power supplies needed to be inside the chamber because there are no high voltage transmission lines through the electrical feedthrough plate (see Figure 4-57(left)) and because transmitting high voltage through a vacuum wall can be dangerous. Wiring harnesses were fabricated to connect the power inputs and data outputs on the payload outside the vacuum chamber to the electrical feedthrough plate and to connect the feedthrough plate to the payload components inside the vacuum chamber.

The VUCL has an absolutely calibrated photodiode that was used for absolute calibrations. The photodiode is attached to a lever that can be rotated from outside of the vacuum chamber so it can be moved into place to capture light from the monochromator and then moved out of the way so the test optics can be calibrated. There is also a mesh diffuser installed on the same lever that has a 1.33% throughput. In addition, the optics table inside the chamber can be translated and rotated to different positions while the chamber is at vacuum.

First, the PMT was absolutely calibrated with the photodiode. The PMT was set on the optics table inside the vacuum chamber and a green laser was used to align the front face with the beam path from the monochromator. The chamber was pumped down, the monochromator was powered on, and measurements from both the photodiode and the PMT were taken. At Lyman-alpha, the PMT has a quantum efficiency of 2.46%±0.16%.

Next, the spectrograph MCP detector was calibrated. The PMT and detector were set up side by side at the same height on the optics table. Both were aligned with the green laser. Once one was aligned, the table was moved by a known distance and the other was aligned. The table was moved back and forth several times to ensure the instruments were still aligned with the beam path even after the table moved (due to problems described in Section 4.3, this caused the longer delays in testing) Next, the chamber was sealed and brought down to vacuum and the monochromator and instruments were powered on. Measurements were taken with one instrument before the table was moved so that measurements could be taken with the other. At Lyman-alpha, the MCP detector has a quantum efficiency of 12.22%±0.46%. This is a weighted average of four measurements and the relative error is 3.80% (relative error is the standard deviation divided by the mean) [54].

To test the throughput efficiency of the magnesium fluoride windows of the detectors, the window on the imager detector was taken off the detector housing. A similar setup to the detector calibration was used for the window calibration except the second window was placed in front of the detector. At Lyman-alpha, the magnesium fluoride windows had a throughput efficiency of 26.0%±2.02%. This is a weighted average of two measurements and the relative error is 7.78%. The raw data for all the results discussed in this section are available in the attached Appendix DVD.

It would be easy to assume that because the window's throughput efficiency is roughly 25%, the quantum efficiency of the detector should be four times higher than reported. However, the magnesium fluoride windows should have much higher overall throughput efficiency, closer to 50%. At the time of testing, the team was unable to switch out the windows, recalibrate the detector with the imager window, and

calibrate the spectrograph detector's window to determine if both had both had been equally contaminated.

### 4.5.4 Calibrating the Spectrograph Box

The spectrograph is the primary scientific payload on VeSpR. Ensuring that it is aligned properly and has maximum throughput is vital to the success of the mission. Having an absolute calibration of the instrument is vital to proper data reduction. Too low of a throughput in the instrument would result in high error in the measurement of D/H in Venus' atmosphere (see Section 5.5).

The detector was mounted back on the spectrograph box and baffles were secured to both sides of the light entrance hole. The box was placed next to the PMT on the optics table. A green laser was used to align both instruments with the moving optics table. Alignment of the spectrograph box was especially difficult, not only because of the size of the box but also because of the precision required. The box was aligned so that the laser beam was centered at ends of both baffles. Because the echelle grating does not disperse green light into the same locations it disperses Lyman-alpha light, it was impossible to check that light would enter the detector with the laser beam.

The angle of the echelle grating was changed by small amounts using 0.5 mm shims stacked beneath the grating. Several tests were performed at different angles to ensure that the 221st order of Lyman-alpha was centered on the detector. This was painstakingly checked by bringing the chamber to vacuum, powering on the monochromator, testing the brightness measured on the PMT compared to the MCP detector, and bringing the whole system back up to air to try a different angle. Because of the system leaks, table jamming problems, and the accidental rotation of the screws the echelle grating rests on, this process took weeks of vacuum chamber time.

Once the team had centered the 221st order on the detector, the final calibration was made. At Lyman-alpha, the spectrograph box optics have a total reflective efficiency of 11.47%$\pm$0.52%. This is a weighted average of three measurements and the relative error is 4.52%. This is a good throughput; if the parabolic mirror has

a reflective efficiency of 75% at Lyman-alpha, this means the echelle grating has a grating efficiency near 20%. Both of those numbers are close to their maximum theoretical values.

After all the tests described in this section were completed, the mirrors were sent to Goddard Space Flight Center (GSFC) to be recoated. This process would bring the efficiencies back to their maximum theoretical efficiencies at Lyman-alpha, which is close to 80%. Once the mirrors were returned to the facilities at BU, they were left in the shipping containers to protect them from dust, humidity, and other airborne contaminants until all other design changes had been finished.

The echelle grating, the MCP detectors, and the magnesium fluoride detector windows stayed at BU. The windows were carefully cleaned with isopropanol and a Q-tip. There are multiple spare windows that were not tested, so when the payload is reassembled, all the windows will be tested and the two windows with the highest throughput will be used. Now that the operating performance of the payload had been characterized, it was time to determine what design aspects needed to change in order for the mission to be successful.

# Chapter 5

# Refurbishing The Venus Spectral Rocket

## 5.1 Tracking Cascading Design Changes

A system engineer does not specialize in designing or understanding every component in every subsystem on a spacecraft. A systems engineer specializes in understanding the relationships between subsystems, the design parameter space, and especially how changes in one subsystem can cascade and cause changes in other subsystems. In testing and preparing the VeSpR hardware for its first flight in over a decade, many design changes had to occur, which caused cascades of other changes. This section explains the top level design changes that caused many other subsystem changes throughout the entire payload and forced new subsystem requirements to be written and satisfied.

### 5.1.1 Changes Due to Upgrading the Detectors

Initial calibration testing (Section 4.5) showed that the Wedge-Strip-Zigzag (WSZ) detectors used in the JASpR payload since 1993 had low quantum efficiency compared to previous calibrations. This quantum efficiency would not be high enough to properly meet the primary science objective to measure the D/H ratio in the upper

atmosphere of Venus. The detectors needed to be refurbished to have better quantum efficiency or be replaced with new ones.

The VeSpR Principal Investigator has a long history of working with Sensor Sciences, a company based in Berkeley, California that developed and delivered the WSZ detectors in 1993 along with the charge amplifiers and analog-to-digital converters (ADC). However, because the WSZ detectors were so old, the equipment required to refurbish the detectors had not been used in a long time. Sensor Science engineers informed the payload team that refurbishing the old detectors would cost even more than purchasing new ones. In addition, Sensor Sciences expressed concern regarding the reliability of the detectors because they were so old.

Over the past two decades, ultraviolet detector technology has greatly improved. Sensor Sciences has been manufacturing a newer type of detector called the Cross-Delay Line (XDL) detector (see Section 2.7). New XDL detectors have higher quantum efficiency and are more reliable compared to refurbished WSZ detectors. In the end, the advantages of having the new XDL detectors outweighed the option to use the original WSZ detectors and pay the high cost of refurbishment.

However, this single top-level (Level 1) design change created the largest cascade of lower-level changes of all the other top-level design changes. As a result, VeSpR is significantly different than JASpR in terms of raw capability, internal part placement, and subsystems components. Figure 5-1 shows a summary of the cascade of design changes that occurred because of this single design change.

Since the XDL detectors have an entirely different output than the WSZ detectors, the Level 2 design changes involved new electronics for receiving data from the detectors. The original ADCs and charge amplifiers needed to be replaced with new ones. Since the XDL measures a time delay to get a reading of position, the electronics require a time-to-digital converter (TDC) instead of an ADC. The XDL also only requires one charge amplifier that can receive all of the necessary outputs of the detector compared to the three amplifiers needed for the three signals coming from the WSZ detector. All of these amplifiers also came from Sensor Sciences.

The XDL detectors also have different power requirements than the WSZ detec-

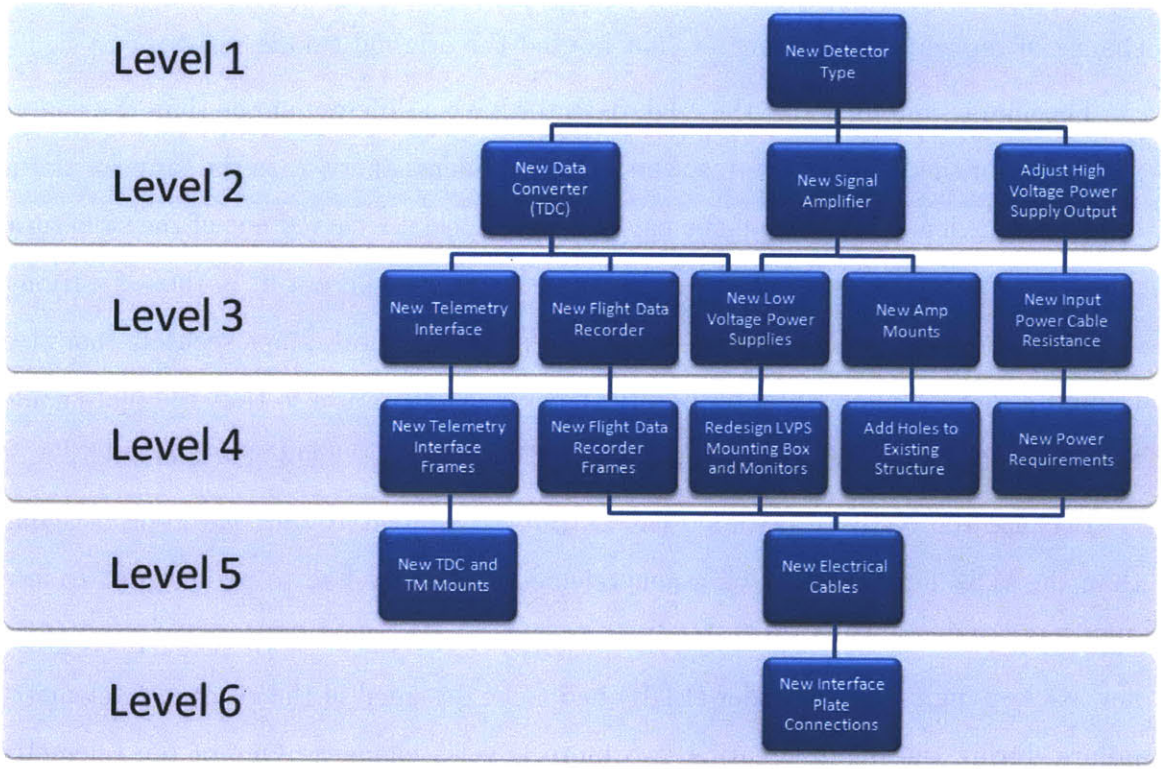


Figure 5-1: Hierarchy of design changes cascading down from the single decision to replace the detectors

tors. Both need high negative voltage to operate, but WSZ detectors required –4.5 kV whereas the XDL detectors require -5 kV. The SPACOM high voltage power supplies that were used to power the WSZ detectors had the capability to power the XDL detectors, but the output voltage needed to be changed. The SPACOM's high voltage output can be tuned by changing the programming resistor that connects into the 9-pin D-sub connector that also provides the input power. This required careful testing to ensure that the output was tuned to the proper voltage within an acceptable error level. The Level 2 change of tuning the voltage created a Level 3 change of replacing the connector that housed the original tuning resistor.

The charge amplifiers for the XDL detector have a different shape than the charge amplifiers for the WSZ detector, so the XDL amplifiers cannot go in the same locations inside the payload. Sections of the payload were specially carved out of the structural plates to support the original amps, but the new ones would not fit in those locations. A Level 3 design change was to redesign the plate that both amps securely mounted to, and a Level 4 change was to modify the existing structure so that the plate could be mounted so as to survive the stresses and vibrations of flight (Section 5.3.5).

Because the XDL detector's TDC outputs a completely different type of signal than the WSZ detector's ADC, a new telemetry interface had to be designed to feed digital signals into the WFF Pulse Code Modulator 93 (PCM-93) parallel port, and a new backup flight data recorder (FDR) had to be designed in the event of a telemetry failure during the flight, creating two more Level 3 changes. One of the telemetry interfaces and the original flight computer were non-functional already (Section 4.4), and since the final JASpR flight Wallops had upgraded to a new telemetry system entirely (see Section 5.1.4), so redesigning the interfaces and designing a new FDR was already being considered during early preparations for flight. Both of these components were developed by the electrical and computer engineers at the MIT Kavli Institute rather than the primary payload scientists and engineers working at Boston University.

The combination of new TDCs, new charge amplifiers, new TM interfaces, and new FDRs brought new power requirements that forced a Level 3 design change in the

low voltage power supply system that powered the original electronics. The original ADC and charge amplifiers required ±12 V and +5 V inputs, whereas the new TDCs and charge amplifiers required ±12 V and ±6 V. Since the new power supplies had to be integrated into the existing structure, this created Level 4 design changes in the low voltage power supply housing box (see Section 5.2.4).

New TM interface and FDR electronics required new frames to support these electronics, both of which were Level 4 changes. The FDR and its frame were designed to be mounted into the same location as the original flight computer (see Section 5.3.3), so no further changes were needed to secure it in the payload. The TM interfaces were designed to mount on the TDCs in the same way that the original TM interfaces mounted to the ADCs on the sides of the spectrograph box (see Section 5.3.4), but since the TDCs have different dimensions than the ADCs, a new mounting plate had to be designed, extending the cascading design change tree down to Level 5.

Another Level 5 design change was redesigning the wiring harnesses that connected and powered all of the electronic components. All of the new components required new cable pinouts, which needed careful planning and documentation so they could be manufactured by the MIT Kavli Institute electrical engineers. These cable changes then forced a Level 6 design change, a redesign of the Interface Plate to the Wallops Attitude Control System (ACS) (see Section 5.3.8).

Luckily, a major Level 2 design change was avoided by the fact that the payload team was able to reuse the original detector housings with the new detectors. If entirely new housings had to be built, there would have been a cascade of major changes to many elements of the payload, including the detector mounts in the optics, the vacuum ion pump (VIP) connections to the detector housings, and the VIP mounts in the payload. Because the same housings are being reused, the only other Level 2 change needed was to design a new back plate that seals the detector in the housing and has the proper terminals to send data to the charge amps (not shown in Figure 5-1).

### 5.1.2 Changes Due to Wallops ACS Rail Position

While the VeSpR/JASpR payload had not changed much in the previous decade, the ACS system developed by Wallops Flight Facility that was going to be used on the VeSpR flight certainly had. One of the seemingly minor changes was the position of the launch rail with respect to the payload. While the telescope section of the payload has rotational symmetry, the rest of the payload, specifically the star tracker and interface plate, does not. Because of the small rotation in the launch rail's location, design changes needed to occur for VeSpR to work with the new systems. In addition, the telemetry channels that originally read the analog output from the star tracker placed in the telescope are obsolete and are not in the current ACS platform Wallops uses.

When the payload team was informed of the rail position change relative to the original zero degree marker from JASpR flights, the payload was in many pieces and needed to be partially reassembled before the exact difference between the zero degree line as defined by Wallops and the zero degree line as defined by the coordinate system of the star tracker could be measured. After pouring through old photographs and struggling to reassemble sections without parts that were either being tested, being replaced, or being refurbished, the payload team was able to back out the difference between the zero degree lines and measure a 15-degree difference between the new rail placement and the spectrograph aperture.

Initially, the Wallops ACS engineers wanted to rotate the star tracker within the payload to match the orientation of the rail, but this option was very quickly ruled out by the Principal Investigator because the incredible precision needed and already achieved in the optics system would be costly and risky to modify. Instead, Wallops decided to change the hardware programming and manually convert X and Y coordinate positioning signals before streaming them through the telemetry. This way, there is no difference between the rail and the star tracker as seen during flight on the ground if a human operator needs to take control in the event of a positioning failure and has to rely on the payload's star tracker for guidance.

However, Wallops ACS engineers wanted the analog signals from the star tracker to be converted to RS-422 signals before exiting the payload, rather than finding another way to accept the analog signals in the ACS section. This required a Level 2 change to the payload to have an analog-to-RS-422 converter designed and installed inside the payload (Section 5.2.3). The RS-422 converter was also designed by the MIT Kavli Institute electrical and computer engineers. This new electronic board created Level 3 design changes, such as the need for a frame to mount the board in and revised power requirements, which then created Level 4 design changes in the wiring harnesses and the interface plate to connect with the Wallops ACS.

Another change in the Wallops ACS from the previous JASpR flight was that the standard bus for the ACS appears to have been rotated relative to its past position. The original placement of the connectors on the interface plate, shown in Figure 5-2, appears to have been influenced by the ACS architecture immediately forward of the interface plate. The connectors are all placed within the half-circle from ~300 degrees to ~120 degrees relative to the original zero degree rail marker (circled in red on Figure 5-2), meaning the inside components of the ACS came down closer to the payload on the other half of the interface plate.

However, after a Wallops mechanical engineer noted the rail placement as it was on JASpR, he informed the payload team that the connectors would have to move because the new ACS had components occupying space from 270 to 90 degrees relative to the rail, or Quadrants 1 and 2 of the coordinate frame shown in Figure 5-3. VeSpR connectors had to be moved to Quadrants 3 and 4 to avoid interfering with those systems, shown from a side view in Figure 5-4.

The unexpected ACS repositioning Level 1 change caused Level 2 changes of moving those connectors to the lower half of the coordinate frame. This was not easy, but a positioning frame was found that did not require any cables that were being reused or changed to be cut, lengthened, or altered in any way. Some of the other cables that were already being changed needed to be rerouted from their original positions, but luckily these Level 3 design changes were small and were made long before those cables were constructed.

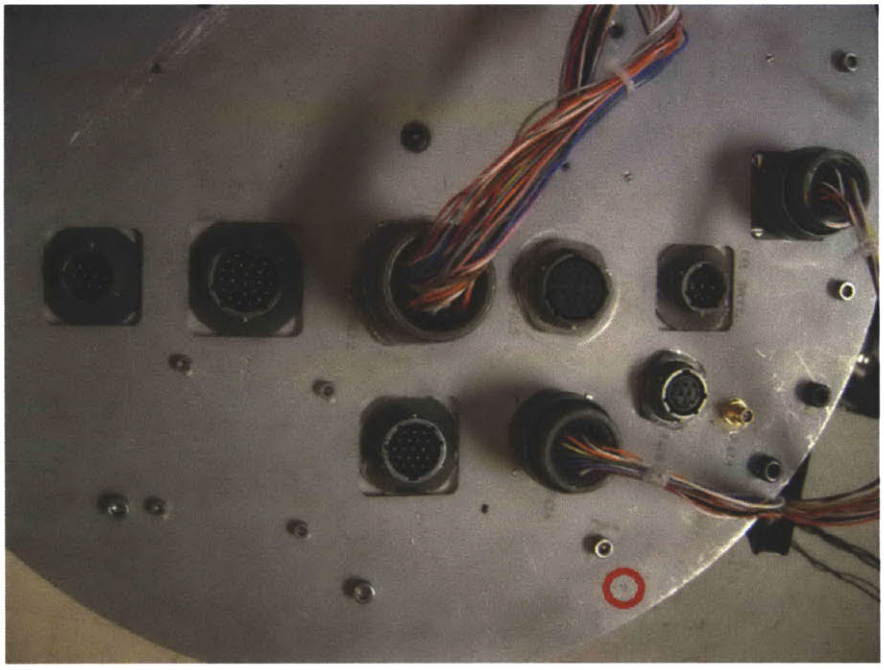

Figure 5-2: View of the JASpR Interface Plate looking toward the tail of the rocket. Previous zero degree line relative to rail marked with R (circled in red)

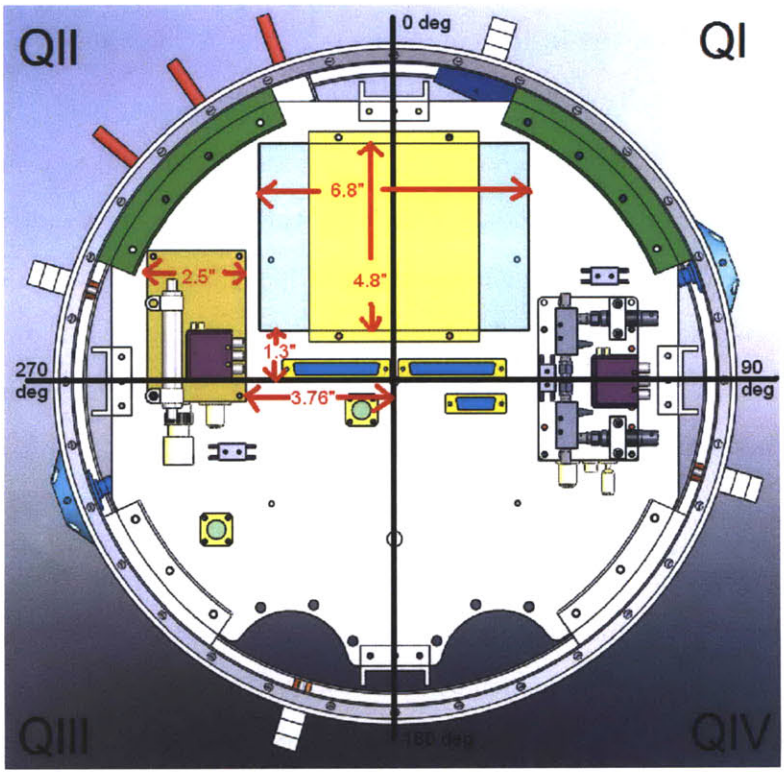


Figure 5-3: View of the ACS system looking toward the nosecone of the rocket

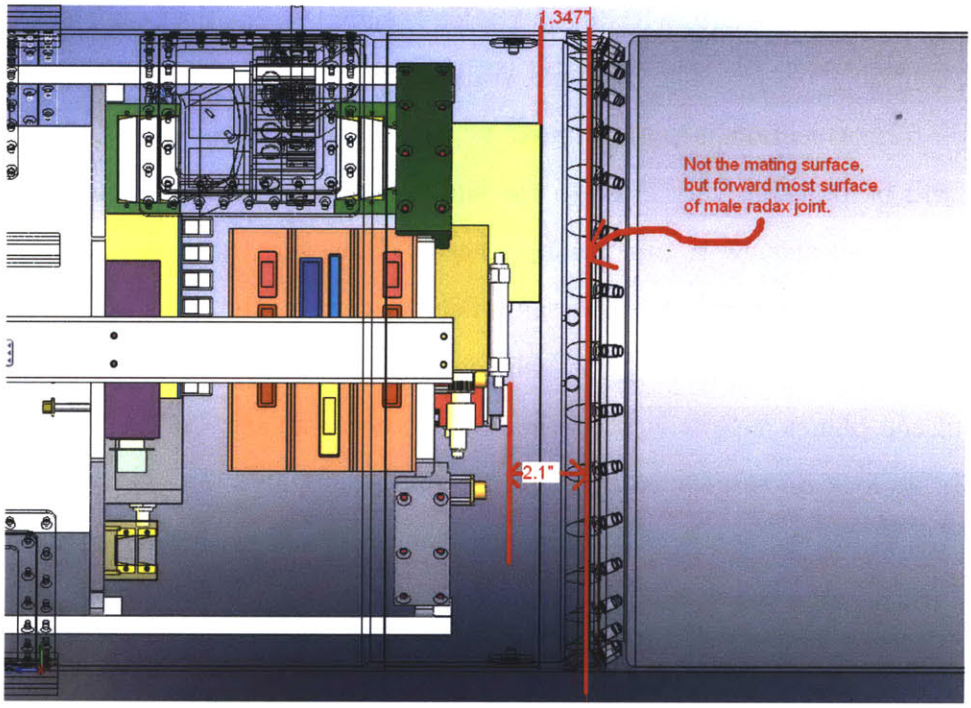


Figure 5-4: View of the ACS looking sideways

### 5.1.3 Changes Due to Increased Pointing Accuracy

One of the advantages that the VeSpR ACS has over earlier JASpR flights is improved pointing accuracy and control. The secondary mirror of the JASpR telescope was automatically controlled by tip/tilt servos that received error signals from the star tracker to compensate for pointing drift. Since the last JASpR flight, one of the two servos burned out and does not work. Even though it is possible to perform spectroscopy with only one servo, these moving parts and the feedback loop between the star tracker and the servos were potential failure modes that could cause a mission failure.

Since the previous JASpR flight, the ACS pointing accuracy has increased enough that pointing accuracy controlled by the secondary mirror is no longer needed. As a consequence, a Level 2 design change was to remove the active tip/tilt stage on the secondary mirror and replace it with a passive, securely aligned system, which removed this potentially hazardous failure mode (see Section 5.3.6).

The star tracker would continue to be used in operation; however, instead of being

transmitted to components within the payload, signals from the star tracker would only be sent to the ACS. The ST-5000 Wallops star tracker mounted in front of the telescope mirror section is programmed to specifically ignore planets, and because VeSpR will be pointing very close to the sunlit horizon, there might not be enough stars in the field of view to our pointing needs. However, the star tracker mounted inside the payload not only has the same field of view as the other scientific instruments, it can transmit signals that help determine exactly how far away from the center of the planet VeSpR is pointing. Using these signals, the ACS can properly maintain its lock on targets during the mission. Removing old, complex wiring and control boxes for the servos and replacing them with one wiring harness connected directly to the ACS was a welcome and easy Level 3 design change.

### 5.1.4 Changes Due to Updated Telemetry Requirements

Another overall improvement in the Wallops ACS since the last JASpR flight was an increase in the rate that data could be transmitted. When the telemetry interfaces were designed in the early 1990's, the telemetry rate was only 1 Mbps. As a consequence of that constraint, the telemetry interfaces were only designed to send out 2,500 counts of data per second. This was not considered a problem, especially considering that the WSZ detectors could only process approximately 5,000 counts per second before dead time effects started degrading quality of the data, and JASpR never viewed targets that produced much more than 1,500 counts per second anyway.

Today, the Wallops ACS uses a 10 Mbps data rate. This order of magnitude increase in available data to stream, compounded by the fact that the XDL detectors can handle 100,000 counts per second with 10% dead time, the payload team decided that the maximum detector count rate through the telemetry stream should be 25,000 counts per second. This order of magnitude increase was also justified by the mission's target selection; during the final seconds above 110 km, VeSpR will observe the sunlit Moon for an additional in-flight calibration, and the spectrograph detector may detect count rates as high as 20,000 counts per second.

The increased telemetry capabilities and the scientific desire to follow suit with

VeSpR's data stream drove the design requirements for the telemetry interface and FDR. While this may not be considered much of a cascade of design "changes" since the design had not been made, this case still illustrates an example of how customers' desires can form the top level requirements that drive the systems engineering approach to designing spacecraft.

### 5.1.5 Combined Changes and Other Design Constraints

Lower level design changes do not necessarily have only one parent Level 1 design change. Many of the lower level design changes had to be made while considering requirements driven from many higher level changes. For instance, the Interface Plate needed Level 6 changes because of the new detectors, but Wallops needed different connector types altogether for many of their connections, which were Level 1 changes. The low voltage power supply also had a variety of parent constraints at different levels.

Unfortunately, the entire scope of all the design changes required and the constraints between all of the working parts was not well known when the refurbishment work was beginning. While each design choice was made to optimize a given set of constraints for each part designed or modified, the global sum of all the design changes is suboptimal in terms of cost and overall performance because not all of the requirements were known well enough in advance. In some cases, constraints added at later times continued to cascade, causing some design decisions, which were thought to be optimal locally, to be suboptimal globally and perhaps more costly than necessary.

One of the major drivers for design constraints was the desire to reuse parts that had already flown on the rocket, not only to avoid further materials, machining, and design costs but also to keep the payload similar enough to its previous flight that it could still be considered a "reflight" to avoid having to get a complete payload certification again. However, in many instances, dropping a cheap constraint (like not reusing existing holes and drilling new ones) drove costs higher in the end. These cases as seen in hindsight will be discussed where appropriate in Sections 5.2 and 5.3.

## 5.2 Designing Payload Electrical Components

The science team at BU does not have the expertise to design all of the new electronic components, so engineers at the MIT Kavli Institute were contracted to design and build the electronics discussed in this section. The science team was primarily responsible for communicating needs, writing requirements, designing the structural housings (see Section 5.3), and testing the final products. The science team worked closely with the Kavli engineers to ensure that the final products were what the VeSpR payload needed.

Many of the requirements for these systems were driven by the characteristics of the new TDCs and charge amplifiers that operated with the new XDL MCP detectors. The old ADCs and charge amplifiers used +5 V and ±12 V power inputs, but the new TDCs and charge amplifiers require ±6 V and ±12 V. For this reason, many of the following components were designed to operate with a +6 V input power rather than the standard +5 V that most digital systems use.

### 5.2.1 Telemetry Interfaces

Since the original Spectrograph TM Interface had burned out, the science team knew from the beginning that the TM Interfaces needed to be redesigned. The new detector data outputs and new Wallops telemetry requirements also served as constraints in the design of the new interfaces. The primary function of the TM Interfaces is to take data from the TDCs, convert it to parallel data, and send it to the Telemetry Section and to the flight computer.

The TM Interface was designed to accept the three sets of signals coming from three 25-pin connectors on the TDC corresponding to X, Y, and P data. X and Y data correspond to the x- and y-positioning of photon counts on the detector while the P data corresponds to pulse height. The TM Interface outputs a 32-bit parallel word that is read by the Telemetry section. The data is also sent to the FDR as two 16-bit words that sync with the Telemetry section.

Due to ITAR restrictions, more details on the design and function of the TM

Interface are not being published here. More information on the output from the detectors is available on the attached Appendix DVD.

### 5.2.2 Flight Data Recorders

The original flight computer was inoperable from the beginning of the project and needed to be removed from the payload. Even though there is no need to control any systems using a flight computer in the payload, there was still a strong desire to have a backup computer recording data from the detectors.

Before choosing a design configuration, the flight data recorder (FDR) requirements were considered. The computer needed to boot up quickly because once power was turned on to the payload, data would start coming in from the detectors that needed to be recorded, and many computer modules have startup times that can be as long as 30 seconds. The computer also needed to be fast enough to record data at the maximum telemetry rate, 25 kHz, but most processors can handle that speed nowadays. The science team would need to retrieve the data easily while the science payload was connected to the rest of the payload during integration testing, so there needed to be a way to do this. The computer would also need to be small enough to fit inside the payload, preferably near the location of the old flight computer.

Initially, the team looked into the components needed to build a custom module, but the Kavli engineers found a commercially available module that would be able to satisfy all of our requirements. The TS-7400 is an embedded computer system module with a 200 MHz ARM9 processor that requires less than 3 Watts of power. It can write data to a standard-capacity SD card and uses USB or Ethernet cables to communicate with other computers. It only takes up 2.9 x 4.7 x 1.5 in of space within a frame and easily fits within the footprint of the old flight computer. Figure 5-5 shows a picture of the TS-7400 module taken from the product manual.

The module requires +5 V power to operate, but since the NLVPS was losing its +5 V power supply module, the Kavli engineers found a way to route power that is stepped down from +6 V to +5 V to the FDR through the TM Interface. This has the advantage that only one cable is needed to support the FDR that carries power

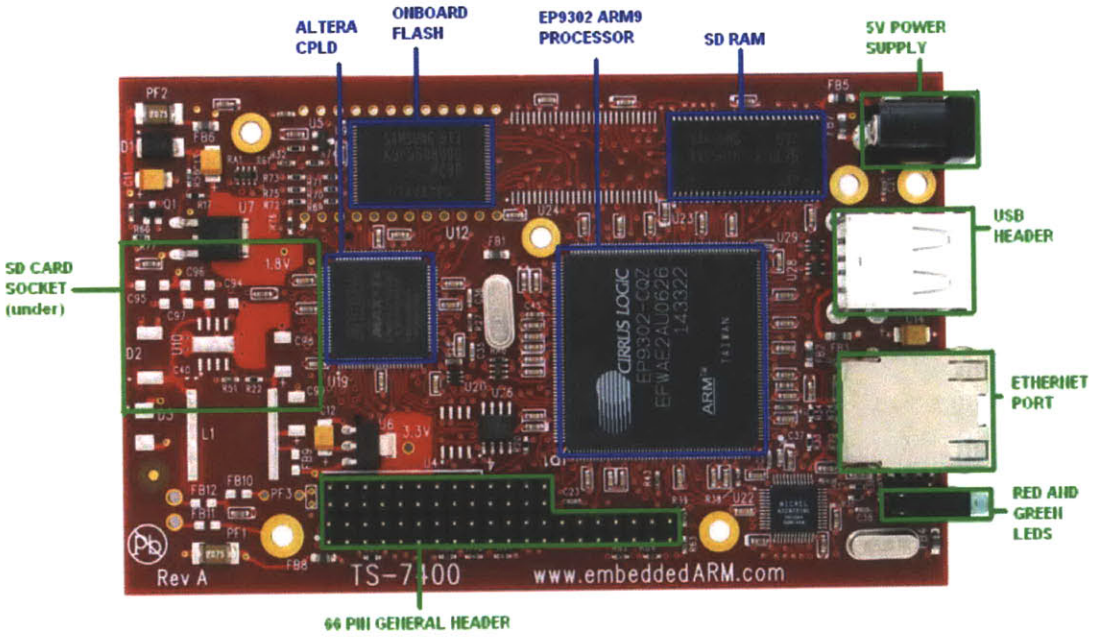


Figure 5-5: Layout of TS-7400 computer module taken from product manual.

and data. The other option would be to take +5 V power from the OLVPS, but that would require new cables routing through J20 and much more rewiring through the top section of the payload with no guarantee that the ±5 V supply module in the OLVPS can even output enough current since there are no longer any product specifications for that module.

During flight, the science payload will be powered on after the entire payload is above 110 km. The Kavli engineers have programmed the FDR to boot up once power is turned on. Boot up time is 1.1 seconds, and a new file is automatically written on the SD card and data from the TM Interface is written to that file after boot up. Since the telescope will not have even pointed to the first target, these 1.1 seconds of data that are lost is inconsequential to the mission outcome.

Because the FDR is only a backup data recording system, it is designed to be passive. It does not send any signals to the TM Interface; instead, the TM Interface automatically supplies data when the Telemetry Section signals the data on the TM Interface to be supplied. This way, a failure of the FDR does not affect the operation of the TM Interface, which is a vital component to the experiment.

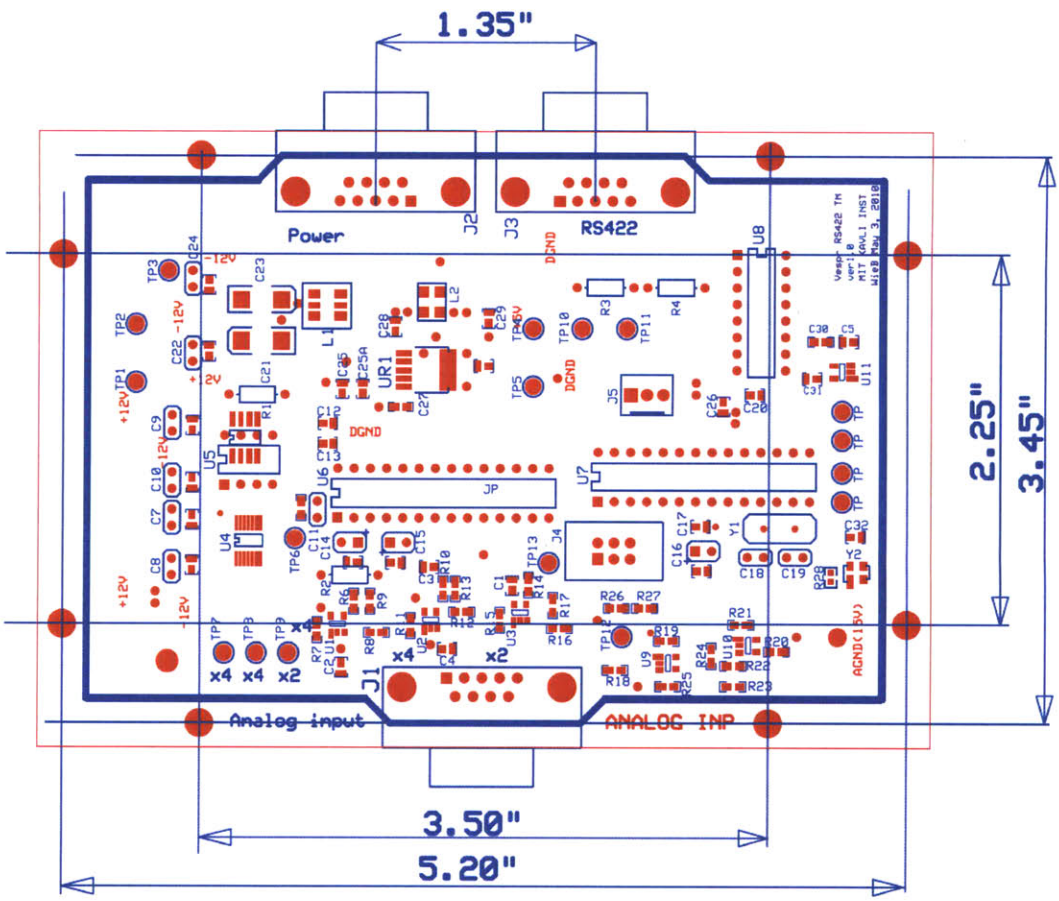


Figure 5-6: Silkscreen schematic of the RS-422 Converter.

### 5.2.3 RS-422 Converter

The SPACOM star tracker that was used to adjust the secondary mirror positioning uses a quadrant photodiode to measure the pointing accuracy of the telescope to within 1 arcsec. Since the pointing accuracy of the entire payload is within $\pm 1.5$ arcsec and the secondary mirror positioning system was being taken out, WFF wanted to use the error signals from this instrument as a backup to obtain an even finer pointing accuracy.

However, the SPACOM star tracker outputs analog signals and WFF wanted signals converted to a specific RS-422 format before they entered the telemetry stream. The MIT Kavli engineers designed the board that would perform this task. A silkscreen of the board is shown in Figure 5-6.

The board was designed to operate with +6V input power. The science team

Table 5.1: Power Requirements for new low voltage systems powered by the New Low Voltage Power Supply (NLVPS) box.

| Part | Qty | +6V(mA) | -6V(mA) | 6V(W) | +12V(mA) | -12V(mA) | 12V(W) |
|---|---|---|---|---|---|---|---|
| Amplifier | 2 | 0 | 0 | 0 | 146 | 36 | 2.73 |
| TDC | 2 | 430 | 730 | 6.96 | 47 | 83 | 1.56 |
| Interface | 2 | 0.25 | 0 | 1 | 0 | 0 | 0 |
| FDR | 2 | 500 | 0 | 3 | 0 | 0 | 0 |
| RS-422 | 1 | 0.25 | 0 | 1 | 0 | 0 | 0 |
| **Total** | | 1860.75 | 1460 | **22.92** | 386 | 238 | **8.58** |

worked closely with WFF engineers and the Kavli engineers to ensure that the signals coming out of the board were to specification. However, because of ITAR restrictions, the nature of this output signal will not be discussed.

### 5.2.4 New Low Voltage Power Supply Box

Since most of the electronics that the New Low Voltage Power Supply (NLVPS) supplied power to were replaced, it had to be redesigned to satisfy the power requirements of the new electronics, shown in Table 5.1. Redesigning this component was more of a systems engineering challenge than an electrical engineering challenge because of all the requirements this component needs to satisfy. Not only must it be able to produce the correct voltages and supply the necessary power, but careful planning was needed to ensure that the wiring required to supply all of these components was possible and would not interfere with any other payload components.

The EMI filter module and the $\pm 12$ V power supply module, both manufactured by Interpoint, were both still in working condition and were able to be reused. Interpoint only had one module that was capable of producing $\pm 6$ V, and its maximum power output of 120 W greatly exceeds the requirements of the system. However, the module is spaceflight qualified, and the team was not able to find a similar component from a competing manufacturer, so the Interpoint module was used in the design.

The box that housed the power supply modules needed to be modified because the $\pm 6$ V supply was not the same size as the other modules. In addition, there needed to be space for a new 9-pin connector to power the RS-422 converter. Appropriate

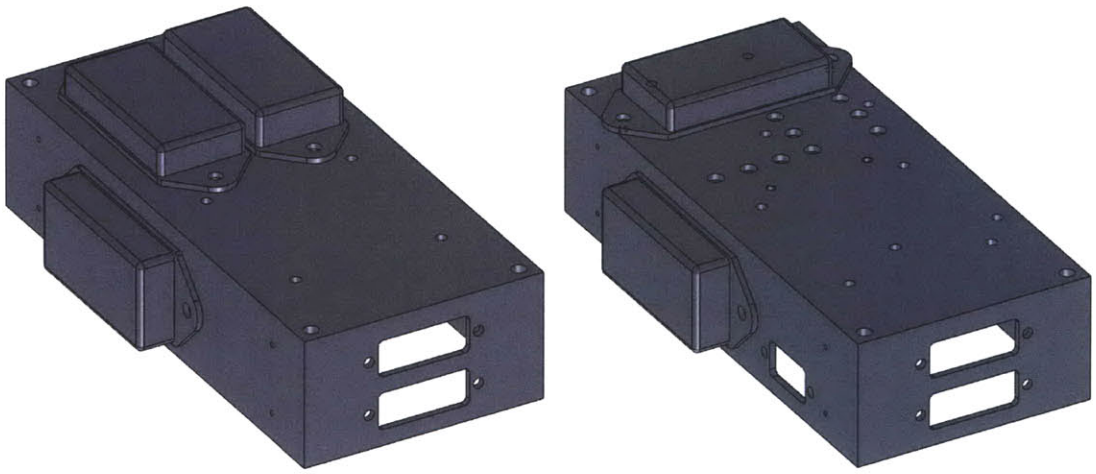

Figure 5-7: Comparison between the housing of the original NLVPS (left) and the modified version (right). The ±6 V power supply module is mounted underneath the top face on the modified version.

holes were drilled so that the EMI filter could be rotated 90 degrees, making enough room on the top to put the ±6 V power supply module. The ±12 V module remained in the same place on the side of the box, and the 9-pin connector that would supply the RS-422 converter was placed on the same side because one of the tripod rails of the structure was blocking the other side. Figure 5-7 shows a comparison between the original and modified NLVPS housing solid models.

In addition, new analog monitors were built inside the housing that output the current being drawn by the power supplies. These monitors are linked to the same pins on the input cable so none of the input wiring needs to be replaced nor does any of the analog telemetry wiring need to be revised. Figure 5-8 shows a map of how power from the NLVPS is distributed to electronics within the payload.

### 5.2.5 Wiring Harnesses

Not only were many electronics systems being replaced, some of the connectors within the payload had been damaged during initial testing, so new wiring harnesses were needed throughout the payload. The payload team worked closely with an electrician from the Kavli Institute to ensure that the new wiring harnesses for all the systems had the correct pinouts, were long enough to go between systems, and were tied down

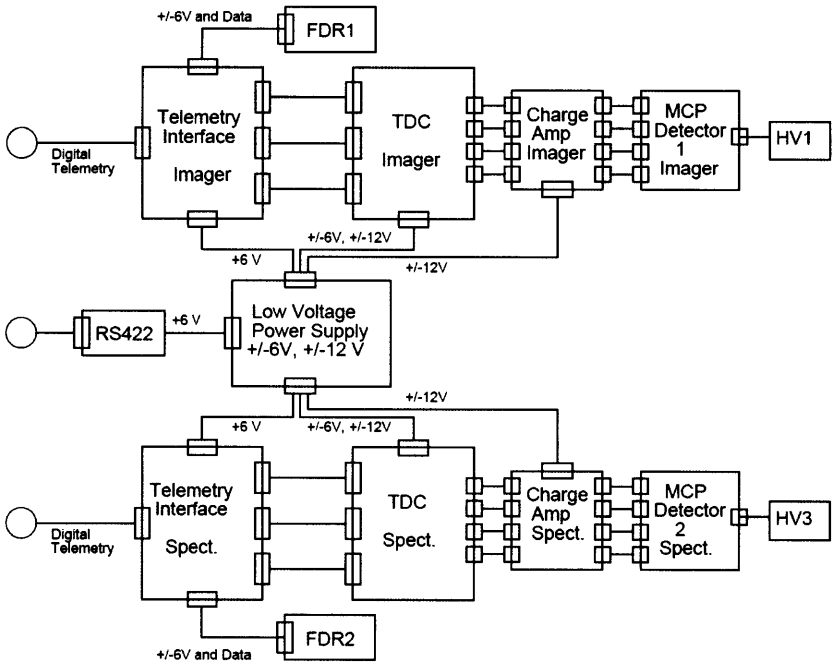


Figure 5-8: Updated New Low Voltage Power Supply (NLVPS) schematic.

tightly enough to prevent vibration stress from damaging the connectors. Although the team fabricated all of their own harnesses for laboratory testing, only the Kavli electrician fabricated harnesses that went into the payload.

After the initial autopsy of the payload, the wiring documentation for the entire payload was digitized and put into a format that the team could edit. As changes were being made throughout the system, pages in the wiring notebook were updated. The Interface Plate's interface control document was also updated as decisions were finalized, and the electrical engineers at WFF were questioned before changes were made to the document to ensure systems would still be compatible and given the revised document after the changes were documented. Due to ITAR restrictions, the wiring notebook cannot be made publicly available.

## 5.3 Designing Payload Mechanical Components

Many of the design changes made to VeSpR during the process of preparing the payload for re-flight were intended to keep the payload as similar to the 13.174 JASpR

V flight as possible to avoid full-payload structural vibration testing during payload integration. Structural vibration testing puts more vibration stress on the payload than the actual flight does, and the Principal Investigator feared that full payload vibration testing could irreparably and needlessly damage the optics.

Great strides were made to position new components in nearly the same locations as they originally were. All new components will undergo individual part vibration testing to ensure they are capable of surviving the launch loads, but with luck the entire payload will not need to be structurally tested.

Since the payload and its new components are being tested in vacuum chambers, many design considerations are shared throughout the payload and its new components. One of the major challenges was ensuring that no threaded hole was unvented or otherwise blocked off. This can create a pocket of air that slowly leaks out into the vacuum chamber. These "virtual leaks" keep the air pressure inside the vacuum chamber higher than desired, which makes pumping down the pressure to adequate levels for ultraviolet testing take much more time. It can also lead to absorption of ultraviolet light in flight. Avoiding virtual leaks was a major challenge in the design of the TM, RS-422, and FDR frames.

In addition, many other subtle design constraints are reflected throughout the design of the following components. For instance, all inner corners of spaces such as D-subminiature connector holes had to be rounded; it is impossible to cut a square hole with a round milling bit. Threaded holes were checked to make sure there are at least four threads per screw. Counter-sinks have tolerances specified to make sure the screw heads are below the surface they share with the part. All mechanical design work was done in SolidWorks. The Boston University Scientific Instruments Facility was contracted to perform most of the machining work, with minor machining done by the experiment team at the MIT Aeronautics and Astronautics machine shop.

### 5.3.1 Telemetry Interface Frames

The frames to house the new telemetry interfaces were the first components to be designed and machined. The JASpR TM interfaces and ADCs were identical in size

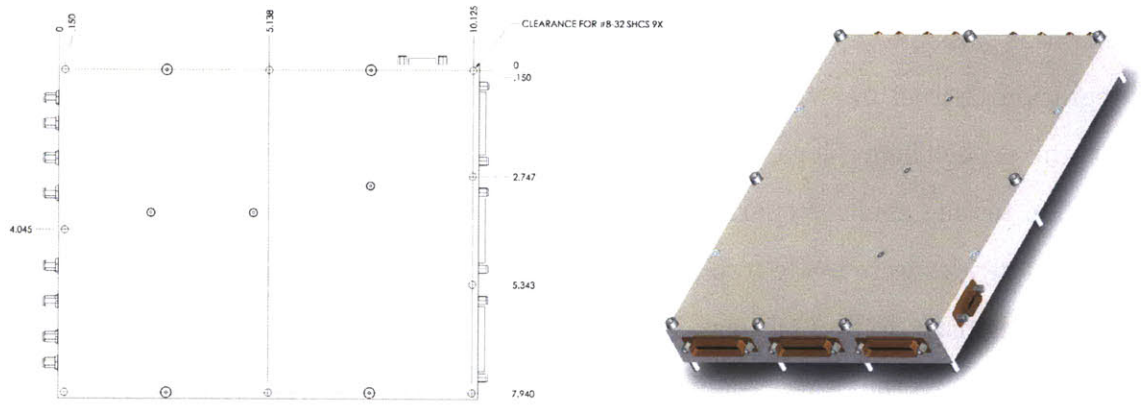


Figure 5-9: Machinist drawing (left) and solid model (right) of the TDC

and mounted on the broad sides of the spectrograph box. This space was adequate to mount the new TDCs and TM interfaces. The TDCs are slightly bigger than the ADCs (10.275 x 8.090 x 1.073 in), and the TM interface was expected not to need nearly as much space, so the TM interface board was sized so it would fit in a frame with a footprint half the size of the TDC. The TM interface and TDC would share the same mounting holes, the three on the bottom near the charge amplifier inputs and the two in the center. The TDC inputs would face the telescope section, which is aft to the whole rocket, and the outputs would face the ACS and nosecone. Figure 5-9 shows the machinist drawing and solid model of the TDC.

The electrical engineers at the Kavli institute worked closely with the payload team to ensure the TM interface frame would be properly designed. There was a strong desire to make the frame out of four sides that connected together rather than carving the frames out of a solid piece of aluminum. In addition to saving material and machining time, the four sided- box design allowed the Kavli engineers easy access to the bottom of the board during testing without needing to remove the board from the frame. No bottom was necessary since it would mount to the TDC lid.

The Kavli engineers showed the payload team some examples of other boards and how a frame of this type could be designed. Important aspects were the inside lip size and depth where the computer board would be mounted and the clearance between the lip and where the connectors would be placed. However, these boards had unusual and undesirable mounting brackets on the outside and did not properly vent all the

threaded holes to prevent virtual leaks. The payload team could not simply copy these frames, but they did use those frames as a basis for designing a better solution.

After four iterations, the experiment team had a design that properly vented the threaded holes that connected the four sides together and the holes that the lid mounted to. It also had proper spacing between the top of the mounting area and the connector holes and proper mounting holes to mount to the top of the TDC. An initial fear was that because the TDC was wider than the old ADC, there would not be enough room inside the payload for the new TM interface to be as tall as the original. It was later shown that there was still more than an inch of clearance even after the TM interface was installed, but because of this concern the height of the TM interface was constrained to 0.75 inches instead of 1 inch.

Figure 5-10 show the four sides of the TM interface. Side #1 faces aft and has no connectors. Side #2 has clearance for the 9-pin D-subminiature connector that provides power input. Side #3 faces the nosecone and has two 37-pin D-subminiature connectors, one for input from the TDC and out for output to the Wallops telemetry. Side #4 has a 35-pin D-subminiature connector for output to the FDR.

Figure 5-11 shows the four sides of the TM interface frame assembled (without the lid). One problem with the final design and fabrication of the TM interface frames was that the D-subminiature connector holes were made too thin. The Kavli engineers needed to file the holes by a few thousandths of an inch to make them wide enough to fit the male connectors in place, but the parts did not need to go back to the machinists for rework or be fabricated all over again. This problem was fixed in future component designs by using a proper sizing chart rather than measurements of the D-subminiature connectors in the laboratory. Figure 5-12 shows the finished TM interface mounted in the frame with the frame mounted on the TDC.

### 5.3.2 RS-422 Converter Frame

The RS-422 Converter and FDR were designed to stack on top of each other and use the same mounting footprint as the original flight computer. One of the initial concerns with this configuration was that the overall height of the two FDRs and

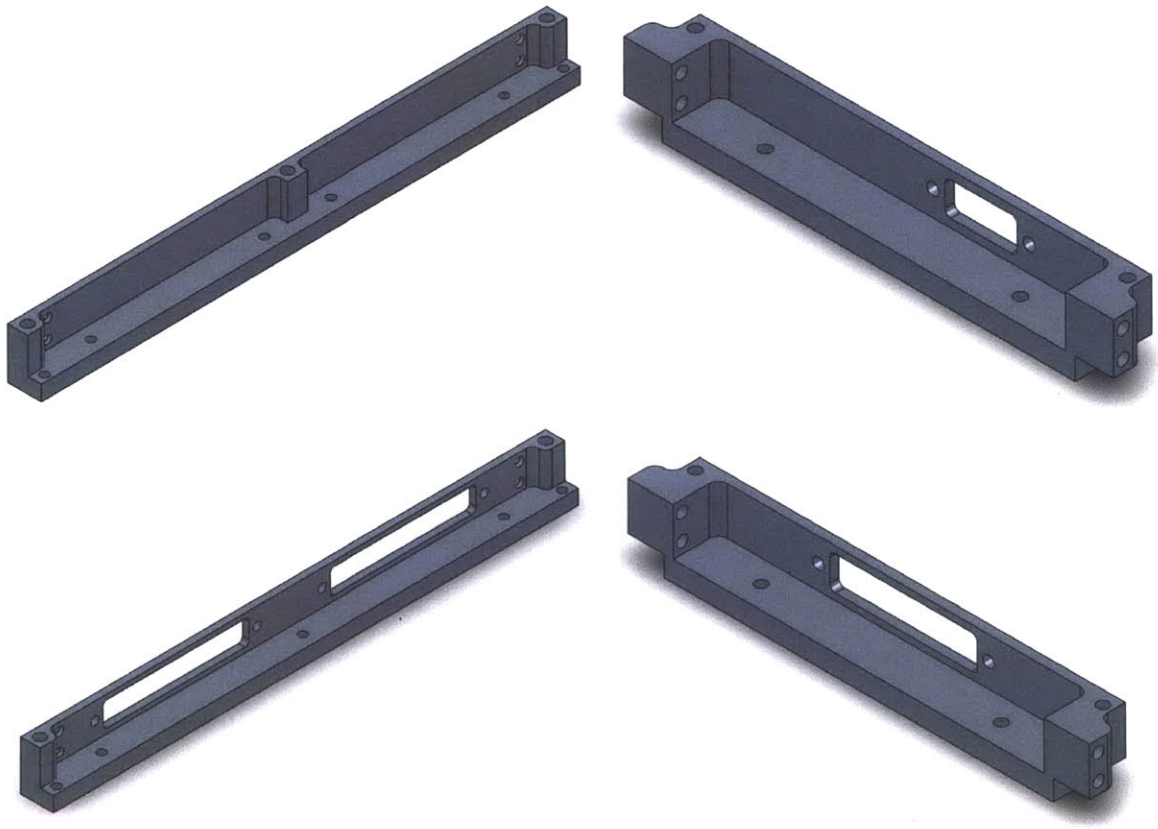

Figure 5-10: Sides of the TM Interface.

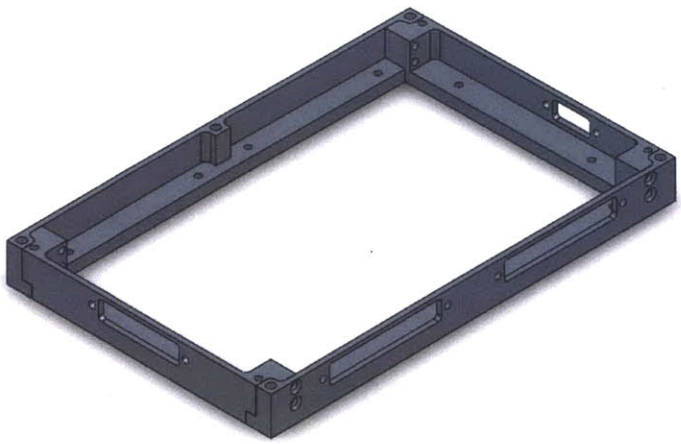

Figure 5-11: All four sides of the TM Interface frame.

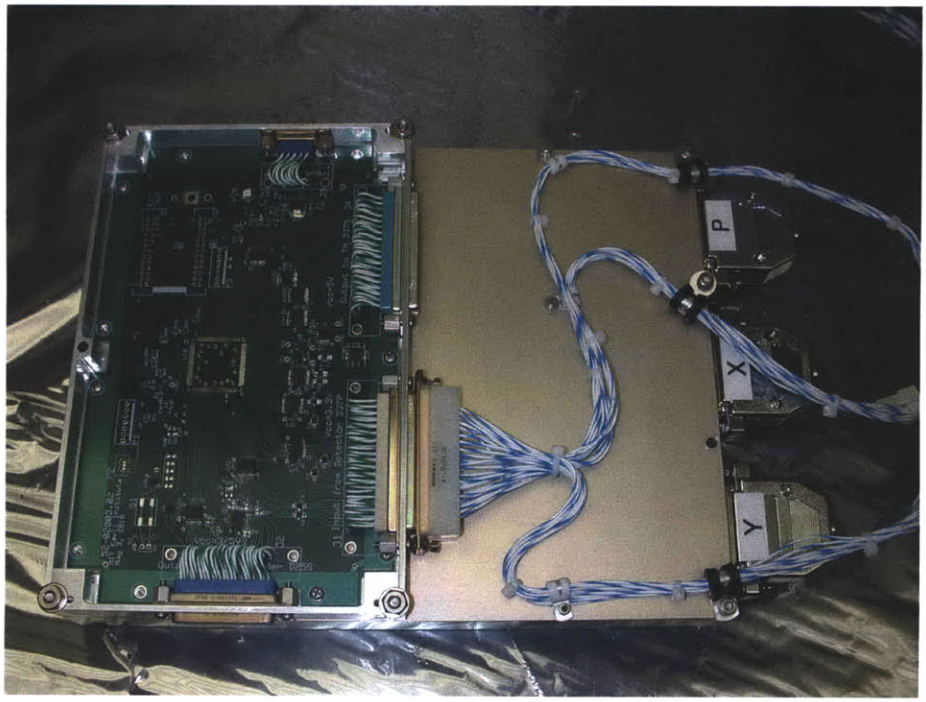


Figure 5-12: TM Interface frame mounted to TDC.

the RS-422 Converter would be too tall. The top of the boxes would start to put pressure on the wiring harnesses mounted to the Semicircular Plate, and if that was raised higher (closer to the Interface Plate) there may not have been enough room for the primary low voltage power supply box or the connectors on the interface plate. However, once the final designs were finished, this concern was ruled out.

While the TM interface frame satisfied all the requirements for its design when it was fabricated, the Kavli engineers were dissatisfied by the fact that the mounting footprint for the board inside the frame was not a perfect rectangle. The frame required sections of the board to be cut out. This is undesirable because there are many thin layers of conductive material sandwiched between the insulating structures, and even careful cuts can cause the conductive layers to short out and damage hardware components. Because of the desire to have a rectangular board, the TM interface frames could not simply be resized to fit the frame for the RS-422 converter.

Two more design iterations of the existing TM interface frame design produced this design for the RS-422 converter. The holes that Sides 2 and 4 mount to are vented by the holes that mount the frame to the payload structure, so virtual leaks are not

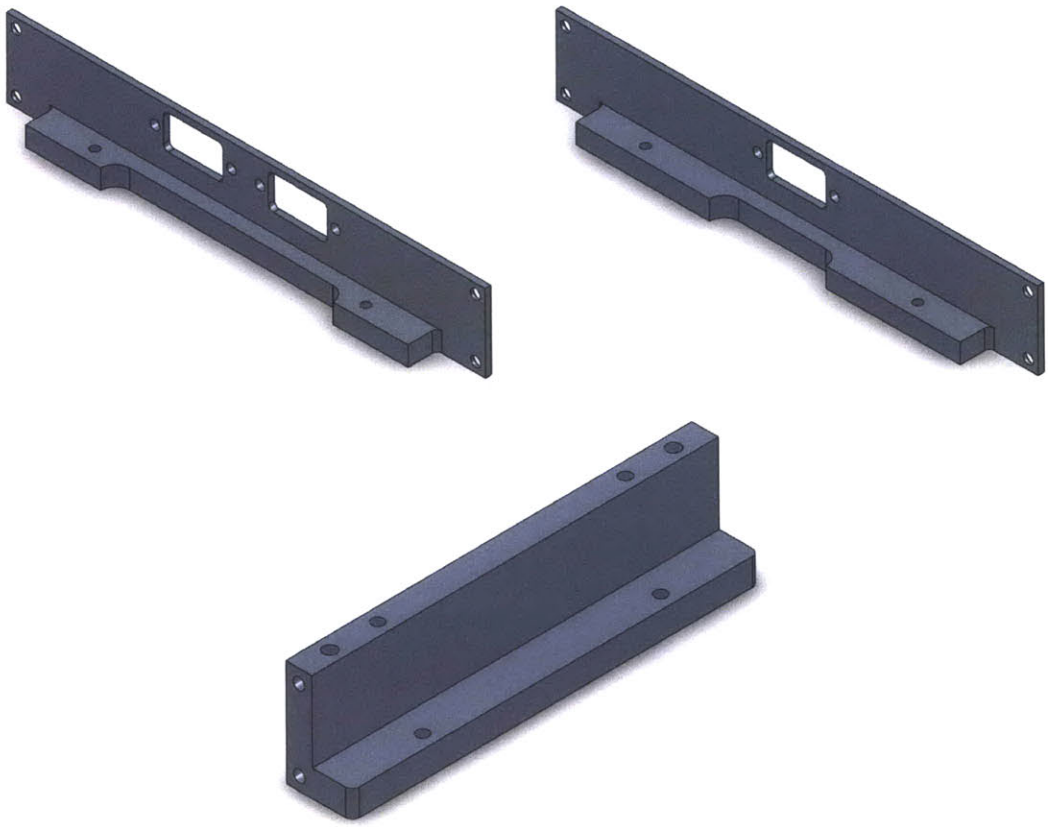

Figure 5-13: Sides of the RS-422 Converter. (Top left) Side #2. (Top Right) Side #4. (Bottom) Sides #1 and #3.

present. This solution could have avoided the unusual computer board footprint in the TM interface boards, but it was too late to incorporate this design configuration by this point.

Figure 5-13 shows the sides of the RS-422 frame. Sides #1 and #3 are identical and have no connectors. Side #2 has two 9-pin D-subminiature connectors, one for power input and one for RS-422 output. Side #4 has one 9-pin D-subminiature connector for analog input from the star tracker.

Figure 5-14 shows the four sides of the RS-422 converter assembled (without the lid). After the frame was machined and the computer board was fabricated, the Kavli engineers noticed that the lip on Sides #2 and #4 came very close to some of the conducting lines on the computer board beneath the D-subminiature connectors, and if any contact was made it would cause a short. Had the Kavli engineers provided

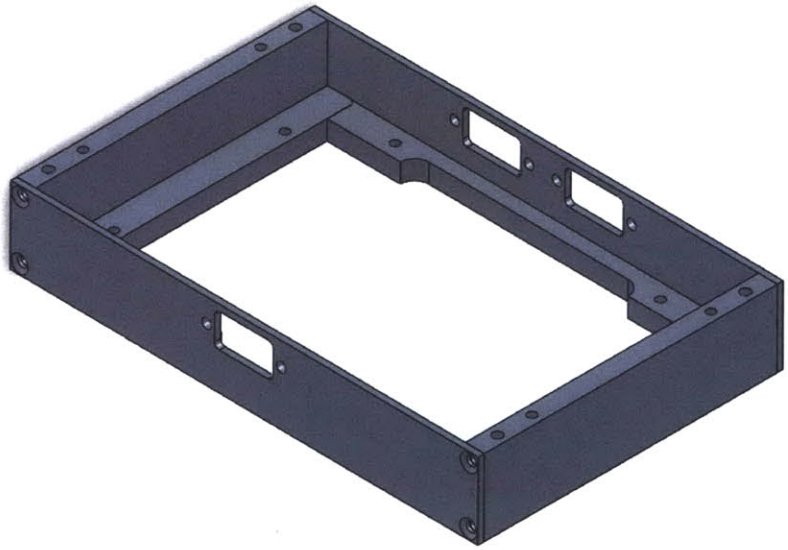

Figure 5-14: All four sides of the RS-422 Converter frame.

the bottom view of the board layout in addition to the top view, this would not have happened. Thankfully, material could be removed from the lips without requiring entirely new parts to be machined. Figure 5-15 shows the RS-422 board mounted in its frame.

### 5.3.3 FDR Frames

The flight data recorders were off-the-shelf TS-7400 cards from Technologic Systems. As a result, the cost was significantly less than the TM interfaces and the RS-422 converter, but there was no interface control document that both the payload team and the Kavli engineers wrote. Since it did not need to be tested like the other two boards, the Kavli engineers did not require the frame to be bottomless; because the computer board does not mount from the edges, a bottom was needed. The computer is small enough that a frame could be built around it that fits the footprint of the original flight computer. Figure 5-16 shows the mechanical layout of the TS-7400 board.

In addition to the board mounting pattern on the frame and the frame mounting pattern on the payload, there were other design constraints. The Kavli engineers

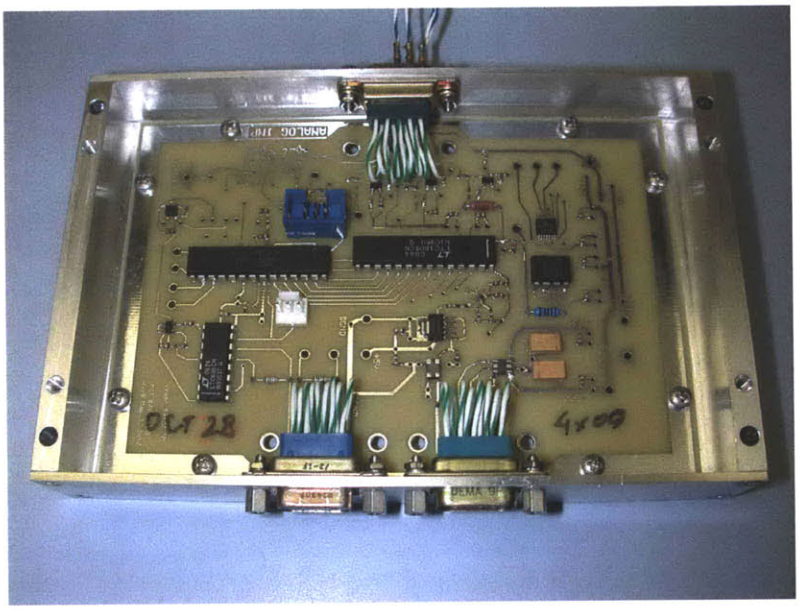

Figure 5-15: RS-422 Converter mounted in its frame.

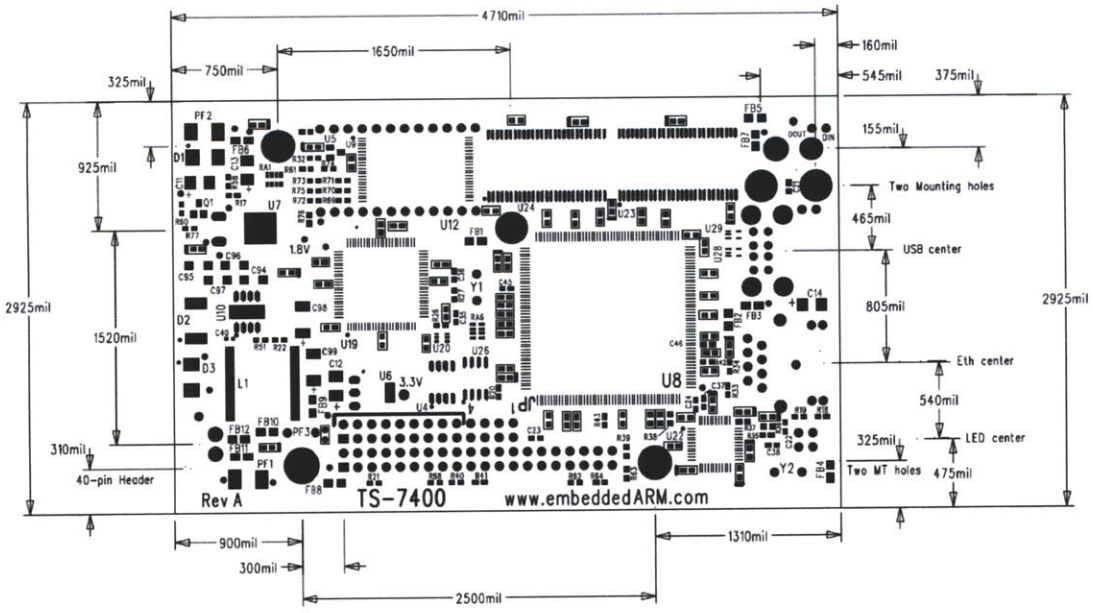


Figure 5-16: TS-7400 embedded computer module board mechanical layout.

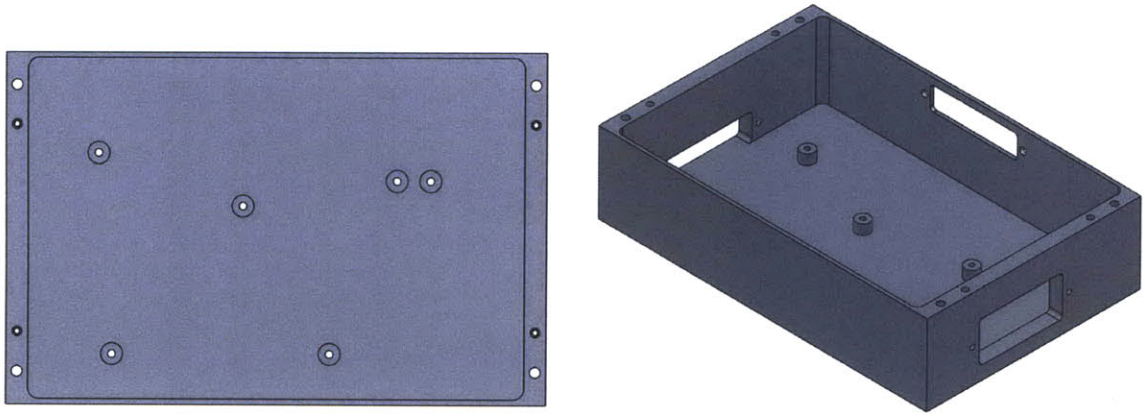

Figure 5-17: Overhead and isometric views of the FDR frame.

needed to build a small programming card to program and communicate with the FDR. This card connects to the top of the TS-7400 and added a half inch to the height of the walls of the frame. The frame needed two access ports, one to retrieve the SD memory card and one to connect to the computer via Ethernet or USB cables. The memory card port needed to be closer to the wall of the frame to make card retrieval easier, so that side was pushed closer. One 25-pin D-subminiature connector is all that is needed power and data input from the TM interface.

Figure 5-17 shows overhead and isometric views of the solid model. Holes for the lid are identical to the holes for the RS-422 converter because the stacking order was not decided before the parts were machined. The lid can be secured to all three parts if the stacking order needs to change at any time, but for now the RS-422 Converter rests on top of the two FDR frames. Figure 5-18 shows the FDR mounted in its frame.

### 5.3.4 TDC and TM Interface Mounts

The TM interfaces and TDCs have different mounting footprints than their predecessors, so new mounts needed to be designed. One side is simply a flat panel, and the layout was very easy. Figure 5-19 shows the first TDC and TM interface mount.

The other interface mount is split into two pieces. This is because a spectrograph box vent gets in the way. As a result, extra care was needed to ensure that the spacing

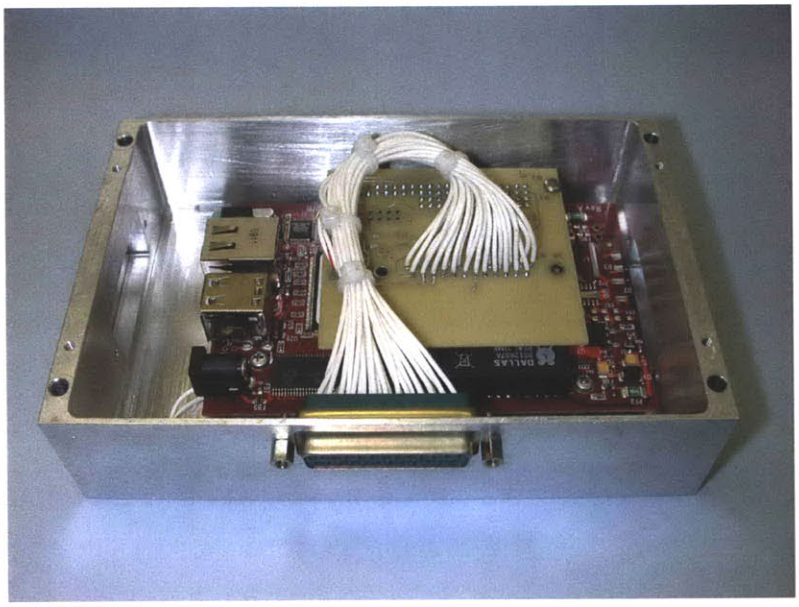

Figure 5-18: FDR mounted in its frame.

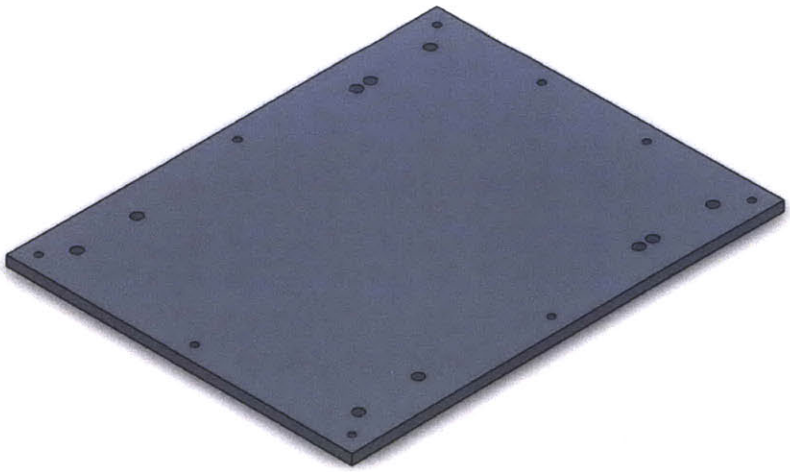

Figure 5-19: TDC and TM Interface Mount #1.

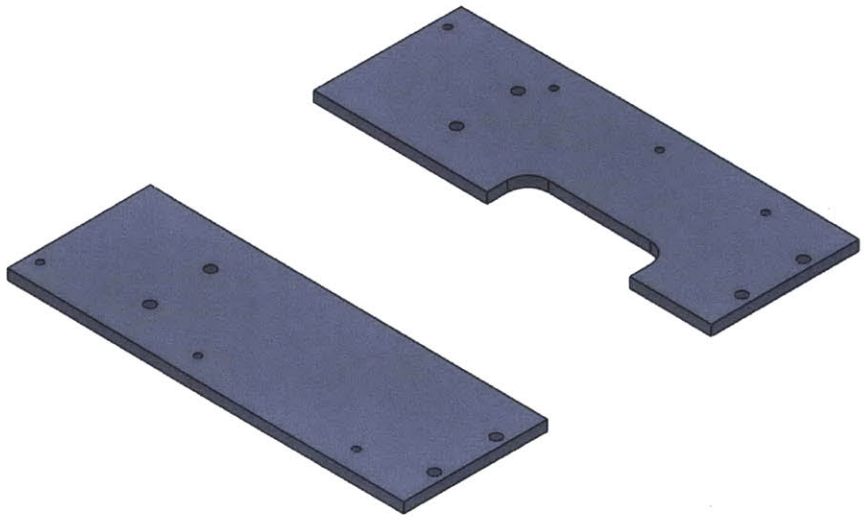

Figure 5-20: TDC and TM Interface Mount #2.

of the holes was properly measured and tolerances were adequate. Figure 5-20 shows the two pieces of the second mount.

Due to work order backup at the BU Scientific Instruments Facility over the summer of 2010, prototypes of the mounts were fabricated from scrap material at the MIT Aeronautics and Astronautics machine shop. These were needed quickly so the Kavli technicians could start planning the wire harness production and get estimates on the harness lengths.

When the payload was partially reassembled for these estimates, an error was found. Because the TDC was wider than the ADC, the TM interface was not able to mount in exactly the same locations because one of the three longirons in the structure was too close. The TDCs needed to be mounted further from the longiron, so the hole positions on the TDC mounts were shifted accordingly. While the prototype of Mount #1 will still be used, Mount #2 was redesigned and machined by the Scientific Instruments Facility later. Figure 5-21 shows the TDCs and TM interface mounts

### 5.3.5 Detector Amp Mount

The old WSZ detectors required three charge amplifiers each, but the new XDL detectors only require one each. However, the XDL detector's charge amplifiers are

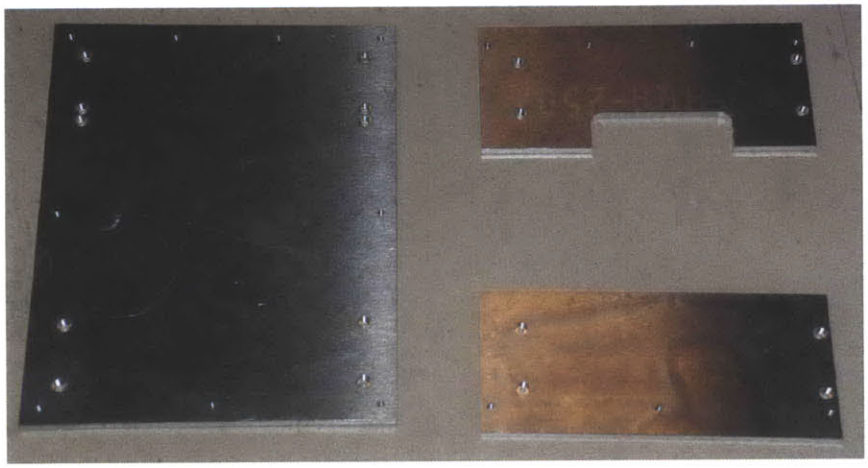

Figure 5-21: TDC and TM Interface mounts.

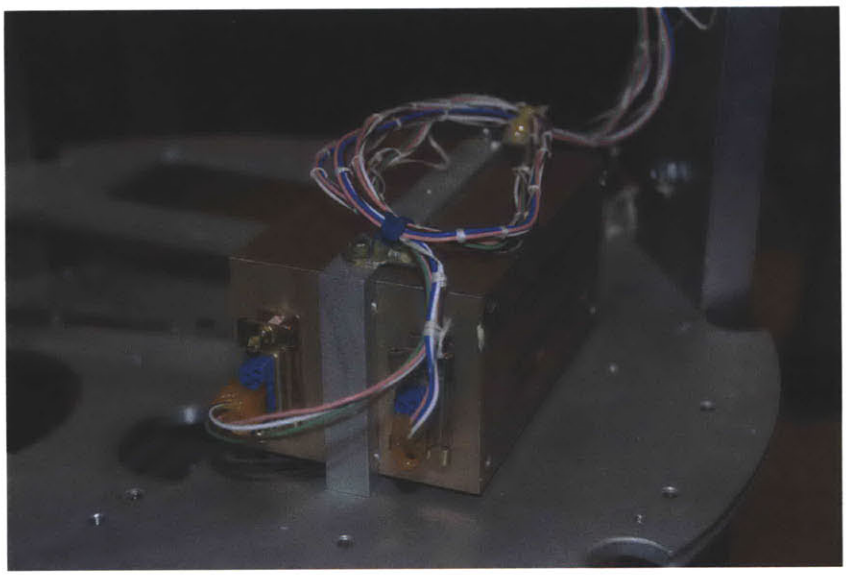

Figure 5-22: Mount for the vacuum ion pump high voltage power supplies.

larger – just large enough that they cannot fit into the same places as the WSZ detector's charge amplifiers. Instead, a new mount needed to be fabricated.

The idea for the charge amplifier mount came from the configuration of the high voltage power supplies for the vacuum ion pumps. The power supplies are bolted to a plate, almost back-to-back, and stand vertically. The plate is then bolted to a structural plate in the payload from the underside. This can be seen in Figure 5-22. A similar plate was designed for the new charge amplifiers, shown in Figure 5-23.

The only major constraint for the placement of the charge amplifiers was that

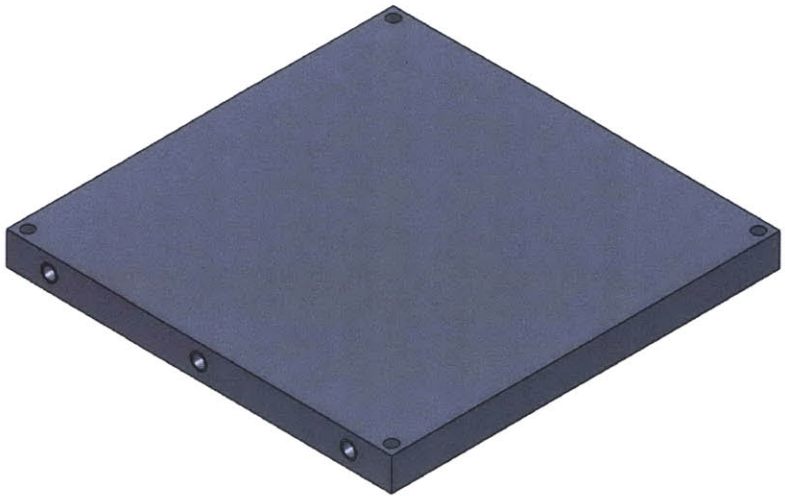

Figure 5-23: XDL Charge Amplifier mounting plate.

the cables connecting the detector to the charge amplifiers needed to be less than 12 inches. This is because there is tremendous line loss due to the very low-voltage signals coming from the detector. There is enough space between the longiron and the spectrograph box on one side of the upper structural plate in the Spectrometer Box section of the payload for this plate to be attached such that the cables to the detectors would be short enough to prevent loss of signal from. Figure 5-24 shows the charge amplifier mounting plate.

### 5.3.6 Secondary Mirror Adjustment Locks

The servomotors mounted to the back of the secondary mirror of the telescope were very precise in changing the position of the mirror so that the target would stay centered in the field of view even while the payload rotated in space away from the target. However, because pointing accuracy of the ACS is good enough to point at the target for VeSpR's pointing accuracy requirement, and because one of the servomotors is broken anyway, this complex mechanism and its associated control electronics could be removed from the payload, decreasing the overall mass, complexity, and number of failure modes.

It was still desired to use the same push pins and backing plate to keep the

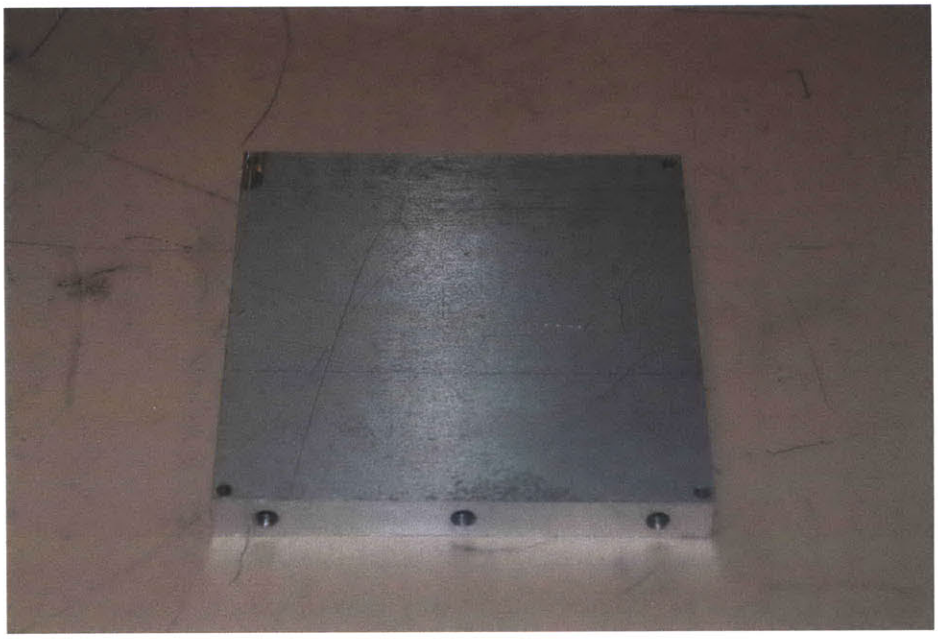

Figure 5-24: XDL Charge Amplifier mounting plate

alignment of the secondary mirror during flight. For that reason, the plate, pins, and the gears that the pins are connected to were kept while a new locking system was built around it. Figure 5-25 shows a model of the remaining parts of the secondary mirror mount.

The payload team had several brainstorming sessions about the best ways to lock these mechanisms in place. A lot of time was spent researching different high thread-count micrometer drives for fine optical adjustment. In the end, none could be found that would reuse more parts and be guaranteed to survive launch loads, so it was decided that this part should keep the same threaded inserts as well.

One of the payload team members came up with a concept to place a Teflon-backed piece of aluminum over the top of the gears and screw it down to hold the gear in place. The Principal Investigator also required a secondary locking mechanism in case the primary, over-the-top mechanism failed, and proposed a concept for a lock that would put pressure on the threads directly. These two concepts were turned into a complete design that adequately locks the mirror alignment rods in place once the mirror is properly aligned. The design required the fabrication of a total of ten new parts, six Teflon pieces and four aluminum pieces, and only countersinking of three

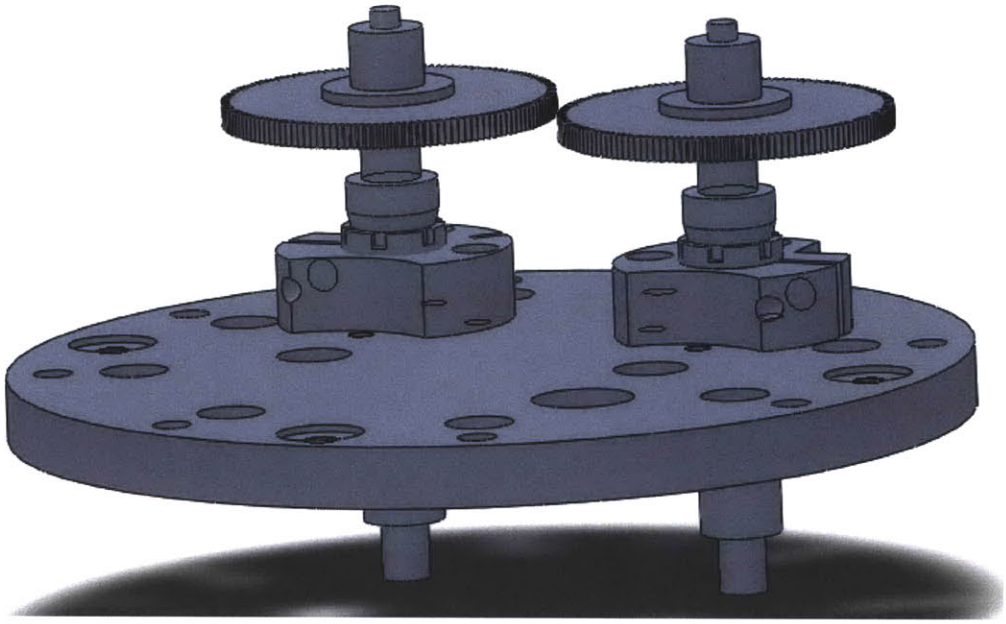

Figure 5-25: Remaining pieces of the secondary mirror mount that were reused and locked in place for flight.

holes on the mounting plate.

The secondary locking mechanisms consist of custom-made C-clamp-like aluminum pieces holding another C-clamp-like ring of Teflon inside. The aluminum clamps, shown in Figure 5-26, are mirrored from each other because they are mounted above the threaded rod insert locks, which are mirror images of each other. The Teflon rings inside the new clamps were designed to be small so that even when the aluminum clamp is loose, there is still resistance to rotation of the gear.

One concern that arose during the brainstorming sessions was that because of this lock, the alignment rods would not be able to go down far enough to push the secondary mirror to the correct location. The range of motion of height of the gear is only decreased by the thickness of the Teflon ring (1/16") plus the thickness of the top layer of the aluminum clamp (1/32"). This is not a problem because in the event that the rods do not go far enough down, more spacers can be added between the alignment rods and the pieces that slide on top of them and directly touch the secondary mirror.

Great care was taken to ensure that the primary mirror locking mechanisms were

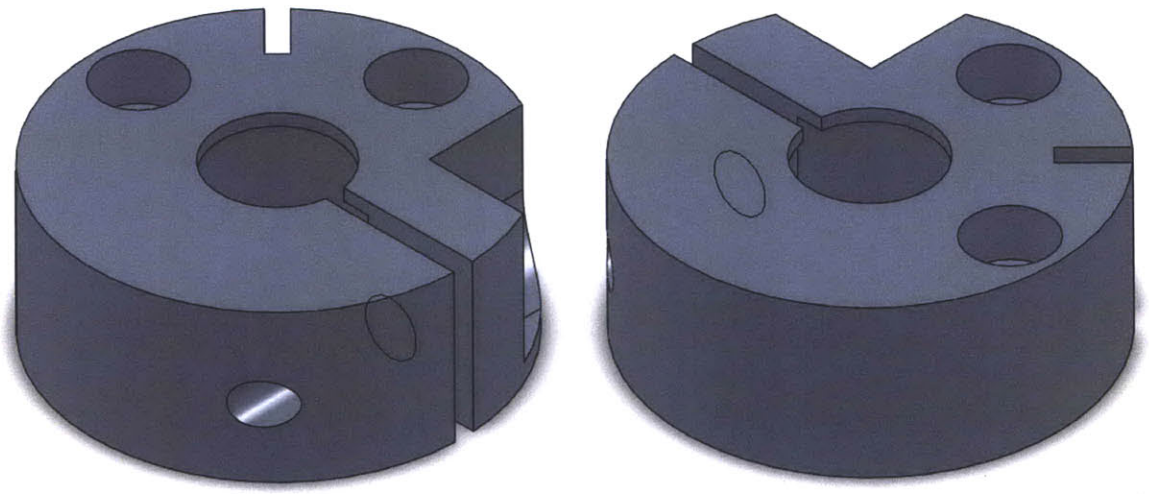

Figure 5-26: Secondary locking clamps.

sized to the greatest precision possible. If it had been possible to put the locking mechanisms in place without sharing a common support, then both sides of the lock could have been the same angle relative to the base plate; however, since these parts would overlap on one side and the gears need to be at roughly the same height, different angles were needed. If one side of the lock touched the gear and the other did not, vibrations could knock the gear (and the entire telescope) out of alignment.

Another major design constraint was the small cross-sectional area that was available to place these mechanisms. No part of the mechanism could hang over the edge of the mounting plate because it would block light entering the telescope. Small-area nuts were chosen over regular sized nuts to hold the support screws to the mounting plate and to lock the angled pieces over the gears since there was not enough room on the high-angled side for a larger nut. After five design iterations, a design solution for the primary locking mechanism was achieved, shown in Figure 5-27.

The Teflon pieces mounted to the inside faces of the aluminum piece both come in contact with the gear at the same time. Two #4-40 screws hold the Teflon pieces in place. On the left side, the gear touches between the two screws; on the right side, it touches beneath the bottom screw. Figure 5-28 shows a side view the primary locking mechanisms in place over the gears. There is enough space between the mechanisms on the shared support screw that the gears can have up to a Œ" difference in height

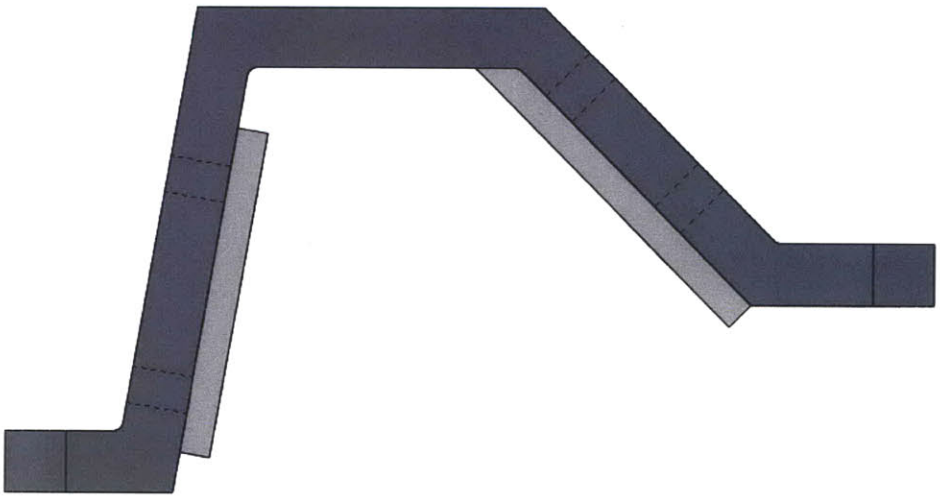

Figure 5-27: Side view of primary mirror locking mechanism with Teflon inserts.

and still not interfere with each other.

Figure 5-29 shows an isometric view of the secondary mirror locking mechanisms. The centers of the gears are gripped by the Teflon on the sides of the primary locking mechanisms, and the secondary locking mechanisms grip the threads from above the threaded insert lock that is mounted to the back plate.

All new parts were fabricated by the BU Scientific Instruments Facility, and when assembled for the first time, the only problem was that one of the #4-40 holes on a primary locking mechanism was not threaded all the way through. After re-tapping the hole, the locking mechanisms performed exactly to specifications. Figure 5-30 shows photos of the final product.

### 5.3.7 Semicircular Plate Modifications

While the semicircular plate did not need to be moved closer to the interface plate because of the FDR and RS-422 frames, other modifications had to be made because of its proximity to the interface plate and the new arrangement of cables required by Wallops. Particularly, the primary low voltage power supply box needed to be clocked nearly 120 degrees (when viewed from above) so that it was primarily located

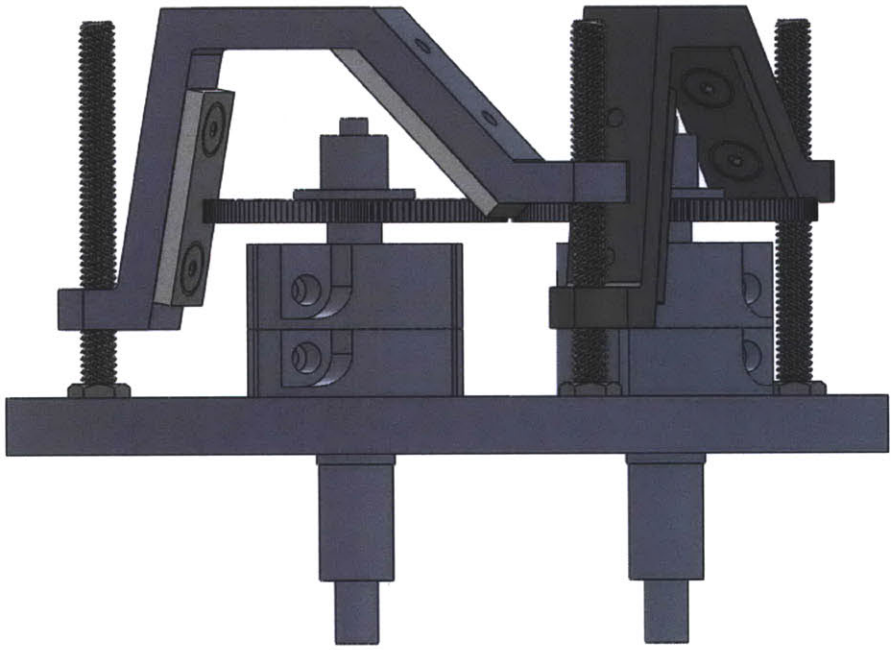

Figure 5-28: Side view of the primary mirror locking mechanisms attached to the secondary mirror alignment stage.

in Quadrant 2 as seen in Figure 5-3. This was a simple task of plotting four new Œ"-28 holes in the plate while ensuring that the P20 cable that served as the hub for the power supply was the same length away as before, none of the connectors mounted on the bottom were interfered with, and none of the standoffs that held the semicircular plate in place were interfered with. Figure 5-31 shows the old mounting holes for the primary low voltage power supply and the power supply mounted in its new position.

### 5.3.8 Interface Plate

The final major component of the payload that required a redesign was the Interface Plate. This was the most difficult part to design because of all of the parent changes the new design of the Interface Plate needed to take account of. In addition, the Interface Plate is one of the most important structure components that does not house any optics; both the Semicircular Plate and Boomerang Plate hang from it; it connects the three longirons that other structural plates are mounted to; the Current

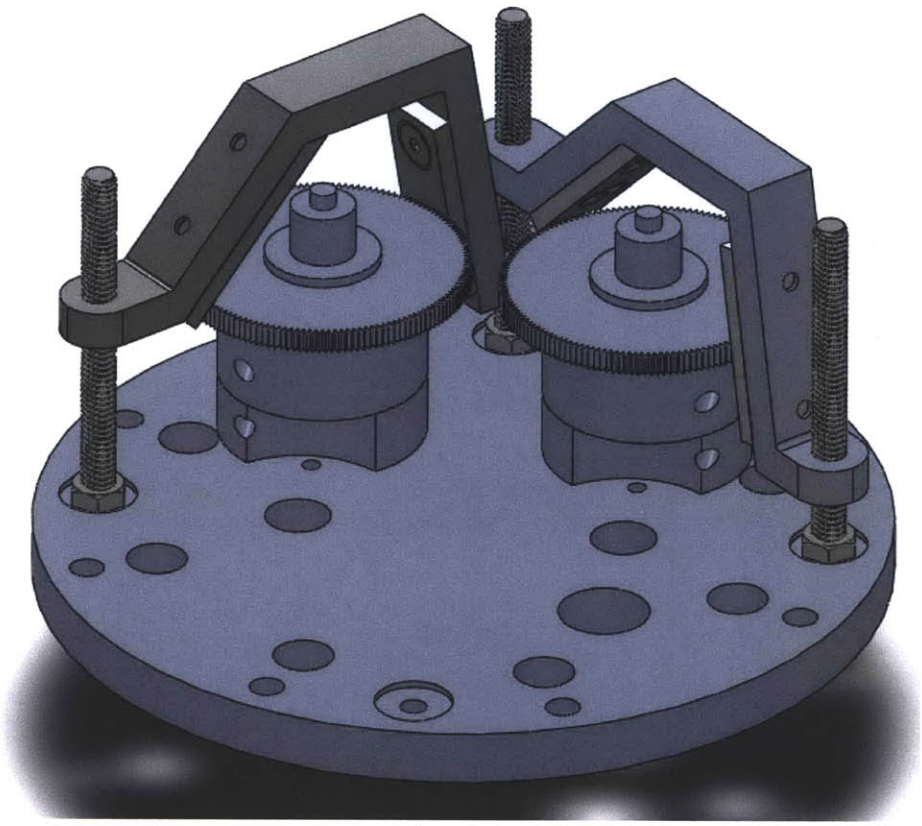

Figure 5-29: Isometric view of the mirror locking mechanisms on the secondary mirror mount.

Figure 5-30: Views of the finished secondary mirror locking mechanisms.

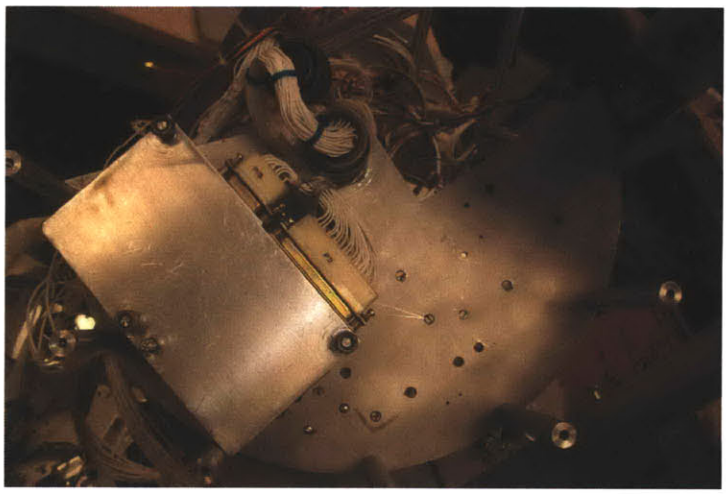

Figure 5-31: Primary low voltage power supply mounted in its new location. Note the location of the previous mounting holes where the power supply was mounted initially.

Monitor box and Altitude Switch are mounted to its bottom face; and every cable that runs from the experiment section to the ACS section runs through it. Ensuring that a new Interface Plate could be made without a cascade of other changes proved to be difficult, but after eight complete design iterations, a final design was finished.

Early iterations of the Interface Plate were designed with poor measurements of the locations of the holes that could not be moved. Machinists at the BU Scientific Instruments Facility made precision measurements of the locations of the holes so measurement errors would not be present in future design iterations. The holes that could not change were the ones where the longiron supports and Semicircular and Boomerang Plates attached. These holes and their associated obstruction patterns are shown in Figure 5-32. The Semicircular and Boomerang Plates were held in place by œ" diameter standoffs, and the longirons are 2.5 x 11/16 in rectangles. Note that all drawings in this section are aligned such that the top of the plate is at the launch rail location, and these are views looking aft toward the experiment and rocket boosters.

Next, the locations that are off-limits for connectors due to obstructions on the Wallops side were drawn in place. Figure 5-3 shows some of these obstructions, but Figure 5-33 shows them as viewed looking aft. The top, left, and right side

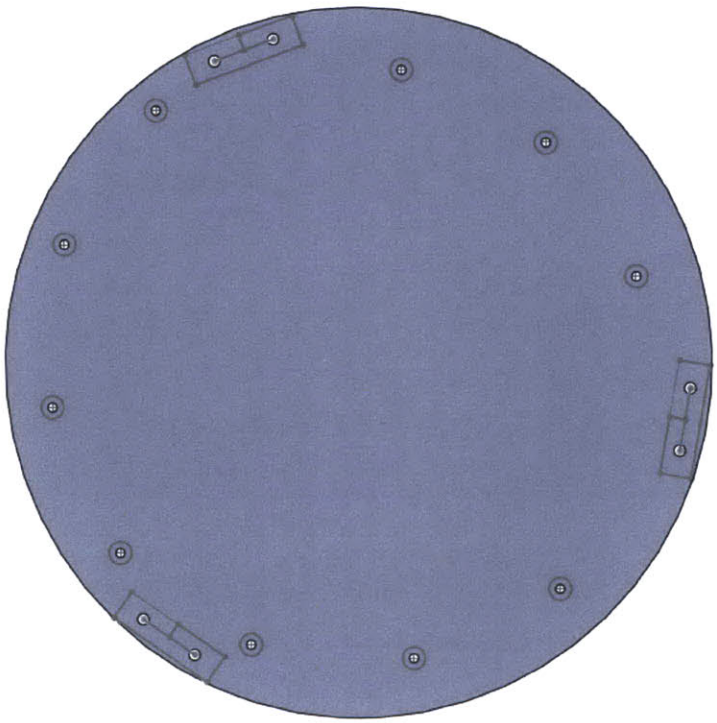

Figure 5-32: Interface Plate with required holes for the Semicircular and Boomerang Plates and tripod longiron and the area obstructed by the mounting structure beneath the Interface Plate.

obstructions were known before design work began, but the center section was not designated as off-limits until design iteration four.

The only major component of the payload that comes close to the Interface Plate and could interfere with connector placement is the primary low voltage power supply. Originally, it occupied most of Quadrant III (Figure 5-3) when looking at the Interface Plate from this direction, but it was successfully moved so that it primarily occupies Quadrant II with only minor obstructions in Quadrant III. The Altitude Switch and the Current Monitor also cause some additional obstructions in the areas that are still free for connectors, but those can be moved and mounted wherever it is convenient. Figure 5-34 shows the area obstructed by the primary low voltage power supply in addition to the Wallops obstructions.

Initially, there was a fear that the harness for the Analog Signals Connector (J983), which was located in an area on the old Interface Plate that is now obstructed, would not have enough slack to move to an unobstructed location. Soon after, the

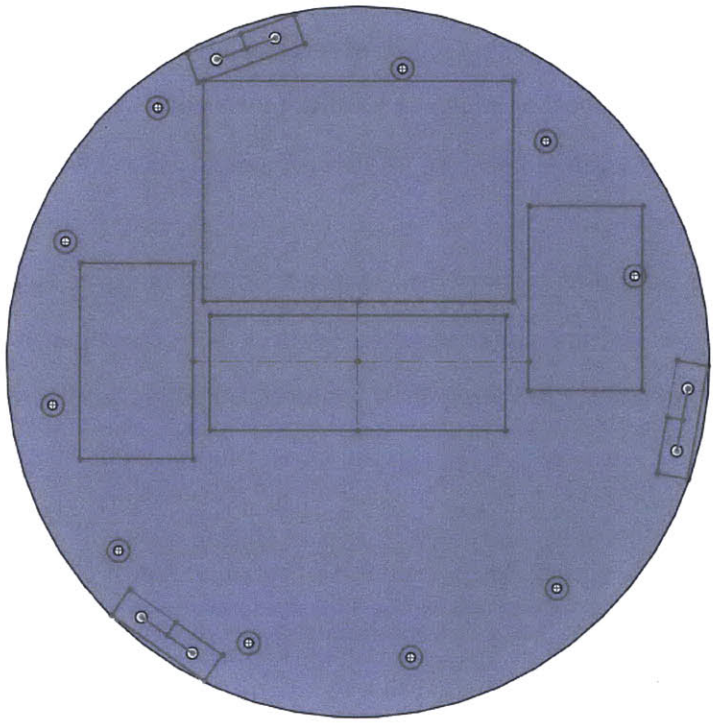

Figure 5-33: Interface Plate with connector obstructions due to Wallops ACS added.

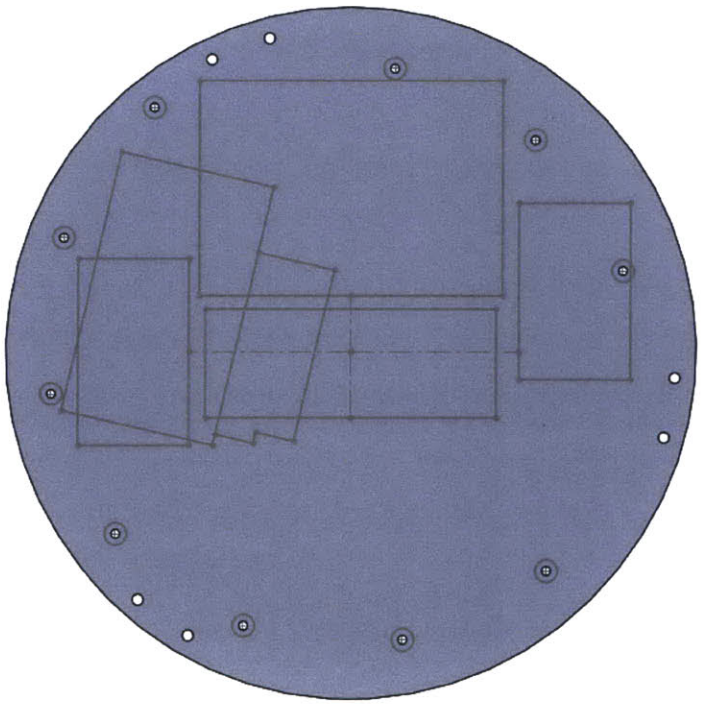

Figure 5-34: Interface Plate with connector obstructions due to primary low voltage power supply added.

experiment team realized that the reason the cable had so little slack was that it was tied down in several locations and tied to several other harnesses. After cutting these free, there was enough slack to place the connector nearly anywhere on the plate. If there had not been enough slack, this connector would have had to be rewired; since this is the largest external connector in the payload, it would not have been easy.

The experiment team also wanted to take advantage of space that had been cut in the plate that separated the Spectrometer Section from the Spectrometer Extension Section. These cuts were made to hold harnesses in place, and now that some were being removed, new ones could be put in their places. The connectors streaming detector data through the telemetry (J981 and P982) are both planned to be brought up through these cuts, which are positioned on both sides of the longiron.

It was also important to try to avoid harnesses that stretch all the way across one section of the payload without attaching to an intermediate point. The vibrations and accelerations the payload experiences during launch can shake harnesses with too much slack strongly enough to rip connectors out of their sockets or wires out of the connectors. This is why the Star Tracker (J733) and Xybion camera power input (P984) and data output (J986) are squeezed into areas that are close to obstructions. All three of these cables move up the payload along the longiron support located closest to launch rail, so they have been positioned as close to the launch rail as possible.

The remaining harnesses connecting to the Interface Plate all originate from center origins in the payload and can be easier moved or fabricated to fit in nearly any location in the unobstructed area. Figure 5-35 shows the final design of the Interface Plate with all the connectors and holes for the Altitude Switch and Current Monitor Box labeled. Figure 5-36 shows the finished Interface Plate mounted on the payload.

### 5.3.9 Mechanical Design Change Review

Despite careful planning and mapping out design details as well as possible in advance, there are design changes that are perhaps more costly or not as optimal as they could have been. Sometimes the desire to reuse parts actually added to the total cost, as

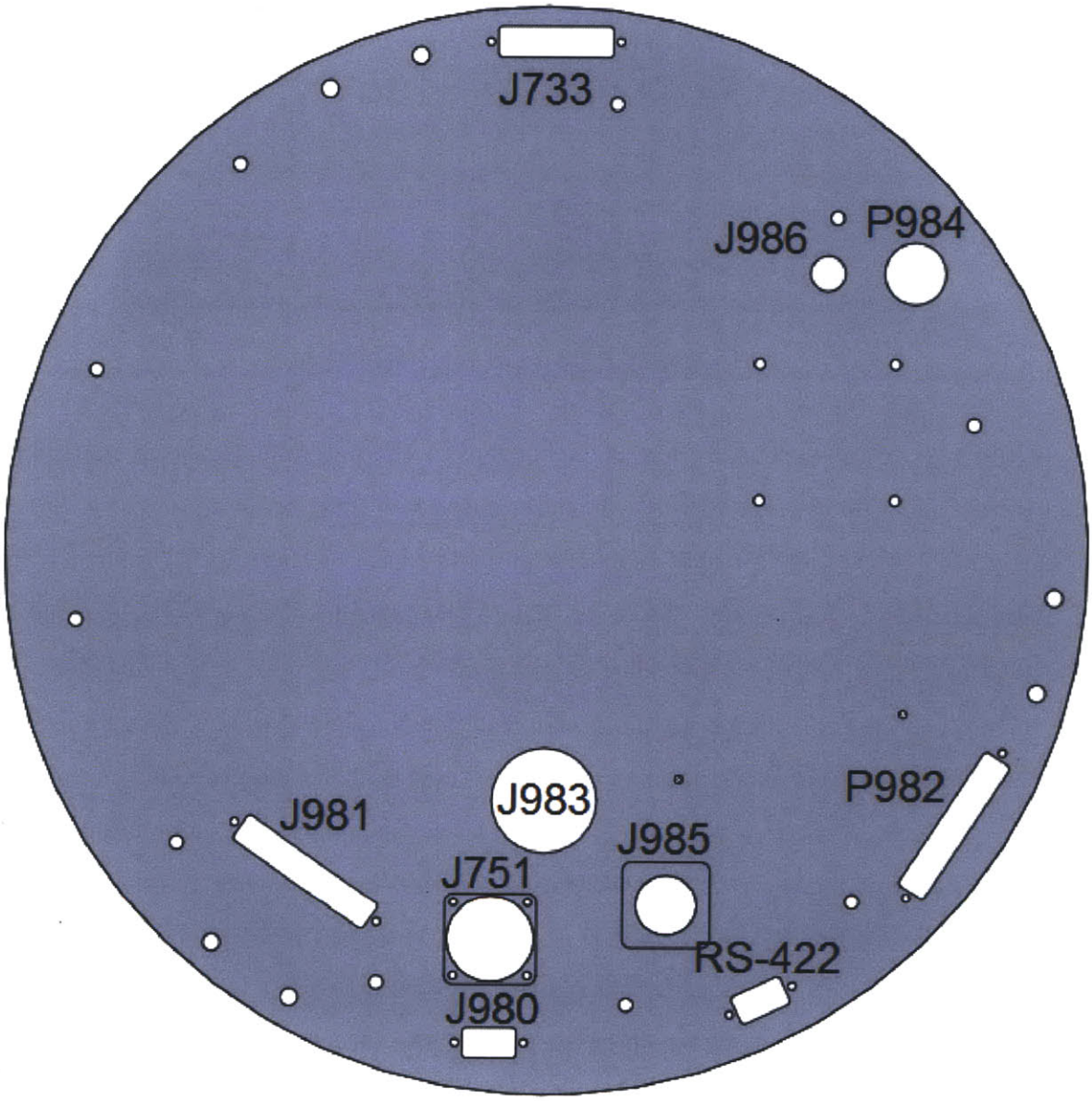


Figure 5-35: Final Design of the Interface Plate.

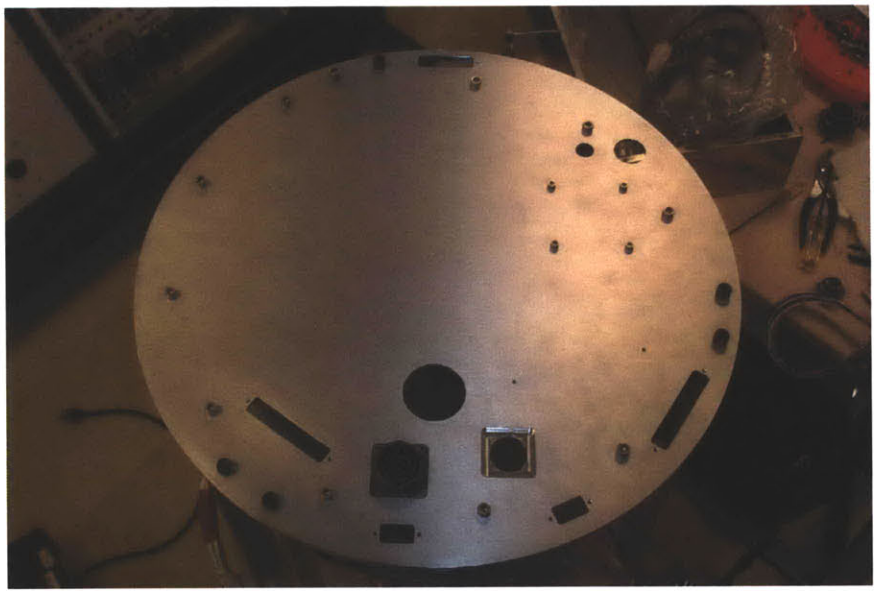

Figure 5-36: Finished Interface Plate.

in the case of the secondary mirror locks, due to the amount of custom machining necessary for the concept to work. In other cases, the total costs were not compared adequately with their alternatives, such as in the case of choosing to refurbish the detectors versus purchasing new ones, where the cascade of design changes due to that choice may have cost more in the end than simply paying for refurbishment.

In all cases, "optimality" in the design was not considered nearly as much as it is when designing other spacecraft systems. There was no strict requirement to minimize the total mass of the new components, only the desire to have the mass lower than it was in previous flights. Practices were used to avoid low-frequency resonance modes like offsetting screw locations, but these were not backed up with solid calculations. Engineers at the Kavli Institute assured the payload team that the thermal capacity of the aluminum frames was enough to prevent the electronics from overheating in vacuum; this is known from experience to be the case, but no formal heat transfer analysis was conducted.

One of the key problems in designing components to see how they affect the entire system is a lack of a complete solid model of the payload. Some of the pieces of this payload date all the way back to 1967; other parts are from the early 1990's at the latest. In all cases, there is no way to predict the vibration modes, stresses, strains,

and factors of safety within the structure before taking the payload to Wallops for systems integration. Building a solid model was considered too time-consuming to the Principal Investigator for this flight, but for future flights or rebuilds it may be worthwhile to have a solid model to do a complete structural and thermal analysis. Any flight engineer working on this payload in the future can use such a solid model and verify its accuracy against test data from the first VeSpR flight's integration testing.

## 5.4 Designing Payload Ground Support Equipment

Since the output of the TM Interface and the communication software Wallops is now using are both completely different from the ones used on the previous JASpR flight, the payload GSE needed to be updated to work with the new systems. In addition, the source files of the software used to read the data cannot be found. Rather than updating the GSE software to work with the new hardware, the science team decided to develop a whole new system.

The GSE computers, as described in Section 4.2.6, were considered obsolete even during the last JASpR flight. In addition, today's computers are so much more powerful that there is absolutely no need to have two computers; one computer should be able to receive, process, and display all of the incoming data from the rocket. Furthermore, there was a desire to make the computer system more portable, not only during integration testing at WFF and WSMR but also during calibration testing at BU and verification testing at MIT. Carting around two large computers, the bit encoder, the spaghetti box, and a power supply and keeping track of the cables and their proper connections was a hassle that the science payload team wanted to eliminate. A laptop with input devices is all that is needed.

The new GSE computer equipment also does not need nor is the payload team able to acquire a PCM identical to the one that will be used in flight to replicate communications with the TM Interface. Rather than having using the PCM to convert the parallel data into a radio signal and having the Bit Sync convert the radio signal

back into parallel data, the parallel data can be read directly from the TM Interface.

Data input requirements for the GSE remained virtually unchanged. While it is desired to view data from both detectors at the same time, both are not required to be monitored and displayed at the simultaneously. During component calibration testing, only one detector is used at a time, and when the payload is fully assembled, the input cables can be easily switched between the spectrograph and the imager detectors. Only one 32-bit parallel data stream needs to be monitored at a time. The analog monitor signals remain unchanged.

Another sounding rocket team at BU uses an AccesIO Products Inc. 16-bit USB Digital Input Module to read 16-bit data from one of their detectors. Their experience and willingness to provide an initial program to read data and help troubleshoot if the VeSpR team decided to use similar products was a major factor in deciding what input modules would be used in the GSE. The downside to this choice was that AccesIO only has 16-bit digital input modules that can read input data. The VeSpR detectors have a 32-bit output. If the VeSpR team had been able to acquire a 32-bit module for a reasonable price, both streams of data from the detectors could have been displayed simultaneously. This is an improvement that can easily be made in the future if such a 32-bit module became available.

Figure 5-37 shows the configuration of the new GSE data input system. The system consists of one laptop computer, three data input modules, a custom timing circuit, and associated wiring, terminal boards, and connectors. The whole system fits in a 15 x 21 x 6 in plastic storage bin that can be easily carried anywhere and does not require external power as long as the laptop batteries are charged. What once required continuous A/C power, weighed over 100 lbs, and could not be moved without careful planning has been replaced with this $<$ 25 lbs system that can be taken nearly anywhere.

The computer is a Lenovo Thinkpad with three USB ports that runs Ubuntu, a Linux-based operating system. Linux was chosen over other operating systems for several reasons. Astronomers typically use IDL (Interactive Display Language) to display, reduce, and analyze data, typically on Macs but it is also easily compatible

Figure 5-37: New GSE computer setup

with Linux (all work in Chapter 6 was done in IDL on a Mac). It is difficult to run IDL on a Windows operating system and it is not user-friendly. While the science team has more experience with Macs, the computer support staff members at BU are experts with Linux. In addition, the AccesIO digital input modules are compatible with Windows platforms but can be easily patched to operate with Linux platforms. Linux was therefore the logical choice because of these reasons.

The laptop connects to three AccesIO input modules; two USB-DIO-16A input modules capable of reading 16-bit digital input/output, and a USB-AI12-64ME analog input module capable of reading 64 analog inputs with 12-bit resolution (more on the analog signals later in this section). These cards are far more capable than they are required to be to sample at the same rate as the telemetry, but most computer components nowadays are. The digital input modules can read data at speeds of up to 40 MHz even though the updated telemetry requirement is 25 kHz, and the analog module can sample the analog monitors at speeds of up to 100 kHz even though the telemetry samples the analog signals at only 10 Hz.

Since the digital input modules have only 16 channels and the detector output from the TM Interface uses 32-bits, half of the outputs go to one module and half

go to the other. Another piece of hardware was needed to properly sync the two inputs. A small timing circuit ensures that the two cards are reading data at the correct frequency and phase. This sets up the cards so that one module is a master and the other is the slave, which ensures that the computer is reading the two 8-bit words from each of the two digital input modules in the correct order that they are sent from the TM Interface. If 32-bit input cards are available for a low price in the future, this timing circuit will not be necessary.

Both digital input modules connect via USB to the GSE laptop. Data from the detectors coming through the modules is displayed on the laptop in real time using an IDL program. The other BU sounding rocket science team also provided a version of this program that was modified to correctly display the data from the two 16-bit modules. Just like the original display program on the DOS computer, it displays the total photon counts, the current count rate in counts per second, the total number of rejected counts, and the total number of bad counts.

The analog input module reads the analog monitors. Although the payload only has 32 monitors, a 64-input module was used in case a future flight ever needed more analog signals to be read. A custom graphical user interface was developed that displays the voltages on the monitors in real time. These monitors are recorded in flight as data that is given to the science team once the mission is completed. For ground testing, these monitors only serve as points that need to be checked against test values to monitor payload health, so it does not matter that they are not sampled at the same rate as they will be sampled in flight.

## 5.5 Data Expectation Modeling

Even though the capabilities of VeSpR have been improved since the JASpR missions, a model of what the expected data output of the spectrograph detector would produce is needed to verify that the system is capable of meeting the system requirements to achieve the scientific objectives. Building models that match experimental data give confidence in the ability of the instruments to meet these objectives in flight.

Table 5.2: Telescope sizing properties used to calculate the total light collecting area.

| **Telescope Size Properties** | **Value** | **Units** |
|---|---|---|
| Primary Mirror Diameter | 35.0 | cm |
| Primary Mirror Area | 962.1 | $cm^2$ |
| Secondary Diameter | 12.0 | cm |
| Secondary Area | 113.1 | $cm^2$ |
| Tripod Support Thickness (Each) | 6 | cm |
| Tripod Support Area (Total) | 207 | $cm^2$ |
| **Total Telescope Collecting Area** | **642.0** | **$cm^2$** |

First, a model of the telescope and spectrograph optics and the spectrograph detector were created to predict the overall throughput of the system. Next, the observation targets were modeled according to their expected position, velocity, and brightness. These two models were combined to calculate the expected count rate, total counts, and the uncertainty in the data taken during flight, and a model spectrum was produced that should match what is seen in flight. The IDL code and Excel spreadsheets for all of these steps are available in the attached Appendix DVD.

### 5.5.1 Modeling Telescope and Spectrograph Optics

Models of the telescope and spectrograph optics were developed previously for the JASpR flights in a ray-tracing program called BEAM4. Since the actual optics have not changed, this model was reused to argue that the telescope and spectrograph could achieve resolution of 1-2 arcsec each and a combined resolution of 2-3 arcsec. This had been shown in early VeSpR calibrations as well, and this information will be considered later in the modeling process.

The first step of the VeSpR modeling process was to find the total light collecting area of the telescope. The primary mirror has a diameter of 35cm, but since the telescope is a Cassegrain design, the secondary mirror and secondary support beams obstruct the view of the primary and block some of the incoming light. Table 5.2 shows information on how the total light collecting area was calculated.

Figure 5-38 shows the BEAM4 model of the telescope and spectrograph box. Light reflects off the primary and secondary mirrors and passes through the objective prism.

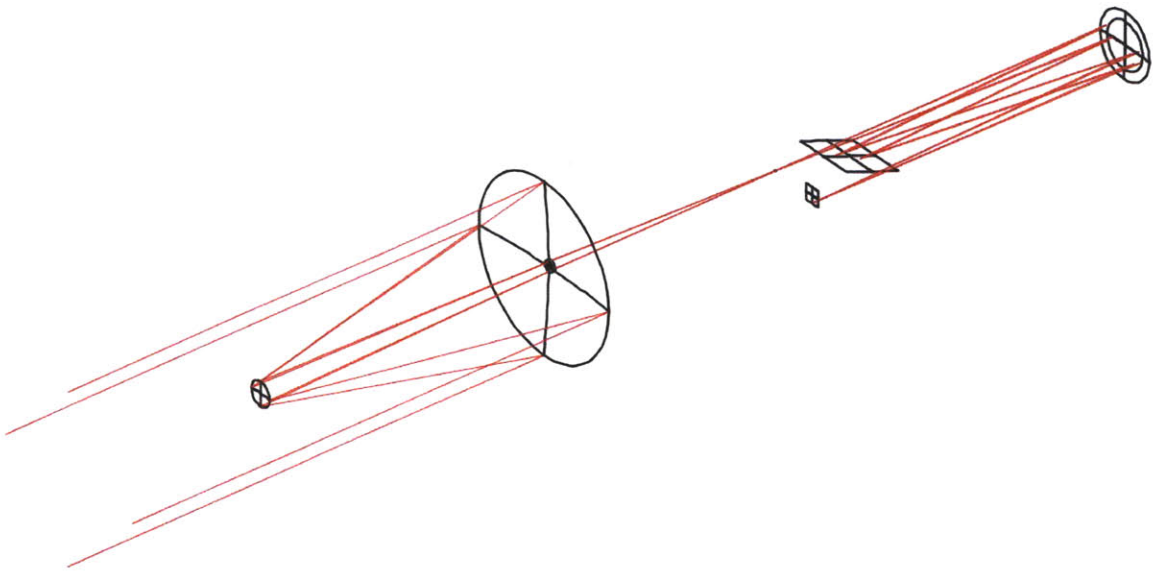

Figure 5-38: BEAM4 model of the path light takes from the telescope to the spectrograph detector.

Light then passes through the spectrograph spit and enters the spectrograph box. Light reflects off the parabolic mirror, then the echelle grating, then the parabolic mirror again before going through the magnesium fluoride window and into the detector. In total, light entering the telescope interacts with 7 different optics before reaching the multi-channel plates in the detector.

All of the major optics except for the echelle grating were sent to NASA Goddard Space Flight Center to be polished and recoated to achieve maximum UV reflectivity. The aluminum mirrors over-coated with magnesium fluoride can achieve reflective efficiencies of over 80%, which is better than what was measured during initial calibration testing for these optics (see Section 4.5). For a nominal case, 75% efficiency is assumed. Table 5.3 shows estimated efficiencies for all of the components of the telescope and spectrograph box at Lyman-alpha wavelengths.

A 0.278% total efficiency for the whole system means that the spectrograph and telescope have an effective collecting area of 1.79 $cm^2$.

The existing BEAM4 model also showed that the plate scale at the focal plane was 26 arcsec/mm. The new XDL MCP detectors have a grid resolution of 25 $\mu m$,

Table 5.3: Estimated efficiencies at Lyman-alpha wavelengths of all of the optics to the spectrograph detector.

| **Throughput/Reflective Efficiency** | % |
|---|---|
| Telescope Optics Properties | |
| Primary Mirror Efficiency | 75.0 |
| Secondary Mirror Efficiency | 75.0 |
| Objective Prism Efficiency | 40.0 |
| Total Telescope Efficiency | 22.5 |
| Spectrograph Optics Properties | |
| Parabolic Mirror Efficiency | 75.0 |
| Echelle Grating Efficiency | 20.0 |
| Parabolic Mirror Efficiency | 75.0 |
| Total Spectrograph Efficiency | 11.3 |
| Detector Subsystem Properties | |
| Window Efficiency | 50.0 |
| Detector Quantum Efficiency | 22.0 |
| Total Detector Subsystem Efficiency | 11.0 |
| **Total VeSpR Optical Efficiency** | **0.278** |
| **Effective Telescope Collecting Area** | **1.79 cm$^2$** |

Table 5.4: Additional instrument properties and spectrograph detector resolution.

| **Property** | **Value** | **Units** |
|---|---|---|
| Plate Scale | 26.0 | arcsec/mm |
| Detector Resolution | 25.0 | $\mu m$/pixel |
| Image Sizing | 0.65 | arcsec/pixel |

which is half the size of the old WSZ detector grid resolution of 50 $\mu m$. Table 5.4 shows these properties and the resultant angular pixel size.

The final step in building a model of the telescope is to find a line-spread function (LSF) of the telescope and spectrograph. At the time of this writing, a true LSF for the payload has not been measured, but Figure 5-39 shows the LSP found during JASpR testing measured at Lyman-alpha generated in IDL. The full-width half maximum (FWHM) at Lyman-alpha is 0.055 Å. This LSF was used to model the measured spectrum, described in the next section.

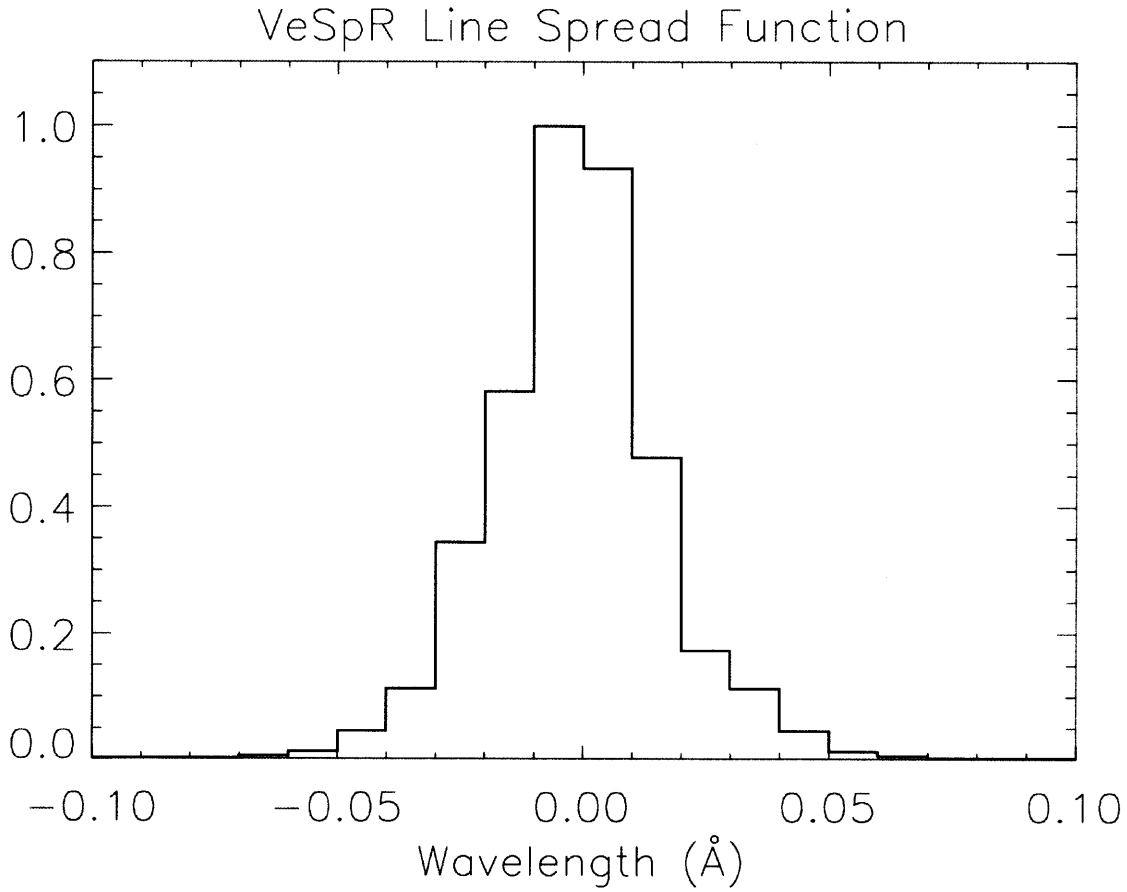


Figure 5-39: Model point spread function of the VeSpR telescope, spectrograph, and detector.

Table 5.5: Venus ephemeris data for April 4th, 2012, the date of Venus' maximum velocity relative to Earth, and telescope scaling properties on that day.

| **Property** | **Value** | **Units** |
|---|---|---|
| Date of Launch | April 4th, 2012 | – |
| Day of Year | 95 | – |
| Right Ascension | 3.80 | hours |
| Declination | 23.77 | deg |
| Angular Diameter | 25.7 | arcsec |
| Distance from Earth | 9.714x107 | km |
| Relative LOS Velocity | 13.445 | km/s |
| Blue Shift | 0.055 | Å |
| Sun-Earth-Venus Angle | 45.8 | deg |
| Plate Scale | 26.0 | arcsec/mm |
| Detector Resolution | 25.0 | $\mu m$/pixel |
| Image Sizing | 0.65 | arcsec/pixel |
| Angular Sizing | 471.0 | km/arcsec |
| **Pixel Sizing** | **306.1** | **km/pixel** |

### 5.5.2 Modeling Targets and Background

During flight, VeSpR will be observing Venus through the top layers of Earth's atmosphere and through interplanetary space. The launch window has been determined by the Principal Investigator to be when Venus is moving towards Earth so the hydrogen and deuterium spectra of Venus are blue-shifted away from Earth's geocoronal emission.

The NASA Jet Propulsion Laboratory's HORIZONS On-Line Solar System Data and Ephemeris Computation Service was used to generate a ephemeris displaying daily positioning information for Venus during the year 2012. This ephemeris data showed that near April 4th, 2012, Venus will have a maximum line-of-sight (LOS) velocity relative to Earth, 13.445 km/s, during this synodic period. If this date were chosen as the launch date, it would create the maximum blue-shift. Coincidentally, the blue-shift at maximum LOS velocity is 0.055 Å, which is very close to the FWHM of the LSF. Table 5.5 shows a sample of the data from this ephemeris on April 4th. The full table is available in the attached Appendix DVD.

Another program developed for use with JASpR data was used to calculate the LOS velocity of the interplanetary medium (IPM), which is composed of neutral

Table 5.6: Estimated brightnesses of Venus and elements of the sky background.

| Emission | Value | Units |
|---|---|---|
| Venus Hydrogen | 9000 | Rayleighs |
| Venus Deuterium | 500 | Rayleighs |
| Earth Hydrogen | 5000 | Rayleighs |
| Earth Deuterium | 50 | Rayleighs |
| Interplanetary Medium | 500 | Rayleighs |

hydrogen in space that also reflects and scatters solar Lyman-alpha light. An observer looking in the direction of Venus on April 4th, 2010 when it is at the declination shown in Table 5.5 will have an LOS velocity relative to the IPM of 22.18 km/s, corresponding to a 0.090 Angstrom red-shift of the IPM Lyman-alpha emission. Even though the IPM emission is faint, observing Venus when it is blue-shifted while the IPM is red-shifted reduces the overlap between the two emissions and increases the signal-to-noise ratio.

The brightness of Earth's geocoronal emission and the IPM are well known from other Lyman-alpha studies. The brightness of Venus' hydrogen is also known, and the deuterium emission has been estimated based on existing D/H ratios (see Section 3.2). Table 5.6 shows the initial estimated brightnesses of the spectra that will be visible on the detector.

The spectrograph aperture is 5 arcsec wide, so the solid angle of the targets can be calculated. With the solid angles, effective light collecting area, and total time observing the target (275 seconds in the nominal mission profile), the brightness of the targets in units of Rayleighs ($10^6$ photons/cm-s into $4\pi$ steradians) can be converted into a photon count rate. Table 5.7 shows the solid angles of Venus, the minimum resolvable area, and the entire sky when viewed through the spectrograph aperture.

### 5.5.3 Model Results

Table 5.8 shows the count rates in photons per second measured by VeSpR for Venus deuterium and hydrogen measured as a bulk of the planet (25.7 arcsec) and Earth hydrogen and deuterium and the IPM for the entire sky background. The table also

Table 5.7: Model target and sky solid angles.

| Property | Value | Units |
|---|---|---|
| Venus Diameter | 25.7 | arcsec |
| Total Venus Area | 128.5 | $arcsec^2$ |
| Minimum Resolution | 2 | arcsec |
| Minimum Resolvable Area | 10 | $arcsec^2$ |
| Aperture Slit Length | 300 | arcsec |
| Total Sky Area | 1500 | $arcsec^2$ |

shows the expected total counts received by each source throughout the flight and the Poisson uncertainty as a function of counts and a percentage of the measurement.

Notice that the expected total count rate is much less than the maximum rate that the TM Interface can send data through the telemetry (25,000 counts per second) and even less than the rate at which dead time effects cause error in the detector's output (100,000 counts per second). Also note that the Venus deuterium count rate is based off of the bulk planet rather than a function of altitude, the count rate calculation was applied to the lowest spatial resolution of the spectrograph. Table 5.9 shows the results for the expected spatial resolution element of 2 arcsec, which corresponds to a distance of 940 km.

An IDL program written previously by the Principal Investigator already exists to model spectral data from HST. This program was heavily modified to model spectral data for VeSpR. A model spectrum was generated by modeling the expected emissions from Venus and the sky background as Voigt profiles convolved with the VeSpR telescope and spectrograph LSF. A Voigt temperature of 300 K was assumed for Venus' upper atmosphere. Figure 5-40 shows the model hydrogen and deuterium spectra of Venus generated in IDL.

A Voigt temperature of 1000 K was assumed for Earth's upper atmosphere for Earth's geocoronal emission, and 30,000 K was assumed for the IPM because it is so broad (see Section 2.5 for more on Voigt profiles). Both of these were compared to geocoronal sky backgrounds taken by Hubble's STIS (see Figure 6-16) to ensure accuracy and then convolved with the VeSpR PSF. Figure 5-41 shows the model spectrum of the geocoronal background and the IPM.

Table 5.8: Calculated results for counts, count rates, and uncertainty in the measurements for the entire disc of the planet.

| Measurement | Value | Units |
|---|---|---|
| **Venus Deuterium Count Rate** | **2.15** | **counts/s** |
| **Venus Deuterium Total Counts** | **591** | **counts** |
| Venus Deuterium Uncertainty (absolute) | 24 | counts |
| Venus Deuterium Uncertainty (relative) | 4.11 | % |
| **Venus Hydrogen Count Rate** | **38.66** | **counts/s** |
| **Venus HydrogenTotal Counts** | **10632** | **counts** |
| Venus Hydrogen Uncertainty (absolute) | 103 | counts |
| Venus Hydrogen Uncertainty (relative) | 0.97 | % |
| **Earth Hydrogen Count Rate** | **251** | **counts/s** |
| **Earth Hydrogen Total Counts** | **68949** | **counts** |
| Earth Hydrogen Uncertainty (absolute) | 263 | counts |
| Earth Hydrogen Uncertainty (relative) | 0.38 | % |
| **Earth Deuterium Count Rate** | **2.51** | **counts/s** |
| **Earth Deuterium Total Counts** | **690** | **counts** |
| Earth Deuterium Uncertainty (absolute) | 26 | counts |
| Earth Deuterium Uncertainty (relative) | 3.81 | % |
| **IPM Count Rate** | **25.07** | **counts/s** |
| **IPM Total Counts** | **6895** | **counts** |
| IPM Uncertainty | 83 | counts |
| IPM Uncertainty | 1.20 | % |
| **Total Count Rate** | **319.11** | **counts/s** |
| **Total Counts** | **87755** | **counts** |

Table 5.9: Calculated results for Venus deuterium counts at a resolution of 2 arcsec.

| Result | Value | Units |
|---|---|---|
| **Venus Deuterium Count Rate** | **0.17** | **counts/s** |
| **Venus Deuterium Total Counts** | **46** | **counts** |
| Venus Deuterium Uncertainty (absolute) | 7 | counts |
| Venus Deuterium Uncertainty (relative) | 14.75 | % |

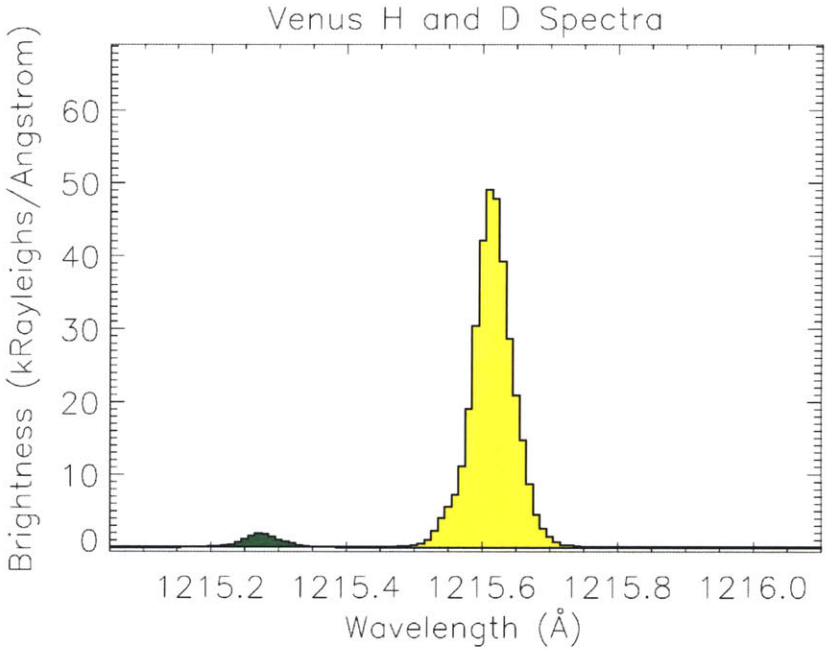


Figure 5-40: Model Venus hydrogen and deuterium spectral profiles convolved with the VeSpR telescope and spectrograph PSF. Venus hydrogen is shown in yellow, deuterium is shown in green.

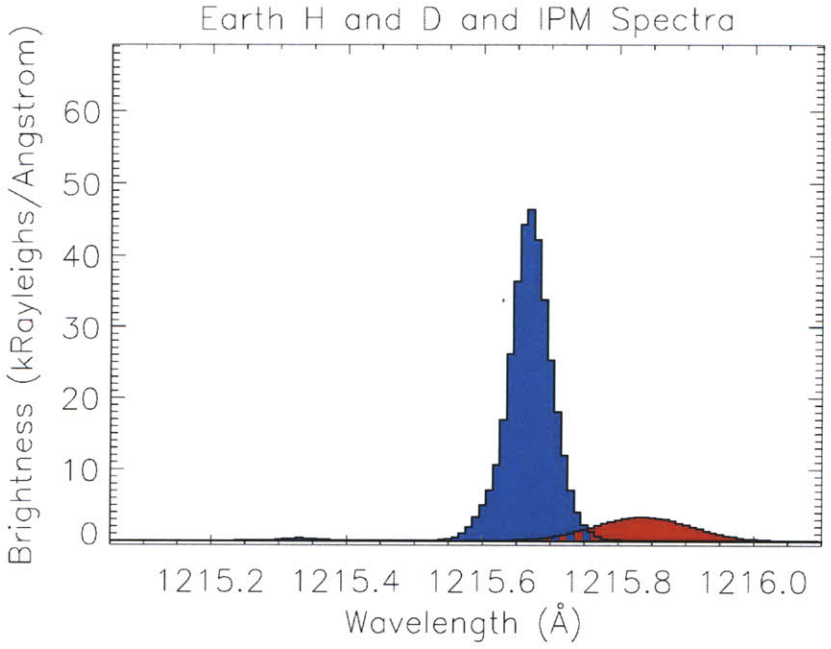


Figure 5-41: Model sky spectral profiles of Earth hydrogen and deuterium and the interplanetary medium (IPM) convolved with VeSpR telescope and spectrograph PSF. Earth hydrogen is shown in blue, the IPM is shown in red, and Earth deuterium is barely visible at 1215.34 Å.

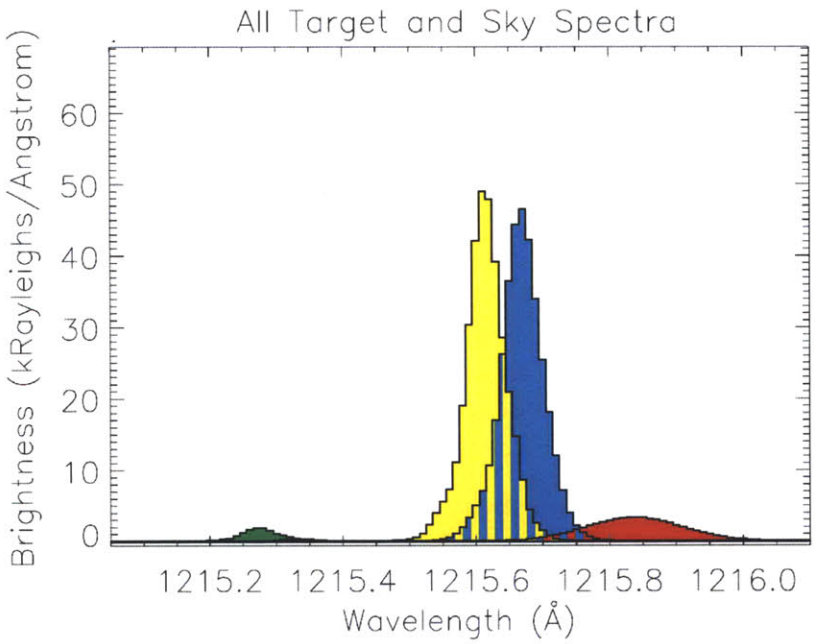


Figure 5-42: All Venus and sky spectral profiles convolved with VeSpR telescope and spectrograph PSF.

Both the Venus spectra and the sky background spectra are shown on the same spectrum in Figure 5-42. The final spectrum is shown in Figure 5-43. Notice the two peaks from Venus and Earth hydrogen Lyman-alpha are resolvable.

### 5.5.4 Sensitivity Analysis and Model Limitations

The modeling results presented in the previous subsection are based on many assumptions for values that may not be correct when VeSpR is launched. An analysis of how the results can change with different parameters will determine how robust the system is and if it can achieve the science objective as the actual performance changes from the nominal performance.

The launch date is of course subject to change. VeSpR was originally scheduled to fly in July 2010 but was delayed because WFF was backed up with other customers. Scheduling conflicts may place VeSpR's launch earlier or later than the ideal date, payload integration may take longer than planned, and weather can cause a scrubbed launch. It is important to know how the conditions will change with the launch date.

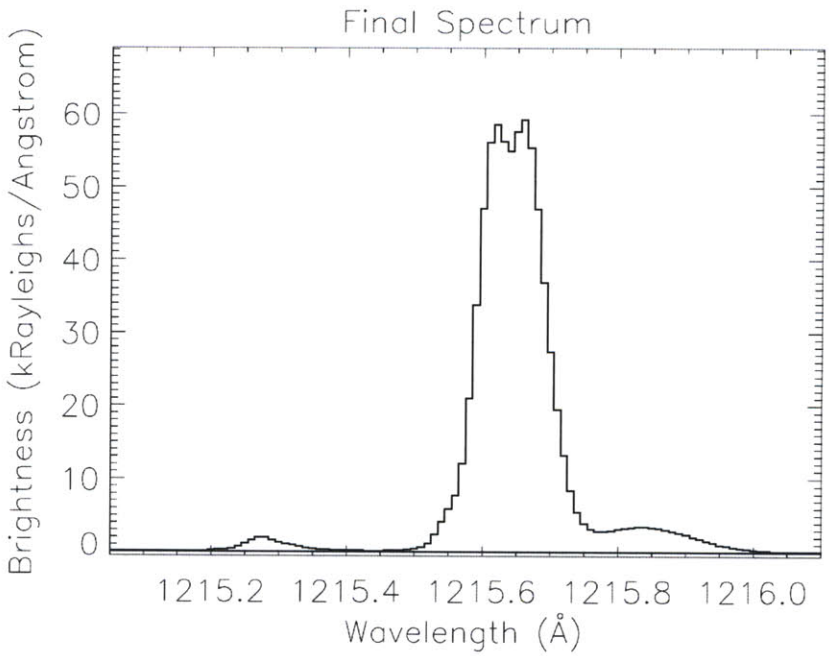


Figure 5-43: The expected spectrum that VeSpR will observe the estimated brightnesses of Venus and elements of the sky background (see Table 5.6).

Figure 5-44 shows the relative velocity between Venus and Earth and how it changes throughout the year 2012. There is a long period of time where the relative approaching velocity of Venus exceed 10 km/s in the beginning of 2010 before it quickly moves between the Earth and the Sun.

The relative velocity is important to resolve the deuterium line profile spectrally; however, because the distance to Venus is decreasing rapidly while Venus emissions are highly blue-shifted, the angular size of Venus is increasing. This increase in angular size corresponds to an increase in spatial resolution and a higher count rate. Delaying launch past the date of maximum relative velocity may increase the performance of the experiment. Figure 5-45 shows Venus' distance relative to Earth as it changes throughout 2012, and Figure 5-46 shows Venus' angular size as viewed from Earth during that same period.

On May 13th, 2012, the relative velocity of Venus slows below 10 km/s, but it is almost 55% closer and has an angular diameter of 45.4 arcsec. This means the telescope can achieve a spatial resolution of 520 km with 2 arcsec image quality compared to 940 km on April 4th. Figure 5-47 shows the final spectra given ephemeris

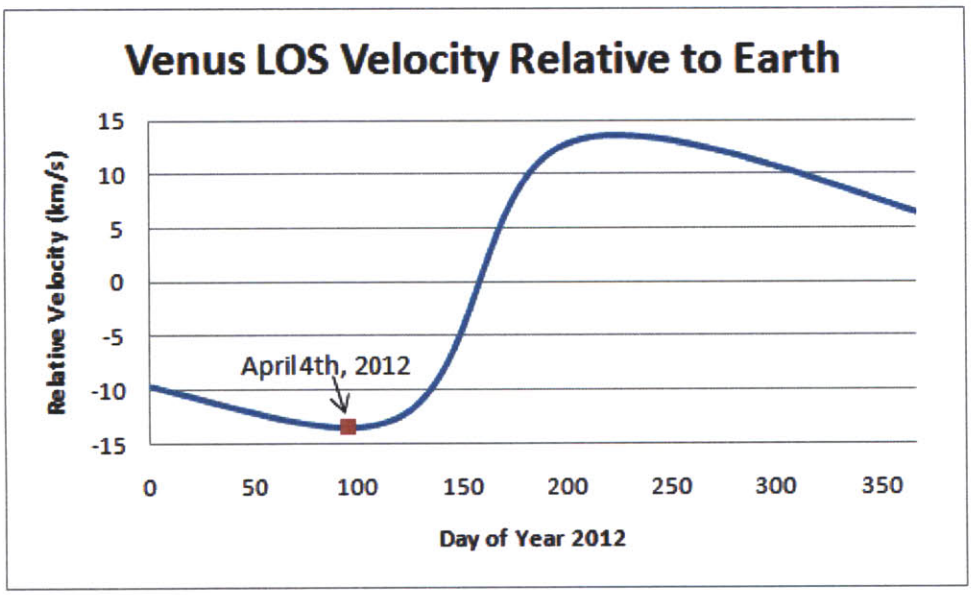


Figure 5-44: Venus' line-of-sight (LOS) velocity relative to Earth as a function of the day of the year in 2012.

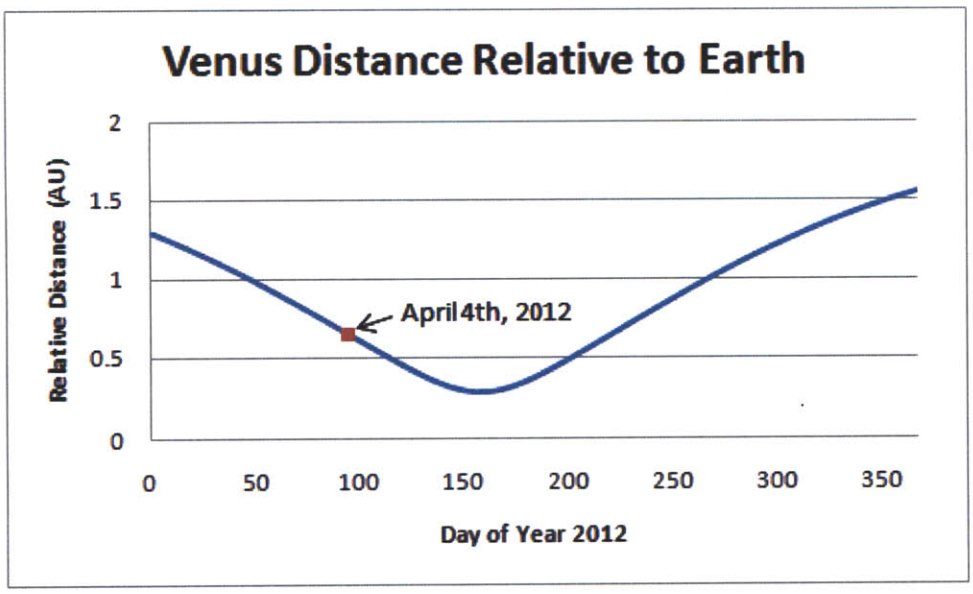


Figure 5-45: Venus' distance relative to Earth as a function of the day of the year in 2012.

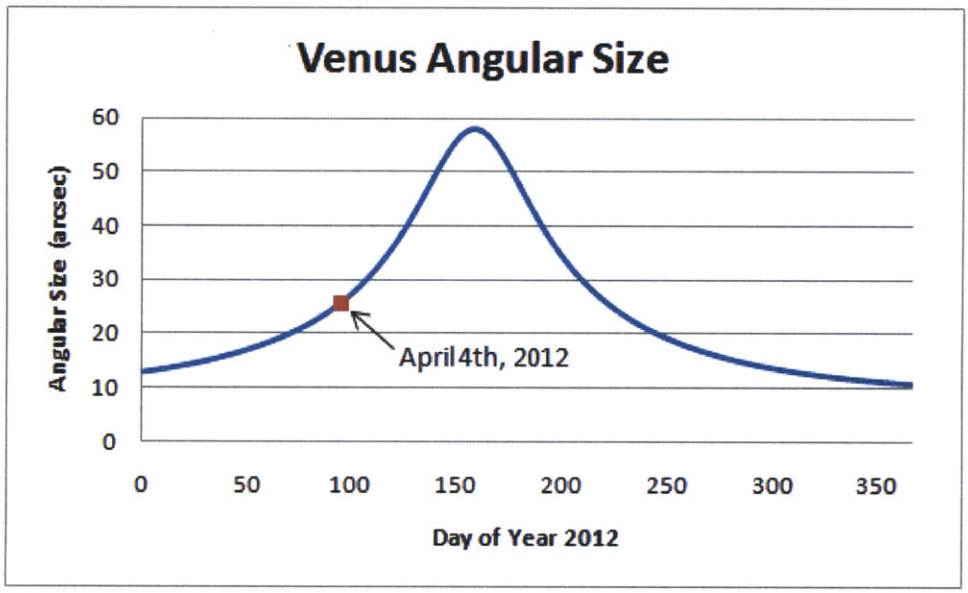


Figure 5-46: Venus' angular diameter as seen from Earth as a function of the day of the year in 2012.

data for May 13th. Notice how even though the peaks of the Venus and Earth hydrogen Lyman-alpha profiles are not resolvable like they are in Figure 5-43 but that the deuterium peak is still resolvable.

This model does not take into account how the sky brightness changes as Venus gets closer to the Sun. On May 13th, the angle between Venus and the sun is only 31.5 degrees from the Sun, and the angle of the ecliptic may not be near perpendicular with the horizon, so the sky brightness and spectral width may increase by high enough factors that it would be impossible to spectrally resolve the deuterium emission of Venus.

In addition, as Venus gets closer to the Sun, a smaller fraction of the planet will be illuminated. The disk of the planet will start to become crescent-shaped and the solid angle that is illuminated will decrease, which would rapidly lower the overall count rate especially when the width of the illuminated crescent is less than 5 arcsec. Since this parameter is sensitive to pointing accuracy and is

Great care is taken in payload maintenance, laboratory testing, shipping, and launch preparations to ensure that the optics are kept as clean as possible. Since ultraviolet light interacts with so many optics, degradation of the optics has a multi-

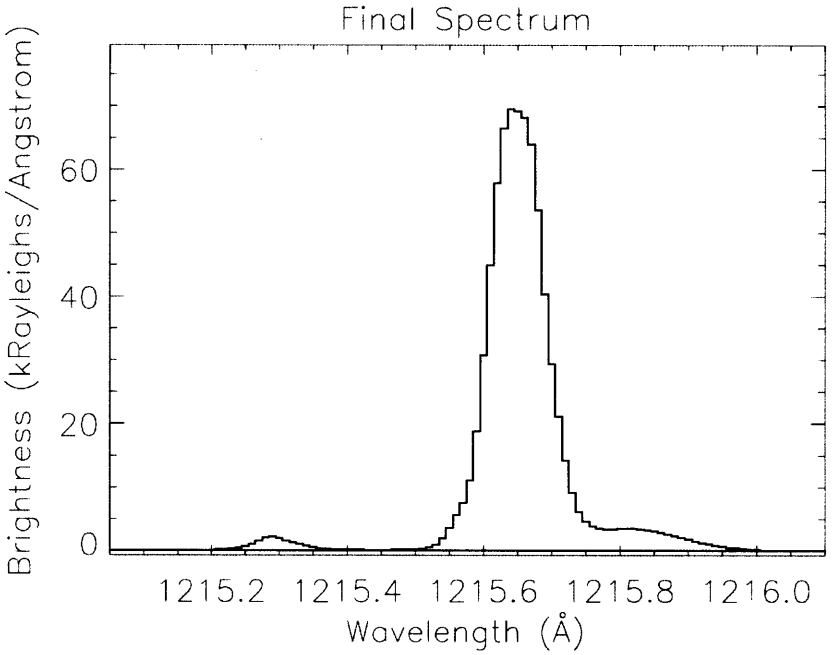


Figure 5-47: The expected spectrum that VeSpR will observe on May 13th.

plicative lowering of the overall efficiency. If the efficiency of one optic is cut in half, the entire system is half as efficient; if the efficiency of two optics are cut in half, the entire system is only one quarter as efficient.

If every aluminum mirror degrades from 75% to 70% efficiency, then the total efficiency goes down from 0.278% to 0.211%. This would decrease the effective telescope area down from 1.79 $cm^2$ to 1.35 $cm^2$. The error in the deuterium measurement of the bulk planet would rise from 4.11% to 4.72%, and the error in the measurement at the best resolution would increase from 14.75% to 16.93%. If the entire payload optical efficiency falls down to 0.5%, the bulk and best resolution deuterium measurement errors would be 6.87% and 24.61% respectively.

Although the brightness of Venus' deuterium Lyman-alpha emission estimated based on data from past experiments, how it varies is unknown; after all, the goal of VeSpR is to measure D/H at the top of the atmosphere. If the brightness in areas of the atmosphere is actually only 100 Rayleighs, the bulk and best resolution errors would be 10.56% and 37.86%, respectively. An undetectable deuterium emission would also be a major finding assuming the total efficiency of the system is high

enough to measure brightness that low.

The brightness of Earth's deuterium line is also dependent on the launch window and time. The estimate of 50 Rayleighs brightness may be too low, and if it rises it would overlap with the Venus deuterium emission. Even though the relative error goes down as brightness goes up, the absolute error goes up as the square root of the brightness, which adds uncertainty in the data when the sky background is subtracted (see Section 6.3.2 for more on sky subtraction and error propagation). The possible variations in Earth's deuterium emission are an argument against having a launch date closer to May 13th than April 4th since the ability to resolve the two becomes harder at lower blue-shifts.

In the near future, this model can be modified to be more accurate in many ways. Full payload calibration will result in a total quantum efficiency measurement of the entire payload and an accurate PSF, both of which can be easily implemented to give more realistic results.

## 5.6 Final Payload Testing

Even though the VeSpR flight was delayed from July 2010 to February 2012, there are still many tasks ahead for the payload team. Although all the components of the new design have been completed, there is still significant testing required before VeSpR is ready for flight. Delays in Wallops readiness caused slips in the BU team's schedule. Resources at BU must also be shared with other rocket projects; when the VeSpR flight was delayed, testing in the VUCL had to stop so another rocket team could use the vacuum chamber for their testing. That team is still using the laboratory, so calibration of the recoated optics has not yet occurred. This section details final testing on components that has already been done and outlines the remaining construction and testing required over the next year.


Figure 5-48: Flow of digital data in the initial TM Interface test at WFF in March 2010.

### 5.6.1 Testing the TM Interface, FDR, and GSE

The TM Interface was the first piece of the payload that was formally tested at NASA's Wallops Flight Facility (WFF). Integration testing was originally scheduled for March 2010 because the payload was originally scheduled for launch in July of that year. However, due to delays in other launches that WFF handles and the shifting duties in personnel on various projects, components for the VeSpR payload were not ready for testing. The only components of the payload that were tested during the scheduled integration were the skin sections and the TM Interface.

At this time, the new MCP detectors had not been removed from their shipping crates, so rather than having actual MCP data input to the TM Interface, simulated data was created using an AccesIO USB-DIO-32 module. This module was originally purchased because its product specifications made it appear to be capable with 32 bits of data what the USB-DIO-16A is capable of doing with 16 bits (Section 5.4). Even though USB-DIO-32 module could not record digital data coming from the TM Interface, it was very useful during testing to send digital data to any component it was connected to.

A laptop was connected to the USB-DIO-32 module. The module was then connected to the TM Interface, which was then connected to a module that is used to simulate the WFF PCM stack for ground testing. This data chain is shown in Figure 5-48. This simulated PCM module's output was connected to the USB-DIO-16A and GSE laptop. Simulated 32-bit detector data was sent through the USB-DIO-32 to the TM Interface. The TM Interface output parallel data that was read by the Wallops GSE module. The Wallops GSE module had a graphical user interface (GUI) that displayed the 32-bit data as four hexadecimal letters, and these hexadecimal letters matched what was being input.

In the first test, data from the Wallops GSE module was being flipped as it came through the USB-DIO-16A into the GSE laptop; the last two letters of the data were not in the right order. The electrical engineer notes that this particular Wallops GSE module was faulty, and another was brought to replace it. This time, the data stream was read in the correct order. The payload team requested that a third Wallops GSE module be used to verify that the test was accurate, so a third module was tested with the TM Interface. Again, data was coming through as expected.

Later testing at the MIT Kavli Institute tested the TM Interface, the FDR, and the GSE all together. Again, simulated detector data was input to the TM Interface. The TM Interface then output parallel data to the GSE, which simulated the WFF PCM module, and the FDR. First, data was sent from the USB-DIO-32 through the TM Interface and USB-DIO-16A module to the GSE laptop. It was verified that all 32 bits of parallel data were being read in the correct order.

Next, the system was powered down and the SD card was removed from the FDR. There was one file on the FDR with a file name corresponding to the time that power was first supplied to the TM Interface and FDR. This file had recorded 32 bits of data at a rate of 25 kHz with the same sequence of changes corresponding to the same times that changes were made in the data coming from the USB-DIO-32 during the test. The file also did not record data after the USB-DIO-32 was powered down, indicating that the FDR was not recording fill data being sent by the TM Interface when no data was coming from the simulated detector data stream. Although this was not an official acceptance test, it did prepare the team for acceptance testing.

### 5.6.2 Testing the High Voltage Power Supplies

Small and affordable high voltage power supplies that are qualified for spaceflight are difficult to find since the SPACOM Corporation dissolved. Rather than find new ones to supply high voltage power to the detectors, the old ones could be re-tuned to supply the correct voltage for the new detectors. Two pins on the input 9-pin connector are attached to a tuning resistor to determine the output voltage of the supply. Inside the payload, the tuning resistor used to tune the voltage for the old

detectors is permanently encased in potting on the connector itself. It will need to be replaced, but the exact resistance needed was unknown, so all the power supplies were tested.

There are five high voltage power supplies that have been used to power the detectors or were purchased as backups. Of the five, one was previously declared unusable back in the JASpR time period. Only one of them came with a test report that showed how output voltage varied with input voltage and tuning resistance, and since the report was generated more than 15 years ago there was no guarantee this was accurate for that power supply.

Figure 5-49 shows the setup used to test the detector high voltage power supplies. The supply is mounted to the breadboard in the top center of the figure. The 9-pin connector on the input side of the supply is connected to the terminal board so that the input voltage, output monitor, and input resistance can be supplied and monitored using multimeters. The potentiometer mounted to the bottom left of the breadboard was used to vary the input resistance from 6 k$\Omega$ down to 900 $\Omega$, which corresponds to -2000 V and -6000 V output for the power supply according to the specification sheet that was available for one of the supplies. The output of the power supply was connected to a 1/1000 voltage divider encased in silicone to prevent high voltage arcing. The resulting output voltage is read on a multimeter and is close to 1/1000th of the actual output voltage.

Initial tests failed because there was a short in the voltage divider. The old box was gutted, new 1 G$\Omega$ and 1 M$\Omega$ resistors were purchased, and the whole box was rebuilt with a new Reynolds high voltage connector. Silicone potting was mixed, vacuumed, poured into the box, and vacuumed again until no more bubbles were rising to ensure that all air had escaped from the inside and there was no danger of high voltage arcing when connected to a high voltage power supply. The divider was tested with a laboratory high voltage power supply while connected to a multimeter. This test showed the voltage divider actually divided the input voltage by 1100 V. Figure 5-50 shows a closer view of the rebuilt voltage divider.

Next, each power supply was tested individually. The test setup was connected to a

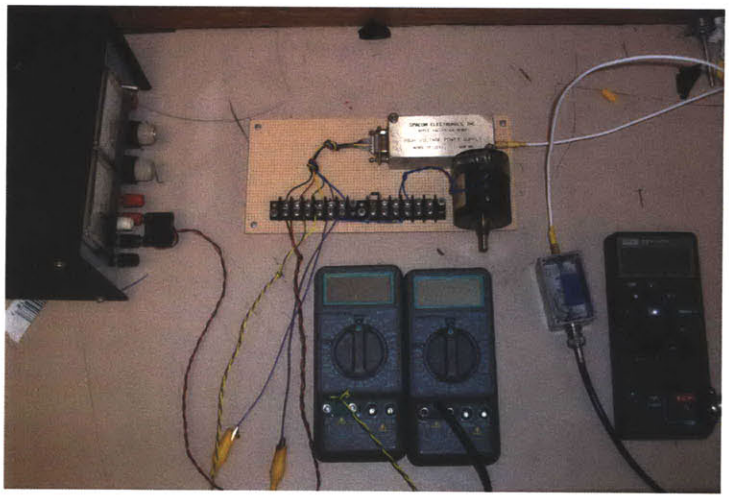

Figure 5-49: Detector high voltage power supply testing setup.

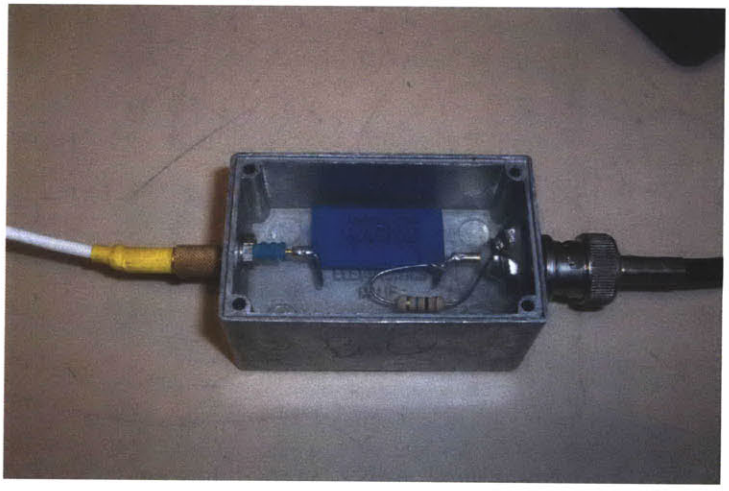

Figure 5-50: The rebuilt voltage divider used to test the output from the high voltage power supplies.

supply and the resistance of the potentiometer was measured before power was turned on. The output voltage was recorded, and then power was turned off. Once power dissipated from the system, the resistance was measured and changed. Each power supply was tested at 11 different resistances to generate a function to determine the output voltage given an input resistance. The input voltage was not varied between +24 V and +32 V, which was a test the specification sheet also showed, but since the change in voltage has little effect on the output and no significant change in voltage is expected in flight, this did not matter. In addition, the resistance function was tested at a higher resolution, 11 samples compared to the specification sheet's 5 samples.

The testing showed that the power supply that had originally been labeled unusable was still working, even though it will not be used in flight without further testing. In addition, the input resistance for the necessary output for the detectors for every power supply was found to be within a 20 Ω range, so if a power supply fails during testing, it can be switched out without requiring a change in the input resistor. All of the supplies are the same model, but the variations between performances still needed to be measured for this assumption. The full results from high voltage power supply testing are available on the attached Appendix DVD.

### 5.6.3 Future Testing and Construction Plan

As stated previously, the division of resources available at BU has caused some delay in the final testing of the payload optics and the new MCP detectors in the VUCL. In addition, the team has encountered problems with the collimating mirror in the VACTEF vacuum chamber, delaying future work for full payload testing. Work is currently underway to realign and reinstall the mirror in the chamber for full payload testing. Without this mirror, a full payload absolute calibration cannot be made in the VACTEF. While progress on Project VeSpR has been hampered, the science team members have been working on additional projects (see Chapter 6), laying the groundwork for changes in the VACTEF to be capable of testing future space flight hardware, rewiring the harnesses that have changed to connect to the payload during vacuum testing, and documenting the new state of the payload to save future team

members time so they do not have to sift through two decade's worth of notebooks from previous payload flights.

The first test the science team will conduct is activating the new XDL MCP detectors. Simply activating the detectors and reading data will do the following; confirm that the detectors were not damaged in shipping; verify that the output cables from the detector are the proper lengths to induce the needed line delay; test the GSE, TM Interface, and FDR with actual MCP data, allowing the components developed by the Kavli Institute to be officially accepted; display MCP data on the GSE computer in real time; and obtain flat field exposures that can be compared with the test report that Sensor Sciences provided for the detectors.

It has still not been officially decided whether the electronics developed at the Kavli Institute will be potted after they have been tested with the MCP detectors or immediately before the Vibration Test during integration testing. The electronics will not be potted before this test because if any modifications are needed to the board, they cannot be made after the board has been potted. The electronics must be potted before the Vibration Test because they will not survive without potting. The decision will be made once WFF informs the payload team whether or not they will be ready for integration testing in spring 2011 (see Section 5.6.4 for more in integration testing). Potting of the electronics and connectors can be done at BU, MIT, or WFF.

After testing and calibrating the MCP detectors, the spectrograph box will be aligned. First, all the components except the coated optics will be bathed in iso-propanol and acetone, and what components are small enough to fit in the ultrasonic bath in the VUCL will be cleaned in there as well. Next, the spectrograph box will be reassembled in the VUCL clean room and placed in the vacuum chamber. The set screwed will be turned to the heights that were determined in previous testing to be where the grating is aligned such that the 221st order of Lyman-alpha will be visible on the detector. The spectrograph box will be aligned in the vacuum chamber with a green laser before the chamber is pumped down and the alignment is checked. If the Lyman-alpha emission line is not centered on the detector, the set screwed will

be measured again and turned to the correct height. Once alignment has been found, the top plates that secure the grating will be installed and alignment will be checked again. Finally, an absolute calibration of the detector with the spectrograph box will be made. Now that the team has considerable practice with this tedious endeavor, it should not take nearly as long as it did during initial payload testing (Section 4.5).

Next, the telescope secondary mirror will be aligned with the VACTEF collimating mirror. The secondary mirror adjustment locks (Section 5.3.6) will be installed and the pushrods will be screwed into place so that the telescope has an optical quality of at least 2 arc sec. Once this has been achieved, the two locking mechanisms will be tightened and the alignment will be checked again to ensure that tightening the locks did not misalign the secondary mirror. The telescope will then be moved to the VACTEF and absolutely calibrated with the PMT (now that the PMT has been absolutely calibrated, the same setup that was described in Section 4.5 to obtain a relative calibration can be used to obtain an absolute calibration).

Next, the entire payload will be reassembled for full payload testing in the VACTEF vacuum chamber. The required screws and other supplemental hardware have already been purchased and the majority of the payload can be reassembled at any time. First, optical alignment of the spectrograph, imager, and Xybion camera will be checked. The Xybion camera will be aligned at atmospheric pressure with a visible light before the chamber is pumped down. The imager detector and Xybion camera should see the same field of view because they are mounted on the same structure, which has not changed. The alignment of the spectrograph box may need to be further adjusted with the Teflon supports mounted in the plate that separates the Spectrometer Section from the Spectrometer Extension Section. Since the VACTEF can be quickly brought to air and pumped down again, this will not take as long as the spectrograph alignment in the VUCL will.

Finally, an absolute calibration of the spectrograph and imager detectors will be made. If the total system performance is not adequate to achieve the science goal (Section 5.5), the payload will be taken apart to locate the degradation in the efficiency. Since the spectrograph box and telescope will have been absolutely calibrated before

the full payload test, there should not be a significant degradation in the efficiency in any optics compared to their calibration tests. If there is, this could mean contamination in the vacuum chamber. Both the VUCL and VACTEF vacuum chambers will be checked for contamination using a mass spectrometer, and individual optics testing will be conducted again.

Once the payload has been thoroughly tested, it will be placed back in storage in the shipping crate that will be used to transport it to Wallops. Power will still be supplied to the VIPs so the MCP detector housings stay at vacuum.

### 5.6.4 Integration Testing Plan

Integration testing will take place at WFF in spring or summer 2011, but the date has not been officially scheduled at this time of writing. Preliminary estimates from VeSpR's new Mission Manager indicate that WFF will still not be ready for integration testing by March; it may be delayed until the summer of this year. The Integration Testing Plan was put forward during the Design Review and has not changed since then. Integration Testing consists of instrumentation, power, and mechanical tests on the payload to ensure that all components are communicating properly and that the system is structurally capable of withstanding launch loads without failing or losing optical alignment during launch.

#### 5.6.4.1 Instrumentation Tests

The first phase of the instrumentation tests is the Pre-Vibration TM Electrical Checkout. This test will be performed based on a customized version of a standard TM Checkout work instruction that is specific to each payload section for this mission. Some of the sections in this work instruction will be repeated and/or completed during Post-Vibration TM Electrical Checkout and At-Range TM Electrical Checkout. The Post-Vibration & At-Range sections of this work instruction are abbreviated versions of the Pre-Vibration TM Electrical Checkout. Major items in this checkout include: setting carrier deviation and radio frequency measurements of system pa-

rameters, power, VSMR, and drop-out; verifying and/or calibrating communication channels; calibrating the monitor circuits for the bus voltage and current monitors; and checking the functionality of all sensors and monitor circuits.

Next is the Pre-Vibration Integration of the subsystems and the experiment. This testing will be performed based on a customized TM Integration procedure that is specific to this mission. Some of the sections in this procedure will be repeated and/or completed during Post-Vibration TM Integration and At-Range TM Integration. The Post-Vibration & At-Range sections of this procedure are abbreviated versions of the Pre-Vibration TM Integration. Major items in the Pre-Vibration TM Integration include; an external power test of the subsystems and experiment; functional testing of break-wires and other components; and a timer sequence test in the flight configuration.

Following the Pre-Vibration Integration is the Vibration Test. Details on the Vibration Test will be discussed with mechanical tests later in this section. During the Vibration Test, the payload will be powered on and in the flight configuration and the telemetry will be monitored throughout the vibration test.

After the Vibration Test are the Post-Vibration Integration and Post-Vibration TM Electrical Checkout tests. These are both abbreviated repeats of the Pre-Vibration tests. There will also be a Post-Vibration Vacuum Test. The objective of this test is to pump down the TM system in a vacuum chamber and verify the transmitter does not experience corona breakdown. However, the experiment will not go into the vacuum chamber because of cleanliness issues encountered during the JASpR 4 integration testing (see Section 3.1).

Repeats of the two Pre-Vibration tests will also be conducted when the payload is transported to White Sands Missile Range (WSMR) before flight.

#### 5.6.4.2 Power Tests

The first phase of the power tests are the Pre-Integration Checks. There are five tests in this phase. First, an electrical checkout will be done on the payload to ensure that all components are operational and receiving the proper amount of voltage. Then,

the altitude switches will be pumped down to verify the altitude that the switches activate and deactivate. Next, an all-fire sequence test will be performed with the timer running and the altitude switches pumped down. The payload will be switched to internal power and the umbilical cables will be pulled to verify no change in the systems' performance. During this test, the Lanyard switches that supply backup power in case of a failure of the main power supply will be tripped in order to ensure that the payload will remain on internal power.

Following the all-fire sequence test, a no-fire sequence test will be performed with the altitude switches not pumped down. This ensures that all altitude switch protected events do not occur. During this test, the payload will be switched to external power and the Lanyard switches will be tripped to ensure that the Lanyard switches will cause the payload to use internal power. Finally, the payload will be turned off and the Lanyard switches will be tripped to ensure that the Lanyard switches will cause the payload to use internal power.

The next phase of the power tests is the Pre-Vibration Tests. First, all interface connectors will be verified with the experiment and subsystem to verify proper functionality. This includes voltages, grounds, relay switching, and more. Next, all experiment and subsystems will then participate in Sequence testing. This is to ensure that everything is ready for vibration testing.

Next is the Vibration Test. During the Vibration Test, match squibs will be installed at all pyrotechnic connectors to monitor for any abnormal squib firings. After the Vibration Test, the Post-Integration Tests will be performed, which are identical to the Pre-Vibration tests. This will ensure that during vibration there were no compromises or broken connections.

Once the payload is moved to WSMR, a final all-fire sequence will be run while the payload is oriented horizontally. This is the last verification that all interface connectors are properly connected prior to moving the payload to the launch rail. Once the payload is moved to the rail, all systems will be turned to verify that they are functioning properly prior to launch.

#### 5.6.4.3 Mechanical Tests

There are four mechanical tests that will be performed during integration testing, the first of which is the Bend Test. The launch configuration of the payload will be subjected to a bending moment based on the largest of the following: 125% of the maximum 6 degrees of freedom (DOF) bending moment; 100% of the RSS bending moment; or 50% of the rated capacity of the motor head cap. The current estimated maximum bending moment at the head cap of the BBV is 202,625 in-lbs (based on the 125% of 6-DOF method). This will require a force of 901.95 lbs to be applied beneath the nosecone to generate the required test moment of 202,625 in-lb. The current predicted tip deflection is 3.7 inches.

For the Vibration Test, the payload will be subjected to; a Thump Test; a Flight Level 2 Random in X and Y Axis including a -12 dB snapshot; a Flight Level 2 Random in Z Axis; a œ g Sine in Z Axis; and Flight Level 2 Sine in Z Axis. The GLNMAC (CACS) and LN-251 (LTM) will be removed and a mass model will be substituted during vibration testing, but the actual LN-200 (S-19L) will remain in the payload for vibration testing.

Next, the final mass properties of the payload, including weight and center of gravity, will be measured in both the launch and reentry configurations. Estimated mass properties of all system components already exist but an accurate measurement is needed for flight modeling and analysis.

Finally, the payload will be put through a Spin Balance Test. The payload will be balanced both statically and dynamically in the launch configuration. Each section will undergo a balance check after the balance weights have been installed. The spin requirement is that the residual dynamic imbalance is less than 20,000 oz-in$^2$ and the residual dynamic imbalance is less than 300 oz-in in the launch configuration. In addition, the tip indicated runout (TIR), which is the amount of lateral misalignment of the payload measured at the nose tip, will be measured at the base of the nosecone in the payload's launch configuration. The TIR is to be less than 0.25 in.

#### 5.6.4.4 Additional Testing

Although it is not the responsibility of the payload team, the S-19L Boost Guidance System will be put through the following tests both before and after vibration: pneumatic high pressure transducer calibration; pneumatic leak test; servo amplifier test; servo bias test; Y and Z channel DC-input measurements; Y and Z channel frequency test; voltage and current consumption; EEprom code verification; autopilot verification; launcher location verification; IMU mode change verification; IMU drift test; total gain test; roll resolving function test; pressurization and R-T-L function test; liftoff and flight program verification tests; battery test; canard decouple test; and pre-vibration and post-vibration sequence tests.

After integration testing at WFF, the payload will be brought back to BU. A final system-wide absolute calibration will be conducted in the VACTEF along with additional system checks to ensure that the system still has a high enough efficiency to achieve the science goals of the mission.

# Chapter 6

# Analyzing the Jupiter Lyman-alpha Bulge

## 6.1 Nature of the Data

The data being analyzed in this study comes from two separate Hubble Space Telescope campaigns using the Space Telescope Imaging Spectrograph (STIS) studying Jupiter. One campaign recorded images, the other recorded spectra, and both campaigns were timed so the observations took place when the Bulge and Anti-bulge regions appeared on the limb of the planet.

### 6.1.1 Image Data

Four exposures were taken using STIS, two while the Lyman-alpha bulge was close to the limb of Jupiter, and two while the Anti-bulge was close to the limb. Table 6.1 summarizes the dates, filters, exposure times, and the central meridian longitudes (CML) at the beginning of the exposures.

Each exposure is centered near a limb of Jupiter and lasts for upwards of 18 minutes. A side-effect of these long exposures is that the planet rotates a considerable amount during the exposures. Jupiter's 9.8 hour rotation period means that it rotates about 11 degrees during each exposure, and another couple of degrees between

Table 6.1: Properties of the STIS UV images of the Bulge and Anti-bulge on the limb of Jupiter

| Region | Date | Start Time | Exposure Time | Filter | CML |
|---|---|---|---|---|---|
| Dawn Bulge | 1999 Jun 28 | 18:36:52 | 1100 | 25MAMA | 132.5 |
| Dawn Bulge | 1999 Jun 28 | 18:58:45 | 1231 | F25SRF2 | 146.4 |
| Dusk Anti-bulge | 1999 Jan 19 | 15:18:02 | 1100 | 25MAMA | 184.5 |
| Dusk Anti-bulge | 1999 Jan 19 | 15:42:25 | 1231 | F25SRF2 | 171.5 |

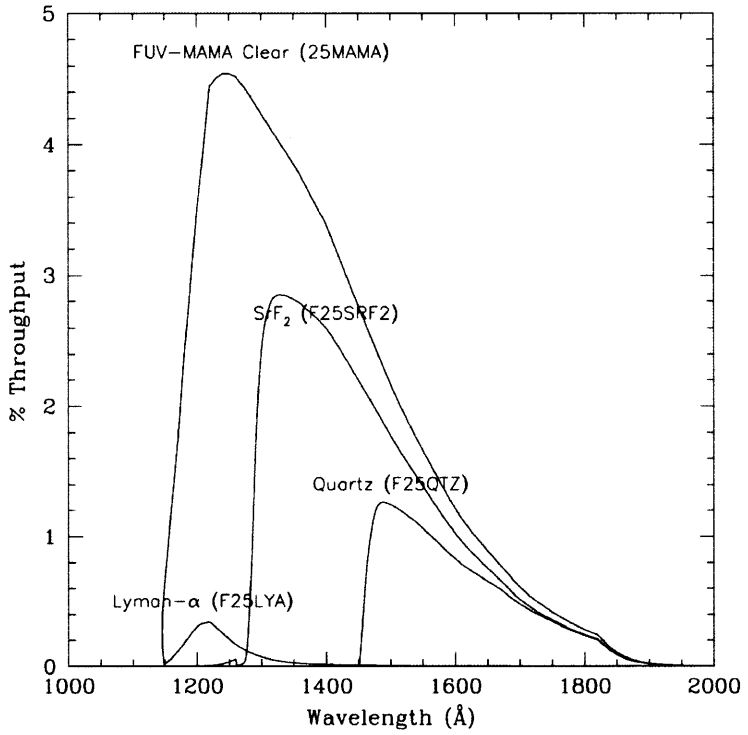


Figure 6-1: Throughput of various filters available for STIS images.

exposures. This decreases our ability to see longitudinal differences in the upper atmosphere, but leaves intact our ability to investigate the atmosphere's latitudinal structure.

The images were recorded with two different filters because the goal is to isolate the Lyman-alpha emission of the planet. Figure 6-1 shows the optical throughput of all the filters available for STIS imaging.

An image on each area was taken with the F25SRF2 filter because it blocks Lyman-alpha light (henceforth called the "filtered" images). The remaining images were taken with the 25MAMA filter because Lyman-alpha has a high throughput (the "clear"

image). The filtered images can be scaled and subtracted from the clear images to isolate the region around 1216 Å, which is the Lyman-alpha emission of the planet. The filtered images were exposed for a longer period of time compared to the clear images because of the decreased throughput. This allows the signal-to-noise ratio of the filtered images to be closer to that of the clear images.

Even though the F25LYA filter is specifically for capturing Lyman-alpha-only images, its optical throughput is so low (~0.4%) that Hubble would require a much longer exposure time in order to take an image with the same signal-to-noise ratio. In addition, in that extra time required, Jupiter would rotate significantly more. Since the clear and filtered images have throughputs of roughly 4.5% and 3%, respectively, and the target does not move as much during the combined exposure time, the technique of subtracting the two images is better overall.

### 6.1.2 Spectrum Data

The goal of the second campaign was to capture high-resolution spectra of the limb of Jupiter using the STIS E140H echelle grating. Spectra with the Bulge and Anti-bulge at the limb were recorded, just like in the image data, but spectra of areas in the latitudes north and south of the bulge were also observed with the use of a long aperture so that all four regions could be compared and contrasted. Comparing the northern and southern regions with the Bulge is important to determine the extent to which the Jovian aurorae are influencing the atmosphere in the Bulge region.

During the first observation window in November 1999, the HST observations were not successful, and as a result, most of the data are unusable. The shutter door failed to open during the Bulge observation. Target acquisition failed before Hubble pointed at the Northern Limb, and the view drifted during both of the observations. Acquisition also failed during the first attempt to observe the Anti-bulge, but it was corrected during the second attempt. A Hubble Operations Problem Report was filed and duplicate observations were rescheduled to January 2001.

Problems were encountered during the second visit as well. The shutter door failed to open during both attempts to observe the Anti-bulge. The first attempt to observe

Table 6.2: Properties of the STIS E140H high resolution spectra of the Bulge, Anti-bulge, and northern and southern latitude on the limb of Jupiter. Exposure times are in seconds, LOS and Rotational velocities are in km/s.

| **Region** | **Exposure Info** | | **Magnetic Coord.** | | | **Line Shift** | | |
|---|---|---|---|---|---|---|---|---|
| | Date | Time | Long | Lat | CML | LOS | Rot | $\Delta\lambda$ |
| Bulge | 2001 Jan 26 | 1740 | 90 | 0 | 180 | 25.35 | 12.73 | 0.154 |
| Anti-bulge | 1999 Nov 11 | 1140 | 90 | 0 | 210 | 10.56 | 12.73 | 0.094 |
| Northern Limb | 2001 Jan 26 | 1140 | 85 | 20 | 205 | 25.36 | 11.96 | 0.151 |
| Southern Limb | 2001 Jan 23 | 1140 | 85 | -10 | 190 | 24.98 | 12.54 | 0.152 |

the Bulge failed because guide star acquisition failed again and there may have been pointing drift. The second attempt to observe the Bulge was successful. Similar problems caused the first attempt to observe the Northern and Southern Limbs to fail, while the second attempts were successful.

After three different visits in 1999 and 2001, one usable observation of each target was made. Table 6.2 summarizes some of the properties of the data used in this study. The coordinate system used to locate the targets is based on the magnetic dip equator, where the Bulge is centered.

All four spectra were observed when Earth had a high receding line-of-sight (LOS) velocity relative to Jupiter to make the emissions from Jupiter red-shifted relative to the geocoronal emission (see Section 2.5). In addition, the spectra were observed on the dusk side of the planet so the fast rotation period also contributed a significant amount to the red-shift away from line center and the geocoronal emission. The Anti-bulge was observed at a different time period where the LOS velocity between Earth and Jupiter was lower, so the geocoronal emission is closer to line center.

## 6.2 UV Image Analysis

The two sets of images were put through a reduction pipeline to obtain the Lyman-alpha-only images of the Bulge and Anti-bulge. This pipeline starts by reading the clear and filtered image data files from one set as an array of brightness per pixel in units of kiloRayleighs (kR). Each image comes with an associated almanac file that lists the right ascension and declination of the observation. From this information,

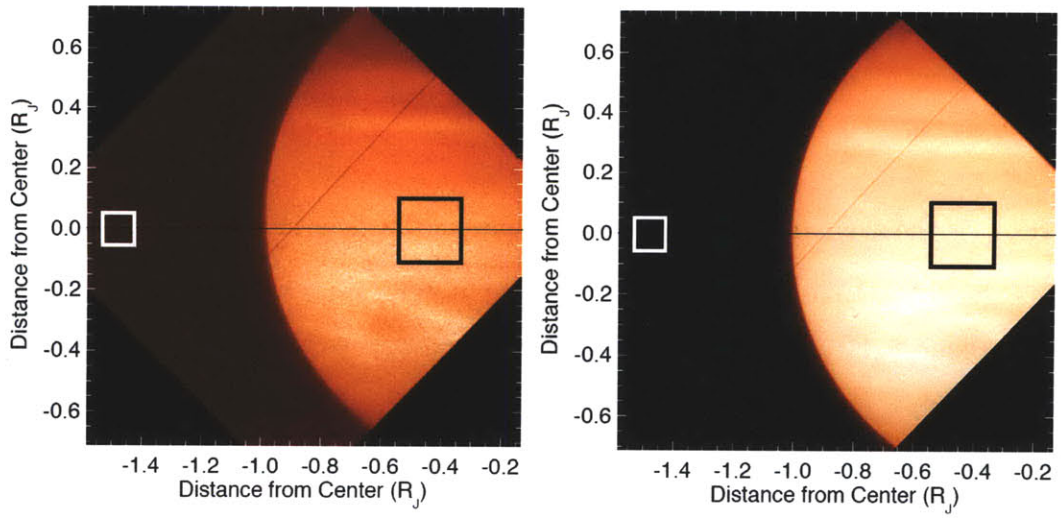


Figure 6-2: The clear 25MAMA (left) and filtered F25SRF2 (right) images of Jupiter with the Bulge on the limb. The off-planet (white) boxes show where the background sky was subtracted. The on-planet (black) boxes show the region where the F25SRF2 scaling factor was determined.

NASA's Navigation and Ancillary Information Facility (NAIF) can be used to derive the location of the center of the planet. The program shifts the center of the planet in the clear image so it is aligned with the center of the planet in the filtered image. Both images are then rotated so Jovian north is pointing up. Figure 6-2 shows the two images when the Bulge is on the limb.

Next, the sky background was subtracted in both images. A 100 x 100 pixel region was defined near the edge of each image, shown in Figure 6-2 as the white box to the left of the planet. The average brightness per pixel was calculated and subtracted from the entire image.

Next, the intensity of the filtered image was scaled to that of the clear image. A 200 x 200 pixel region was defined near the center of each image, shown in Figure 6-2 as the black box near the right side of the image, and the average brightness per pixel in the region was calculated. It is known that the average brightness of the Lyman-alpha emission on the disc of the planet is about 8 kR. To account for the difference in sensitivities between the 25MAMA and F25SRF2 filters, a scaling factor was calculated to use the known difference in brightness on the disc between the two images because of the filter and sensitivity and exposure time differences. The scaling

factor $S$ was defined as

$$S = \frac{A_C - A_{Ly\alpha}}{A_F} \tag{6.1}$$

where $A_C$ is the average brightness of the square in the clear image, $A_{Lya}$ is the average brightness of the Lyman-alpha emission (8 kR), and $A_F$ is the average brightness of the square in the filtered image. The filtered image was then multiplied by this scaling factor.

Finally, the Lyman-alpha image of Jupiter, shown in Figure 6-3, is obtained by subtracting the scaled filtered image from the clear image. The darker diagonal line that appears in each of the original images is an instrumental artifact caused by the shadow of a repeller wire within the STIS instrument. The wire is designed to increase the quantum efficiency of the microchannel plate detector. Pixels on these lines were disregarded during the analysis. The high noise levels seen on the disc result from subtracting two large numbers. Larger variations in brightness are due to the planet rotating between observations, so a brighter region would be overly subtracted and dark in one spot and brighter in another in the Lyman-alpha-only image.

Next, the brightness across the limb as a function of latitude was found. First, the location of the limb was calculated. Because Jupiter rotates so quickly, it is not spherical, so the location of the limb as a function of latitude was calculated using the known polar and equatorial radii. Then, the image was rotated at one degree intervals between $\pm 40$ degrees latitude. At each line of latitude on the limb, a region 20 pixels tall that stretched across the entire length of the image was defined. Figure 6-4 shows an example of this process where the image rotated to 25 degrees latitude. The yellow box outlines the 20 pixel tall region, and the black line near the center of the box is the calculated 1-bar level of the cloud tops.

The averages and standard deviations of the vertical columns of each of these regions were calculated and plotted as an intensity trace across the limb. An exponential function was fit from the peak intensity down to the first point where the brightness went below zero to calculate the scale height at each line of longitude.

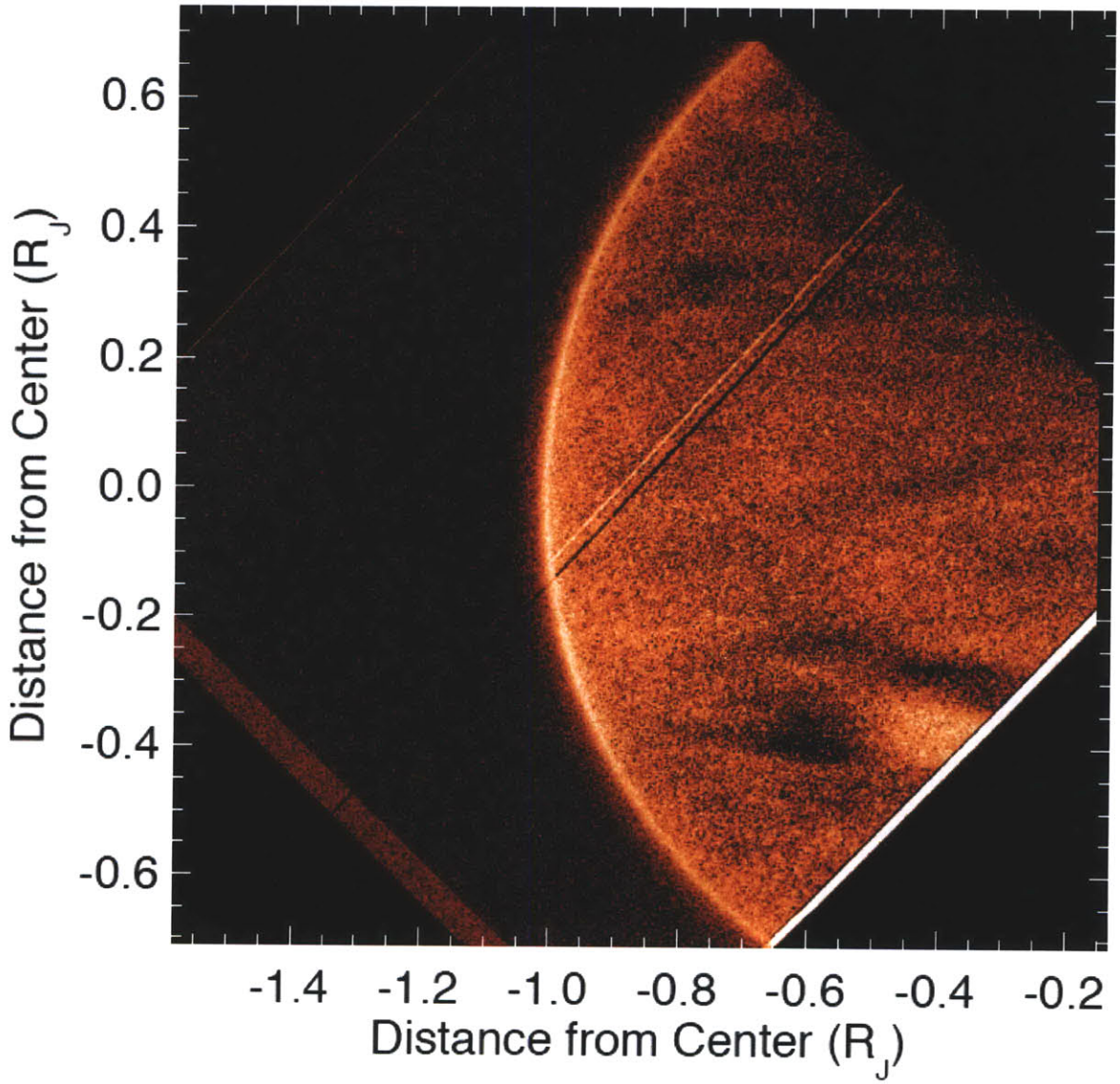


Figure 6-3: Lyman-alpha image of Jupiter with the Bulge on the limb. See text for an explanation of the noise on the disc.

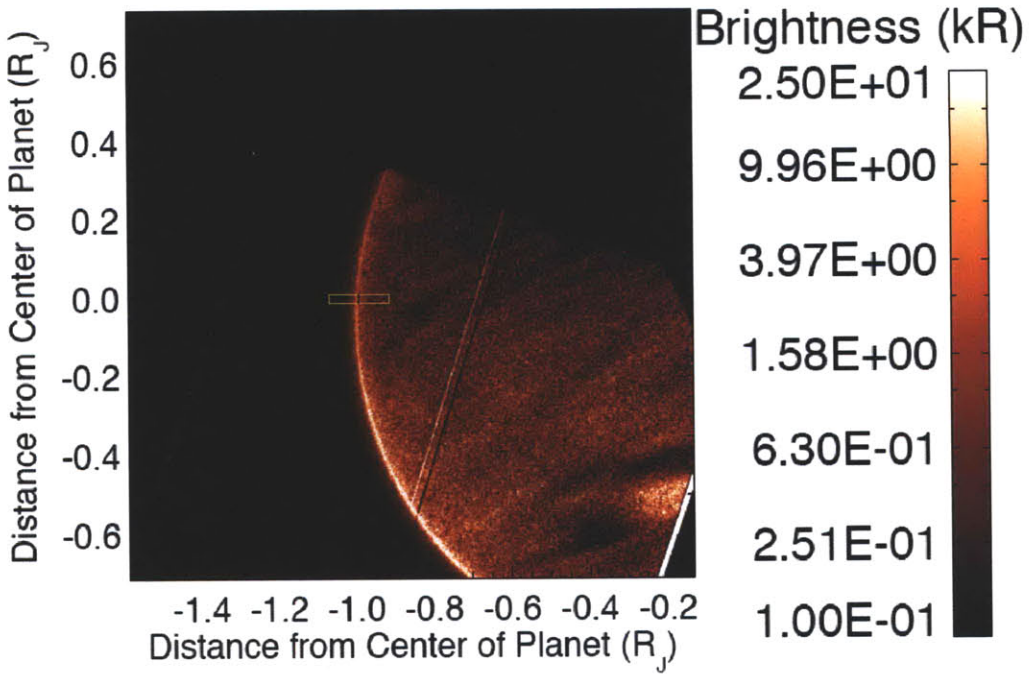


Figure 6-4: Example region on the limb at 25 degrees latitude defined to calculate the brightness across the limb.

Figure 6-5 shows an example of an intensity trace across the equator. The white line shows the average value of the pixels in each vertical column and the black regions show the standard deviation. The red shaded region indicates the brightness within $\pm 5$ pixels from the peak brightness across each intensity trace. These values were averaged to obtain the mean limb brightness at this longitude. The thin red line indicates the best fit exponential function to the brightness curve above the Lyman-alpha peak.

The mean limb brightness was plotted as a function of latitude for both the Bulge and Anti-bulge Lyman-alpha images, shown in Figure 6-6. The error bars indicate the standard deviation in the calculation of the mean brightness, and the black data points indicate the latitudes where the repeller wire interfered with the intensity trace across the limb.

When the Bulge was observed, the magnetic equator is about 15-20 degrees north of the rotational equator. The analysis shows that a peak in hot hydrogen brightness occurs near 10-20 degrees north latitude, although the repeller wire limits the ability

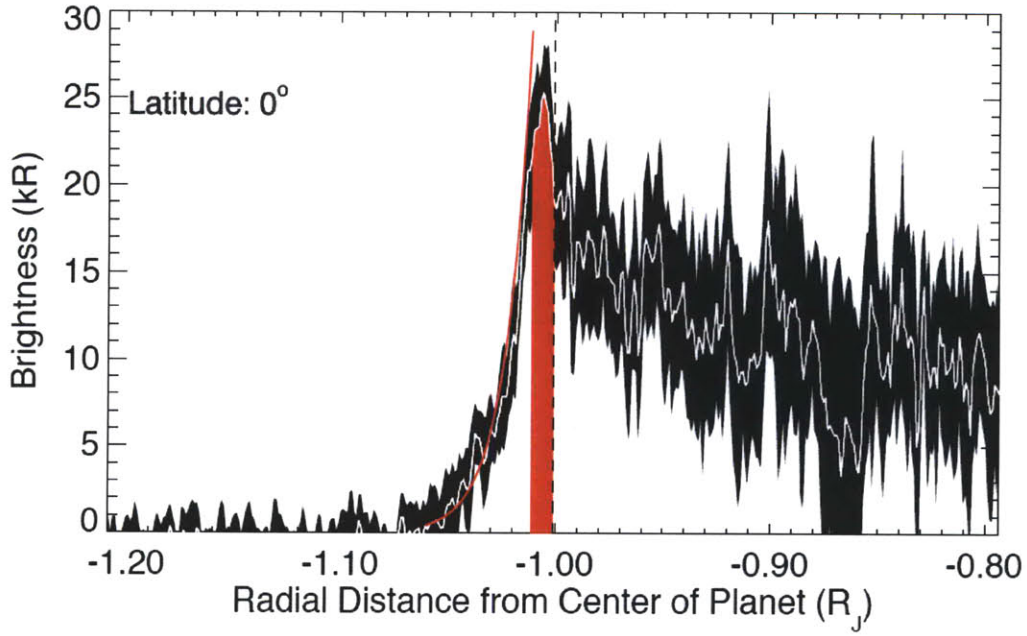


Figure 6-5: Example plot of the intensity trace across 0 degrees latitude. The white line shows the average value of the pixels in each vertical column and the black regions show the standard deviation. The red shaded region shows the area where the mean limb brightness was calculated and the thin red line indicates the best fit exponential function to the brightness curve.

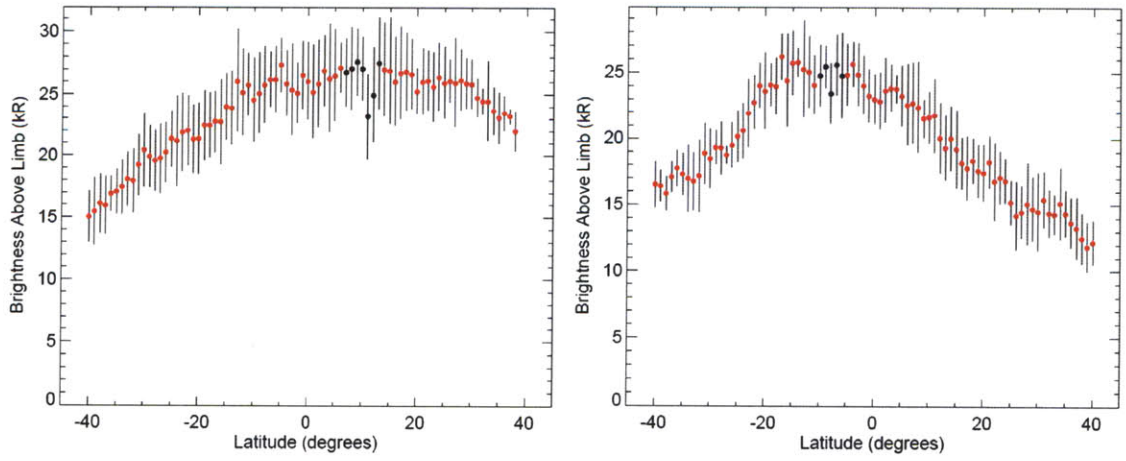


Figure 6-6: Limb brightness as a function of latitude for the Bulge (left) and the Anti-bulge (right)

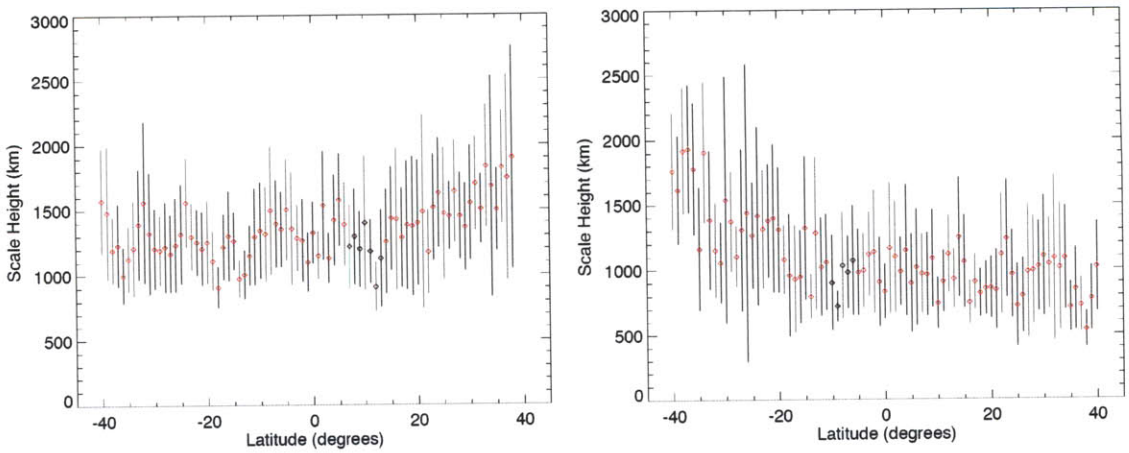


Figure 6-7: Scale height variation with latitude on the Bulge (left) and Anti-bulge (right)

to resolve the exact peak. This observation is consistent with the Bulge being centered around the magnetic equator.

At the Anti-bulge, the peak of the brightness of the hot hydrogen upper atmosphere is well south of the rotational equator. The magnetic dip equator on the limb at the time of the observation was between 0 and -5 degrees south latitude. Again, the repeller wire limits the ability to resolve the exact peak, but the peak may be further south than the magnetic magnetic equator; is certainly not aligned with the rotational equator.

The exponential function fit to the decay in brightness with increasing altitude at each line of latitude was used to find the scale height. Figure 6-7 shows the variation in the atmospheric scale height as a function of latitude along the limb of the two images.

The only trend in both cases is an increase in scale height toward a pole. In the Bulge image, where the magnetic equator and peak brightness were north of the rotational equator, the scale height increases at latitudes higher than 20 degrees north of the rotational equator. In the Anti-bulge image, where the magnetic equator and peak brightness were south of the rotational equator, the scale height increases at latitudes lower than 20 degrees south of the rotational equator. The average scale height on the Bulge limb is approximately 250 km higher than at the Anti-bulge

limb. This is more evidence that the phenomena observed at the magnetic equator are being influenced by activity in higher latitudes.

The analysis of these Lyman-alpha images of the Jupiter limb provides strong evidence that the center of brightness along the limb is not tied to the rotational equator. The analysis also shows strong evidence that the center of brightness along the limb is tied to the magnetic equator. There is also some supporting evidence that activity along the magnetic equator is influenced by higher latitudes.

## 6.3 Spectrum Analysis

### 6.3.1 Spectrum Reduction Pipeline

Data from the spectral observing campaign were downloaded from the Space Telescope Science Institute (STScI), which stores data from all Hubble observations for anyone to download and analyze. Unlike the images, the spectra need to be corrected for distortions before they can be analyzed. The data are available in several different forms that have some level of corrections, but for this analysis the raw data files were put through an IDL reduction pipeline described here to obtain the reduced spectra for data analysis. Figure 6-8 shows the raw data from the Bulge observation.

The raw data are represented in IDL as a 2048 x 2048 array with values corresponding to individual photon counts recorded by the detector. This array is first shrunk to a 1024 x 1024 array that preserves the total counts but does not otherwise change the data as it appears in Figure 6-8. The next step is to remove the dark counts data from the raw data. The dark data file is taken from STScI and multiplied by the exposure time then subtracted from the raw data to obtain the dark-corrected data. The difference between the raw and the dark-corrected data is almost unnoticeable but is nevertheless important.

Next, flat-field corrections were implemented to correct for changing sensitivity across the field of view. There are two flat field corrections implemented in this pipeline, low-order and pixel-to-pixel. The low-order flat field correction corrects for

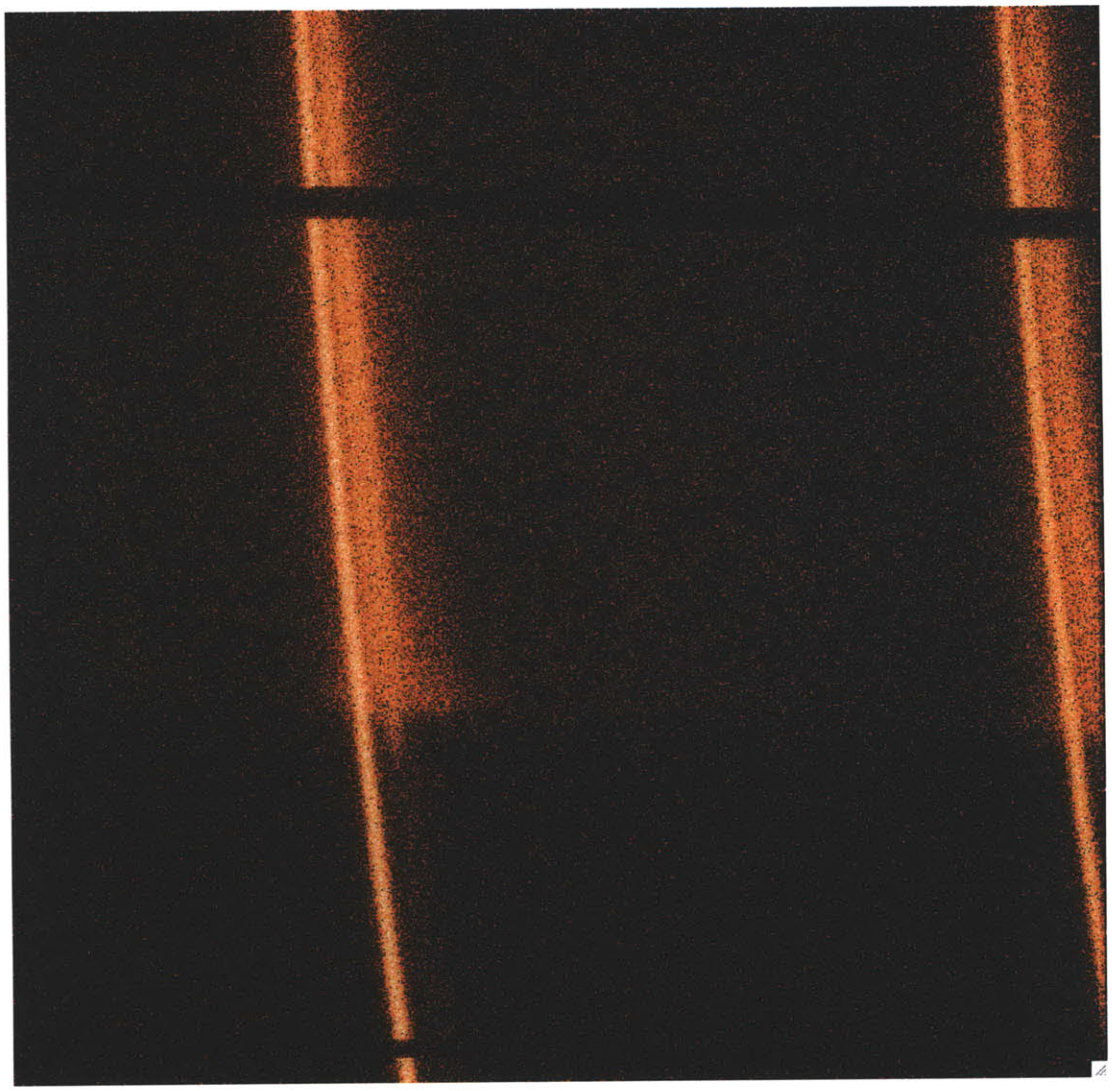

Figure 6-8: Raw data for Hubble STIS spectral-spatial observation of the Jupiter Lyman-alpha Bulge

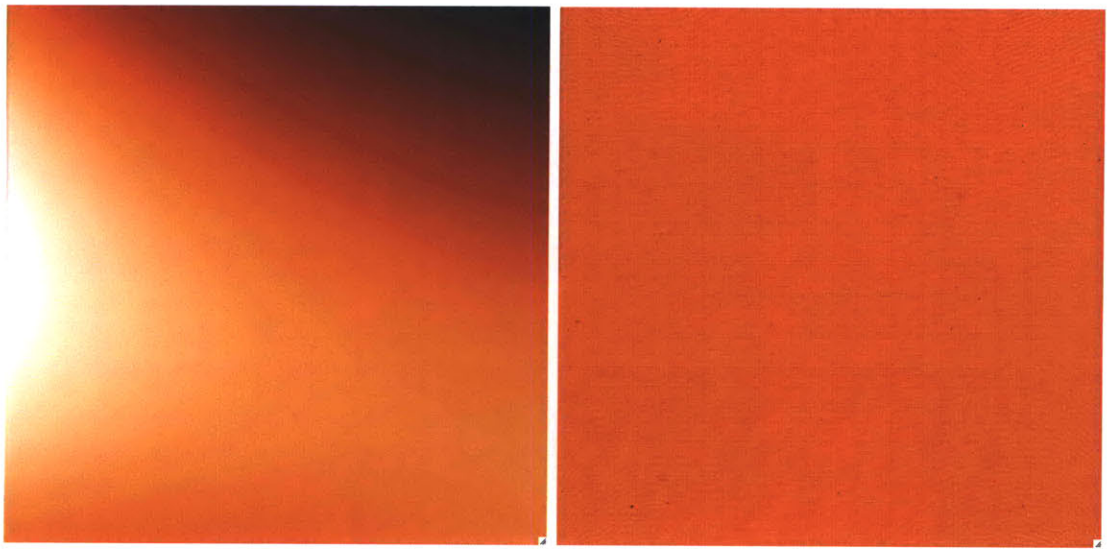

Figure 6-9: Low-order flat field (left) and pixel-to-pixel flat field (right) corrections for E140H data. Values on the low-order flat field range from 0.837 to 1.049. Values on the pixel-to-pixel flat field range from 0.001 to 1.433.

variations in sensitivity of the optics in HST. The pixel-to-pixel flat field correction corrects the spectrum for variations in the sensitivity in the detector. Figure 6-9 shows both the low-order and flat-field corrections. Notice the hexagonal grid pattern in the pixel-to-pixel flat field that corresponds to the detector's multichannel plate bundles. Photons striking the edges of these bundles have a decreased probability of registering a count in the detector.

These two flat field corrections are multiplied together to form the combined flat field correction. The dark-corrected data is then divided by this combined flat field correction to obtain the flat field corrected data. Both the combined flat field correction and flat field corrected data are shown in Figure 6-10.

Notice that the strong line corresponding to the geocoronal emission running from top to bottom of the data is not a straight line. This results from the echelle dispersion and cross-dispersion. The properties of this dispersion are known from calculations and previous observations and are used to regrid the flat field corrected spectrum so that movement along a vertical line corresponds only to movement along the spatial dimension. After the spectrum is regridded, the columns of the array do not change in wavelength. Figure 6-11 shows the flat field corrected spectrum next to the regridded

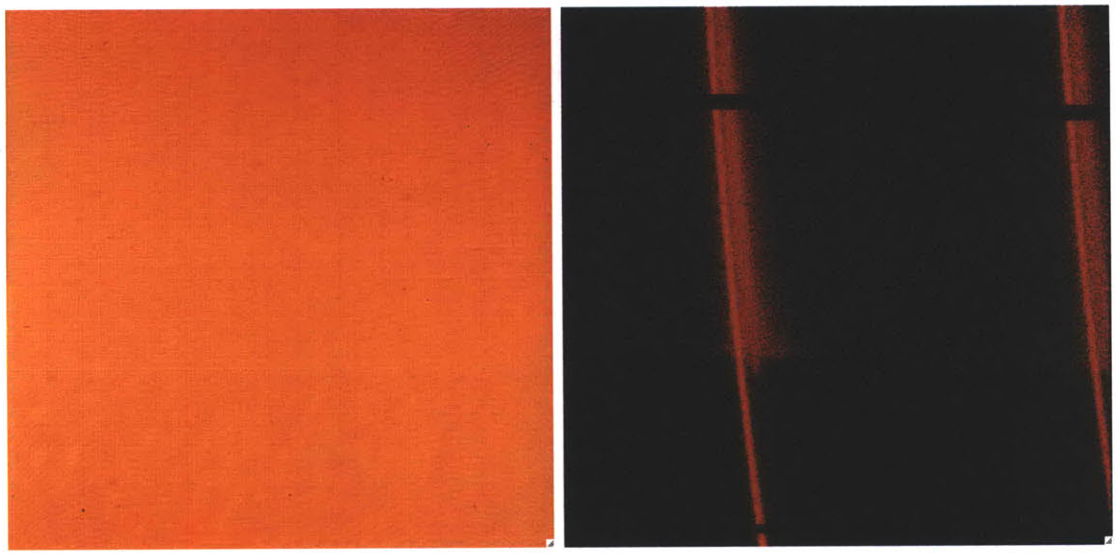

Figure 6-10: Combined flat field data (left) and flat field corrected data (right). Values on the combined flat field correction range from 0.001 to 1.353.

spectrum.

One final correction is necessary before the spectrum can be analyzed. Dispersion sensitivity varies perpendicularly to the wavelength axis. Like the properties of the cross-dispersion, the properties of perpendicular dispersion sensitivity are known. Figure 6-12 shows this sensitivity as a function of pixel location and as spectral data. The regridded spectrum is divided by the dispersion sensitivity correction spectrum to obtain the final reduced spectrum, shown in Figure 6-13, which can be used for data analysis.

### 6.3.2 Obtaining the Bulge Spectrum

The final reduced spectrum shows Lyman-alpha echelle order 30 left of the center and order 31 cut off on the right side. Order 30 is what was analyzed in this analysis (see Section 2.6 for echelle basics and what the orders are). Figure 6-14 shows a zoomed in view of the area of the spectrum that is of interest, the limb of the planet, and labels some of the features that can be seen from inspection.

To obtain the spectrum from only the limb, the sky background must be subtracted. An IDL routine had already been written to do this task, but it was modified

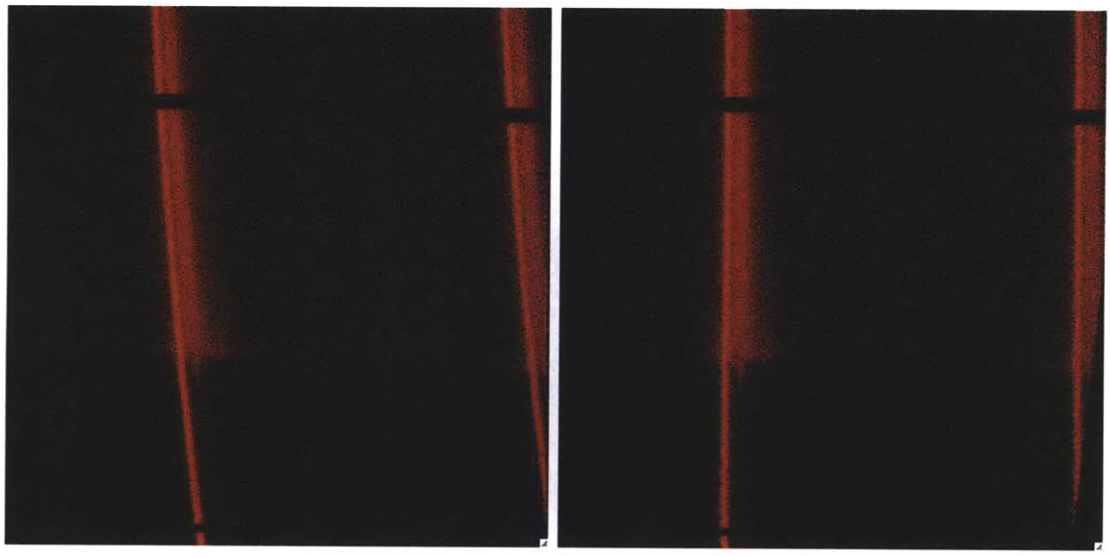

Figure 6-11: Flat field corrected spectrum (left, same as Figure 6-10) and regridded spectrum (right).

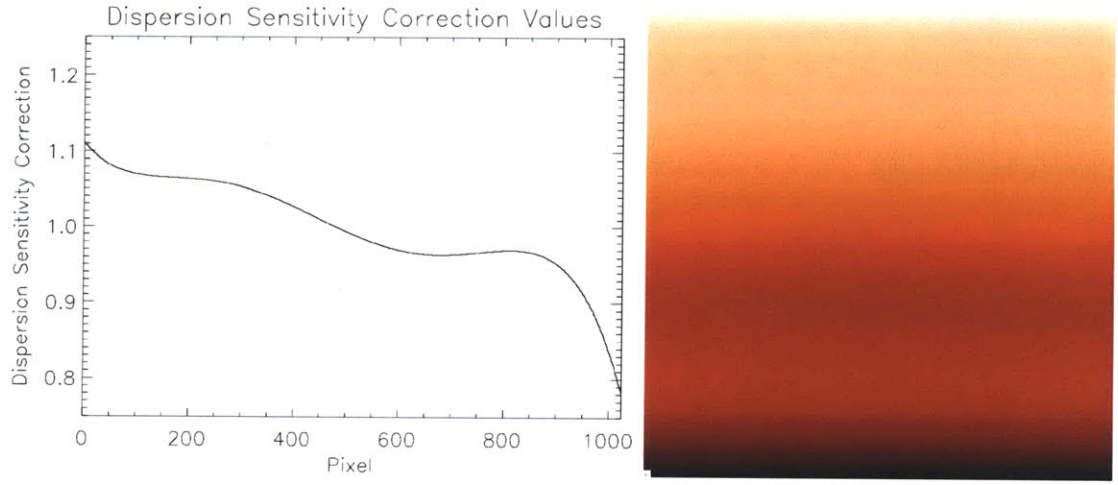


Figure 6-12: Perpendicular dispersion sensitivity correction plot (left) and equivalent spectral data (right).

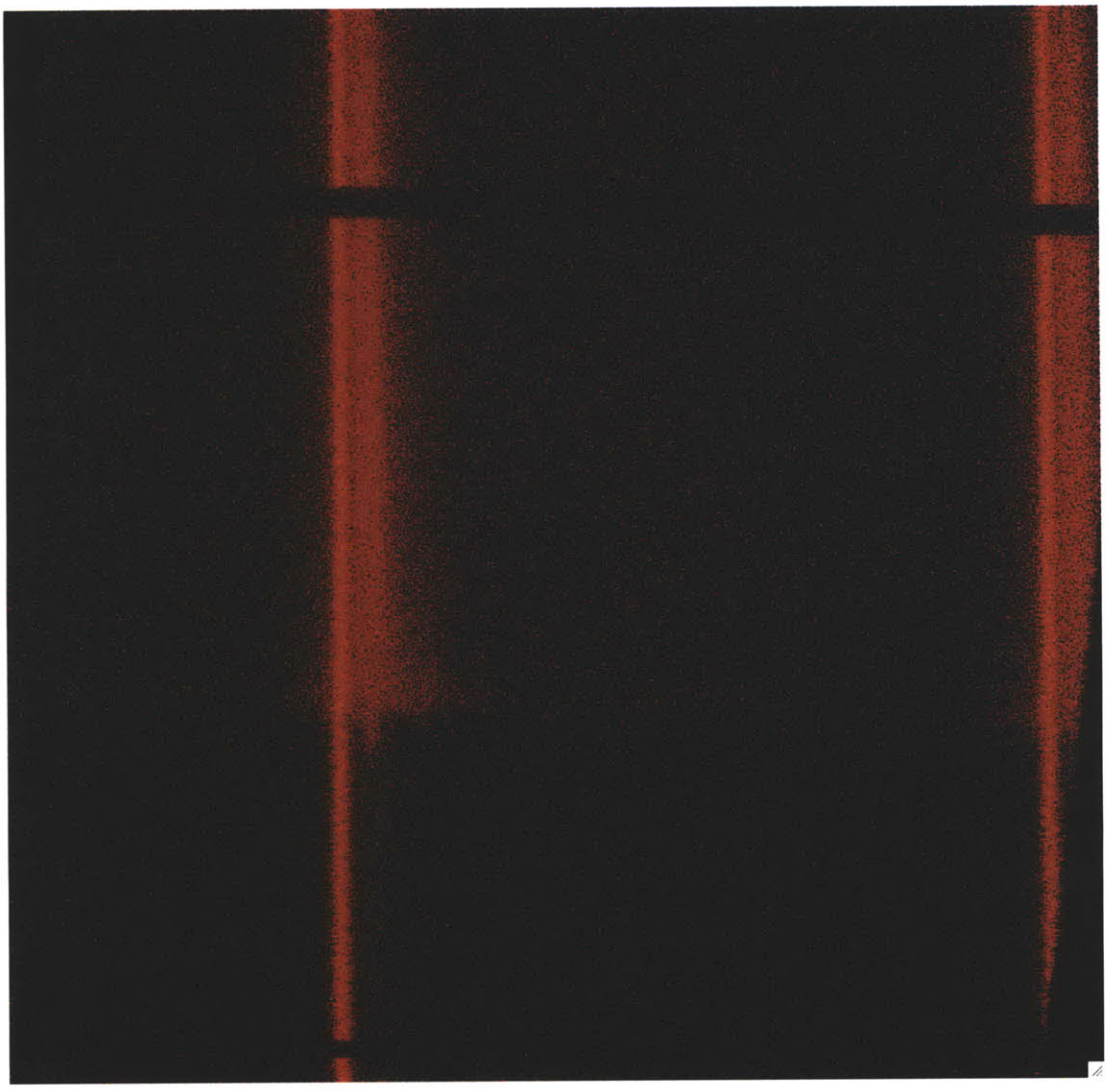

Figure 6-13: Final reduced STIS spectrum of the Jupiter Lyman-alpha Bulge.

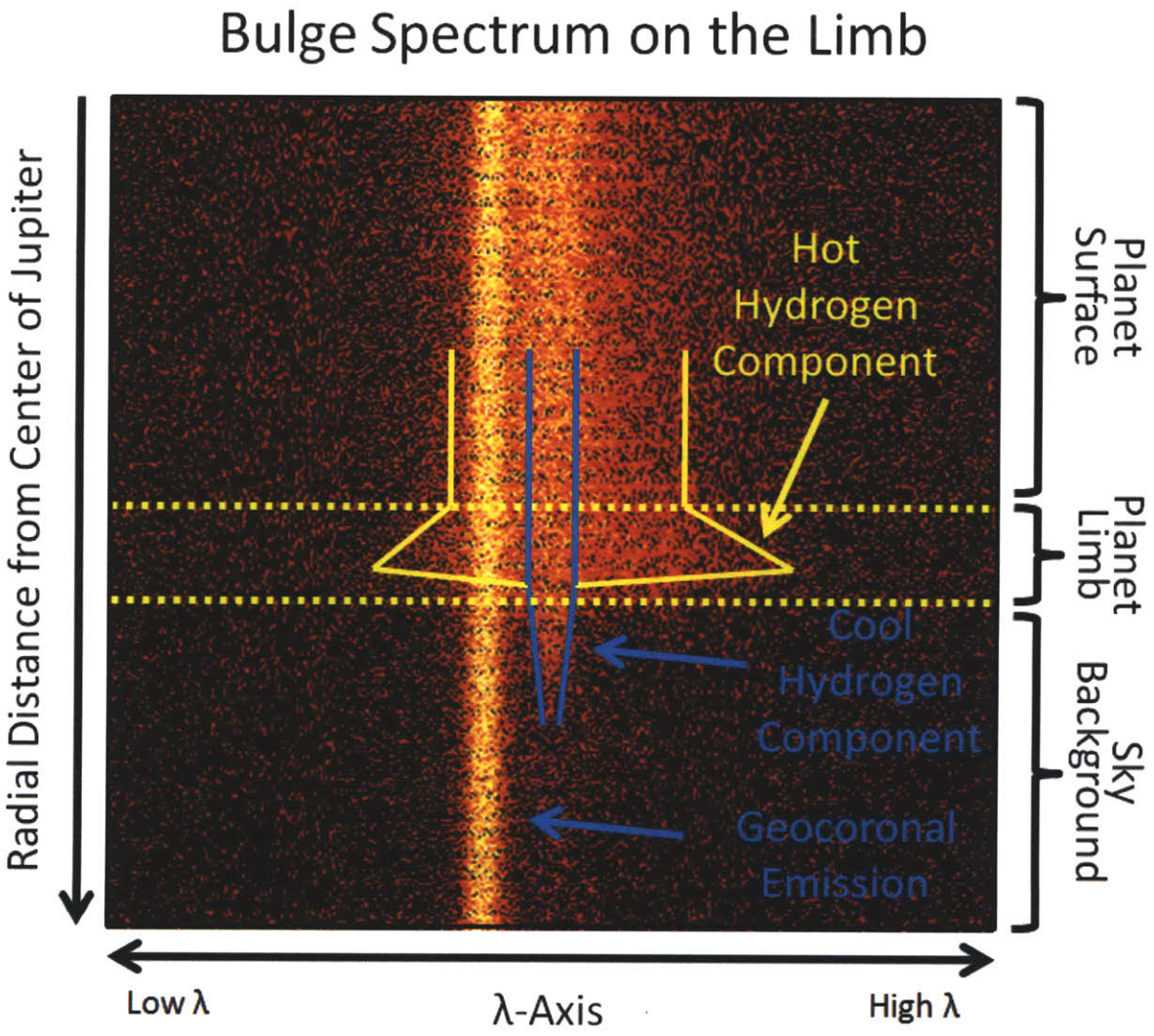


Figure 6-14: Zoomed-in view of the spectrum showing the limb in more detail.

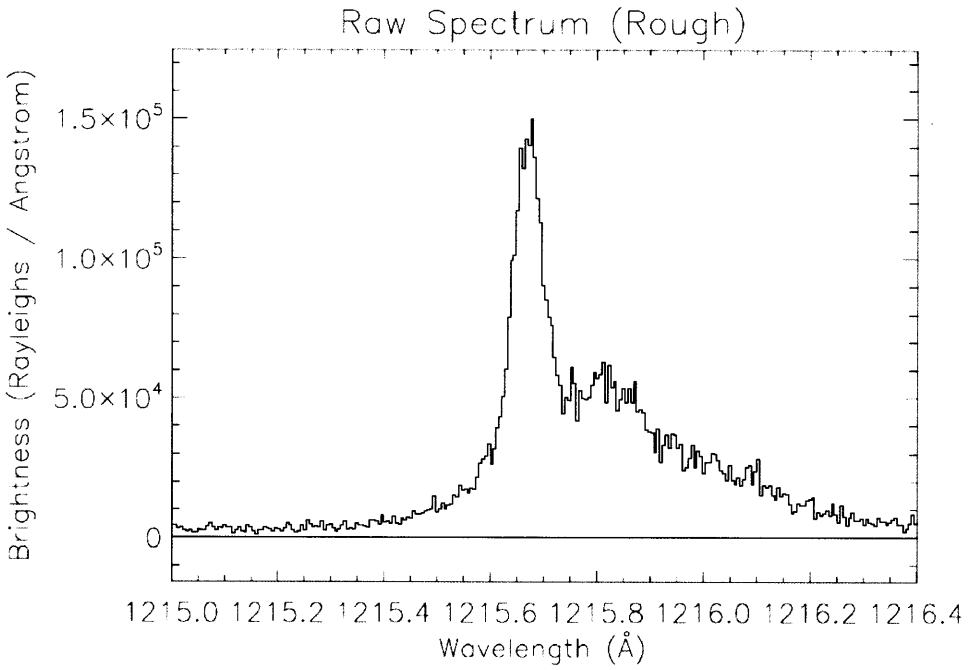


Figure 6-15: Raw spectrum of the limb.

for this analysis to calculate uncertainty in the removal of the sky background. First, the routine performs a horizontal intensity trace along a selected region. A horizontal region 40 pixels wide shown by the yellow dotted lines in Figure 6-14 was chosen. The brightness in each column is added and plotted as a function of wavelength. Figure 6-15 shows the spectrum that results from the intensity trace across the limb region.

Next, the routine selects a region of the sky background to subtract out of the spectrum of the limb region. In most of the spectra, there is an area at least 250 pixels tall that can be used to obtain a sky background spectrum, and large regions are better because of the reduced uncertainty in the total count rate compared to smaller regions. An intensity trace is performed across the selected sky region, and all the pixels in each column are added together and plotted as a function of wavelength. Figure 6-16 shows the spectrum of the sky background.

The large peak at 1215.67 Å is the geocoronal background emission, and the area on the right of the geocoronal peak that is brighter than the left side is emission from the interplanetary medium (IPM).

The Poisson uncertainty, defined as the square root of the number of counts in

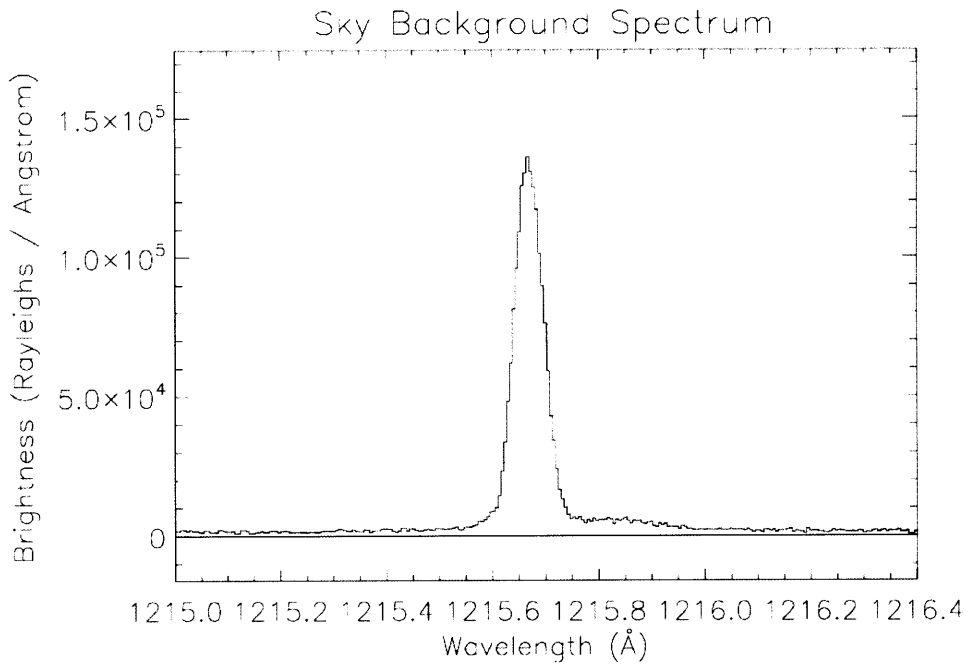


Figure 6-16: Sky background spectrum.

each wavelength bin, is calculated for both the raw spectrum and the sky background. Then, the sky background is subtracted from the raw spectrum, resulting in the limb spectrum. The uncertainty in the limb spectrum is also calculated as the square roots of the sum of the squares of the raw and sky background uncertainties.

Figure 6-15 shows the resulting limb spectrum when the sky background is subtracted from the raw spectrum. The spectrum was plotted again in Figure 6-18 using an IDL smoothing function that alters the spectrum data on the plot for clarity. Subsequent plots will also use this line smoothing technique, but all calculations described hereafter are performed on the actual spectrum data and not the smoothed data.

The sky background appears to be oversubtracted in Figure 6-18. This is expected because light from Jupiter at the same wavelength as the geocoronal hydrogen atoms will be scattered by those atoms. Some light will be scattered by neutral hydrogen in Earth's atmosphere. Another IDL routine was written to vary the intensity of the sky background spectrum before it is subtracted from the raw spectrum and displays a closer view of the corrected limb spectra. Figure 6-19 shows a closer view of the limb spectrum with the sky background scaled to 92% of its original intensity before

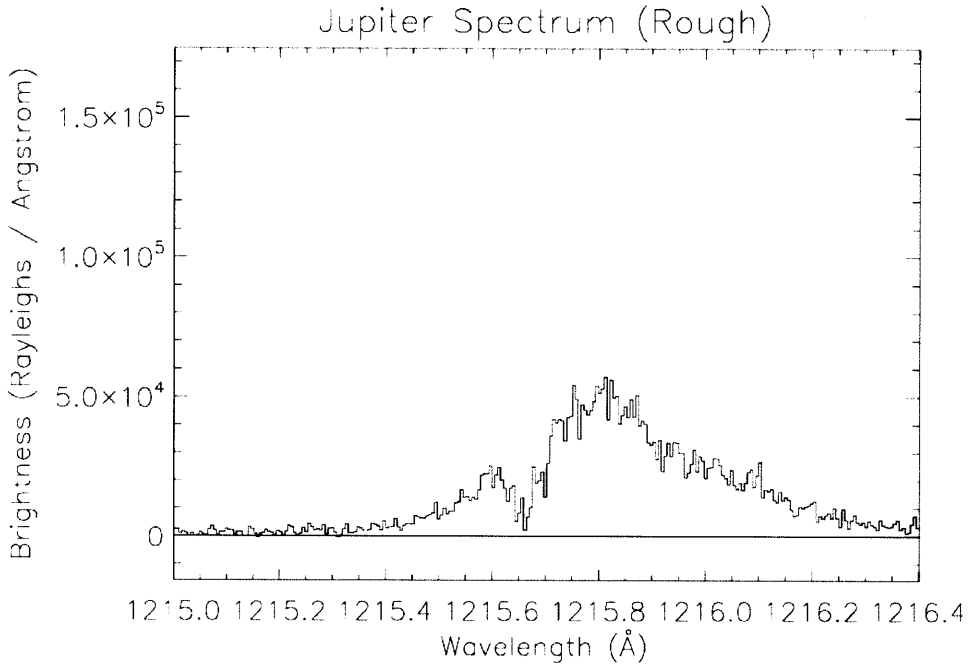


Figure 6-17: Rough spectrum of the limb with the sky background subtracted.

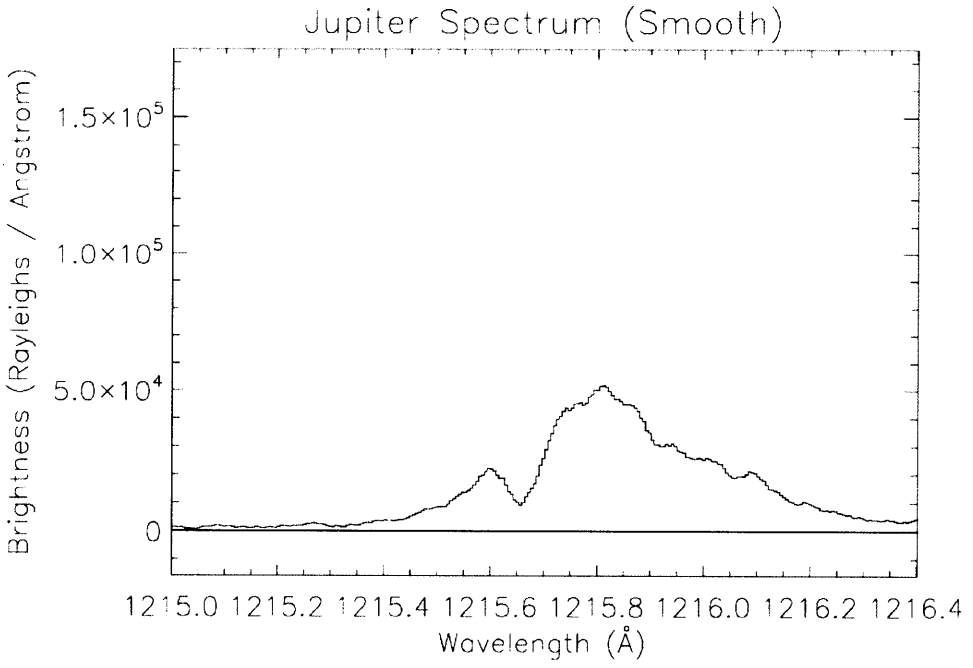


Figure 6-18: Spectrum of the limb with an IDL smooth function applied.

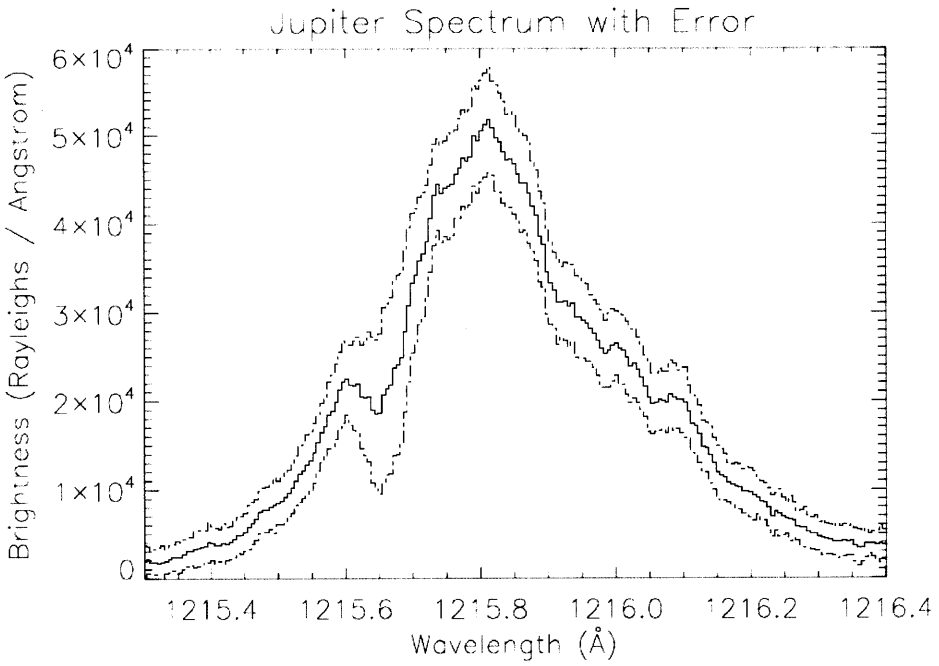


Figure 6-19: Closer view of the limb spectrum with the adjusted background subtraction. The solid line is the smoothed data and the dashed lines show ±1-sigma uncertainty with Poisson statistics.

it was subtracted. The Poisson error is also plotted with the spectrum. Notice the higher relative error near 1215.65 Å where the sky was subtracted. This is a result of error propagation and needs to be accounted for when modeling the spectrum.

### 6.3.3 Modeling the Hot and Cold Components

It is known that the broad spectrum in the Bulge is the result of a two-component structure, one composed of cold neutral hydrogen and the other composed of super-thermal hydrogen. The atmosphere in this region is optically thick, so a Voigt profile will not provide an accurate fit to the data (see Section 2.5). A full radiative transfer model is the only way to model the entire spectrum. However, the super-thermal (hot) hydrogen is a much smaller part overall and is optically-thin compared to the cold component, so a Voigt profile can be fit to the super-thermal component and subtracted from the spectrum, leaving only the cold component.

A new IDL routine was written from scratch that fits a Voigt profile to the wings of the spectrum using a least-squares fitting algorithm. First, the bounds of the regions

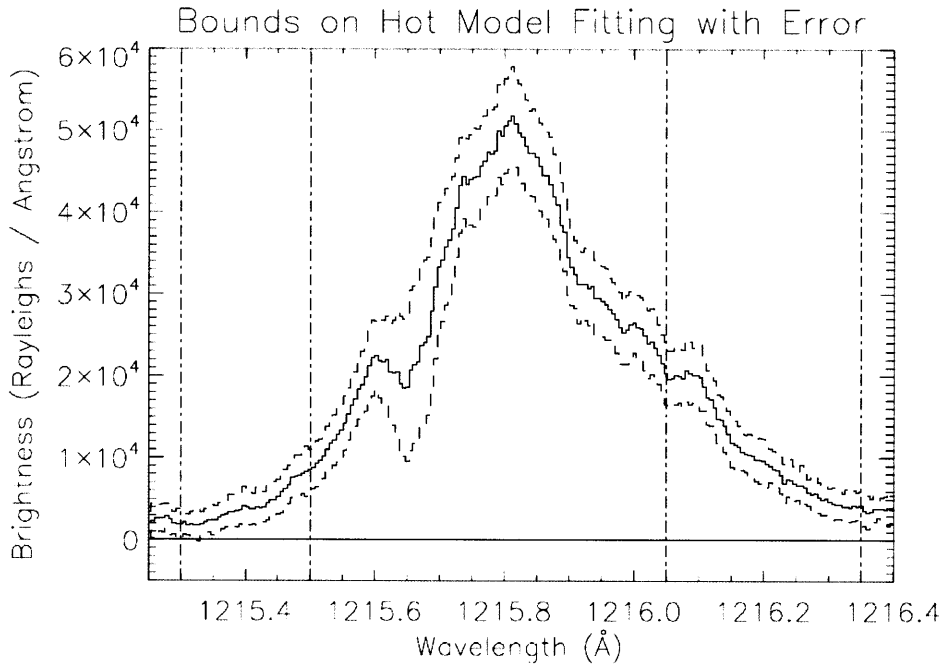


Figure 6-20: Limb spectrum showing bounds on where the hot component Voigt profile was fit.

Table 6.3: Range, step sizes, and initial guesses of the Voigt profile variables for the hot model fit of the Bulge spectrum.

| **Variable** | **Low** | **High** | **Step Size** | **Initial Guess** |
|---|---|---|---|---|
| Temperature (K) | 200000 | 500000 | 2500 | 325000 |
| Line Center (Å) | 1215.7 | 1215.9 | 0.005 | 1215.8 |
| Peak Brightness (R/Å) | 10000 | 40000 | 100 | 30000 |

on both sides of the central peak of the spectrum are defined where the Voigt profile will be fit. Figure 6-20 shows these bounds on the limb spectrum.

Next, ranges of values and step sizes for the temperature, line center, and peak brightness of the Voigt profile are defined. Table 6.3 lists the ranges and step sizes of the variable used in the example shown.

The fitting algorithm starts by fixing the line center and peak brightness values at the initial guesses and reading the lowest value of the temperature range. It builds a Voigt profile for the hot hydrogen Lyman-alpha component of the spectrum and convolves it with the STIS E140H line spread function (LSF). Then, the algorithm linearly interpolates the Voigt profile to the same wavelength scale as the limb spectrum. A subroutine calculates the sum of the least squares of the difference between

the values of the model and the data and reports the chi-squared value. This value is stored and the temperature is increased by a step. This is repeated until the highest temperature in the range has been used. The temperature with the lowest chi-squared value is stored.

Next, the algorithm runs a second loop creating a Voigt profile, convolving it with the E140H LSF, and finding the chi-squared value, but it fixes the temperature at the value that was found in the previous loop, sets the peak brightness equal to the initial guess, and varies the line center. The line center that produces the lowest chi-squared value is then used with the best fit temperature from the first loop as the starting points for a third loop that sweeps the values of peak brightness.

These three loops are repeated, varying one variable while using the best guess of the other two variables from the previous overall iteration, until the final chi-squared values converges to within $1x10^{-5}$. Convergence has occurred every time the algorithm has been executed within 4 iterations. After the algorithm converges on a solution, the best fit values of the three variables are again used to create a Voigt profile convolves with the E140H LSF and interpolated with the limb spectrum.

In an earlier version of this program, the three variables were not swept one at a time, but all possible combinations of the three variables were used in a triple FOR loop that calculated Voigt profiles and found chi-squared values. This algorithm was slow when the step size for the variables was small, which corresponds to a high resolution fit. It required a number of calculations on the order of $\mathcal{O}(n^3)$ to finish, where $n$ is the number of values a variable could be within the defined range. It was a brute force way to find a solution, not a smart way. The new version of the algorithm requires a number of calculations on the order of $\mathcal{O}(mn)$, where $m$ is the number of iterations required to reach convergence. Each of the three variables is swept once per iteration, and a much higher resolution can be used to find the best fit in the same time period.

After the best fit model is found, it is subtracted from the limb spectrum. The algorithm outputs the best fit variables, the best fit model, and the result from subtracting the model from the data. Figure 6-21 shows the resulting Voigt profile of

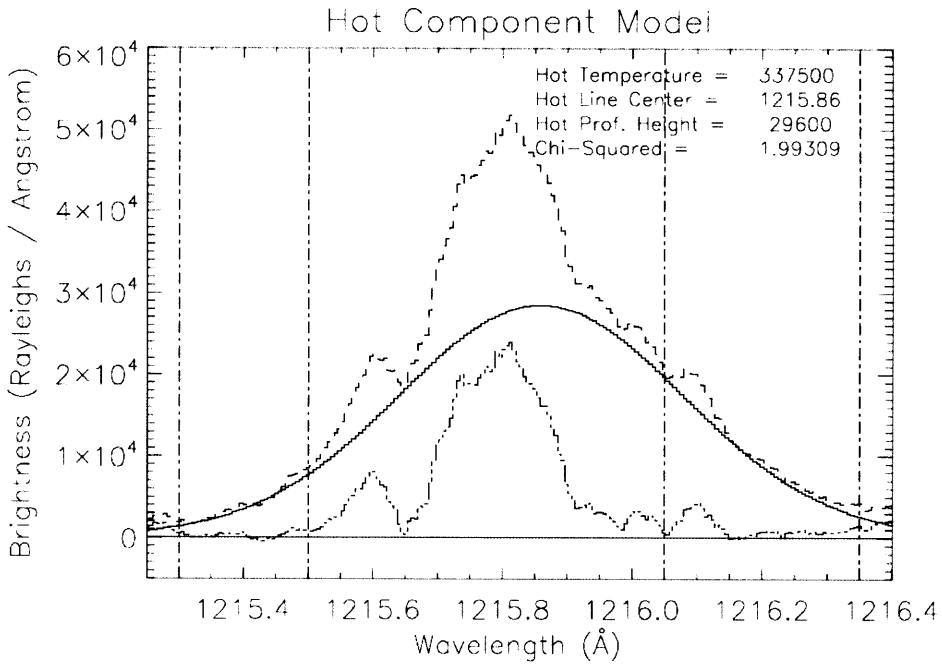


requires

Figure 6-21: Voigt profile of the model hot component plotted with the limb spectrum and the remainder when the model is subtracted from the limb spectrum.

the hot component (solid line) plotted against the limb spectrum (dashed line). The remaining spectrum (dotted-dashed line beneath the model) is the cold component, which can be modeled using a similar algorithm.

The best fit of the line center does not appear to be very sensitive to changes in the bounds, but the other two variables are quite sensitive to where the boundaries of the fit are chosen. If the right boundary of the left side moves into the area where the uncertainty is higher due to the subtraction of the sky, the chi-squared value of the best fit will be higher. If the left boundary of the right side is moved closer to the line center, the dips caused by turbulence can cause the peak intensity to decrease and the temperature to increase to compensate for the loss. If the bounds are too thin, the peak intensity can overshoot the entire spectrum. Clearly, there are limitations as to how well this algorithm fits the data because the Voigt profile is a simplified but inaccurate way to model this complex area of Jupiter's atmosphere.

Just like with the hot component, the uncertainty must be considered when choosing the boundaries to fit a model of the cold component. On this spectrum, the increased uncertainty from the sky is reaching into the left side of the cold peak, so

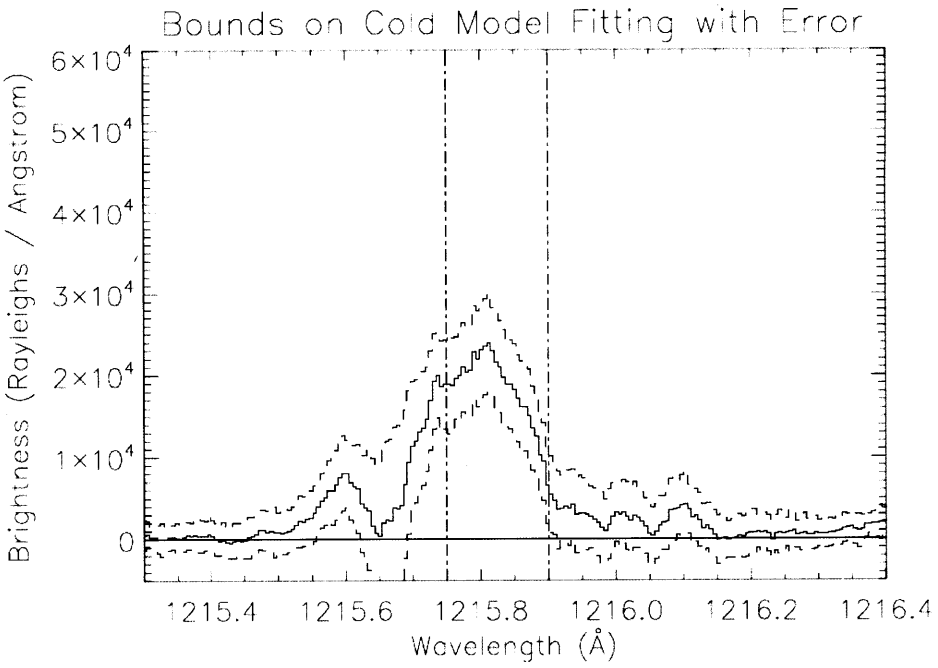


Figure 6-22: Remainder of the limb spectrum after the hot model spectrum was subtracted showing bounds on where the cold component Voigt profile was fit.

Table 6.4: Range, step sizes, and initial values of the Voigt profile variables for the cold model fit of the Bulge spectrum. These values are not representative of the true conditions because this simplified model does not take into account line broadening effects caused by radiation transfer in an optically thick column of gas.

| Variable | Low | High | Step Size | Initial Guess |
|---|---|---|---|---|
| Temperature (K) | 10000 | 40000 | 100 | 25000 |
| Peak Brightness (R/Å) | 20000 | 40000 | 100 | 30000 |

the right side is used more than the left for the model fit. Figure 6-22 shows the remaining cold component of the spectrum plotted with the uncertainty values and the boundaries used to fit a Voigt profile to the cold component.

Another algorithm was written from scratch that is very similar to the hot model algorithm, but instead of fitting all three variables required to generate a Voigt profile, the line center is found first using a peak-finding subroutine, so only the temperature and peak intensity ranges need to be swept to find a model with the best least squares fit. Table 6.4 shows the range, step size, and initial guesses used in the second least-squares fitting algorithm to model the cold component.

These bounds do not reflect the actual conditions of the cold component of hy-

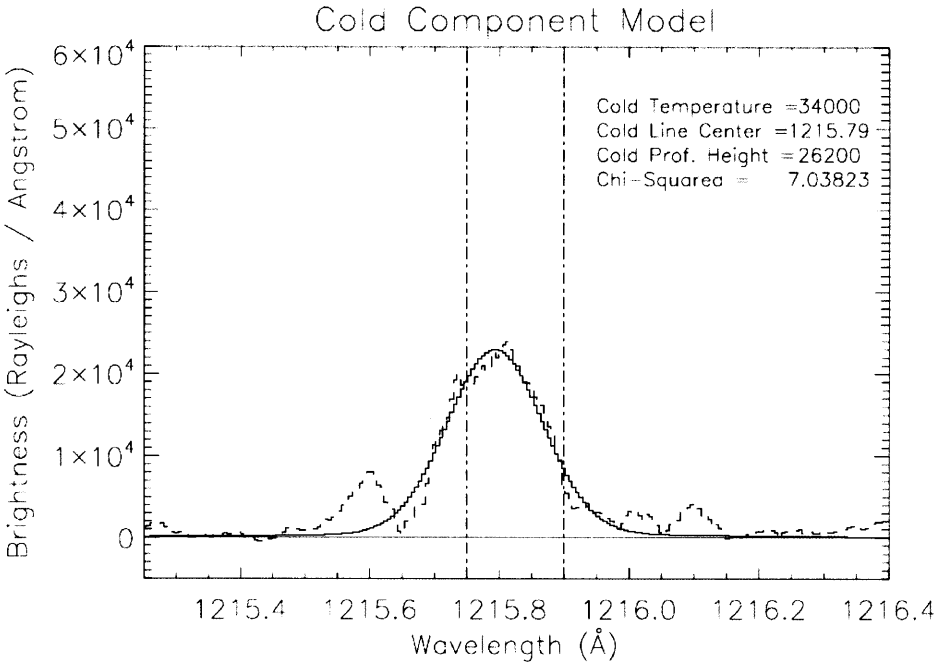


Figure 6-23: Voigt profile of the model hot component plotted with the remainder of the limb spectrum after the hot component was subtracted.

drogen; to gather a fully realistic set of bounds, a full radiative transfer model would be needed to account for the line broadening. The artificially high temperature given here is what artificially broadens the Voigt profile model so it fits the remainder of the spectrum after the hot component has been subtracted out. Figure 6-23 shows the cold component model plotted over what remained after the hot model was subtracted from the Bulge limb spectrum with the bounds that the model is fit to.

Finally, Figure 6-24 shows the combination of the hot and cold models plotted over the data along with the values of the model parameters. As expected, the features that show evidence of turbulence do not match the simplified model, but aside from these bumps the overall shape fits the data well. Also as expected, the temperature values used to broaden the Voigt profiles are unrealistically high because optical depth broadens the line profiles.

An unexpected finding was the large difference between the best fit of the line centers at the Bulge, marked by the two vertical lines in Figure 6-24. The hot component's best fit for the line center was red-shifted by 0.07 Å compared to the line center of the cold component, which was in agreement with the predicted line center

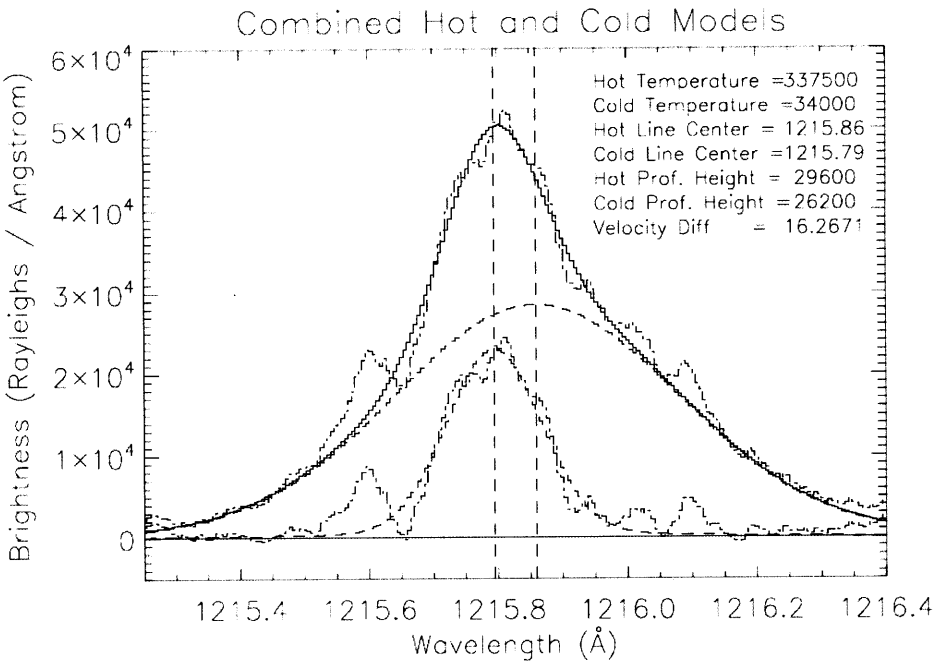


Figure 6-24: Combined hot and cold models plotted against the original limb spectrum. Vertical lines are the line centers of the two component models.

given the LOS velocity of Jupiter relative to Earth and rotational velocity of the limb. This line center different corresponds to a velocity difference of 16 km/s between the hot component and the cold component. The spectral asymmetry had been noticed in previous studies but was never formally calculated until now.

The data reduction, sky subtraction, and two-component model fitting pipelines described in this section were also applied to the other three spectra. Table 6.5 shows the numerical results and Figure 6-25 shows the plots of all four spectra. The total Lyman-alpha brightness was calculated by integrating the spectrum over 1.0625 Å centered at the peak, large enough to capture the wings of the emission but not the background noise left over after the sky subtraction. The values for temperature and peak brightness of the cold component listed here also are not representative of the true conditions because the simplified nature of the model.

In the regions north and south of the Bulge, there is a similar line separation between the hot and cold components, but the corresponding velocity difference is a few kilometers per second less than at the Bulge. This is strong evidence that the Bulge is influenced by and possibly energized by the auroral regions. The hot

Table 6.5: Model outputs for all four limb spectra. The temperature and peak brightness values of the cold component do not represent accurate values because a full radiative transfer analysis was not used in this model.

| | **Bulge** | **Anti-bulge** | **Northern** | **Southern** |
|---|---|---|---|---|
| Total Spectrum Brightness | 21.0 | 20.4 | 20.3 | 20.3 |
| **Model Outputs** | | | | |
| **Hot Component** | | | | |
| Temperature (K) | 337500 | 350000 | 330000 | 297500 |
| Line Center (Å) | 1215.86 | 1215.79 | 1215.85 | 1215.84 |
| Peak Brightness (kR/Å) | 29.6 | 30.0 | 30.0 | 29.7 |
| **Cold Component** | | | | |
| Temperature (K) | 34000 | 9100 | 15000 | 25000 |
| Line Center (Å) | 1215.79 | 1215.77 | 1215.80 | 1215.80 |
| Peak Brightness (kR/Å) | 26.2 | 29.7 | 28 | 30.2 |
| **Velocity Difference (km/s)** | **16.3** | **7.1** | **12.2** | **11.6** |

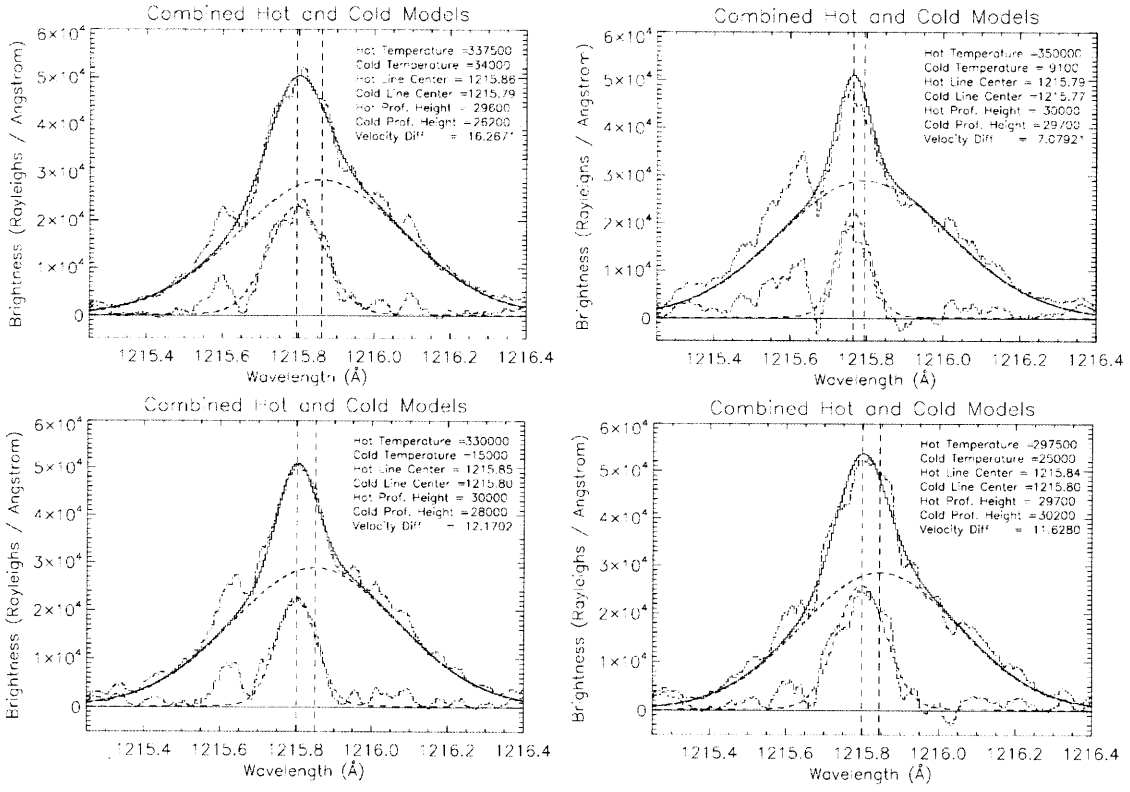


Figure 6-25: Combined hot and cold component fits to the spectra. (Top Left) Bulge limb. (Top Right) Anti-bulge Limb. (Bottom Left) Northern Limb. (Bottom Right) Southern Limb.

and cold components of the Anti-bulge spectra have an even smaller line separation compared to the Bulge, corresponding to a smaller velocity difference between the two components.

The modeled temperature in the hot component of the Bulge is higher than in the regions to the north and south. However, the modeled temperature of the hot component in the Anti-bulge is much higher than the other three spectra. This does not agree with data from the image analysis (Section 6.2); the average scale height at the Bulge was 250 km greater and therefore should have a higher temperature.

Upon closer inspection of Figure 6-25(top right), note that this spectrum looks broader and therefore should have a higher temperature value for a Voigt profile. The model hot component is also a much larger percentage of the whole spectrum in the Anti-bulge, which may help explain why the model is not much less brighter overall compared to the Bulge. See Section 6.3.4 for more on a possible reason why the modeled temperatures of the hot components are lower than the Anti-bulge.

A caveat in this analysis is that the four observations were not all taken in the same time period (see Table 6.2). The Anti-bulge spectrum was observed 14 months prior to the other three spectra, and the Southern Limb spectrum was observed three days prior to the Bulge and Northern Limb spectra. Previous studies have shown that there are variations in the brightness of the Bulge that correspond to changes in the Solar cycle [41]. The Solar Lyman-alpha flux on the day the Anti-bulge was observed was approximately 10% stronger that it was during the time the Bulge, Northern, and Southern Limbs were. The Anti-bulge is therefore brighter as a result.

In addition, the Anti-bulge spectrum was observed at a time when the LOS velocity between Jupiter and the Earth was lower than it was during the other observations. The geocoronal emission spectrum was therefore closer to the line center of the Jupiter data, and the relative error in the Voigt profile model fitting was higher.

Furthermore, the lower LOS velocity between Jupiter and Earth makes the sky subtraction in Anti-bulge more difficult. Choosing different parameters for the strength and shift in the sky background before it is subtracted from the raw spectrum changes the final output of the model. Given one set of parameters, the line shift between the

hot and cold models can correspond to a velocity difference as low as 0 km/s or as high as 10 km/s. Also, because the Solar Lyman-alpha flux was higher, the geocoronal and IPM emissions were also brighter, bringing the total error in the model fittings even higher. Use of a comprehensive radiative transfer model could more accurately subtract the sky background so that this model could more accurately calculate the line separation and the relative velocity between these two components.

### 6.3.4 Optical Depth and Column Density Analysis

Even though the overall optical depth of the hydrogen in the spectra is too high to calculate the column density without requiring a complex radiative transfer model to account for multiple scattering, a simplified analysis can be performed on the hot component because the wings of the line are optically thin. In an optically thin gas ($\tau = 1$), it can be assumed that photons are scattered by only one atom ("single scattering") and brightness is directly proportional to the column density of atoms along the line of sight. The following analysis to calculate the column density of the hot population of neutral hydrogen atoms in the Jupiter spectra is based on R.R. Meier's work [43] for a single scattering radiative transfer from Solar Lyman-alpha light.

The column density can be calculated by

$$N = \frac{B}{g} \tag{6.2}$$

where $N$ is the number density of hydrogen along a column, $B$ is the total brightness of the measured emission, and $g$ is the Solar g-factor. The Solar g-factor is defined as the numbers of photons per second an atom will produce from reflecting Solar radiation and is calculated as

$$g = (\pi F_S \sqrt{\pi} \Delta\lambda_D)\sigma_0 \tag{6.3}$$

where $\pi F_S$ is the Solar flux in photons per square centimeter per second per Angstrom, $\Delta\lambda_D$ is the Doppler width with respect to wavelength, and $\sigma_0$ is the resonant scat-

tering cross section of hydrogen at line center. This formula assumes constant Solar flux at all wavelengths and constant scattering cross section, both of which are good assumptions when the Lyman-alpha spectral line profile is thin compared to the Solar Lyman-alpha profile. In the case of the Jupiter Bulge, however, this is not true. The Jupiter line profile is very broad, so the variations in the Solar Lyman-alpha flux and the scattering cross section must be accounted for. A more general case of the Solar g-factor equation will be developed later in this section to solve for the column density.

Figure 6-26 shows a model of the Solar Lyman-alpha flux at Jupiter and the model Voigt profile of the hot component of the Bulge found in Section 6.3.3. The Solar profile is centered at the rest wavelength of Lyman-alpha (1215.67 Å) and the hot component model is centered at the best fit line center found in the fitting algorithm, which was shown to be even more red-shifted from the line center than if only planetary rotation was causing a line shift.

Two observations are significant in this figure. First, notice that the Solar Lyman-alpha flux is not constant across all wavelengths. The dip in the center is due to resonant scattering by colder hydrogen gas in the Solar atmosphere, but light further from line center is brighter per unit Angstrom on both sides. Clearly, the change in the Solar flux at different wavelengths must be accounted for.

Second, notice how wide the hot component model is compared to the Solar profile. Both profiles are nearly 1 Angstrom wide, and both profiles decay at similar rates at higher wavelengths (right side of the graph). This means there could be more hydrogen moving at greater speeds relative to the planet, but there is simply no Solar Lyman-alpha flux at those wavelengths for the hydrogen to reflect. This possibility will be revisited later in this section.

The resonant scattering cross section of neutral hydrogen is dependent on temperature and wavelength. An advantage of the Voigt profile is that it shows how the scattering cross section varies with wavelength relative to the cross section at line center. The cross section at line center varies inversely with the square root of the temperature, or $\sigma \propto T^{1/2}$. The scattering cross section in the hot component can be

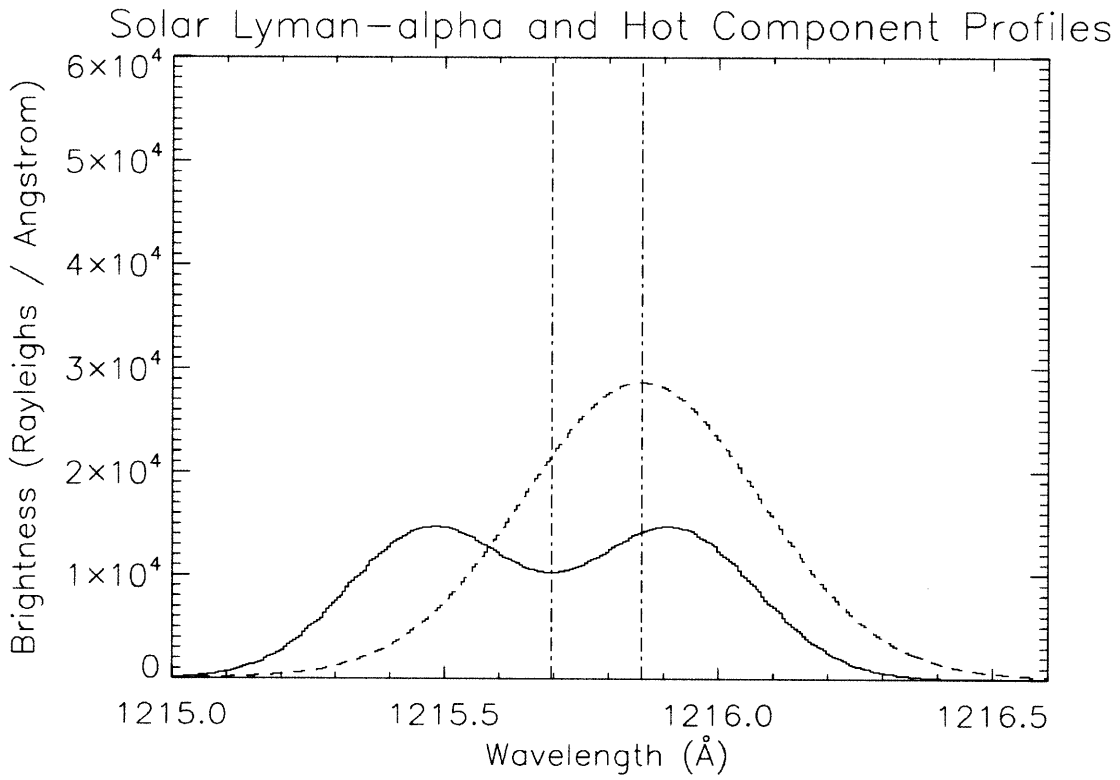


Figure 6-26: Model Solar Lyman-alpha flux at Jupiter (solid line) plotted over the hot component spectrum model (dotted line). Notice the Solar Lyman-alpha flux is diminished in the center because of scattering by colder atoms in the Solar atmosphere, so there are two peaks.

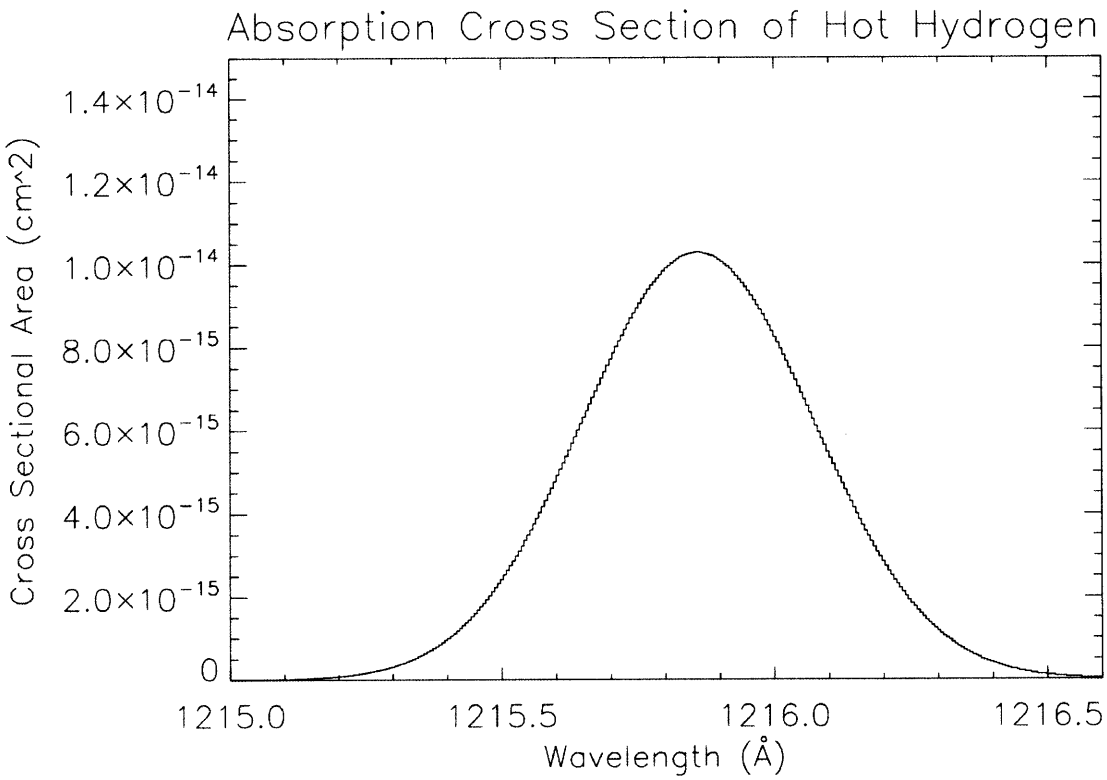


Figure 6-27: Resonant scattering cross section of the model hot component.

calculated using a known value at a given temperature. Wiese et al. [57] measured a scattering cross section of neutral hydrogen at 1000 K of 1.865 x $10^{-13}$ $cm^2$. The scattering cross section in the hot component was calculated by

$$\sigma_{T_{BF}} = \sigma_{1000K}\sqrt{\frac{1000}{T_{BF}}} \tag{6.4}$$

where $\sigma_{1000K}$ is the cross section at 1000 K and $T_{BF}$ is the best fit temperature of the Voigt profile of the hot component. The cross section at line center can be used to scale the Voigt profile to model how scattering cross section changes with wavelength, shown in Figure 6-27.

Now the Solar g-factor per Angstrom can be found with

$$g(\lambda)d\lambda = \sqrt{\pi} \cdot \pi F(\lambda) \cdot \sigma(\lambda)d\lambda \tag{6.5}$$

Figure 6-28 shows $g(\lambda)d\lambda$. The curve is skewed to the right because the hot

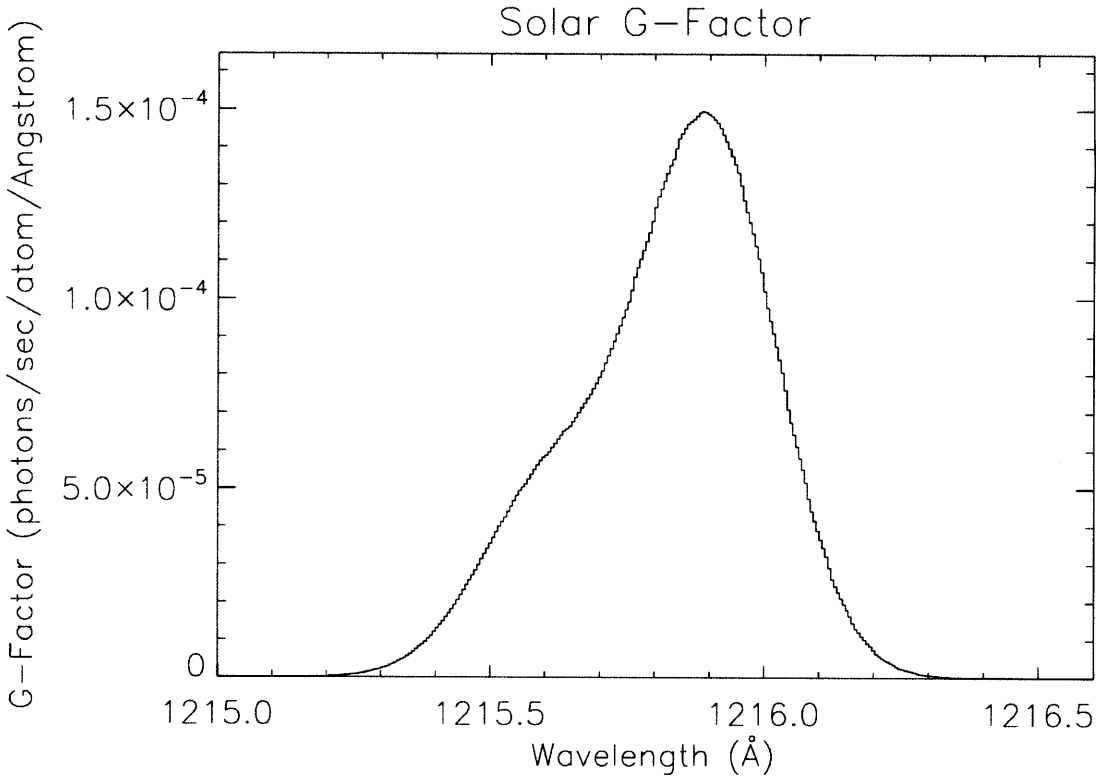


Figure 6-28: Solar g-factor as a function of wavelength.

Table 6.6: Results from the column density analysis of the hot component of the spectra.

| Model Outputs | Bulge | Anti-Bulge | Northern | Southern |
|---|---|---|---|---|
| Scattering Cross Section ($cm^2$) | 1.03 x $10^{-14}$ | 9.97 x $10^{-15}$ | 1.03 x $10^{-14}$ | 1.08 x $10^{-14}$ |
| Solar G-Factor (photons/s-atom) | 1.08 x $10^{-4}$ | 1.10 x $10^{-4}$ | 1.09 x $10^{-4}$ | 1.11 x $10^{-4}$ |
| Column Density ($atoms/cm^2$) | 1.46 x $10^{14}$ | 1.50 x $10^{14}$ | 1.46 x $10^{14}$ | 1.35 x $10^{14}$ |

component peak matches closely with the right peak of the Solar Lyman-alpha flux.

When $g(\lambda)d\lambda$ is integrated, the result is the Solar g-factor. When the hot component model is integrated, the result is the total brightness of the hot component. The column density is the brightness divided by the Solar g-factor. Table 6.6 shows the results from this process applied to all four spectra.

The scattering cross-sections are on the order that was expected when compared to the value reported by Wiese et al. [57] and considering the high temperature. The values of the Solar g-factor are also comparable given the increased distance from the Sun and lower Solar Lyman-alpha flux. The column density calculated in the Bulge

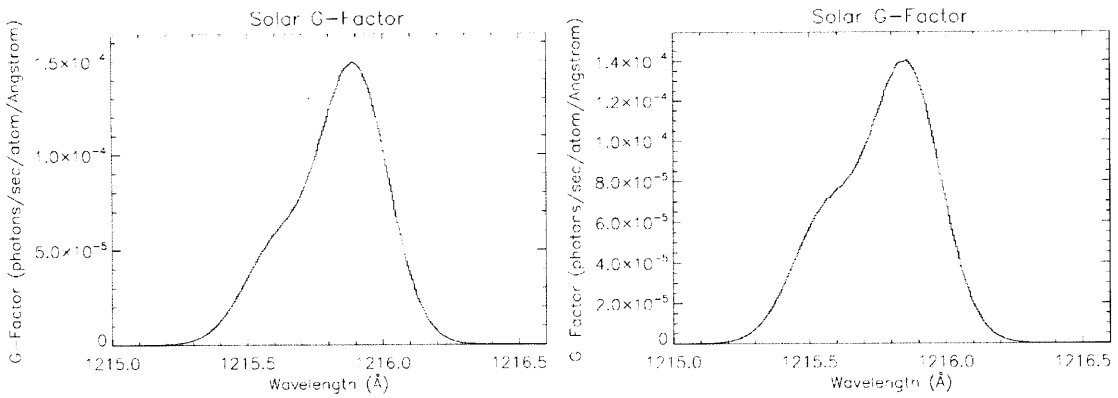


Figure 6-29: Comparison of the Solar g-factor function in the Bulge (left) and Anti-bulge (right) spectra.

region atmosphere is consistent with estimates made by Emerich et al. [11].

The higher calculated column density in the Anti-bulge atmosphere compared to the Bulge atmosphere can be explained by the red-shift of the hot components relative to the expected values. Figure 6-29 shows the Solar g-factor as a function of wavelength in the Bulge and Anti-bulge spectra. Because the hot component of the Anti-bulge is closer to the line center of the Solar Lyman-alpha flux, more photons on the blue-shifted peak left of the center (see Figure 6-26) are being scattered by the hot atoms on the blue-shifted wing of the hot component. Since there are more Solar Lyman-alpha photons that can be scattered by these atoms, it results in a higher calculated column density.

This could also explain why the temperature calculated in the model was higher in the Anti-bulge than in the Bulge. Because of the high red-shift of the hot component in the Bulge, not as many atoms were able to reflect Solar Lyman-alpha light. Figure 6-26 shows that the red-shifted edge of the hot model is further away from the red-shifted edge of the Solar Lyman-alpha profile. This could be an indication that there are more hot atoms than what was calculated here traveling at higher speeds around the planet. These would not be seen because they do not scatter Solar Lyman-alpha light. In contrast, the Anti-bulge hot component is closer to the Solar Lyman-alpha line center and can scatter more light.

If there were in fact more hot atoms moving at higher relative velocity to the cold

atoms in the Bulge, the distribution would have a broader model spectrum because of the higher Voigt temperature. If the temperature is increased by an order of magnitude in the column density analysis, the column density changes by a factor less than two. There may be much more happening in Lyman-alpha Bulge of Jupiter that has not been observed.

## 6.4 Discussion of Results

In summary, the results from the analyses of the images and spectra have shown:

1. The center of brightness in Lyman-alpha along the limb of the planet is aligned with the magnetic equator, not the rotational equator.

2. The emission scale height of higher latitudes on the hemisphere that is closer to the magnetic equator is higher than the emission scale height of the other hemisphere (see Figure 6-7).

3. The average scale height of the limb of the planet when the Bulge is on the limb is 250 km higher than the average scale height of the limb when the Anti-bulge is on the limb.

4. All four spectra qualitatively show evidence of turbulence. Turbulence causes the line profile to increase outside of line center, creating the bumps seen on the sides of the line center peaks in Figure 6-25.

5. All four spectra have broad, superthermal components that are red-shifted relative to the center of the peak emission, corresponding to velocity differences between the hot and cold components ranging from 16.3 km/s in the Bulge to 7.1 km/s in the Anti-Bulge.

6. The Northern and Southern limb spectra show lower velocity differences between the hot and cold components than the velocity difference between the hot and cold components at the Bulge.

7. The Bulge Lyman-alpha line profile is broader than the Northern and Southern limbs as indicated by the best fit temperature of the hot component model.

8. The spectral width of the hot components are comparable to the Solar Lyman-alpha profile, indicating that there could be more neutral hydrogen moving at higher speeds that is simply not scattering the Solar Lyman-alpha emission.

9. The column densities of the superthermal components of all four regions are comparable.

The alignment of the peak limb brightness with the magnetic equator is evidence that supports both the "equatorial electrojet and the "charged particle motion along magnetic filed lines" hypotheses. Since the aurorae are not aligned with the rotational axis of the planet, is is possible for a neutral high altitude jet from the aurora moving from high latitudes to low latitudes to brighten the entire magnetic equator and make one side even brighter..

The equatorial electrojet argument is further strengthened by the presence of a broad spectral component on the Anti-bulge side of the planet and by the large velocity difference between the hot and cold components observed on both sides of the planet. Again, depending on how the observed neutral winds from high latitudes move to lower latitudes and interact with the equatorial electrojet, this could the brightness of the magnetic equator to vary with longitude.

The increase in scale height in the higher latitudes near the magnetic equator is evidence that the temperature in these regions are higher. This could be influence from the aurorae. However, it is not certain whether this is caused by neutral high altitude jets or by charged particles moving down magnetic field lines. Either scenario would produce collisions in the upper atmosphere that would produce a Lyman-alpha emission. This emission would also be present on the night side of the planet due to scattering of the interplanetary emission, which is consistent with previous observations from Voyager [4].The increased scale height could be a sign that an equatorial electrojet is encountering more resistance as the magnetic equator peaks relative to the rotational equator.

The difference in the average emission scale height measured across the entire limb between the Bulge and Anti-bulge images corresponds to a temperature increase of 25% on the Bulge side compared to the Anti-bulge, since emission scale height increases linearly with temperature. The actual temperature cannot be calculated without a full radiative transfer analysis.

The hot component of the Bulge is moving more than 16 km/s faster than the atmosphere below it. For context, the rotational speed of the planet at the equator is approximately 12.5 km/s and the orbital speed at the exobase is approximately 40 km/s. This means the average superthermal hydrogen atom is moving at over half of the remaining the speed required to achieve orbit. This can easily explain why such a broad superthermal component exists at the Bulge and still has a high velocity separation from line center; such a large amount of the hydrogen could be traveling on suborbital trajectories that would take some of the atoms to the other side of the planet.

Additionally, because the Doppler broadening causes the spectral profile to be so broad, a large percentage of the hot component has enough energy to escape from Jupiter entirely. The hot component's Voigt profile at the Bulge showed that 27% of the hot emission was shifted such that its velocity was more than 60 km/s, which exceeds the escape speed of Jupiter.

The high velocity difference in the Bulge is much higher than what was observed in the aurorae [15]. Even if both auroral regions were contributing hydrogen at 5 km/s, which is higher than what was observed by Rego et al., this would not be enough to generate a high enough velocity to match the spectral separation observed in the Bulge.

However, the Rego et al. observations measured jets near the homopause. The pressure and density are orders of magnitude higher, so moving mass at high speeds is much more difficult. It is still possible that hydrogen higher in the atmosphere could be moving faster than the jets at lower altitudes.

The difference in velocity between the Bulge and the Northern and Southern limbs is consistent with friction causing the hydrogen to slow down more further from the

magnetic equator, as would be in the case of an equatorial electrojet. Alternatively, these higher velocities could be explained by matter from higher latitudes gradually colliding and changing from a north-south orientation to a westward direction, but this seems unlikely because the pressure is too low to transfer momentum gradually. Additionally, the Coriolis Force is strong and such changes would happen quickly.

Although the most published theory was that the turbulence inside the Bulge region was being caused by activity in the poles of Jupiter, this study shows evidence that activity along the magnetic equator may be responsible for the added brightness of the Bulge. It is not conclusive evidence, however, but it does add to the body of knowledge regarding the Bulge and the magnetic equator of Jupiter by describing characteristics that have not been reported otherwise.

Because of the problems with the spectral data, and because the spectral data cover such a limited range of Jupiter, it would be better to have more data with fewer complications than the present spectra. Whether or not a follow-on study was planned is unknown, but in August 2004, a failure in the STIS power system caused STIS to be inoperable, so no more high-resolution spectral data could be recorded. However, STIS was repaired during Servicing Mission 4 in May 2009, so a follow-on study could now be proposed.

If a future Hubble campaign was proposed to improve upon this data, additional spectral data sets from higher latitudes along the Bulge limb and at more points along the magnetic equator would be desirable. In this campaign, there is only one image and one spectrum each of the Bulge and Anti-bulge. Additionally, the latitudes sampled in the regions above and below the Bulge are not far enough away to examine what could be happening at mid-latitudes.

Additional spectra of the limb of the planet at higher latitudes would reveal whether there is any western motion at higher latitudes; if the Bulge is being energized by the poles, the relative motion would be north/south and would not create any red-shifting like what is seen in the spectral data from this campaign.

More spectra from around the magnetic equator would help characterize the fast hydrogen moving around the planet. If the velocity of the superthermal component

at longitudes near ~200 degrees is in between what was measured at the Bulge and Anti-bulge, and if the velocity of the superthermal component at longitudes near ~20 degrees is less than what is measured at the Anti-bulge, this would be an indication that equatorial electrojets are not influencing the Bulge. Equatorial electrojets would instead be weakest at the Anti-bulge and stronger in the regions in between the Bulge and Anti-bulge, climaxing at the Bulge.

# Chapter 7

# Conclusions

VeSpR was originally scheduled for flight in July 2010, but because of delays at Wallops Flight Facility, the payload was not ready for integration testing and launch before the launch window closed. Because of the low difference in orbital periods between Venus and Earth, potential launch windows are over a year and a half apart, corresponding to dates when Venus will have a high incoming line-of-sight velocity. As described in Section 5.5, the next launch window is in early 2012.

The year and a half delay in the launch date relaxed deadlines for new parts that were being fabricated in the BU Scientific Instruments Facility. Other BU rocket programs that required machine shop time received priority over VeSpR, so the fabrication of many of the parts described in Section 5.3 was delayed by several months. This caused fabrication of the flight wiring harnesses to be delayed, which in turn caused the testing of the new XDL detectors to be delayed past the point when the test results could be included in Chapter 5.

VeSpR is now far ahead of schedule for a 2012 launch. With additional payload testing at Wallops now scheduled for March 2011 and full payload integration and testing scheduled for the summer, VeSpR should have no problems launching during the next available launch window. Until then, the science team will be testing the systems in vacuum and troubleshooting the ground support equipment.

Addition upgrades will be made to the VACTEF to prepare the facility for future testing of spaceflight hardware. The Mars Atmosphere and Volatile Evolution Mis-

sion, or MAVEN, will require components that must be tested in vacuum at lower wavelengths than what is currently available for testing. Plans are already underway to install a new monochromator in the vacuum chamber that is capable of testing optics at much lower wavelengths than is currently available in the VACTEF. Over the next six months, work on this project will start as other work on VeSpR will continue as planned.

Meanwhile, the analysis of the raw data from the Jupiter Lyman-alpha Bulge is complete. The results presented here will be compared with existing radiative transfer models to see if the spectral data matches the model's output, but the conclusions from this study may be used to further strengthen the validity of the model. As of this writing, model profiles are being constructed that can be compared to the data.

Additionally, now that STIS has been repaired, there is an opportunity to observe the Bulge with Hubble again. The deadline for proposals for the next Hubble cycle is at the end of February 2011. If the radiative transfer model's output cannot be reconciled with the data from the 1999 and 2001 observations, there would be a strong case to submit a proposal for Hubble observation time. If another Hubble campaign was accepted, it would have stricter requirements on the observation windows and include blue-shifted observations on the day side in addition to red-shifted observations on the night side.

While these two projects were not strongly related on a technical level aside from the design of the spectrograph instruments, the experience working on two very different realms within space science has essentially condensed the lifecycle of a large-scale space science operation into a timeframe that made it possible to complete a Master's degree. Work on the pre-launch phase of VeSpR and the post-processing phase of the Bulge data was happening concurrently so the author could experience both the engineering build-up of a space mission and the scientific analysis of the raw data.

It is especially important for systems engineers to understand the "big picture." While most systems engineers are intimately familiar with the design of spacecraft components and the emergent behaviors that arise in complex systems, not all of them have worked with the final results from the spacecraft and have an intimate knowledge

of the needs of the scientists who receive the final data from the spacecraft. The combination of the two projects here involved the design of single parts, tracking of emergent behaviors of complex spacecraft systems, modeling the hardware to generate expected results, and reducing data from an actual spacecraft in a similar way that the VeSpR science team will do after launch.

# Bibliography

[1] P. Z. Takacs B. R. Sandel D. E. Shemansky J. B. Holberg J. M. Ajello S. K. Atreya T. M. Donahue J. L. Bertaux J. E. Blamont D. F. Strobel J. C. McConnell A. Dalgarno R. Goody M. B. McElroy A. L. Broadfoot, M. S. Belton. Extreme ultraviolet observations from voyager 1 encounter with jupiter. *Science*, 204:979–982, June 1979.

[2] C. W. Bowers S. Kraemer M. E. Kaiser A. C. Danks J. F. Grady J. J. Loiacono M. Brumfield L. Feinburg T. R. Gull S. R. Heap S. P. Maran D. Linder D. Hood. W. Meyer C. VanHouten V. Argabright S. Franka R. Bybee-D. Dorn M. Bottema R. Woodruff H. Garner J. G. Timothy M. Blouke C. L. Joseph G. Hartig R. F. Green E. B. Jenkins J. L. Linsky J. B. Hutchings H. W. Moos A. Boggess F. Roesler D. Weistrop B. E. Woodgate, R. A. Kimble. The space telescope imaging spectrograph design. *Publications of the Astronomical Society of the Pacific*, 110:1183–1204, October 1998.

[3] A. L. Broadfoot J. L. Bertaux J. E. Blamont M. J. S. Belton J. M. Ajello J. B. Holberg S. K. Atreya T. M. Donahue H. W. Moos D. F. Strobel J. C. McConnell A. Dalgarno R. Goody M. B. McElroy P. Z. Takacs B. R. Sandel, D. E. Shemansky. Extreme ultraviolet observastions from voyager 2 encounter with jupiter. *Science*, 23:962– 966, November 1979.

[4] D. F. Strobel B. R. Sandel, A. L. Broadfoot. Discovery of a longitudinal asymmetry in the h lyman-alpha brightness of jupiter. *Geophysical Research Letters*, 7(1):5–8, January 1980.

[5] Charles A. Barth. Interpretation of the mariner v lyman alpha measurements. *Journal of Atmospheric Sciences*, 25:564–567, July 1968.

[6] Chin-Ping Liu Mohammed Bahou Yuan-Pern Lee Yuk L. Yung M. F. Gerstell Bing-Ming Cheng, Eh Piew Chew. Photo-induced fractionation of water isotopomers in the martian atmosphere. *Geophysical Research Letters*, 26(24):3657–3660, December 1999.

[7] Dale A. Ostlie Bradley W. Carroll. *An Introduction to Modern Astrophysics*. Addison Wesley, 2 edition, 2007.

[8] H. A. Weaver J. A. McClintock C. B. Opal, P. D. Feldman. Two-dimensional ultraviolet imagery with a microchannel-plate/resistive-anode detector. *Proceedings of the International Society of Optics and Photonics (SPIE): Instrumentation in astronomy III*, 172:317–320, 1979.

[9] Tobias Owen David Crisp Jean-Pierre Maillard-Barry L. Lutz Catherine de Bergh, Bruno Bézard. Deuterium on venus: Observations from earth. *Science*, 251(4993):547–549, February 1991.

[10] Kenneth K. Kelly Lloyd Wallace William G. Fastie Charles A. Barth, Jeffrey B. Pearce. Ultraviolet emission observed near venus from mariner v. *Science*, 158(3809):1675–1678, December 1967.

[11] John T. Clarke Renée Prangé G. Randall Gladstone Joel Sommeria Gilda Ballester Claude Emerich, Lotfi Ben Jaffel. Evidence for supersonic turbulence in the upper atmosphere of jupiter. *Science*, 273(5278):1085–1087, August 1996.

[12] John T. Clarke Y. Kim G.E. Ballester R. Prangé J. Sommeria Claude Emerich, Lotfi Ben Jaffel. Hot hydrogen belt detected with ly-a high resolution observations of jovian atmosphere. *Bulletin of the American Astronomical Society*, 32(DPS Meeting 32):1641, 2000.

[13] John T. Clarke Y. Kim G.E. Ballester R. Prangé J. Sommeria Institut d'Astrophysique Spatiale Team Institut d'Astrophysique de Paris Team Claude Emerich, Lotfi Ben Jaffel. Hot atomic hydrogen in the upper jovian atmosphere confirmed with ly-a high resolution stis observations. *Bulletin of the American Astronomical Society*, 33(DPS Meeting 33):1067, 2001.

[14] D. McCoy J.-P. Lebreton S. Barabash J.-L. Bertaux P. Drossart V. Formisano B. Haeusler O. I. Korablev W. Markiewicz D. Neveance M. Petzold G. Piccioni T. L. Zhang F. W. Taylor E. Lellouch D. Koschny O. Witasse M. Warhaut A. Acomazzo J. Rodrigues-Cannabal J. Fabrega T. Schirmann A. Clochet M. Coradini D. V. Titov, H. Svedhem. Venus express: Scientific goals, instrumentation, and scenario of the mission. *Cosmic Research*, 44(4):334–348, 2006.

[15] Tom Stallard Steve Miller-Renee Prange Michele Dougherty Robert D. Joseph Daniel Rego, Nicholas Achilleos. Supersonic winds in jupiter's aurorae. *Nature*, 399:121–124, May 1999.

[16] William G. Fastie. A small plane grating monochromator. *Journal of the Optical Society of America*, 42(9):641–647, September 1952.

[17] D. Mugglestone G. D. Finn. Tables of the line broadening function h(a,v). *Monthly Notices of the Royal Astronomical Society*, 129:221–235, 1965.

[18] J. R. Barry G. J. Rottman, H. W. Moos. Lyman-alpha emission from arcturus. *The Astrophysical Journal*, 165:661–664, May 1971.

[19] G. J. Rottman H. W. Moos. Oi and hi emissions from the upper atmosphere of venus. *The Astrophysical Journal*, 169:L127–L130, November 1971.

[20] J. R. Barry J. L. Buckley H. W. Moos, R. C. Vitz. Small lif prism spectrometer for space applications. *Applied Optics*, 9(3):601–603, 1970.

[21] George R. Harrison. The production of diffration gratings: Ii. the design of echelle gratings and spectrographs. *Journal of the Optical Society of America*, 39(7):522–528, July 1949.

[22] Eugene Hecht. *Optics.* Addison Wesley, 4 edition, 2002.

[23] Jack J. Lissauer Imke de Pater. *Planetary Sciences.* Cambridge University Press, 2 edition, August 2001.

[24] R. R. Hodges J. H. Hoffman. Composition of the venus lower atmosphere from the pioneer venus mass spectrometer. *Journal of Geophysical Research*, 85(A13):7882–7890, December 1980.

[25] C. S. Freer H. W. Moos J. W. Giles, W. R. McKinney. An image-stabilized telescope - ten channel ultraviolet spectrometer for sounding rocket observations. *Space Science Instrumentation*, 1:51–59, February 1975.

[26] Franck Montmessin Jean-Loup Bertaux. Isotopic fractionation through water vapor condensation: The deuteropause, a cold trap for deuterium in the atmosphere of mars. *Journal of Geophysical Research*, 106(E12):32,879–32,884, December 2001.

[27] John T. Clarke Jean-Loup Bertaux. Deuterium content in the venus atmosphere. *Nature*, 338:567–568, April 1989.

[28] O. Korablev E. Villard E. QueŽmerais E. Neefs F. Montmessin F. Leblanc J.-P. Dubois E. Dimarellis A. Hauchecorne F. Lefevre P. Rannou J. Y. Chaufray M. Cabane G. Cernogora G. Souchon F. Semelin A. Reberac E. Van Ransbeek S. Berkenbosch R. Clairquin C. Muller-F. Forget F. Hourdin O. Talagrand A. Rodin A. Fedorova A. Stepanov I. Vinogradov A. Kiselev Yu. Kalinnikov Georges Durry B. Sandel A. Stern J. C. GeŽrard Jean-Loup Bertaux, D. Nevejans. Spicav on venus express: Three spectrometers to study the global structure and composition of the venus atmosphere. *Planetary and Space Sciences*, 55:1673–1700, 2007.

[29] Oleg Korablev E. Villard A. Fedorova D. Fussen E. QueŽmerais D. Belyaev-A. Mahieux F. Montmessin C. Muller E. Neefs D. Nevejans V. Wilquet J. P. Dubois A. Hauchecorne A. Stepanov I. Vinogradov A. Rodin the SPICAV/SOIR Team

Jean-Loup Bertaux, Ann-Carine Vandaele. A warm layer in venus' cryosphere and high-altitude measurements of hf, hcl, h2o and hdo. *Nature*, 450:646–649, November 2007.

[30] J. Hunter Waite Jr. John T. Clarke, John Trauger. Doppler shifted h ly-a emissionfrom jupiter's aurora. *Geophysical Research Letters*, 16(6):587–590, June 1989.

[31] Lotfi Ben Jaffel John T. Clarke, G. Randall Gladstone. Jupiter's dayglow h ly-a emission line profile. *Geophysical Research Letters*, 18(11):1935–1938, November 1991.

[32] P. D. Feldman H. W. Moos W. G. Fastie John T. Clarke, H. A. Weaver. Spatial imaging of hydrogen lyman alpha emission from jupiter. *The Astrophysical Journal*, 240:696–701, September 1980.

[33] Paul D. Feldman John T. Clarke, H. Warren Moos. Iue monitoring of the spatial distribution of the h ly-a emission from jupiter. *The Astrophysical Journal*, 245:L127–129, May 1981.

[34] T. Owen A. Nagy John T. Clarke, Jean-Loup Bertaux. Hst/stis observations of the extended martian upper atmosphere. *Bulletin of the American Astronomical Society*, 36:1182, 2004.

[35] Anton Tremsin Oswald Siegmund John Vallerga, Jason McPhate. The current and future capabilities of mcp based uv detectors. *Journal of Astrophysical Science*, 320:247–250, May 2009.

[36] Bruce Fegley Jr. Katharina Lodders. *The Planetary Scientist's Companion*. Oxford University Press, 1998.

[37] Charles F. Hall Lawrence Colin. The pioneer venus program. *Space Science Reviews*, 20:283–306, 1977.

[38] A. Vidal-Madjar Lotfi Ben Jaffel, C. Magnan. The lyman alpha albedo of jupiter. *Astronomy and Astrophysics*, 204(E12):319–326, December 1988.

[39] John T. Clarke Lotfi Ben Jaffel, Y. J. Kim. The h lyman-alpha emission line from the upper atmosphere of jupiter: Parametric radiative transfer study and comparison with data. *Icarus*, 190:504–527, April 2007.

[40] Renee Prange G. Randall Gladstone Alfred Vidal-Madjar Lotfi Ben Jaffel, John T. Clarke. The lyman alpha bulge of jupiter: Effects of a non-thermal velocity field. *Geophysical Research Letters*, 20(8):747–750, April 1993.

[41] H. W. Moos M. A. McGrath, G. E. Ballester. Jovian h2 dayglow emission (1978-1989). *Journal of Geophysical Research*, 95(A7):10,365–10373, July 1990.

[42] H. W. Moos M. Bottema, W. G. Fastie. A rocket telescope spectrometer with high precision pointing control. *Applied Optics*, 8(9):1821–1826, September 1969.

[43] R.R. Meier. Ultraviolet spectroscopy and remote sensing of the upper atmosphere. *Space Science Reviews*, 58:1–185, 1991.

[44] Donald M. Hunten Michael B. McElroy. The ratio of deuterium to hydrogen in the venus atmosphere. *Journal of Geophysical Research, Space Physics*, 74(7):1720–1739, April 1969.

[45] Jose M. Rodriguez Michael B. McElroy, Michael J. Prather. Escape of hydrogen from venus. *Science*, 215(4540):1614–1615, March 1982.

[46] J. Bixler S. Chakrabarti J. Vallerga S. Bowyer R. F. Malina O. H. W. Siegmund, M. Lampton. Wedge and strip image readout systems for photon-counting detectors in space astronomy. *Journal of the Optical Society of America*, 3:2139–2145, December 1986.

[47] J. M. Grebowsky H. G. Mayr R. E. Hartle, T. M. Donahue. Hydrogen and deuterium in the thermosphere of venus: Solar cycle variations and escape. *Journal of Geophysical Research*, 101(E2):4524–4538, February 1996.

[48] Laurent Pallier Lotfi Ben Jaffel Claude Emerich Joe Ajello John T. Clarke Gilda E. Ballester Renee Prange, Daniel Rego. Detection of self-reversed ly-a line from the jovian aurorae with the hubble space telescope. *The Astrophysical Journal*, 484:L169–L193, August 1997.

[49] François Robert. *Solar System Deuterium/Hydrogen Ratio*, chapter 17, pages 341–351. University of Arizona Press, 2006.

[50] Barbara Ryden. *Introduction to Cosmology*. Addison Wesley, 2003.

[51] Agustin Sanchez-Lavega. *An Introduction to Planetary Atmospheres*. Taylor and Francis, 2011.

[52] Jean Schneider. The extrasolar planets encyclopaedia. Online [http://exoplanet.eu/], February 1995. Accessed January 21, 2010.

[53] R. R. Hodges A. J. Watson T. M. Donahue, J. H. Hoffman. Venus was wet: A measurement of the ratio of deuterium to hydrogen. *Science*, 216(4546):630–633, May 1982.

[54] John R. Taylor. *An Introduction to Error Analysis: The Study of Uncertainties in Physical Measurements*. University Science Books, 2 edition, 1997.

[55] David A. Vallado. *Fundamentals of Astrodynamics and Applications*. Microcosm Press and Klumer Academic Publishers, 2 edition, 2001.

[56] G. Randall Gladstone Vladimir A. Kransnopolsky, Michael J. Mumma. Detection of atomic deuterium in the upper atmosphere of mars. *Science*, 280:1576–1580, June 1998.

[57] B. M. Glennon W. L. Wiese, M. W. Smith. *Atomic Transition Probabilities*, volume 1. U.S. Government Printing Office, 1966.

[58] John W. Caldwell Paul D. Feldman Brett C. Bush Daniel M. Cotton Supriya Chakrabarti Walter M. Harris, John T. Clarke. High-resolution ultravi-

olet spectrograph for sounding rocket measurements of planetary emission line profiles. *Optical Engineering*, 32(12):3016–3027, December 1993.

[59] Joseph Ladislas Wiza. Microchannel plate detectors. *Nuclear Instruments and Methods*, 162:587–601, 1979.